



**MEDNARODNA
PODIPLOMSKA ŠOLA
JOŽEFA ŠTEFANA**

**5. ŠTUDENSKA KONFERENCA
MEDNARODNE PODDIPLOMSKE ŠOLE
JOŽEFA ŠTEFANA**
Zbornik - 1. del

**5th JOŽEF ŠTEFAN
INTERNATIONAL POSTGRADUATE SCHOOL
STUDENTS' CONFERENCE**
Proceedings - Part 1



23. 05. 2013, LJUBLJANA

Zbornik 5. Študentske konference Mednarodne podiplomske šole Jožefa Stefana
(Proceedings of the 5th Jožef Stefan International Postgraduate School Students Conference)

Uredniki:

Nejc Trdin
Andraž Rešetič
Majda Pavlin
Božidar Cvetković

Založnik:

Mednarodna podiplomska šola Jožefa Stefana, Ljubljana

Tisk:

TISKARNA PLEŠKO d.o.o.

Naklada:

150 izvodov

Ljubljana, maj 2013

IPSSC organizira študentski svet Mednarodne podiplomske šole Jožefa Štefana
(IPSSC is organized by Jožef Stefan International Postgraduate School - IPS student council)

CIP - Kataložni zapis o publikaciji
Narodna in univerzitetna knjižnica, Ljubljana

5/6(082)
378.046-021.68:001.891(497.4)(082)

MEDNARODNA podiplomska šola Jožefa Stefana. Študentska konferenca (5 ; 2013 ; Ljubljana)
Zbornik = Proceedings / 5. študentska konferenca Mednarodne podiplomske šole Jožefa Stefana = 5th Jožef Stefan International Postgraduate School Students Conference, 23. maj 2013, Ljubljana, Slovenija ; [organizira študentski svet Mednarodne podiplomske šole Jožefa Štefana = organized by Jožef Stefan International Postgraduate School - IPS Student Council] ; uredili, edited by Nejc Trdin ... [et al.]. - Ljubljana : Mednarodna podiplomska šola Jožefa Stefana, 2013

ISBN 978-961-92871-5-6

1. Trdin, Nejc 2. Mednarodna podiplomska šola Jožefa Stefana (Ljubljana)
266944512

5. ŠTUDENTSKA KONFERENCA
MEDNARODNE PODIPLOMSKE ŠOLE
JOŽEFA STEFANA

ZBORNIK - 1. DEL

*5th JOŽEF STEFAN INTERNATIONAL
POSTGRADUATE SCHOOL STUDENTS'
CONFERENCE*

Proceedings - Part 1

Uredili / Edited by

Nejc Trdin, Andraž Rešetič, Majda Pavlin in Božidara Cvetković

23. 05. 2013, Ljubljana

Organizacijski odbor / Organising Committee

Nejc Trdin

Dejan Petelin

Andraž Rešetič

Majda Pavlin

Božidara Cvetković

Redakcijski odbor / Technical Review Committee

prof. dr. Marko Debeljak

prof. dr. Barbara Malič

prof. dr. Milena Horvat

prof. dr. Nives Ogrinc

prof. dr. Radmila Milačič

prof. dr. Janez Ščančar

prof. dr. Ester Heath

prof. dr. Boris Žemva

doc. dr. Tomaž Javornik

doc. dr. Aleš Švigelj

doc. dr. Darja Lisjak

doc. dr. Goran Dražić

doc. dr. Miha Čekada



Beseda predsednika MPŠ

Za uspešno ekonomsko tekmo v globalnem prostoru so potrebne nove in odlične ideje, ki so rezultat intenzivnih vlaganj v raziskave in inovacije. Živimo v času, ko je le odlično znanje pogoj za uspešno konkurenčnost gospodarstva. To pa pomeni tudi nova delavna mesta in bolj kvalitetno življenje. Ekonomski krizi so se v dobri meri izognile države, ki so se pravočasno zavedale pomena vlaganj v svojo znanost in raziskave, kot so skandinavske države, Nemčija, Švica, Nizozemska, da naštejemo le nekatere uspešne evropske države. Podobno velja tudi za nekaj drugih neevropskih držav. Še posebej pa se moramo zavedati, da ekonomsko uspešne države vlagajo velika finančna sredstva v znanost in raziskave in ob tem privabljajo mnoge uspešne uveljavljene raziskovalce, pa tudi odlične talentirane podiplomce in dodiplomce na delo in študije za potrebe njihovega nadaljnega ekonomskega razvoja v ekonomski tekmi na globalni ravni.

Ne glede na to, da smo del evropske skupnosti 27 držav, pa pametne med njimi in njihovi politiki vlagajo velika sredstva v razvoj lastnega gospodarstva in kakovosti življenja, zato so tudi uspešne pri tekmovanju za pridobivanje skupnih EU sredstev, ki jih financirajo v obliki Okvirnih programov, ERC projektov odličnosti in mnogih drugih razpisov. Skratka, če se hočemo izvleči iz stanja, v katerega smo zašli, bo potrebno slediti uspešnim. To pa zahteva premike v glavah odgovornih.

Da bi se Slovenija rešila nakopičenih problemov, ki so nas pripeljali v težko gospodarsko (tudi moralno) krizo, moramo dvigniti finančna vlaganja v možgane! Le to nam bo lahko omogočilo trajnostni razvoj. Smo namreč priča velikemu povečanju bega možganov in če hočemo to smer zaustaviti, moramo takoj ukrepati, da ne bo prepozno. Naporji naj bodo usmerjeni v promocijo in izboljšanje visokošolskega

izobraževanja ter raziskovalne dejavnosti. To je izziv za nove generacije, ki so upravičene do boljše prihodnosti, kot jim jo ponuja sedanost. Dolžni smo jim omogočiti, da se uspešno spopadejo z izzivi v domačem okolju, ne pa da iščejo izpolnitve svojih ambicij in eksistenčnih možnosti z odhodom v tujino.

Letos praznujemo 10. obletnico ustanovitve Mednarodne podiplomske šole Jožefa Stefana (MPŠ). S podporo uspešnih slovenskih gospodarskih podjetij je Institut »Jožef Stefan« ustanovil samostojni visokošolski zavod. Študijske usmeritve zajemajo nova področja, kot so nanotehnologije in nanoznanosti, informacijske in komunikacijske tehnologije, ekotehnologije ter s tem povezan menedžment. Upravičenost ustanovitve te podiplomske šole potrjuje dejstvo, da je bilo na primer v šolskem letu 2012/2013 vpisanih 154 podiplomcev. Od ustanovitve šole pa do danes je bilo podeljenih 118 doktoratov in 51 magisterijev.

Institut »Jožef Stefan« in MPŠ tesno sodelujeta in izkoriščata moderno in odlično raziskovalno opremo vključno s Centri odličnosti. Vrhunski kadrovske potenciali in izjemna vpetost v mednarodne povezave na globalnem nivoju omogočajo usposabljanje na najvišji ravni ter prenašanje znanja, pridobljenega na temeljnih in aplikativnih raziskavah, tudi v gospodarstvo. To je misija Mednarodne podiplomske šole ter prispevek k pospešenemu zagonu slovenskega gospodarstva ter hitrejšemu prehodu iz vsesplošne krize v družbo znanja.

Še enkrat bi poudaril: znanje je vrednota, ki omogoča narodu ekonomski razvoj in obstoj! Mladi vrhunski raziskovalci, ki so pogoj za uspešen gospodarski in vsesplošen razvoj, pa so srce družbe znanja.

Prof. dr. Vito Turk
Predsednik MPŠ



Beseda dekana MPŠ

Peta študentska konferenca Mednarodne podiplomske šole dosega presežnike, ki so si jih kot cilje zastavili naši podiplomci: kakovostnih prispevkov je več kot prejšnja leta, znanstvena raven je visoka in sodelovanje z gospodarstvom še močneje poudarjeno, poleg doktorandov in magistrandov so pritegnjeni tudi izbrani dodiplomci in vložek mentorjev ter recenzentov se je zvišal. To se ni rodilo spontano. Študentski svet MPŠ na čelu z Nejcem Trdinom je opravil izjemno zahtevno in obsežno delo, naše čestitke in priznanja so prigarani.

Zakaj ocenjujemo to konferenco kot zelo pomembno - ne le za MPŠ, tudi širše?

Dejstvi, da omogoča celoviti prikaz raziskovalnih dosežkov podiplomcev MPŠ in njihovih mentorjev ter da je ta konferenca v rokah študentov že po svoji zasnovi originalna, sta pomembni, vendar ne odločilni. Kar prepriča, je napor za uresničevanje vseh treh ključnih razsežnosti znanosti.

Prva razsežnost znanosti je - in bo ostala - odkrivanje novega znanja, prepoznavanje pojavov in iskanje resnice ali vsaj približevanje le-tej. Vsi udeleženci konference načrtno predstavljajo to iskanje kot znanstveno metodo, ki terja objektivno opazovanje in učinkovite, a tudi vse bolj zahtevne pristope in tehnike ter razvoj sposobnosti za postavljanje in preverjanje hipotez. Konferenco odlikuje tudi gojenje kakovostne predstavitve raziskovalnih dosežkov, tako v pisnih prispevkih kot v grafičnih prikazih.

Druga razsežnost znanosti je njen potencial za ustvarjalnost v proizvodnji in storitvah, kar je marsikdo žal spoznal šele v obdobju hude gospodarske krize. Ta konferenca kaže, da se mladi raziskovalci tega potenciala dobro zavedajo in zavzeto

razmišljajo, kako posredovati možnosti uporabe svojih raziskovalnih dosežkov v gospodarstvu. Dosedanjo kar še vedno globoko vrzel med znanostjo in gospodarstvom je nujno zapolniti - in ta konferenca je prispevek k temu. Zavedati pa se moramo, da znanstveni dosežki niso neposredne rešitve v gospodarstvu. Ti dosežki so le kot seme žita, ki pa je neogibni pogoj zato, da imamo kruh. Raziskovalci so dolžni poskrbeti, da je seme res kakovostno in primerno za izbrano njivo ter pomagati gospodarskim menedžerjem, ki morajo zagotoviti učinkovito setev, gojenje in žetev ter predelavo zrnja do kruha. Samo taka skupna pot vodi do dodane vrednosti kot materialnega pogoja za kakovost življenja.

In - ne nazadnje - tretja razsežnost znanosti: znanstvena kultura. Značilnosti zanjo so zlasti iskanje novih poti, spodbujanje različnih možnosti, objektivnost ocenjevanja in vse bolj tudi multidisciplinarna sinteza, spoštovanje znanja kot glavne človekove dobrine, upiranje predsodkom in pritegovanje čim širšega, čimbolj raznolikega dela prebivalstva v razumevanje znanstvenih kriterijev in ravnanje po njih. Naši podiplomci posvečajo veliko skrb ponazarjanju znanstvenih metod in dosežkov v naravnem jeziku - in prav to je najtežje: pisati tako, da bo čim širše razumljivo in hkrati skrbeti, da je znanstveno točno.

Prav zaradi načrtnega gojenja vseh treh glavnih razsežnosti znanosti bo 5. Študentska konferenca MPŠ zagotovo odmevala daleč prek zidov šole in instituta.

Prof. dr. Aleksandra Kornhauser-Frazer
Dekan MPŠ



Beseda predstavnice gospodarstva

Na svetovnem trgu lahko nastopamo med vodilnimi proizvajalci samo, če imamo podporo raziskovalnih inštitucij. Za najboljše rešitve, ki se uvrščajo v svetovni vrh v specifičnem tržnem programu podjetja, so potrebni znanje, ustvarjalnost, pogum in izkušnje. Prav to pa dosežemo z združevanjem raziskovalnega dela, s posluhom za sodelovanje tako na strani industrije kot raziskovalcev in s hitrim prenosom znanj v rešitve in izdelke za globalni trg.

To omogoča tudi razvoj MPŠ skupaj z IJS, ki si vsako leto nabirata izkušnje z novimi projekti. Prav tako pa predstavniki iz industrije, ki imamo vizijo trajnostnih inovativnih rešitev in nenehnega iskanja boljših tržnih priložnosti, iz lastnih razvojnih področij in s podporo raziskovalnih inštitucij, med katerimi IJS in MPŠ igrata pomembno vlogo, ustvarjamo rešitve, ki so v samem vrhu v svetovnem merilu ali pa celo narekujemo svetovne trende v globalnih tržnih nišah.

Letna študentska konferenca MPŠ je priložnost za spoznavanje novih znanstvenih dosežkov podiplomskih študentov in iskanje presečnih polj med idejnimi in laboratorijskimi rešitvami s področja znanosti ter novih priložnosti na globalnem trgu, ki jih prepozna industrija.

Kjer se srečujejo različni ljudje in z različnih področij, ki si znajo prisluhniti in sodelovati, se rojevajo najboljše rešitve. Iz globokega znanja, mladostne svežine, poguma in vztrajnosti v sodelovanju z izkušeno in prekaljeno industrijo se bodo rodile nove rešitve za zahtevni globalni trg, ki pričakuje - celo terja - vedno boljše, izvirnejše, zanesljive in cenejše rešitve.

Dr. Jožica Rejec
Predsednica uprave Domel d. d.



Andraž Rešetič (NANO), Majda Pavlin (EKO), Nejc Trdin (IKT), Božidara Cvetković (IKT)

Želiš prispevati k trajnostnemu razvoju? Spodbudi industrijo s svojo inovacijo!

Kot že v lanskem letu, smo organizatorji konference tudi letos dobili veliko podporo vodstva MPŠ, mentorjev in odličien odziv visokotehnoloških podjetij ter s tem potrditev, da študentska konferenca napreduje v prikazu znanstvenih dosežkov podiplomcev in je tudi vedno bolj zanimiva tako za podjetja kot za študente. Zato smo se z velikim zagonom in željami po ponovnih presežkih lotili organizacije že 5. študentske konference Mednarodne podiplomske šole Jožefa Stefana, ki je namenjena predvsem predstavitvi naših raziskav in možnosti njihove uporabe, tako visokotehnološkimi podjetjem kot širši publiki, v želji po našem prispevku k uveljavljanju znanosti in krepitvi povezav z gospodarstvom.

Ob začetku študijskega leta smo ponudili knjižico s splošnim opisom študentske konference, njenim namenom, dosedanjimi nagrajenci ter navodili za pripravo prispevkov za sodelovanje na konferenci. V sredini študijskega leta smo organizirali tudi sestanek z mentorji, na katerem smo podrobneje predstavili študentsko konferenco in poslanstvo le-te ter zahteve za učinkovito predstavitev dosežkov raziskovalnega dela podiplomcev. Priprave na konferenco smo obravnavali na sejah koordinacije, senata in upravnega odbora MPŠ. Prav tako smo tudi vsebino konference promovirali na socialnih omrežjih, z željo po čim večji udeležbi. Vse te zgodnje priprave so se obrestovale, saj smo letos prejeli kar 47 prispevkov. S tem smo dobili tudi potrditev študentov, da se zavedajo pomembnosti konference in si želijo sodelovanja s podjetji. V tem letu smo na konferenci prvič ponudili možnost sodelovanja odličnim dodiplomskim študentom. Od prejetih prispevkov so dodiplomski študenti prispevali tri.

Pri tako številnih prispevkih smo želeli zagotoviti visoko kvaliteto le teh, zato smo v letošnjem letu še razširili redakcijski odbor, ki je štel kar 13 članov. Vsak prispevek je bil temeljito pregledan s strani vsaj enega člana redakcijskega odbora. Recenzenti so se poleg znanstvene kakovosti prispevkov, tako plakatov, kot člankov, osredotočali tudi na pravilnost in razumljivost besedila ter še posebej na kakovost širše razumljivega povzetka, saj je ta bistvenega pomena za razumevanje naših raziskav, kar odpira tudi možnosti uporabe njihovih dosežkov.

Za posebno spodbujanje povezovanja med študenti in podjetji smo tudi letos pripravili panelno razpravo, na kateri bodo skupaj s študenti sodelovali vodilni razvojni strokovnjaki visokotehnoloških podjetij in mentorji ter vodstvo Mednarodne podiplomske šole Jožefa Stefana. Pri tem si želimo, da bi se srečanje razvilo v aktivno in produktivno razpravo, ki bo gradila most med pogledi razvojnikov iz gospodarstva in pogledi raziskovalcev na aktualne visokotehnološke probleme. S tem bi radi pripomogli k še tesnejšemu in uspešnejšemu skupnemu iskanju rešitev.

Ob pripravah na to zahtevno konferenco bi se radi v prvi vrsti zahvalili za sodelovanje in zaupanje študentom in njihovim mentorjem, saj njihovi prispevki odpirajo poglede na visoke dosežke naših raziskav in spodbujajo sodelovanje z gospodarstvom - torej nosijo konferenco. Zahvala gre tudi sodelujočim podjetjem, ki so kljub težkim časom pokazala veliko pripravljenost za sodelovanje. Brez njih bi konferenca izgubila ključni namen podpore prenosu znanja, pomagali pa so nam tudi pokriti nujne stroške konference.. Naša zahvala gre sodelavcem Mednarodne podiplomske šole Jožefa Stefana za vso pomoč in podporo. Posebej bi se radi zahvalili dekanji, prof. dr. Aleksandri Kornhauser-Frazer, ki je ogromno prispevala k sami konferenci s svojo neposredno podporo ter z odlično vizijo in idejami za prenos znanja, posebej za sodelovanje z gospodarstvom. Za pritegnitev gospodarstva bi se radi zahvalili dr. Emilu Rojcu, saj je skrbno iskal podjetja in jih pritegnil k sodelovanju na konferenci. Zahvala gre tudi mag. Sergeji Vogrinčič in Tadeji Samec, saj sta nam ves čas nudili pomoč pri reševanju organizacijskih problemov konference.. Veliko zahvalo dolgujemo članom redakcijskega odbora, ki so temeljito pregledali vse prispevke in s tem neposredno pripomogli k višanju kakovosti naše konference.

V konferenco je bilo vloženih veliko idej in priprav - upamo, da bo potekla uspešno in živela dalje kot še en prispevek mladih k ustvarjanju in prenosu znanja za trajnostni razvoj, ki je pogoj za višanje kakovosti življenja.

Uredniški odbor

Kazalo (Table of Contents)

Ekotehnologija (Ecotechnology)	2
Optimization of derivatization process for human metabolites of common cytostatics cyclophosphamide and ifosfamide <i>Marjeta Česen, Tina Kosjek, Ester Heath</i>	4
Determination of the isotopic composition of polycyclic aromatic hydrocarbons in environmental samples <i>Marinka Gams Petrišič, Nives Ogrinc</i>	15
Implementation and results of Research Fund for Coal and Steel funded project CoGasOUT at Coal-Mine Velenje <i>Sergej Jamnikar, Jerneja Lazar, Simon Zavšek, Ludvik Golob</i>	22
A novel method for speciation of Pt in human serum incubated with cisplatin, oxaliplatin and carboplatin by conjoint liquid chromatography on monolithic disks with UV and ICP-MS detection <i>Anže Martinčič, Radmila Milačič, Maja Čemažar, Gregor Serša, Janez Ščančar</i>	33
Chromate cannot exist in food samples <i>Breda Novotnik, Tea Zuliani, Janez Ščančar, Radmila Milačič</i>	40
Behaviour of Benzophenones under the Influence of Natural Sunlight <i>Kristina Pestotnik, Tina Kosjek, Uroš Kranjc, Ester Heath</i>	50
Stability of mercury compounds at high temperatures <i>Matej Sedlar, Majda Pavlin, Sani Bašič, Milena Horvat</i>	60
Molybdenum coordination compounds as precursors for the preparation of MoS₂ <i>Gleb Veryasov, Adolf Jesih</i>	70

Simulation of <i>mer</i>-[$MoBr_3Py_3$] Raman spectrum by DFT method	
<i>Gleb Veryasov, Dmitry Morozov, Adolf Jesih</i>	77
Karakterizacija mleka in sira z uporabo stabilnih izotopov lahkih elementov (<i>C</i>, <i>N</i> in <i>O</i>) v Sloveniji	
<i>Urša Vežjak, Kanduč Tjaša, Nives Ogrinc</i>	84
Fatty acid composition as a tool for determination of geographical origin and authenticity of milk and dairy products	
<i>Adrián Vicent, Marinka Petrišič, Marijan Nečemer, Nives Ogrinc</i>	90
Uporaba izotopov pri raziskavah podzemnih vod	
<i>Janja Vrzel, Nives Ogrinc</i>	97
Informacijske in komunikacijske tehnologije (Information and Communication Technologies)	106
Sensor as a Service using the VESNA Sensor Platform	
<i>Adnan Bekan, Carolina Fortuna, Matevž Vučnik, Mihael Mohorčič</i>	108
Estimation of Human Energy Expenditure Using Inertial Sensors and Heart Rate Sensor	
<i>Božidara Cvetković, Mitja Luštrek</i>	116
Potential Usage of Smartphone Inertial Sensors in Healthcare Applications	
<i>Hristijan Gjoreski, Simon Kozina, Matjaž Gams, Mitja Luštrek</i>	126
Business simulation game - an innovative pedagogical approach in business environment	
<i>Andrej Jerman Blažič, Tanja Arh</i>	136
Time-window selection for optimal generalization with noise	

variance reduction in ecological data <i>Vladimir Kuzmanovski, Marko Debeljak, Sašo Džeroski</i>	148
Gene function prediction for <i>Solanum tuberosum</i> from time-series gene expression data <i>Jurica Levatič, Živa Ramšak, Tjaša Stare, Dragi Kocev, Kristina Gruden, Sašo Džeroski</i>	158
Network Coding Aware Routing for Performance Boost in Wireless-Mesh-Networks <i>Erik Pertout, Kemal Alič, Aleš Švigelj, Mihael Mohorčič</i>	168
Learning bagged models of dynamic systems <i>Nikola Simidjievski, Ljupco Todorovski, Sašo Džeroski</i>	177
Pharmacokinetic model for the evaluation of a proposed drug delivery system <i>Maja Somrak, Miha Moškon, Dušan Vučko, Boštjan Pirš, Miha Mraz, Roman Jerala</i>	189
Semi-automatic construction of pattern rules for translation of natural language into semantic representation <i>Janez Starc, Dunja Mladenič</i>	199
Automated modeling of Rab5–Rab7 conversion in endocytosis <i>Jovan Tanevski, Ljupčo Todorovski, Sašo Džeroski</i>	209
Analysing Financial Vocabulary Using a New Semantic Subgroup Discovery System Hedwig <i>Anže Vavpetič, Petra Kralj Novak, Nada Lavrač</i>	219
Nanoznanosti in nanotehnologije (Nanosciences and Nanotechnologies)	230
Hidrotermalna sinteza fotokatalitične prevleke iz TiO_2 na aluminiju <i>Anže Abram, Goran Dražič</i>	232

- Transformations of alcohols mediated by N – halosuccinimides: reactions in solution or under solvent-free conditions**
Njomza Ajvazi, Stojan Stavber 239
- Electrical and thermal properties of polymer systems with coexisting ferroelectric and relaxor states**
Goran Casar, Xinyu Li, Jurij Koruza, Qiming Zhang, Vid Bobnar 250
- Synthesis of superparamagnetic clusters as a carrier for wine fining agents**
Peter Dušak, Slavko Kralj, Darko Makovec 257
- Investigation of the structural, optical and electrical properties of Ta_2O_5 -rich thin films from solution**
Raluca C. Frunză, Martin Strojnik, Marko Jankovec, Marko Topič, Barbara Malič 268
- Co-sintering of magnetoelectric composites of Co-ferrite and selected ferroelectrics**
Petra Jenuš, Darja Lisjak, Danjela Kuščer, Darko Makovec, Miha Drogenik 278
- The influence of oleic acid on the morphology and magnetic properties of $CoFe_2O_4$ nanoparticles**
Sonja Jovanović, Matjaž Spreitzer, Mojca Otoničar, Danilo Suvorov 288
- Microstructure, Yield Stress and Hardness in Weld Heat-Affected Zone of 9-12% Cr Steels**
Fevzi Kafexhiu, Franc Vodopivec, Jelena V. Tuma 296
- Single-step decoration of $MoSI$ based nanowires with platinum nanoparticles**
Andrej Kovič, Sumeet Kumar, Aleš Mrzel, Mojca Vilfan 304
- Photocatalytic water treatment with TiO_2 : slurry reactor vs. microreactor**

<i>Matic Krivec, Luka Suhadolnik, Kristina Žagar, Miran Čeh, Goran Dražić</i>	313
Raziskave tekočerkristalnih elastomerov z jedrsko magnetno resonanco <i>Jerneja Milavec</i>	323
Synthesis of LaF_3 nanoparticles <i>Olivija Plohl, Darja Lisjak, Darko Makovec, Miha Drogenik</i>	331
Analysis of the background under the e-beam and x-ray induced Auger peaks <i>Besnik Poniku, Igor Belič, Monika Jenko</i>	339
Preparation of stable colloidal aqueous suspensions of magnetic iron-oxide nanoparticles using aspartic acid as surfactant <i>Klementina Pušnik, Mihael Drogenik, Darko Makovec</i>	349
Obdelava polimernih podlag z nizkotlačno kisikovo plazmo za boljšo vezavo malignih človeških kostnih celic <i>Nina Recek, Alenka Vesel, Miran Mozetič</i>	357
The effect of silica sol infiltration on the properties of dental 3Y – TZP ceramics <i>Anastasia Samodurova, Andraž Kocjan, Irena Pribošič, Tomaž Kosmač</i>	366

Ekotehnologija (Ecotechnology)

Optimization of derivatization process for human metabolites of common cytostatics cyclophosphamide and ifosfamide

Marjeta Česen^{1,2}, Tina Kosjek^{1,2}, Ester Heath^{1,2}

¹ Department of Environmental Sciences, Jožef Stefan Institute, Ljubljana, Slovenia

² Jožef Stefan International Postgraduate School, Jamova 39, 1000 Ljubljana, Slovenia

marjeta.cesen@ijs.si

Abstract. In order to develop an analytical method for simultaneous determination of human metabolites of cytostatics cyclophosphamide and ifosfamide in aqueous matrices optimization of derivatization process, which improves sensitivities of such highly polar compounds in chemical analysis by gas chromatography-mass spectrometry (GC-MS) was studied. For this purpose, we performed experiments using different derivatization agents in diverse solvents and under various experimental conditions. Following compounds: carboxycyclophosphamide, carboxyifosfamide, 4-ketocyclophosphamide, 4-ketoifosfamide, N-dechloroethylcyclophosphamide (or 3-dechloroethylifosfamide) and 2-dechloroethylifosfamide were subject of this study. Results showed the need to split the method into three parts using one derivatization agent, N-(tert-butyldimethylsilyl)-N-methyltrifluoroacetamide with 1% tert-butyldimethylchlorosilane (MTBSTFA with 1 % TBDMCS). For N-dechloroethylcyclophosphamide and ketocyclophosphamide the highest responses were achieved when using 0.25 mL of acetonitrile with addition of 15 µL of derivatizing agent at 75 °C for 20 h and 90 °C for 16 h, respectively. Highest responses for 2-dechloroethylifosfamide were achieved when using 0.25 mL of toluene and 30 µL of derivatizing agent at 75 °C for 20 h.

Keywords: cytostatic, metabolite, derivatization, gas chromatography-mass spectrometry

1 Introduction

The increasing consumption of pharmaceuticals raises concerns about their presence and effects in the environment, which is especially alarming in case of cytostatics since they exhibit cytotoxic, genotoxic, mutagenic and teratogenic effects. Among them, cyclophosphamide (CP) and ifosfamide (IF), which belong to a group of alkylating agents, are one of the most commonly prescribed drugs in chemotherapy. As all xenobiotics, CP and IF undergo partial metabolism in human body, which is followed by their elimination *via* urine in unchanged forms or as metabolites. Studies by Joqueviel et al. and Gilard et al. reported that cumulative drug excretion measured over 24 h in patients was around 50 % of the injected CP and IF dose, where approximately 70 % of it were excreted as metabolites (carboxycyclophosphamide (carboxy-CP), ketocyclophosphamide (keto-CP), N-dechloroethylcyclophosphamide (N-dechloroethyl-CP), 2-dechloroethylifosfamide (2-dechloroethyl-IF), 3-dechloroethylifosfamide (structural analogue of N-dechloroethyl-CP), carboxyifosfamide (carboxy-CP), etc.)) [1],[2]. These pharmacokinetic data together with unknown effects of CP's and IF's metabolites in aqueous environment reveal the need to include them in studies concerning environmental behaviour of parent compounds, which to our knowledge have not been performed yet. Based on already published papers concerning environmental concentrations of CP and IF in surface waters and wastewaters [3],[4] and pharmacokinetic studies, the expected concentrations of their metabolites are in ng L^{-1} up to $\mu\text{g L}^{-1}$ ranges, hence, the application of highly sensitive analytical methods for trace amounts of analytes, such as liquid chromatography or gas chromatography coupled to mass spectrometry (GC-MS), is needed. Furthermore, the sensitivity of GC-MS analysis can be improved by derivatization process, which as preliminary step also transforms such highly polar substances to more volatile derivatives (Figure 1).

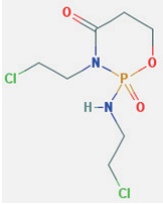
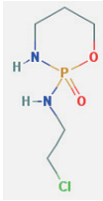
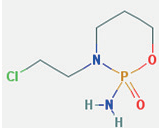
Figure 1: Analytical method for chemical analysis of aqueous samples.



In order to develop analytical method for trace amounts of CP's and IF's metabolites (Table 1) in aqueous samples by GC-MS, the optimization of derivatization process is presented in this study.

Table 1: Names, structures and molecular weights (MW) for selected metabolites of CP and IF.

Name and abbreviation IUPAC name	Structure	MW
carboxycyclophosphamide carboxy-CP 3-[amino-[bis(2-chloroethyl)amino]phosphoryl]oxypropionic acid		293.08
carboxyifosfamide carboxy-IF 3-bis(2-chloroethylamino)phosphoryloxypropionic acid		293.08
4-ketocyclophosphamide keto-CP 2-[bis(2-chloroethyl)amino]-2-oxo-1,3,2λ5-oxazaphosphan-4-one		275.07

<p>4-ketoifosfamide keto-IF</p> <p>3-(2-chloroethyl)- 2-(2-chloroethylamino)-2-oxo-1,3,2λ5- oxazaphosphinan-4-one</p>		275.07
<p>N-dechloroethylcyclophosphamide or 3-dechloroethylifosfamide N-dechloroethyl-CP</p> <p>N-(2-chloroethyl)-2-oxo-1,3,2λ5- oxazaphosphinan-2-amine</p>		198.59
<p>2-dechloroethylifosfamide 2-dechloroethyl-IF</p> <p>3-(2-chloroethyl)-2-oxo-1,3,2λ5- oxazaphosphinan-2-amine</p>		198.59

2 Materials and methods

2.1 Reagents, chemicals and standards

Carboxy-CP, carboxy-IF, 4-keto-CP, 4-keto-IF, N-dechloroethyl-CP (or 3-dechloroethylifosfamide) and 2-dechloroethyl-IF were obtained from Niomech - IIT GmbH (Bielefeld, Germany). The isotopically labelled internal standard (\pm)-ibuprofen-d3 (α -methyl-d3) (dIBU, 99.4 % atom % D, CAS 121662-14-4) was purchased from C/D/N Isotops (Quebec, Canada). Derivatizing agents heptafluorobutyric anhydride (99 %, CAS 375-22-4) and trifluoroacetic anhydride (99 %, CAS 407-25-0) were purchased from Fluka (Buchs, Switzerland), N-(tert-butylidimethylsilyl)-N-methyltrifluoroacetamide (MTBSTFA, 97 %, CAS 77377-52-7) was purchased from Acros Organics (New Jersey, USA), N-methyl-N-(trimethylsilyl)trifluoroacetamide (MSTFA, 98.5 %, CAS 24589-78-4), acetic anhydride (Ac₂O, 98 %, CAS 108-27-7), heptafluorobutyric anhydride (HFBA, 99 %, CAS 32477-35-3), N-methyl-bis(trifluoroacetamide) (MBTFA, 99 %, CAS 685-27-8),

2,3,4,5,6-pentafluorobenzyl bromide (PFBBBr, 99 %, CAS 1765-40-8), 2,3,4,5,6-pentafluorobenzoyl chloride (PFBCl, 99 %, CAS 2251-50-5) were purchased from Sigma Aldrich (Steinheim, Germany), N-(tert-butyldimethylsilyl)-N-methyltrifluoroacetamide with 1% tert-butyldimethylchlorosilane (MTBSTFA with 1 % TBDMCS, 95 %, CAS 77377-52-7) was purchased from Aldrich (Steinheim, Germany). Solvents acetone, dichloromethane, ethyl acetate and methanol were purchased from J. T. Baker (Deventer, Netherlands), pyridine and toluene were purchased from Merck (Darmstadt, Germany) and were all of analytical grade purity. Stock solutions for chemical analysis of selected compounds were prepared in methanol at approximate concentrations 50 $\mu\text{g mL}^{-1}$.

2.2 Instrumental analysis

The analytical method was based on GC-MS. HP 6890 series (Agilent, Waldbron, Germany) gas chromatograph with a single quadrupole mass selective detector was used. The programme of GC oven was as follows: an initial temperature 65 °C was held for 3 min, then ramped at 20 °C min^{-1} to 280 °C and finally held for 2 min. Total GC-MS runtime was 15.75 min. A capillary column, with He as the carrier gas, was a DB-5 MS 30 m \times 0.25 mm \times 0.25 μm (Agilent J&W, CA, USA). Aliquots (1 μL) of the samples were injected in splitless mode at 280 °C. The MS operated in EI ionisation mode at 70 eV. The GC-MS used Chemstation software for instrumental control and data processing.

3 Results and discussion

3.1 Optimization of derivatization process

Optimization of derivatization process started with 30 μL of different derivatizing agents (MSTFA, MTBSTFA, MTBSTFA with 1 % TBDMCS, HFBA, TFAA, HFBI, MBTFA, PFBCl, Ac_2O , PFBBBr and PFBHA) according to functional groups of selected metabolites, where 1 mL of ethyl acetate as solvent was used (Table 2). Experiments were performed at 60 °C and 80 °C for 1 h – 16 h.

Table 2: Derivatization agents.

Type	derivatizing agent	Functional groups of analyte
Silyating agents	MSTFA	-NH -COOH
	MTBSTFA	
	MTBSTFA with 1 % TBDMCS	
Acylation agents	HFBA	
	TFAA	
	HFBI	
	MBTFA	
	PFBCl	
	AC ₂ O	
Alkylating agent	PFBBr	-NH -COOH
Other	PFBHA	-CO

The comparison of chromatographic responses and thermal stability in full scan spectra by GC-MS in EI ionization mode revealed that the optimal derivatizing agent was MTBSTFA with 1 % TBDMCS for (successful derivatization of) three metabolites: N-dechloroethyl-CP, 2-dechloroethyl-IF and keto-CP. The characteristic ion fragments for each metabolite and internal standard dIBU, derivatized with MTBSTFA with 1 % TBDMCS were determined for selective ion monitoring (Table 3).

Table 3: Metabolite derivatives with retention times and ion fragments.

compound derivative	retention time (min)	characteristic ion fragments
N-dechloroethyl-CP	12.84	308, 280, 195
2-dechloroethyl-IF	13.15	257, 255, 136
keto-CP	13.65	297, 295, 242
dIBU	12.03	266, 205

Further optimization involved the use of different solvents (acetone, acetonitrile, cyclohexane, dichloromethane and toluene) with 30 μ L of MTBSTFA with 1 % TBDMCS at fixed time and temperature of the reaction (16 h at 80 °C). The results showed large differences in responses among solvents, e.g. 2-dechloroethyl-IF gave highest responses in toluene, whereas in acetonitrile and acetone the derivatization was not successful. On the contrary, derivatization of keto-CP and N-dechloroethyl-CP was the most successful in acetonitrile and acetone and not in toluene. Due to observed frequent evaporation of acetone in reaction chambers despite using glass

vials with teflon septums during derivatization process, this solvent was abandoned in further experiments.

In order to estimate the influence of time and temperature on reaction responses, we performed experiments with MTBSTFA with 1 % TBDMCS and solvents chosen above for each metabolite at several times and temperatures. Since responses of analytes after 1 h and 2 h were very low in first experiment, we performed reactions at longer periods of time (16 h, 20 h, 24 h, 28 h and 32 h). To examine the influence of temperature, we performed experiments for each time at 60 °C, 75 °C and 90 °C. The dependence of responses on time and temperature is represented in Figures 2, 3 and 4 (for N-dechloroethyl-CP, 2-dechloroethyl-IF and keto-CP, respectively).

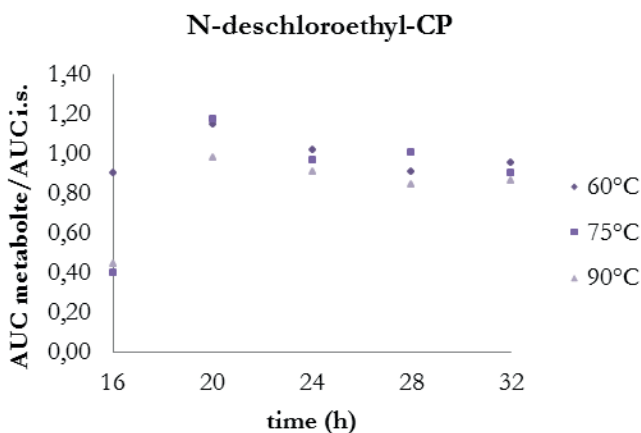


Figure 2: Ratios between responses shown as AUC (area under the curve) of N-dechloroethyl-CP and dIBU at different times and temperatures..

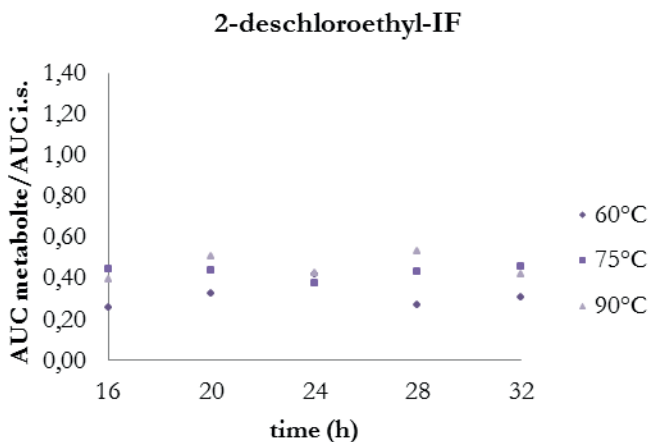


Figure 3: Ratios between responses shown as AUC of 2-dechloroethyl-IF and dIBU at different times and temperatures.

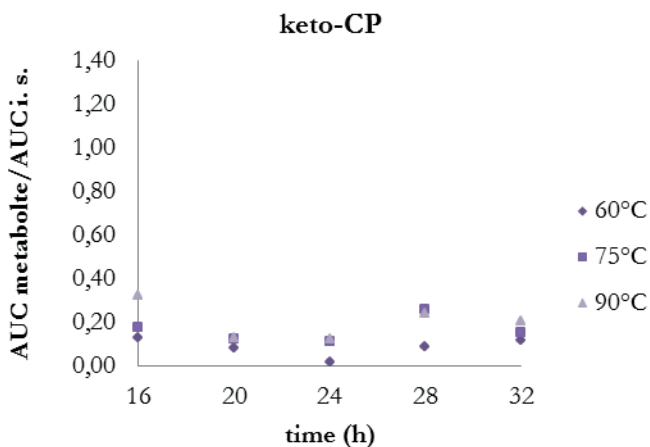


Figure 4: Ratios between responses shown as AUC of keto-CP and dIBU at different times and temperatures.

The comparison of Figures 1, 2 and 3 reveals that derivatization of N-dechloroethyl-CP gave highest responses, which were achieved when the process was performed at 75 °C for 20 h. The influence of time and temperature was not that crucial in case of 2-dechloroethyl-IF, therefore, further experiments were performed at same

conditions as for N-dechloroethyl-CP (20 h at 75 °C). Responses of derivatized keto-CP were lower, however, the highest were achieved when process was performed at 90 °C for 16 h.

Furthermore, the variations in quantitative ratios between derivatizing agent and solvent were also examined by varying both volume of solvent (0.25 mL – 1 mL) and derivatizing agent (5 µL – 30 µL). Results showed that the optimal volume of solvent was 0.25 mL for all selected compounds. Further, for N-dechloroethyl-CP and keto-CP 15 µL of derivatizing agent was the appropriate amount, whereas for 2-dechloroethyl-IF, 30 µL gave highest responses.

Based on these experiments, the optimal conditions of derivatization process (time and temperature, the amount of derivatizing agent and appropriate solvent) for each metabolite are stated in Table 4.

Table 4: The optimal conditions for derivatization process of each compound.

compound	time / temperature	V _{solvent}	V _{der. agent}
N-dechloroethyl-CP	75 °C / 20 h	0.25 mL (acetonitrile)	15 µL
2-dechloroethyl-IF	90 °C / 16 h	0.25 mL (toluene)	30 µL
keto-CP	75 °C / 20 h	0.25 mL (acetonitrile)	15 µL

3.2 Further work

We are currently proceeding with development of analytical method for determination of selected compounds in aqueous matrices. Once analytical method is developed and validated, it will be applied in further investigations, including quantitative analysis of Slovene wastewaters and surface waters and degradation studies, such as biological treatment and abiotic water treatments (e.g. UV degradation). Furthermore, in order to gain knowledge concerning the effects in the aqueous environment, ecotoxicological tests for parent compounds and their metabolites will be assessed.

References:

- [1] C. Joqueviel, R. Martino, V. Gilard, M. C. Malet-Martino, U. Niemeyer. Urinary Excretion of Cyclophosphamide in Humans, Determined by Phosphorus-31 Nuclear Magnetic Resonance Spectroscopy. *Drug Metabolism and Disposition*, 26: 418-428, 1998

- [2] V. Gilard, M. C. Malet-Martino, M. de Forni, U. Niemeyer, J. C. Ader, R. Martino. Determination of the urinary excretion of ifosfamide and its phosphorylated metabolites by phosphorus-31 nuclear magnetic resonance spectroscopy. *Cancer Chemotherapy and Pharmacology*, 31(5): 387-94, 1993
- [3] T. Steger-Hartmann, K. Kümmerer, J. Schecker. Trace analysis of the antineoplastics ifosfamide and cyclophosphamide in sewage water by twostep solid-phase extraction and gas chromatography-mass spectrometry. *Journal of Chromatography A* 726: 179-184, 1996
- [4] J. Yin, B. Shao, J. Zhang, K. Li. A Preliminary Study on the Occurrence of Cytostatic Drugs in Hospital Effluents in Beijing, China. *Bulletin of Environmental Contamination and Toxicology*, 84: 39-45, 2010

For wider interest

Cyclophosphamide and ifosfamide are drugs, mainly used in chemotherapy to treat cancer and some autoimmune diseases. After chemotherapy, these compounds undergo metabolism in human body and are finally excreted *via* urine in initial form and as metabolites. There is still little known about the occurrence and transformations of cytostatic drugs in aqueous environment and even less about the fate of their human metabolites. In our study, we will develop an analytical method for determination of human metabolites of cyclophosphamide and ifosfamide in low environmental concentrations in aqueous matrices. We have already optimized the first step – derivatization process, which is necessary for chemical analysis with gas chromatography coupled to mass spectrometry. Following step will be optimization of solid phase extraction of aqueous samples, which will enable us to quantitatively determine their presence in Slovene wastewaters and surface waters. In addition, we will perform laboratory-scale experiments for degradation studies of selected metabolites of cyclophosphamide and ifosfamide (N-dechloroethyl-CP, 3-dechloroethyl-IF, 2-dechloroethyl-IF and keto-CP).

Determination of the isotopic composition of polycyclic aromatic hydrocarbons in environmental samples

Marinka Gams Petrišič^{1,2}, Nives Ogrinc^{1,2}

¹ Department of Environmental Sciences, Jožef Stefan Institute, Ljubljana, Slovenia

² Jožef Stefan International Postgraduate School, Ljubljana, Slovenia

marinka.petrisic@ijs.si

Abstract. Much interest has recently been paid on the source identification of polycyclic aromatic hydrocarbons (PAH) in environmental studies. This paper presents the study where compound specific carbon isotope analysis was performed to determine the source inputs of PAH to sediments of Lake Bled, Slovenia. Analysis of $\delta^{13}\text{C}$ values of individual PAH pure standards and in the standard mixture of PAHs were performed with the accuracy ranging between 0.2 and 1.0‰. Due to these analytical limitations isotopic characterization was performed in lake sediments at the depth of 12-14 cm and 14-16 cm corresponding to the period 1944-1961. The distribution of $\delta^{13}\text{C}$ values of individual PAH ranging between -29.5‰ and -21.7‰ showed that PAH input to lake sediments was of pyrolytic origin, likely dominated by coal/wood burning. PAH from carsoots could also contribute to the overall isotope signatures at the depth of 12-14 cm.

Keywords: polycyclic aromatic hydrocarbons; tracers; stable carbon isotopes; lake; sediments

1 Introduction

A number of environmental geochemistry techniques have been used to study organic pollutants over the past few decades in response to growing concerns about human impact. These techniques also exploit the unique molecular and isotopic compositions of polycyclic aromatic hydrocarbons (PAH) which are planar, high molecular weight organic compounds of environmental concern due to their suspected mutagenic and carcinogenic properties [1]. PAH exhibit different molecular distribution according to their origin formed during incomplete organic matter combustion (pyrolytic origin) or natural and anthropogenic fossil fuel

combustibles (petrogenic origin). Recently the application of compound-specific stable isotope analysis (CSIA) is receiving increasing attention as an innovative approach to address the origin of organic pollutants such as PAH in the environment [2, 3]. Source identification using stable isotopes is only possible if organic compounds are resistant to chemical and biological alteration processes.

The primary objectives of the proposed study were: (1) to determine the precision and accuracy of the isotopic composition of PAH in standards using GC-C-IRMS and (2) the determination of the carbon isotopic composition of individual PAH in sediments of Lake Bled.

Lake sediments were found to be more useful in evaluating and reconstructing historical records of contaminant inputs such as PAH comparing to sea sediments due to limitation of post-depositional mixing processes. However, studies on stable carbon isotope composition of PAH in sediment cores to determine their sources are limited [9].

2 Methods

2.1 Sample collection

Sediment samples were taken in Lake Bled in October 2011 at the deepest part of the lake where anoxic conditions prevail during the whole year. Sediment samples were taken using a gravity core sampler equipped with a Plexiglas tube (6 cm i.d.) and were extruded and sectioned into 1 and 2 cm intervals, freeze-dried, homogenized and ground to a fine powder for analyses.

2.2 GC-C-IRMS precision and accuracy measurements

The precision and accuracy of the $^{13}\text{C}/^{12}\text{C}$ ratio of individual compounds in PAH standards was determined using two different techniques. First $^{13}\text{C}/^{12}\text{C}$ ratios of individual PAH were determined using an elemental analyzer and isotope ratio mass spectrometer (EA-IRMS). The 250-500 μg of individual PAH standard was loading into tin capsules in triplicate. The measurements were performed on Europa Scientific 20-20 mass spectrometer with ANCA-SL preparation module for solid and liquid samples. Second PAH standards were prepared by weighing approximately 20 mg of each individual compound and dissolved with dichloromethane. Standards ranging in concentrations from 50 to 2200 ng L^{-1} were then prepared from these original stock solutions and analysed by GC-C-IRMS [4]. PAH standard mixtures with nominal concentrations of 500 ng L^{-1} was prepared for instrument

standardization and calibration. In addition the mixed solution with individual PAH was prepared and measured by GC-C-IRMS.

2.3 Determination of the concentrations and $\delta^{13}\text{C}$ values of PAH in samples

Sediment samples were extracted by Soxhlet extraction and extracts concentrated by rotary evaporator, solvent-exchanged to hexane and fractionated on a glass silicagel column. After eluting aliphatic hydrocarbon, PAHs were eluted using 25 ml of hexane and 20 ml of hexane:toluene (3:1). Both PAH fractions were combined and concentrated with rotary evaporator. Fractions were dried using nitrogen and redissolved in iso-octane and continued with instrumental analysis. The individual compounds of PAH were analyzed and identified with a Hewlett-Packard 6890 GC coupled to an MSD mass spectrometer using a DB-5ms (30 m \times 0.25 mm i.d., 0.25 μ m) capillary column with helium as a carrier gas.

Compound specific stable isotope ratios were determined using an Isoprime GV GC-C-IRMS system. Samples were injected and stable carbon isotopic composition determined by duplicate analyses. Carbon isotope measurements were reported in delta notation (δ) relative to the Vienna-Pee Dee Belemnite (V-PDB) standard as follows (in ‰):

$$\delta^{13}\text{C} = \left[\frac{\left(\frac{^{13}\text{C}}{^{12}\text{C}} \right)_{\text{sample}}}{\left(\frac{^{13}\text{C}}{^{12}\text{C}} \right)_{\text{standard}}} - 1 \right] \cdot 1000 \quad (1)$$

$\delta^{13}\text{C}$ values in samples were calibrated against reference CO_2 . The reference CO_2 was previously calibrated against V-PDB and introduced directly into the source two times at the beginning and end of every isotopic GC determination. The precision of measurements on EA-IRMS was 0.2‰, while on GC-C-IRMS the precision was on average 0.5‰.

3 Results and Discussion

3.1 GC-C-IRMS precision and accuracy measurements

The average isotope ratio for individual 11 PAH standards are presented in Fig. 1, which includes the values obtained by EA-IRMS and GC-C-IRMS. The PAHs exhibit $\delta^{13}\text{C}$ values in the range from -27.3 to -22.7 ‰ with GC-C-IRMS values always higher comparing to values obtained by EA-IRMS. The isotopic composition of the EA-IRMS measurements is taken as a ‘true values’ of the standard PAH and thus the accuracy of the GC-C-IRMS determinations ranged between 0.5 and 1.0‰.

$\delta^{13}\text{C}$ values of Ace, F, Py, BaA, Cry, BbFl and BaPy are comparable with the data obtained by O'Malley et al. [4, 5] with the lowest $\delta^{13}\text{C}$ value determined in BaA.

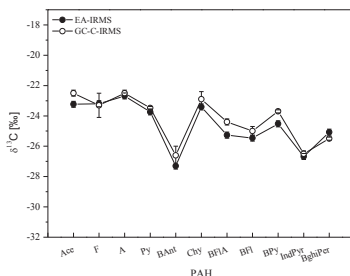


Figure 1: Comparison between $\delta^{13}\text{C}$ values obtained for the PAH pure standards using conventional EA-IRMS and GC-C-IRMS. Acenaphthene, Ace; fluorine, F; phenanthrene, Ph; anthracene, A; fluoranthene, Fl; pyrene, Py; benz(a)anthracene, BaA; chrysene, Chy; benzo(b)fluoranthene, BbFl; benzo(a)pyrene, BaPy; benzo(ghi)perylene, BghiPer; indeno(123-cd)pyrene, IndPy.

3.2 Lake sediment samples

Concentrations of total PAHs were $4,380 \text{ ng g}^{-1}$ at the surface and they decreased with depth. The maximum concentration of $7,650 \text{ ng g}^{-1}$ was reached at the depth from 12-16 cm. This section was dated previously as about 1944 to 1961 [6]. The concentrations dropped after 16 cm and then again increased at the depth of 24-28 cm (deposited around 1894-1911) where the concentrations were up to $2,470 \text{ ng g}^{-1}$. Individual PAH content ranged from 26 to 250 ng g^{-1} , while at the maximum concentrations they ranged from 35 ng g^{-1} to 758 ng g^{-1} . It was found that PAH have a pyrolytic origin (fluoranthene (Fl), pyrene (Py), benzo[a]anthracene (BaA), chrysene (Chy), benzo[e]pyrene (BePy), benzo[a]pyrene (BaPy), indeno[1,2,3-cd]pyrene (IndPy), benzo[ghi]perylene (BghiPer)) and they exhibited similar depth profile, although their abundances differed.

The isotopic composition of different PAH was only possible at the depths with higher PAH concentrations at 12-14 and 14-16 cm and for those PAHs which concentration was higher than 30 ng g^{-1} . Sample purification has demonstrated that a significant portion of interfering material was eliminated, however benzo(e)pyrene/benzo(a)pyrene was difficult to analyzed separately due to poor peak quality and size.

Pyrolysis has been suggested as the dominant contributor of PAH to Lake Bled excluding retene and perylene, which were mainly of natural origin [7]. In fact the

$\delta^{13}\text{C}$ values of different PAH confirmed this assumption. $\delta^{13}\text{C}$ values ranged between -29.5‰ to -21.7‰ . The lowest $\delta^{13}\text{C}$ value of -29.5‰ was determined in Chy at the depth of 14-16 cm, while the highest $\delta^{13}\text{C}$ value of -21.7‰ was found in Py at the depth of 12-14 cm. Higher $\delta^{13}\text{C}$ values indicate anthropogenic source of PAHs. The $\delta^{13}\text{C}$ values of individual PAHs were higher than the bulk organic carbon $\delta^{13}\text{C}$ values that ranged between -34.8 and -31.5‰ in the same sediment interval [8]. Higher variations were observed for the low molecular than for the high-molecular weight species at different sediment depth. The $\delta^{13}\text{C}$ values were higher for 4- and 5-ring PAHs, particularly for Py with $\delta^{13}\text{C}$ values of -21.7‰ and -22.7‰ at the depth of 12-14 cm and 14-16 cm, respectively. The difference between $\delta^{13}\text{C}$ values at two different depths was observed for 3- and 4-ring PAHs, while 5-ring PAHs have similar $\delta^{13}\text{C}$ values. $\delta^{13}\text{C}$ values increased from F to Py from -28.2 to -21.7‰ at the depth of 12-14 cm. Similar trend in $\delta^{13}\text{C}$ values were typically observed in carsoots fingerprint found in literature [2, 5, 9]. Unlike the carsoots the wood burning source is characterized by ^{13}C -enriched BaA relative to Fl and Py. Unfortunately it was not possible to determined $\delta^{13}\text{C}$ values in BaA in our study and thus could not be compared with O'Malley et al. [5] data. In addition in his study ^{13}C -depletion in Chy and BFl was also observed in the fireplace soot samples. Our data showed higher $\delta^{13}\text{C}$ values for BFl and lower $\delta^{13}\text{C}$ values for Chy at both depths. In addition the measured $\delta^{13}\text{C}$ value of -28.4‰ for A at the depth of 14-16 cm is outside the range reported by O'Malley et al. [5]. Similar observation was also found in the study performed by Stark et al. [10] in St. Lawrence River sediments suggesting that type of wood could influence the $\delta^{13}\text{C}$ values of PAHs. The type of burning material could be also the reason for the differences in the PAHs $\delta^{13}\text{C}$ values observed in our study. It was suggested that coal is the main burning material in Lake Bled sediments [6]. However, combustion of different fuels can yield similar mixtures of pyrogenic PAHs and the range in $\delta^{13}\text{C}$ values of the main energy sources (coal, petroleum and wood) greatly overlaps in the -30 to -20‰ range. Hence, the difficulty in relying solely on $\delta^{13}\text{C}$ values to separate the contribution of PAH derived from one combustion process versus another. On balance, however, our results overlap with $\delta^{13}\text{C}$ values measured by O'Malley et al. [5] implying that combustion were the main source of PAH in Lake Bled sediments at the depth 14-16 cm, while at the depth of 12-14 cm a vehicular emissions could also represent an important source of PAH.

4 Conclusion

Compound specific carbon isotope analysis was performed on individual PAH pure standards and in the standard mixture of PAHs with a precision of 0.2 to 0.4‰ and an accuracy ranging between 0.3 and 1.0‰. GC-C-IRMS measurements in sediment samples were performed with a precision of 0.3‰ for well separated PAH compounds and up to 1.0‰ for some coeluting isomers. The overall trend in PAH $\delta^{13}\text{C}$ values ranging between -29.5‰ and -21.7‰ were quite distinct and were useful to identify possible source of contamination. The dominant signatures identified at the depth of 12-14 and 14-16 cm in sediments of Lake Bled were mainly attributed to a coal/wood burning source, but PAH from carsoots could also contributed to the overall isotope signatures at the depth of 12-14 cm. The 12-14 cm and 14-16 cm depths in sediments correspond to the period 1953-1961 and 1944-1953, respectively. This study indicates that isotopic composition of PAH is a useful parameter to obtain more detailed source identification of organic pollutants in environmental samples including sediments.

References:

- [1] E. Wilkes. Isotopic and molecular methods: sourcing environmental PAHs: a review. *Dartmouth Undergraduate Journal of Science*, 33-36, 2011.
- [2] V. P. O'Malley et al. Stable carbon isotopic apportionment of individual polycyclic aromatic hydrocarbons in St. John's Harbor, Newfoundland. *Environmental Science and Technology*, 30: 634-639, 1996.
- [3] C. McRae et al. $\delta^{13}\text{C}$ values of coal-derived PAHs from different processes and their application to source apportionment. *Organic Geochemistry*, 30: 881-889, 1999.
- [4] V. P. O'Malley et al. Using GC-MS/Combustion/IRMS to determine the $^{13}\text{C}/^{12}\text{C}$ ratios of individual hydrocarbons produced from the combustion of biomass materials—application to biomass burning. *Organic Geochemistry*, 27: 567-581, 1997.
- [5] V. P. O'Malley et al. Determination of the $^{13}\text{C}/^{12}\text{C}$ ratios of individual PAH from environmental samples: can PAH sources be apportioned? *Organic Geochemistry*, 21: 809-822, 1994.
- [6] G. Muri, S. G. Wakeham. Source assessment and sedimentary record of pyrolytic polycyclic aromatic hydrocarbons in Lake Bled (NW Slovenia). *Acta Chimica Slovenica*, 56: 315-321, 2009.
- [7] G. Muri, S. G. Wakeham. Effect of depositional regimes on polycyclic aromatic hydrocarbons in Lake Bled (NW Slovenia) sediments. *Chemosphere* 77: 74-79, 2009.
- [8] I. Mandić-Mulec et al. Methanogenesis pathways in a stratified eutrophic alpine lake (Lake Bled, Slovenia). *Limnology and Oceanography*, 57: 868-880, 2012.
- [9] T. Okuda et al. Molecular composition and compound-specific stable carbon isotope ratio of polycyclic aromatic hydrocarbons (PAHs) in the atmosphere in suburban areas. *Geochemical Journal*, 38: 89-100, 2004.
- [10] A. Stark et al. Molecular and isotopic characterization of polycyclic aromatic hydrocarbon distribution and sources at the international segment of the St. Lawrence River. *Organic Chemistry*, 34: 225-237, 2003.

For wider interest

The identification and quantification of organic compounds present in the environment are major areas of application in modern analytical chemistry. However, it is still scarcely recognized that, in addition to the chemical identity and concentration of organic compounds, there is more information to be found about their source and fate in the environment from their isotope composition. Isotope ratio mass spectrometry (IRMS) following on-line combustion (C) of compounds separated by gas chromatography (GC-C-IRMS) has been commercially available only since 1990. Our understanding of the isotope composition of organic compounds in different studies is therefore still somewhat limited.

In this work, the stable isotope approach was further used to identify the sources of polycyclic aromatic hydrocarbons (PAHs) in sediments, which was not possible based only on the concentration distribution of individual PAH.

Implementation and results of Research Fund for Coal and Steel funded project CoGasOUT at Coal-Mine Velenje

Sergej Jamnikar¹, Jerneja Lazar¹, Simon Zavšek¹, Ludvik Golob¹

¹Premogovnik Velenje (Coal-Mine Velenje), Velenje, Slovenia

sergej.jamnikar@rlv.si

Abstract. CoGasOUT is a research and development project with an international partner consortium funded by European Commission Research Fund For Coal and Steel. Project group combines multiple scientific and industrial partners as listed: Imperial College, Mine Rescue Service Limited, Coal-Mine Velenje, DMT, K-UTEC, Główny Instytut Górnictwa, Hullera Vasco Leonesa, AITEMIN and Hornonitrianske bane Prievidza. CoGasOUT project started with a Kick-off meeting in July 2010, followed by annual project group meetings and reports for EU Commission TGC 1 evaluators group. Main tasks include mine in-situ and laboratory experiments, data analysis, modelling and pilot tests of new developed technologies. By July 2013 project will conclude with final activities, dissemination and reports.

Keywords: CoGasOUT, coal seam gas, seam gas drainage

1 Introduction

Key aspect of CoGasOUT project is design and development of novel techniques for safer underground mining concerning coal gas hazards. Project work is divided into theoretical background set-up and revision of existing data, followed by experiment design and digital model creation and final implementation of designed experiment. Experimental results will be used in digital model creation and its calibration.

Over project's 3-years duration time, several research campaigns, experiments, tests, analyses and revision have been performed. Coal-Mine Velenje is the key partner for field work and underground in-situ measurements. On the basis of preliminary and preparation activities we are focused on a final deliverable of Coal-Mine Velenje's part of CoGasOUT project – underground gas drainage of excavation pillar.

2 Measurements and methodologies

Underground measurement and monitoring campaigns at excavation pillars and long-wall faces in Coal-Mine Velenje included the following activities: seam gas pressure measurements, seam gas composition measurements and gas isotopic composition determination, gas content experiments, geo-technic parameters measurements and long-wall face ventilation data monitoring.

2.1 Seam gas pressure measurements

Seam gas pressure monitoring was established with the purpose to correlate gas pressure behaviour in dependence of long-wall face approach with geotechnical monitoring, especially stress measurements. Geotechnical monitoring over past years showed certain dynamics of rock stress manifestation in dependence of distance to long-wall face. Presumably, wave of rock stress increase caused changes in permeability of coal seam which was described also as “opening and closing” of fault and crack system.

2.2 Seam gas composition measurements

Seam gas composition measurements were taken at boreholes, drilled during development and preparatory work for long-wall faces in Coal Mine Velenje mines. Gas concentrations were monitored at two different types of boreholes, where both exact gas composition could be analysed as well as basic trends for gas composition changes in dependence of long-wall face advance could be monitored. Gas composition and isotopic composition determination include mine gas sampling and laboratory analyses at laboratories of Coal-Mine Velenje and Institute Jože Stefan.

2.3 Gas content experiments

Based on the observation and results of desorption experiments on Velenje lignite coal samples during 1999 – 2011, research of lost gas determination methodology, litho-type influence and equipment design started in order to characterized Velenje lignite desorption properties.

During desorption experiments in 2010-2011 a frequent leakage of equipment was recorded. To avoid un-controlled events of gas leakage, new experiment equipment for desorption tests was designed and crafted.

2.4 Geo-technic parameters measurements

Geotechnical monitoring included measurements of primary stress state changes in dependence of long-wall face advance. Observations of stress state changes showed significant correlations with seam gas pressure behaviour.

2.5 Long-wall face ventilation data monitoring

Continuous monitoring of coal gas emissions released as a result of coal crushing at long-wall face was performed with stable mine gas and ventilation air velocity sensors, placed by the end of return gate-road. Recorded data are stored and processed together with other technologic parameters. The same procedure was used for all long-wall face at Coal Mine Velenje. Gas concentrations were continuously monitored at all operating long-wall faces at coal mine Velenje since 2010. Measured concentrations were used for gas capacity calculations where daily coal tonnage was taken into account.

Mid-term results show significant influence of geo-technical impacts on seam gas behaviour. Monitoring results describe several gas migration events in excavation pillars in dependence of long-wall face advance. The obtained methodology and knowledge were further used in underground gas drainage design, especially on drainage objects positioning and drainage protocol design. Efficient gas drainage of excavation pillar could reduce gas emission.

3 Results

All of described methodologies, monitoring and measurements were performed within the CoGasOUT project in the last three years. In the following paragraphs, only some major results are given and discussed.

3.1 Combined seam gas pressure and composition, geotechnical monitoring and interpretation

Seam gas pressure and rock stress monitoring was performed with separate analysis and result interpretations. In 2012 a combined analysis was presented on the basis of monitoring results from observations at long-wall face K. -50 C in Mine Pesje.

Combined interpretation of seam gas pressure and rock stress data was processed in dependence of long-wall face advance. Previous monitoring campaigns showed significant relations between seam gas pressure and rock stress parameters.

Assumptions of possible correlations were proved at long-wall face K. -50 C monitoring. First assumption for correlations between rock stress, seam permeability changes and gas pressure dynamics were discussed after seam gas pressure monitoring at borehole jpk 34(+2°)/10.

Combined presentation of seam gas pressure and rock stress measurement results are shown in Figure 1. Measuring point at long-wall face K. -50 C was equipped with seam gas pressure monitoring well (jpk 34 (+2°)/10), rock stress monitoring well (jgm 39 (-2°)/10) and gas sampling well (jpk 32 (+2°)/10).

Well jgm 39 (-2°)/10 was equipped with two pairs of stress cells. Pair of cells at 25m depth was chosen for further discussions due to the best recording of dynamic stress changes ahead of the advancing long-wall face. Stress cells recorded stress changes in excavation pillar.

Results from rock stress monitoring (jgm 39 (-2°)/10) and seam gas pressure monitoring (jpk 34 (+2°)/10) are combined together on a single chart. Figure 1 represents comparison of stress and gas pressure changes. Stress change is shown in MPa while gas pressure is scaled in bars. Values of stress and gas pressure changes are presented as dependence of long-wall face advance.

In Figure 1 influence of stress state changes and gas pressure dynamics are presumably explained by “cleat system opening and closing”. When long-wall face distance to monitoring point is longer than approximately 70 meters, stress influence causes several in-seam deformations. Seam gas can move through seam, thus measured gas pressure decreased. When long-wall face approaches towards monitoring point, rock stress increases, the cleats closes and seam gas is trapped into closed volume. Consequently seam gas pressure increases. Seam gas pressure increases until the maximum coal strength is achieved (50 – 30 m). After stress peak is achieved (30 – 0 m), deformations of excavation pillar increases and seam gas escapes from cleat system.

The behaviour of gas could be further characterized by isotopic composition of carbon isotope ^{13}C in carbon dioxide and methane as it was discussed in papers (Kanduč, 2005). Figure 1 shows changes in the isotopic composition of carbon in carbon dioxide and methane analysed at the Department of Environmental Sciences at Jožef Stefan Institute. Samples were taken at well jpk 32 (+2°)/10 and represented further study and research task.

Values of the isotopic composition of CO_2 ($\delta^{13}\text{C}_{\text{CO}_2}$) sampled in long borehole jpk 32 (+2°)/10 changed with long-wall face advance from +1.0 to -9.7‰. $\delta^{13}\text{C}_{\text{CO}_2}$ values between -10 to -5‰ are typical for coal gases with higher amount of CO_2 of endogenic origin. Higher values of CDMI index (Carbon dioxide – Methane Index) and positive $\delta^{13}\text{C}_{\text{CO}_2}$ values indicated mixed origin of carbon dioxide of biogenic (CO_2 reduction) and endogenic origin.

Initial $\delta^{13}\text{C}_{\text{CH}_4}$ values were around -60‰ indicating that methane was produced by the CO_2 reduction. At the distance from the LW face around 300 m we observed the change in the methane isotopic composition in coal gas samples. $\delta^{13}\text{C}_{\text{CH}_4}$ values became lower ranging from -45 to -31‰ showing that alternative type of methane – biogenic methane from microbial acetate fermentation methane, migrated through the coal seam. As discussed before, stress influenced permeability changes, which is seen in seam gas pressure changes and also in gas migrations in coal seam. Alternative values remained the same until methane escape through the rock stress caused cleat/ porous system. After structure deformation, original gas had low $\delta^{13}\text{C}_{\text{CH}_4}$ values.

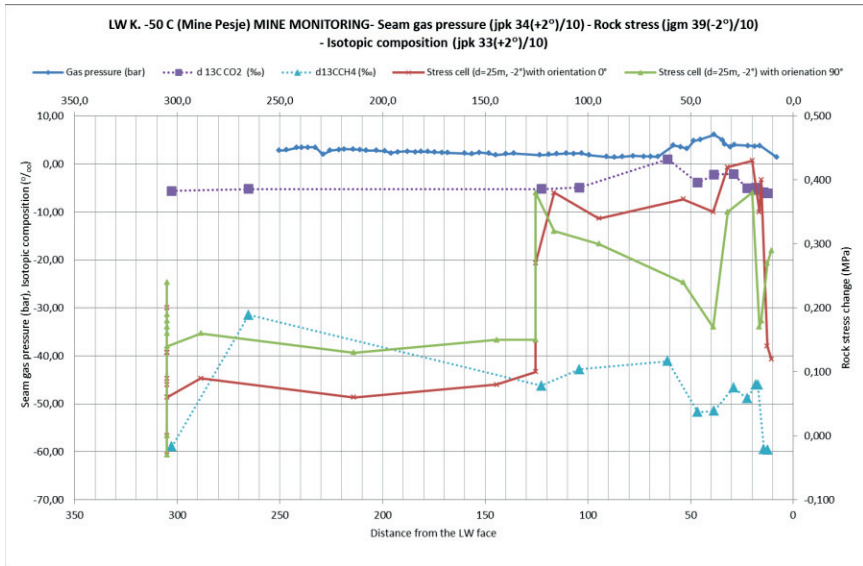


Figure 1: Relation between seam gas pressure and rock stress state change in dependence of the distance to long-wall face. Rapid increase of stress at 305 m and 125 m represent stress cell settings with additional fluid injection.

3.2 Gas content experiments

A total of 29 experiments for gas content determination were performed in 2012 at Velenje Coal Mine at different mine locations.

All samples were used to perform mine experiments for lost gas content share. In addition in selected samples the complete gas content determination was performed according to US Bureau of Mines direct method and Australian Standard method (Diamond, Schatzel, 1996). A special emphasis was put on the lost gas content determination, since previous experiments at Coal Mine Velenje excluded the influence of gas which migrates from sample in time between drilling and sample storage. During experiments, released gas volume was measured at time intervals until release gradient dropped.

In next step, lost gas determination was evaluated as a measurement of square root of time versus desorbed gas volume release after storing sample into the cannister as suggested by Diamond, Schatzel, Garcia, Utery Lost gas content determination experiment could optionally be upgraded with laboratory gas content experiment.

Figures 2 and 3 show an example of gas content determination experiments.

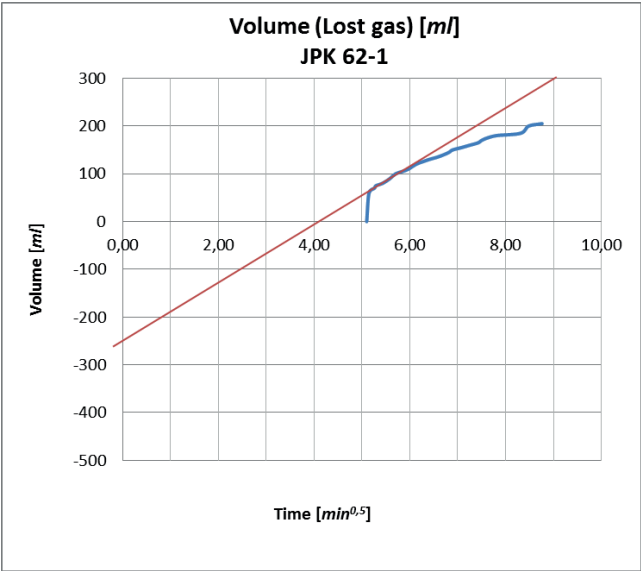


Figure 2: Lost gas content determination curve (Gas content is measured in time dependence and presented in square root of time. Tangent line is used to determine the lost gas quantity between drilling and sample storage at crossing with Y-axis)

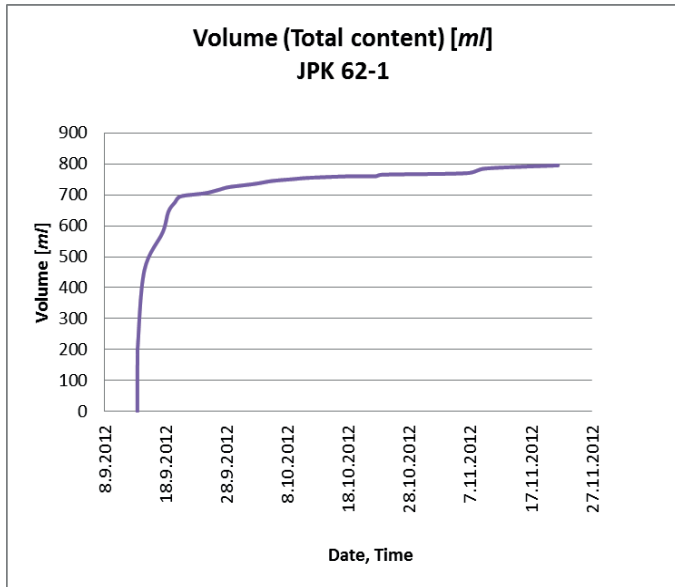


Figure 3: Total gas content determination curve (laboratory determination of gas content, measured for two months time).

3.3 Pilot gas drainage trials

Pilot gas drainage trial was placed in chosen location of excavation pillar K. -65 F in Pesje Mine. Pilot gas drainage trials are planned to start in March 2013 and conducted until April 2013 (until long-wall face advance passed trials area).

By the end of February, a total of 4 drainage wells were drilled and equipped with perforated antistatic plastic tubes. Maximum coverage of different sections of excavation pillar (roof, floor, pillar) was achieved with different well orientations.

Besides drainage wells and system, a complete monitoring system was established in order to record rock stress influences on a seam gas migrations and movements.

Trial preparations included workshop vacuum pump testing and safety power supply disconnection in case of emergency including:

- pump was tested at different simulated pressures on pipe-line together with other parameter monitoring;
- tests showed pump capacity of approximately 450 m³/h;

- due to mine regime, safety disconnections were installed into pump control system (presence of explosive mixture of methane in pipe-line, vacuuming pressure increase and over-heating of water in pump);
- after system installation in mine and test run in mine, system was equipped with additional filters and cleaning elements to prevent any pump damage.

Gas drainage system, separate elements and monitoring equipment is shown in figures 4 and 5.



Figure 4: Gas drainage system

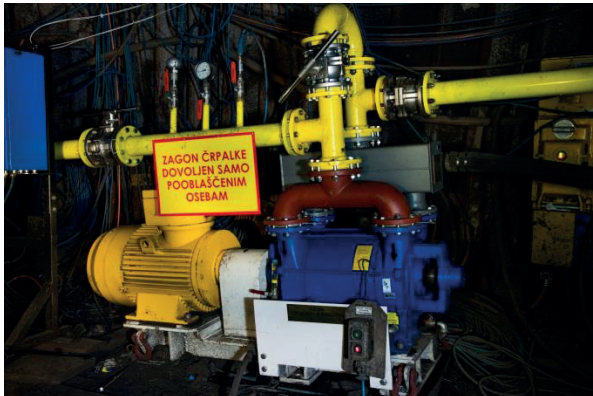


Figure 5: Vacuum pump and monitoring equipment

4 Conclusions

Research and development project CoGasOUT allowed Coal-Mine Velenje to join international partner group and to design and test several activities to explain seam gas behaviour around working long-wall faces. Continuous measurements and experience exchange lead to final planned deliverable – pilot seam gas drainage trials, which we had undertaken early in 2013. At the moment we are performing short-time tests of equipment and performing initial optimisations. Initial drainage trials results proved the assumptions of possibility of seam gas drainage from excavation pillars. Efficient gas drainage is mainly dependent on size of rock stress induced deformation area in front of the long-wall face. Deformation area, caused by rock stress is represented by secondary cracks and voids in the pillar that allow seam gas to migrate.

All drainage trial operations are monitored in order to achieve maximum coverage of gas concentrations, pressure, temperature and quantities. During initial tests we recorded 100 – 180 m³/h of drained gas with average composition in ratio CH₄ /CO₂ = 1/2.

References:

- [1] Diamond, W.P., Schatzel, S., Measuring the gas content of coal: A review., 1986. *International Journal of Coal Geology* 35, 311-331, 1998.
- [2] Diamond, W. P., Schatzel, S. J., Garcia, F., Ulery, J. P., The modified direct method: A solution for obtaining accurate coal desorption measurements. National Institute for Occupational Safety and Health (NIOSH), Office for Mine safety and Health Research, Pittsburgh Research Laboratory.
- [3] Durucan, S. and Edwards, J.S., The Effects of Stress and Fracturing on Permeability of Coal, 1986. *Mining Science and Technology*, 3, 205-216, 1986.
- [4] Jamnikar, S., Desorption properties of Velenje lignite and measurement methodology development, 2011. Balkanmine Mining Congress, Paper, 2011.
- [5] Jamnikar, S., Lazar, J., Lah, R., Žula, J., Burič, E., Zavšek, S. Poročila o spremljanju tehnoloških, plinskih in geotehničnih parametrov na odkopih G2/B, K. -50 A, K. -120 B, K. -50 B, G 2/C, K.-50 C. 2008 – 2012. Premogovnik Velenje, 2008 – 2012.
- [6] Jamnikar, S., Lazar, J., Zavšek, S. Annual CoGasOUT Reports 2011 – 2013.
- [7] Kanduč, T., Izotopske značilnosti premogovega plina v velenjskem bazenu. University of Ljubljana, Faculty of natural sciences and engineering department of geology. *M. Sc. Dissertation*, 2004.
- [8] Kanduč, T., Pezdnič, J., Origin and distribution of coalbed gases from the Velenje basin, Slovenia. *Geochemical Journal*, Vol.39, 2005.
- [9] Kanduč, T., Pezdnič, J., Lojen, S., Zavšek, S., Study of the gas composition ahead of the working face in a lignite seam from the Velenje basin. *RMZ – Materials and Geoenvironment*.
- [10] Markič, M., Petrology and genesis of the Velenje lignite. University of Ljubljana, Faculty of natural sciences and engineering department of geology. *Ph.D. Dissertation*, 2009.

- [11]Pezdič, J., Markič, M., Letič, M., Popovič, A., Zavšek, S., Laboratory simulation of adsorption – desorption processes on different lignite lithotypes from Velenje lignite mine. *RMZ – Materials and Geoenvironment*, Vol. 46, No. 3, 555-568, 1999.

Implementation and results of Research Fund for Coal and Steel funded project CoGasOUT at Coal-Mine Velenje

CoGasOUT is a research and development project with interdisciplinary international partner project group funded by European Commission Research Fund For Coal and Steel. Project group includes scientific and industrial partners as listed: Imperial College, Mine Rescue Service Limited, Coal-Mine Velenje, DMT, K-UTEC, Glowny Instytut Gornictwa, Hullera Vasco Leonesa, AITEMIN and Hornonitrianske bane Prievdza. CoGasOUT project started with a Kick-off meeting in July 2010, and will conclude in July 2013 project with final activities, dissemination and reports.

Key aspect of project is design and development of novel techniques for safer underground mining concerning coal gas hazards. Project work is divided into theoretical background set-up and revision of existing data, followed by experiment design and digital model creation and final implementation of designed experiment. Experimental results will be used in digital model creation and its calibration.

Over project's 3-years duration time, several research campaigns, experiments, tests, analyses and revision have been performed. Coal-Mine Velenje is the major partner for field work and underground in-situ measurements. On the basis of the preliminary and preparation activities we focused on final deliverable of Coal-Mine Velenje's part of CoGasOUT project – underground gas drainage of excavation pillar.

A novel method for speciation of Pt in human serum incubated with cisplatin, oxaliplatin and carboplatin by conjoint liquid chromatography on monolithic disks with UV and ICP-MS detection

Anže Martinčič^{1,2}, Radmila Milačič^{1,2}, Maja Čemažar³, Gregor Serša³,
Janez Ščančar^{1,2}

¹ Department of Environmental sciences, Jožef Stefan Institute, Ljubljana, Slovenia

² Jožef Stefan International Postgraduate School, Ljubljana, Slovenia

³ Institute of Oncology, Department of Experimental Oncology, Ljubljana, Slovenia

anze.martincic@ijs.si

Abstract. The aim of this work was to develop a new method for rapid two-dimensional chromatographic separation of unbound Pt-based drugs and their complexes with proteins in human serum. For this purpose conjoined liquid chromatography (CLC) monolithic column was constructed by placing one CIM Protein G and one CIM diethylamino (DEAE) disk in a single housing. This enabled two-dimensional separation in a single chromatographic run. Speciation analysis of cisplatin, carboplatin and oxaliplatin interaction with synthetic mixture of serum proteins and human serum was performed. Separated Pt-species were monitored on line by UV and ICP-MS detection.

Keywords: Pt-based drugs, conjoined liquid chromatography (CLC), ICP-MS

1 Introduction

For cancer treatment, three Pt-based chemotherapeutic drugs are applied worldwide; cisplatin (*cis*-diaminedichloro-platinum(II)), carboplatin (*cis*-diammine(1,1-cyclobutanedicarboxylato)platinum(II)) and oxaliplatin, ((1R,2R)-cyclohexane-1,2-diamine)(ethanedioato-O,O')platinum(II)) [1]. A major limitation of chemotherapy with platins is their unwanted toxicity towards healthy tissues producing severe side effects, like nephrotoxicity, ototoxicity, emetogenesis, neurotoxicity, and drug resistance in the targeted tumour cells [2]. Serum proteins are the first biological

ligands to interact with the administered drugs. Knowledge of drug interactions in blood serum is very important in order to avoid severe side effects and to optimise or individualise dosage adjustment in clinical chemotherapy [3].

In speciation analysis of platinum in human serum, ion exchange (IE) chromatography is frequently used. As an alternative to classic – particle packed IE columns, monolithic supports have been successfully applied. They have several advantages over classical columns (e.g. greater robustness) but both are unable to separate unbound drug from immunoglobulins (IgG), which co-elute at the same retention time t_0 (Figure 1) [4]. To overcome this problem a conjoint liquid chromatography (CLC) column, containing one CIM Protein G and one CIM DEAE monolithic disk in a single housing, was constructed. Such set up allows two dimensional separation in one chromatographic run. CIM Protein G disk (affinity chromatography) binds Fc region of IgG thus separating free Pt-based drug from portion that is bound to IgG, while on a weak anion exchange CIM DEAE disk serum transferrin and albumin were separated. For separation, isocratic elution with Tris-HCl - NaHCO₃ buffer (pH 7.4) in the first min, followed by gradient elution with 1 mol L⁻¹ NH₄Cl (pH 7.4) in the next 9 min, and acetic acid (AcOH) in the last 4 min was applied. To quantify separated Pt species and to compensate for different nebulisation and ionisation of solvents, which impair inductively coupled plasma mass spectrometry (ICP-MS) detection, post column isotope dilution (ID) was used.

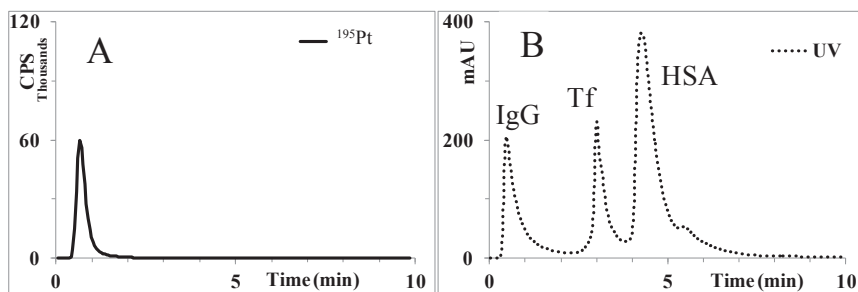


Figure 1: Co-elution of unbound drug and IgG. A) Chromatogram of cisplatin diluted in buffer A. B) Chromatogram of the mixture of standard serum proteins.

2 Materials and methods

Separations were performed by using Agilent (Tokyo, Japan) series 1200 HPLC system on a CLC column constructed with CIM DEAE-1 and CIM Protein G monolithic disks (Bia Separations, Ajdovščina, Slovenia). Protein signals were followed online with UV-Vis detector at 278 nm and ^{194}Pt , ^{195}Pt signals with Agilent 7700x ICP-MS. All reagents were from Merck (Darmstadt, Germany)

Buffer A: 0.05 mol L^{-1} Tris-HCl + 0.03 mol L^{-1} NaHCO_3 , pH 7.4.

Buffer B: Buffer A + 2 mol L^{-1} NH_4Cl , pH 7.4.

Eluent C: 0.5 mol L^{-1} AcOH.

Buffer D: 0.2 mol L^{-1} Tris-HCl, pH 7.4.

Human serum apo-transferrin (Tf), human serum albumin (HSA) and γ -globulins (IgG) were purchased from Sigma-Aldrich (Steinheim, Germany). Cisplatin was obtained from Medoc (Hamburg, Germany), carboplatin from Actavis (Nerviano, Italy) and oxaliplatin from Sanofi Winthrop (France). Platinum enriched in ^{194}Pt isotope (Pt metallic plate, 15 mg) obtained from Oak Ridge National Laboratory (Oak Ridge, TN, USA) was used as post column spike.

Speciation was carried out at a flow rate of 1 mL min^{-1} and injection volume of 0.1 ml. To improve the resolution of unbound Pt species and Tf, isocratic elution with 100 % buffer A was applied in the first min, followed by linear gradient elution from buffer A to 50 % buffer B in the next 9 min, in order to separate Tf from HSA. IgG was then eluted from the column by isocratic elution with 100 % eluent C for 3 min. The eluate from the CLC column was passed through the UV and ICP-MS detection systems. Regeneration and equilibration steps were done at a flow rate of 6 mL min^{-1} ; CLC column was first rinsed for 3 min with 100 % buffer D, than for 7 min with buffer 100 % B and 4 min with 100 % buffer A. In the final step, the column was equilibrated for 0.5 min with buffer A at a flow rate of 1 mL min^{-1} . The eluate from the regeneration and equilibration steps was directed to waste through a software controlled six-port valve. By applying the procedure described above at least 30 serum samples could be analysed without additional cleaning.

3 Results and discussion

The behaviour of Pt-based chemotherapeutic drugs on the CLC monolithic column was examined by two-dimensional chromatographic separation of 5-times diluted

samples of mixtures of standard serum proteins (Fig 2) and serum samples (Fig 3). The Pt mass flow was calculated using Pt^{195}/Pt^{194} isotope ratio.

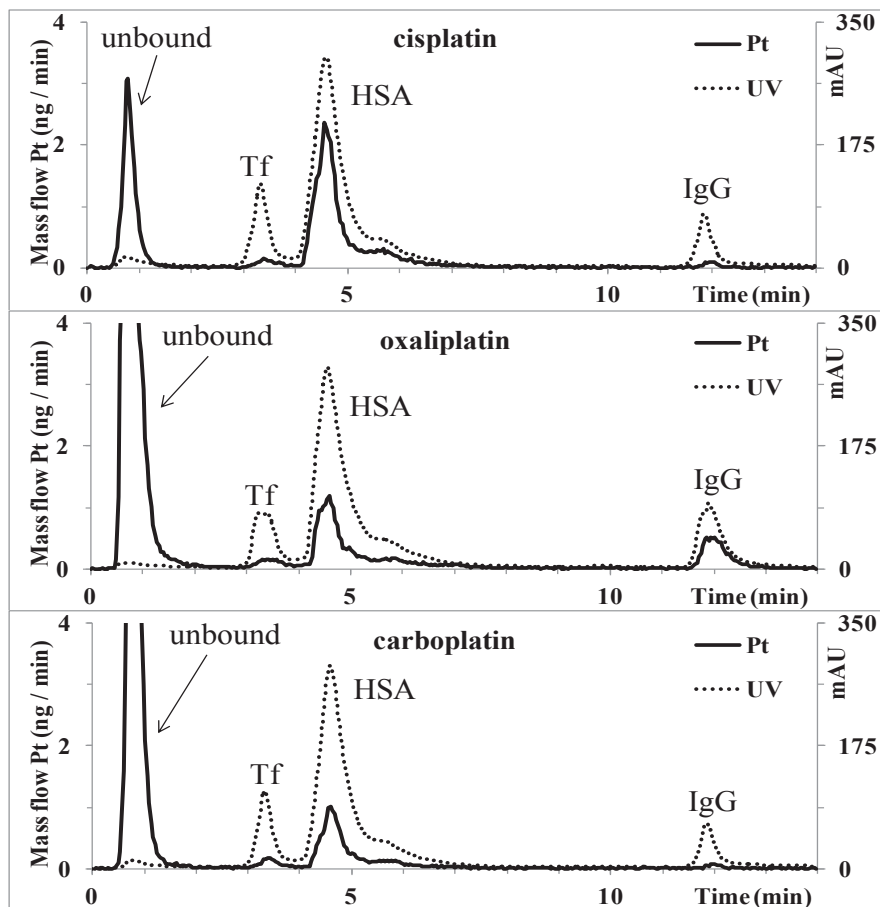


Figure 2: Chromatographic separation of a synthetic mixture of serum proteins spiked with a single Pt-based drug (100 to 200 ng Pt mL⁻¹, incubation time 24 h).

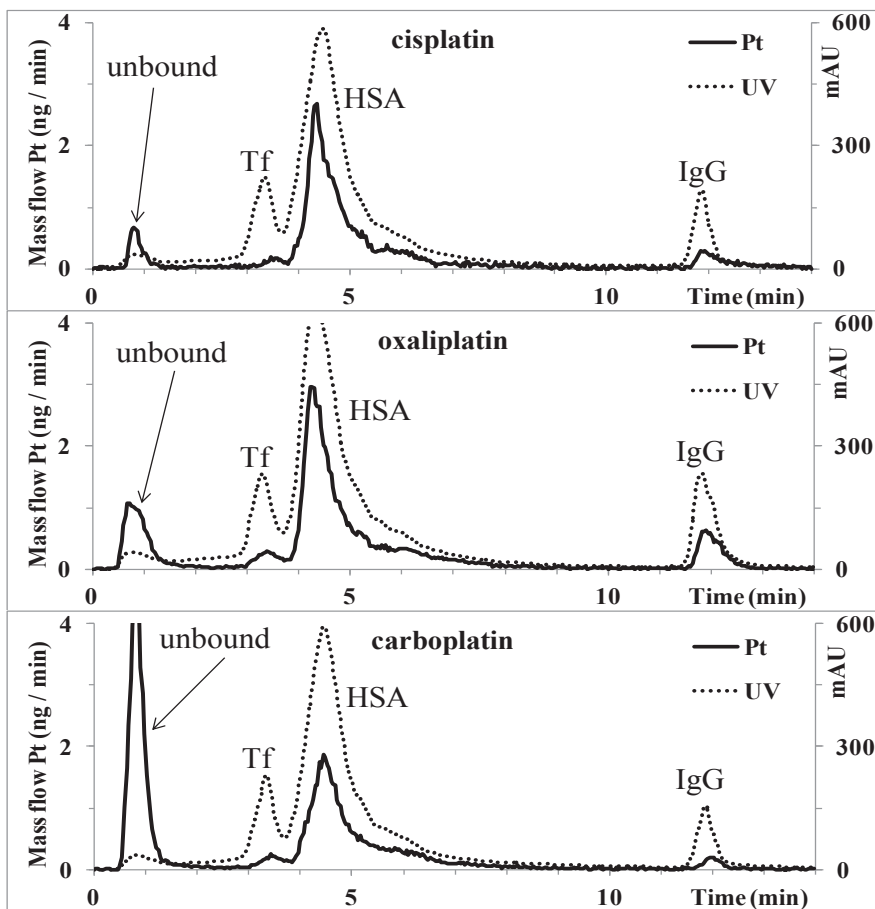


Figure 3: Chromatographic separation of human serum spiked with a single Pt-based drug (100 to 200 ng Pt mL⁻¹, incubation time 24 h).

As can be seen from Figures 2 and 3, the developed method separates all the major Pt species found in human serum. The use of post-column ID adequately compensated the changes in eluent composition, while also providing the means for quantifying our results. Unbound chemotherapeutic drugs in spiked samples of the synthetic mixture of serum proteins and serum samples were eluted from 0.4 to 1.3 min, while those bound to serum proteins were eluted under the chromatographic peaks of Tf (2.9 to 3.6 min), HSA (3.6 to 6.6 min) and IgG (11.7 to 12.7 min).

Detailed speciation data (summarised in table 1) is in good agreement with the literature [4].

Table 1: Distribution of Pt in human serum.

Pt drug	Incubation time (h)	Pt spike added	Unbound Pt	Pt bound to Tf	Pt bound to HSA	Pt bound to IgG	Column recovery
		(ng mL ⁻¹)	(%)				
Cisplatin	24 h	137.4±1.1	19.5±0.1	2.50±0.02	103.5±0.8	5.00±0.04	95
Oxaliplatin	24 h	153.7±1.2	27.0±0.2	4.01±0.03	102.1±0.8	16.0±0.1	97
Carboplatin	48 h	165.6±1.3	77.5±0.6	3.02±0.02	75.5±0.6	3.01±0.03	96

4 Conclusions

The developed method is uniquely able to separate unbound drug from drug bound to IgG while preserving all the advantages of monolithic chromatography, mainly speed and robustness.

References:

- [1] A. Boneti, R. Leone, F.M. Muggia, S.B. Howell. *Platinum and Other Heavy Metal Compounds in Cancer Chemotherapy*, Humana Press: New York, 2009.
- [2] M. Sooriyaarachchi, A. Narendran, J. Gailer. N-Acetyl-L-cysteine modulates the metabolism of cisplatin in human plasma in vitro. *Metallomics*, 3:49-55, 2011.
- [3] L. Kelland. The resurgence of platinum-based cancer chemotherapy. *Nat. Rev. Cancer* 7:573-584, 2007.
- [4] A. Martinčič, R. Milačić, M. Cemazar, G. Sersa, J. Ščančar. The use of CIM-DEAE monolithic chromatography coupled to ICP-MS to study the distribution of cisplatin in human serum. *Anal. Methods*, 4:780-790, 2012.

For wider interest

Our work is based on monolithic chromatography, which offers several advantages over standard (particle packed) chromatographic columns. Monolithic supports have high permeability and therefore allow thorough cleaning during regeneration after each separation run. This enables great robustness of such chromatographic columns which in turn enables higher throughput of samples. Monolithic supports are also cheaper and offer possibilities to be applied in numerous chromatographic separations of compounds in environmental and biological samples.

Combining affinity and anion exchange monolithic disks enables us to construct so called conjoined liquid chromatography columns (CLC) that can perform 2D chromatographic separations in a single run.

Chromate cannot exist in food samples

Breda Novotnik^{1,2}, Tea Zuliani¹, Janez Ščančar^{1,2}, Radmila Milačič^{1,2}

¹ Department of Environmental Sciences, Jožef Stefan Institute, Ljubljana, Slovenia

² Jožef Stefan International Postgraduate School, Ljubljana, Slovenia

breda.novotnik@ijs.si

Abstract. Several papers have recently been published on the presence of Cr(VI) in teas, bread and plants, in spite of a well-known fact that Cr(VI) cannot be present in these organic matter rich matrices as it is readily reduced. These conclusions were made on the basis of determination of total Cr concentrations in alkaline extracts, without applying any speciation analysis. Because bread is a staple food and tea a popular beverage, a huge part of the world's population would be at health risk, if Cr(VI) was really present. To prove that the reported data are an artefact of wrongly applied methodology, the aim of our work was to repeat the same extraction procedures in tea and bread samples as reported in the literature, but, instead of determination of total Cr concentrations, performing speciation analysis of Cr(VI) by high performance liquid chromatography-inductively coupled plasma mass spectrometry (HPLC-ICP-MS). In our study, stable isotopes of ⁵⁰Cr(VI) and ⁵³Cr(III) were used to follow species interconversions during the extraction procedure. In all samples analysed, Cr(VI) concentrations were below the limit of detection. ⁵⁰Cr(VI) was reduced in tea infusions and bread samples even at highly alkaline pH of extracts (pH 12) due to the presence of antioxidants and organic matter. The results of our investigation proved that Cr(VI) cannot exist in food samples.

Keywords: chromium speciation, Cr(VI), tea, bread, aqueous and alkaline extractions, HPLC-ICP-MS

1 Introduction

Chromium (Cr) is a naturally occurring element, but is also a common environmental contaminant due to its wide industrial use. In the environment Cr(VI) and Cr(III) are the most stable Cr forms. The toxicity and essentiality of Cr depend

on its oxidation state. Cr(VI) is carcinogenic, mutagenic and can cause skin dermatitis [2,7], whereas Cr(III) is considered to be an essential micronutrient for humans [2]. In the environment Cr(VI) is readily reduced to Cr(III) by organic matter. Therefore, in biological samples Cr is exclusively present as Cr(III) except shortly after exposure. Despite this known fact, several papers have been published in recent years on the presence of total Cr(VI) in tea leaves [3], bread samples[6] and plants[1]. Water and alkaline extraction ($0.1 \text{ mol L}^{-1} \text{ Na}_2\text{CO}_3$) of tea was performed and Cr determined in the extract with electrothermal atomic absorption spectrometry (ETAAS), without any application of speciation analysis. The reported Cr(VI) concentration in tea infusions were up to $17.5 \mu\text{g L}^{-1}$, what is more than the threshold limit of $2 \mu\text{g Cr(VI) L}^{-1}$ for drinking water. Cr(VI) was also reported in alkaline extracts ($0.01 \text{ mol L}^{-1} + 0.1 \text{ mol L}^{-1} \text{ Na}_2\text{CO}_3$) of bread samples, without applying speciation analysis, based only on the determination of Cr by ETAAS [6].

These studies, lacking in Cr speciation analysis, also did not take into consideration the presence of organic matter and antioxidants that make the existence of Cr(VI) almost impossible, because of its reduction to Cr(III).

Since Cr(VI) is toxic and its presence in food samples such as bread and tea would represent a health risk for general population, the aim of our work was to repeat the experiments of Mandiwana *et al.* [3] and Soares *et al.* [6] and to check, by applying speciation analysis of Cr by high performance liquid chromatography – inductively coupled plasma mass spectrometry (HPLC-ICP-MS), whether the data reporting the existence of Cr(VI) in tea infusions and bread could be confirmed or shown to be an artefact of inappropriate methodology. Extracting solutions were spiked with enriched stable isotopes of $^{50}\text{Cr(VI)}$ and $^{53}\text{Cr(III)}$ to follow species interconversions during the extraction procedures.

2 Materials and methods

2.1 Instrumentation

HPLC separation was performed using MonoQ HR 5/5 column. A linear gradient from 100 % water to 100 % $0.7 \text{ mol L}^{-1} \text{ NaCl}$ in 10 min at a flow rate of 1.5 mL

min⁻¹ was used. For detection of separated species inductively coupled plasma mass spectrometer (ICP-MS), model 7700x (Agilent Technologies) was used. To eliminate polyatomic interferences, high energy collision mode was applied (HECM) [4].

2.2 Preparation of enriched ⁵⁰Cr(VI) and ⁵³Cr(III) isotopic spike solutions

Enriched ⁵⁰Cr₂O₃ and ⁵³Cr₂O₃ were purchased. ⁵⁰Cr(VI) solution was prepared by alkaline melting (NaKCO₃ and NaOH). Quantitative oxidation to ⁵⁰Cr(VI) was achieved with air oxygen at alkaline pH. The melt was dissolved with HCl. ⁵³Cr(III) was prepared with microwave assisted digestion using HNO₃ which was after the digestion, evaporated to 200 µL and HCl was added to acidify the solution [5].

2.3 Sample preparation

White and wholegrain bread were purchased from a local bakery and 13 most popular teas were obtained from a tea shop (Table 1).

Total Cr concentrations: Bread and tea samples were subjected to closed vessel microwave assisted digestion and Cr was determined with ICP-MS. For quality control SRM 1573a was also digested.

Cr in tea infusion: 2.0 g of tea was weighted in a glass beaker and 200 mL of boiling water was added. The tea infusion was spiked with 10 µg L⁻¹ ⁵⁰Cr(VI) and 10 µg L⁻¹ ⁵³Cr(III). Teas were left to soak according to the instructions (3 – 10 min), followed by filtration and analysis by ICP-MS for total Cr concentrations and HPLC-ICP-MS for speciation analysis.

Cr in alkaline extracts of tea: The alkaline extract was prepared as described by Mandiwana *et al.* [3]. 0.25 g of tea was weighted in a beaker and 25 mL of boiling 0.1 mol L⁻¹ Na₂CO₃ was added. The alkaline solution was spiked with 10 µg L⁻¹ ⁵⁰Cr(VI) and 10 µg L⁻¹ ⁵³Cr(III), capped and boiled for 3 min. The extract was filtered and analysed by HPLC-ICP-MS.

Cr in alkaline extracts of bread: The alkaline extracts were performed as described by Soares *et al.* [6]. 1.0 g of dried powdered bread was weighted in a Teflon tube and 9 mL of 0.01 mol L⁻¹ NaOH, doubly spiked with 10 µg L⁻¹ ⁵⁰Cr(VI) and 10 µg L⁻¹ ⁵³Cr(III), was added. The solution was shaken horizontally at 300 rpm for 17 h, than 1 mL of 1 mol L⁻¹ NH₄NO₃ was added. The solution was again quickly shaken and

centrifuged for 30 min at 10 000 rpm. The supernatant was analyzed by HPLC-ICP-MS.

Table 1: The selection and description of tea samples

Sample	Description (country, type/ingredients)
Ajuverdian tea	European Union; ginger, coriander, cardamom, curcuma
Organic herbal tea blend	European Union; rosemary, nettle, rosehip, rooibos tea, lavender, ginger, PU ERH, mate tea, cumin, pepper, cloves
Hibiscus	European union; hibiscus
Bancha	Japan; green tea
Pai mu tan	China; white tea
China gunpowder Temple of heaven	China; green tea
PU ERH	China; red tea
China Oolong se chung	China; red tea
Assam TGFOP1 Dirial	India; black tea
Yunnan	China; black tea
Keemun	China; black tea
Golden Nepal Himalayan Shangri La	Sri Lanka; black tea
Kenya GFOP Mariny	Africa; black tea

3 Results and discussion

3.1 Speciation of Cr by HPLC-ICP-MS

When applying Mono Q anion exchange column, Cr(VI) is quantitatively eluted at 430 to 470 sec (Fig. 1) at a pH range from 3 to 13. Speciation of Cr(III) depends on the pH, for pH below 4, Cr(III) is in the form of $[\text{Cr}(\text{H}_2\text{O})]^{3+}$, which is eluted with the solvent front (Fig. 1), at pH 7, it forms $\text{Cr}(\text{OH})_3$ that is strongly adsorbed by the column resin. Neutral complexes of Cr that are formed with organic ligands are also adsorbed on the column, whereas negatively charged complexes are eluted at 200 sec and are separated from the Cr(VI) peak. At alkaline pH, Cr(III) is partially transformed from $\text{Cr}(\text{OH})_3$ to a more soluble $\text{Cr}(\text{OH})_4^-$, that is eluted as a small peak at 200 to 250 sec, the remaining $\text{Cr}(\text{OH})_3$ is adsorbed on the column.

To follow species interconversions during analytical procedures, a double spike of $10 \mu\text{g L}^{-1}$ of $^{50}\text{Cr}(\text{VI})$ and $10 \mu\text{g L}^{-1}$ of $^{53}\text{Cr}(\text{III})$ was added to the investigated sample. Fig. 1 represents a typical chromatogram of $10 \mu\text{g L}^{-1}$ $^{50}\text{Cr}(\text{VI})$ and $10 \mu\text{g L}^{-1}$ $^{53}\text{Cr}(\text{III})$.

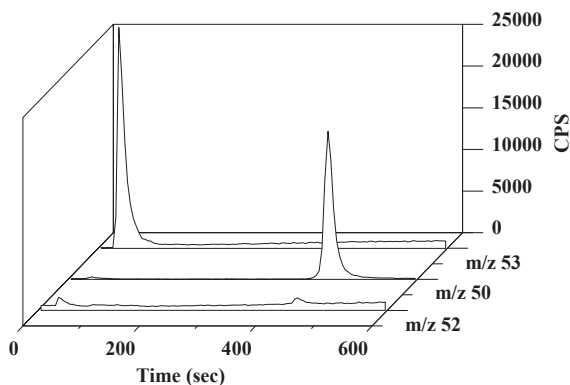


Figure 1: A typical chromatogram of $10 \mu\text{g L}^{-1}$ $^{50}\text{Cr(VI)}$ and $10 \mu\text{g L}^{-1}$ of $^{53}\text{Cr(III)}$ at pH 4.5 obtained by HPLC-ICP-MS at m/z 50, 52 and 53

From Fig.1 a difference in peak areas for Cr(III) and Cr(VI) can be observed. This is due to the gradual increase of NaCl concentration during HPLC separations, which influence the nebulisation efficiency, and consequently the mass transport into the ICP plasma source.

3.2 Total Cr concentrations and Cr speciation in tea infusions

Aqueous tea extracts were prepared as described previously [3]. Mandiwana *et al.* [3] determined Cr in the water extract with ETAAS without speciation analysis and prescribed the determined Cr concentration to be the water soluble Cr(VI).

In our experiment, total Cr concentrations in tea after microwave assisted digestion and in the tea infusions were determined by ICP-MS and are presented in Table 2.

Table 2 Concentrations of total Cr in tea samples after microwave digestion and total Cr in tea infusions determined by ICP-MS.

No.	Sample	Total Cr in tea (mg kg ⁻¹)	Total Cr in tea infusion (mg kg ⁻¹)
1	Ajuverdian tea	0.143±0.002	0.0164±0.0002
2	Organic herbal tea blend	0.173±0.003	0.0239±0.0003
3	Hibiskus	3.50±0.05	0.115±0.002
4	Bancha	0.88±0.01	0.064±0.002
5	Pai mu tan	0.192±0.003	0.0041±0.0001
6	China gunpowder Temple of heaven	0.510±0.007	0.0198±0.0003
7	PU ERH	0.92±0.02	0.059±0.001
8	China Oolong se chung	0.153±0.002	0.0111±0.0002
9	Assam TGFOP1 Dirial	0.520±0.008	0.187±0.003
10	Yunnan	0.66±0.01	0.158±0.002
11	Keemun	0.314±0.005	0.0340±0.0005
12	Golden Nepal Himalayan Shangri La	0.81±0.01	0.083±0.001
13	Kenya GFOP Mariny	1.98±0.03	0.76±0.01

As can be seen from Table 2, total Cr in teas ranged from 0.15 (Ajuverdian and China Oolong) to 3.5 mg kg⁻¹ (hibiskus tea), while the Cr in tea infusions ranged from 0.0041 (white tea) to 0.187 mg kg⁻¹ (black tea).

To support our assumptions, that Cr(VI) cannot exist in food samples as they are high in organic matter and antioxidants, speciation studies were performed on the tea infusions with the double spike of 10 µg L⁻¹ ⁵⁰Cr(VI) and 10 µg L⁻¹ of ⁵³Cr(III). In 13 teas analysed, three typical patterns of Cr speciation were observed and are presented in Fig.2.

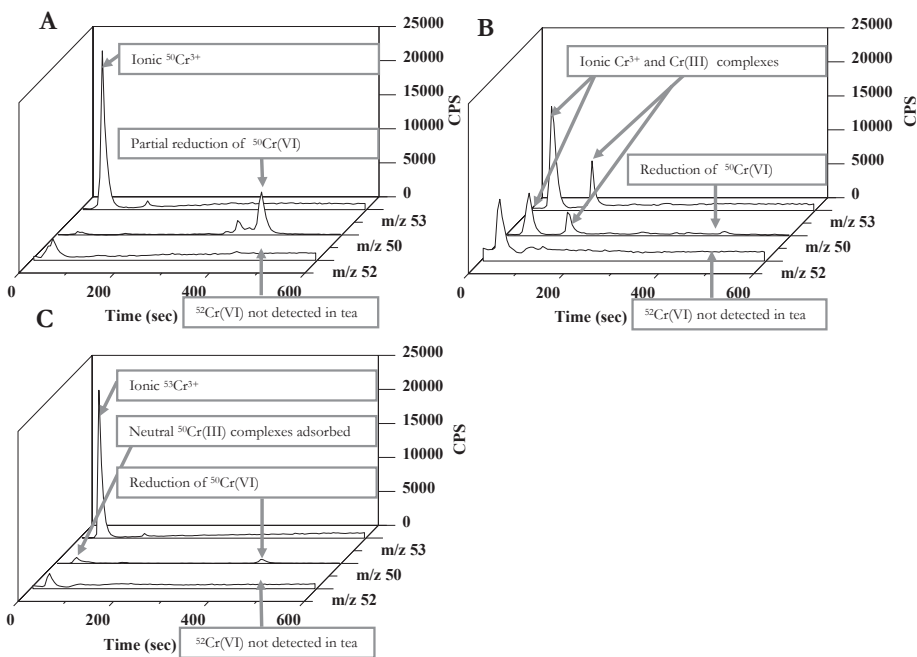


Figure 2 : Chromatograms of three typical tea infusions : Chromatogram of tea infusion of Ajuverdian tea (A), organic herbal tea blend (B) and Hibiskus (C), obtained by HPLC-ICP-MS procedure recorded at m/z 50, 52 and 53. All tea infusions were doubly spiked with $10 \mu\text{g L}^{-1}$ $^{50}\text{Cr(VI)}$ and $10 \mu\text{g L}^{-1}$ of $^{53}\text{Cr(III)}$

$^{52}\text{Cr(VI)}$ was not detected in any of the tea infusion samples what can be seen from the absence of a Cr(VI) peak at 430-470 sec (m/z 52), confirming our hypothesis that $^{\text{nat}}\text{Cr(VI)}$ is not present in tea infusions. The added $^{50}\text{Cr(VI)}$ was either partially reduced (Fig. 2A) or completely reduced (Fig. 2B, 2C). After reduction, neutral $^{50}\text{Cr(III)}$ species that are adsorbed on the column (Fig. 2A, 2C) were formed, or ionic Cr^{3+} and negatively charged Cr(III) complexes occurred, which were eluted with a solvent front or around 200 s (Fig. 2B), respectively. These findings additionally confirmed that Cr(VI) cannot exist in a tea infusion, as it is readily reduced with the antioxidants present. The added $^{53}\text{Cr(III)}$ was not oxidized and was eluted as ionic Cr^{3+} (Fig. 2A, 2C) or as negatively charged Cr(III) complex (Fig. 2B).

These results oppose the data provided by Mandiwana *et al.* [3] and suggest that their results are based on wrongly applied methodology and the lack of speciation analysis.

3.3 Cr speciation in alkaline extracts of tea and bread

Mandiwana *et al.* [3] performed alkaline extractions of tea and Soares *et al.* [6] of bread samples. The Cr in the extract determined with ETAAS was assigned, without any speciation analysis, to be total Cr(VI). In order to check the reliability of these results, the alkaline extraction protocol was repeated and $10 \mu\text{g L}^{-1}$ $^{50}\text{Cr(VI)}$ and $10 \mu\text{g L}^{-1}$ of $^{53}\text{Cr(III)}$ double spike was added to follow species interconversions. Speciation analysis with HPLC-ICP-MS of these alkaline extractions was performed and the results are presented in Fig. 3.

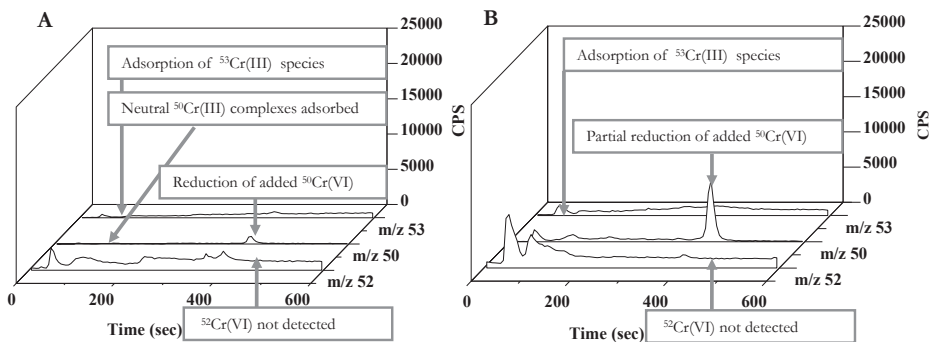


Figure 3: Chromatogram of alkaline extract of tea (A), alkaline extract of wholegrain bread (B) obtained by HPLC-ICP-MS procedure recorded at m/z 50, 52 and 53. Alkaline extracts were doubly spiked with $10 \mu\text{g L}^{-1}$ $^{50}\text{Cr(VI)}$ and $10 \mu\text{g L}^{-1}$ of $^{53}\text{Cr(III)}$

From Fig. 3 it can be seen that $^{52}\text{Cr(VI)}$ was not detected (no Cr peak was observed at 430-470 sec at m/z 52), again proving that $^{\text{nat}}\text{Cr(VI)}$ is not present in these samples. $^{53}\text{Cr(III)}$ was present mainly as Cr(OH)_3 and was adsorbed by the column resin. The added $^{50}\text{Cr(VI)}$ was, despite the high pH, either partially (bread) (Fig. 3B) or completely (tea) (Fig. 3A) reduced and adsorbed on the column, indicating the strong reduction potential of organic ligands present in the samples to reduce Cr(VI). These results again suggest that the data on the presence of Cr(VI) in tea [3] and bread [6] obtained without speciation analysis are erroneous.

4 Conclusions

The data of present investigation, based on the speciation analysis by HPLC-ICP-MS and supported by the use of $^{53}\text{Cr}(\text{III})$ and $^{50}\text{Cr}(\text{VI})$ isotopic solutions proved, that Cr(VI) does not exist in foodstuffs of plant origin and provided some conclusive evidence that the same can be expected for foods of animal origin.

References:

- [1] L. Elci, U. Divrikli, A. Akdogan, A. Hol, A. Cetin and M. Soylak. Selective extraction of chromium(VI) using a leaching procedure with sodium carbonate from some plant leaves, soil and sediment samples, *Journal of Hazardous Materials*, 173: 778-782, 2010
- [2] S. Langård and M. Costa. *Handbook on the Toxicology of Metals. Chromium. 3rd edition*, Academic Press, Inc. 2007
- [3] K. L. Mandiwana, N. Panichev, S. Panichev. Determination of chromium(VI) in black, green and herbal teas. *Food Chemistry*, 129: 1839-1843, 2011
- [4] B. Novotnik, T. Zuliani, A. Martinčič, J. Ščančar, R. Milačič. Preparation of Cr(VI) and Cr(III) isotopic spike solutions from ^{50}Cr and ^{53}Cr enriched oxides without the use of oxidizing and/or reducing agents, *Talanta*, 99: 83-90, 2012
- [5] B. Novotnik, T. Zuliani, A. Martinčič, J. Ščančar, R. Milačič. Effective reduction of polyatomic interferences produced by high chloride and carbon concentrations in determination of Cr(VI) by FPLC-ICP-MS, *Journal of analytical atomispectrometry*, 27: 488-495, 2012
- [6] M.E. Soares, E. Vieira, M. de Ludres Bastos. Chromium speciation analysis in bread samples. *Journal of Agricultural and Food Chemistry*, 58: 1366-1370, 2010
- [7] A. Zhitkovic. Importance of Chromium-DNA adducts in mutagenicity and toxicity of Chromium(VI). *Chemical research in toxicology*, 18: 3-11, 2005

For wider interest

Recently several papers have been published on the presence of Cr(VI) in tea infusions, bread samples and plants in spite of the well known fact, that Cr(VI) cannot exist in these samples as it is readily reduced by organic matter. The assumptions were made on the basis of total Cr determination in alkaline and aqueous sample extracts by ETAAS, without applying any speciation analysis. If Cr(VI) really exists in bread samples and tea infusions, consuming bread and tea would represent a long-term chronic exposure to Cr(VI) and health threat for most of human population. To confirm our hypothesis that the data published in the literature is erroneous, the aim of our work was to repeat the extraction procedures described in the literature and with speciation analysis using HPLC-ICP-MS confirm or negate the data on the presence of Cr(VI) in bread and tea samples. To follow Cr species interconversions stable isotopes of $^{50}\text{Cr(VI)}$ and $^{53}\text{Cr(III)}$ were added to the samples. Our results have shown that Cr(VI) concentrations in the samples were below the limit of detection. Additionally, $^{50}\text{Cr(VI)}$ that was added to tea and bread samples was reduced by organic matter in spite of the high pH (12), providing additional proof that Cr(VI) cannot exist in food samples.

Behaviour of Benzophenones under the Influence of Natural Sunlight

Kristina Pestotnik^{1,2,3}, Tina Kosjek¹, Uroš Kranjc³, Ester Heath^{1,2}

¹ Department of Environmental Sciences, Jožef Stefan Institute, Ljubljana, Slovenia

² Jožef Stefan International Postgraduate School, Ljubljana, Slovenia

³ Ecological Engineering Institute Ltd, Maribor, Slovenia

kristina.pestotnik@ijs.si

Abstract. This study evaluates photolytic behaviour of benzophenone derived pharmaceuticals and personal care products (PPCPs) including a pharmaceutical ketoprofen (KP), its phototransformation products 3-ethylbenzophenone (EtBP) and 3-acetylbenzophenone (AcBP) and UV filters benzophenone (BP), 4-hydroxybenzophenone (H-BP), 2-hydroxy-4-methoxybenzophenone (HM-BP), 2,4-dihydroxybenzophenone (DH-BP) and 2,2'-dihydroxy-4-methoxybenzophenone (DHM-BP). Since photodegradation may be of great significance in the natural elimination process of organic compounds, we have evaluated the behaviour of these compounds under the influence of natural sunlight. The investigated benzophenones were exposed to solar irradiation for different periods of time. After 24 h of exposure the amount of KP decreased from 1 µg/L to below the limit of detection, indicating the compound is prone to sunlight and degrades easily. Also for EtBP we determined low photostability, where 1 week of irradiation resulted in concentration below its limit of detection. Degradation of AcBP, BP and DH-BP followed a pseudo-first-order kinetics with the half-life of 12.98, 13.25 and 12.36 days, respectively. Other UV filters (H-BP, HM-BP and DHM-BP) were found resistant to solar irradiation – after 2 weeks of exposure they remained unchanged. Finally, 4 weeks of irradiation resulted in elimination of 41 %, 43 % and 38 % for H-BP, HM-BP and DHM-BP, respectively, which indicates they have the potential of being persistent in the environment.

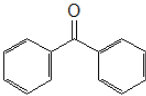
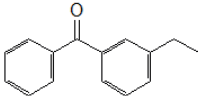
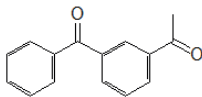
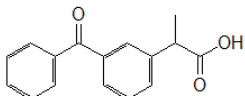
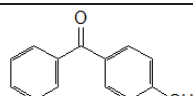
Keywords: benzophenones, ketoprofen, UV filters, photodegradation

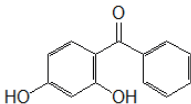
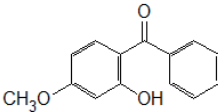
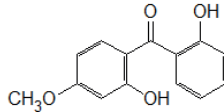
1 Introduction

Pharmaceuticals and personal care products (PPCPs) are a diverse group of compounds used as therapeutic drugs or consumer products for use on the human body (e.g. skin care, dental care and hair care products, sunscreen agents, soaps and cleaners, insect repellents, fragrances and flame retardants). PPCPs are produced in large quantities throughout the world and their consumption continues to rise [1]. Consequently, these compounds enter the environment globally. In recent years the occurrence and fate of PPCPs in the environment have become one of the emerging issues in environmental chemistry.

Among numerous PPCPs, this study is focused on the benzophenone derived compounds including a pharmaceutical ketoprofen, its phototransformation products 3-ethylbenzophenone and 3-acetylbenzophenone and UV filters benzophenone, 4-hydroxybenzophenone, 2-hydroxy-4-methoxybenzophenone, 2,4-dihydroxybenzophenone and 2,2'-dihydroxy-4-methoxybenzophenone. Their chemical structures and abbreviations are presented in Table 1.

Table 1 : Abbreviations and chemical structures of the investigated compounds.

Compound	Abbreviation	Chemical structure
benzophenone	BP	
3-ethylbenzophenone	EtBP	
3-acetylbenzophenone	AcBP	
ketoprofen	KP	
4-hydroxybenzophenone	H-BP	

2,4-dihydroxy- benzophenone	DH-BP	
2-hydroxy-4-methoxy- benzophenone	HM-BP	
2,2'-dihydroxy-4- methoxy- benzophenone	DHM-BP	

To date, little is known about the presence, behaviour and fate of these compounds in the environment. Studies report the level of ketoprofen in wastewaters, rivers and lakes in the ng L⁻¹ range [2],[3]. AcBP and EtBP may be formed in the environment as transformation products of ketoprofen under the influence of sunlight, but their environmental occurrence is yet to be addressed. The presence of benzophenone-type UV filters has been reported in ng L⁻¹ levels in surface waters – seawaters, lakes and rivers, and in µg L⁻¹ in wastewaters [4],[5],[6].

Photodegradation is one of the most important natural abiotic elimination processes determining the fate of organic compounds in the aquatic environment [7]. Studies report that exposure of PPCPs to UV light may lead to photodegradation reactions that can compromise their physical properties and further lead to the formation of undesirable transformation products [8]. When released into the environment, PPCPs are expected to undergo the same reactions in the presence of natural sunlight. Nevertheless, only a few photodegradation studies have been performed regarding the environmental fate of benzophenone based PPCPs. Ketoprofen's photostability has been researched mostly as part of the clinical trials and drug formulation studies. It was established that it rapidly degrades into benzophenone derivates, which cause skin photosensitivity disorders as an adverse effect after its administration [2]. The same transformation reactions may also occur in the environment. Kosjek at al. (2011) proposed a breakdown pathway for ketoprofen by exposure to artificial UV light. Among others, EtBP and AcBP have been identified as transformation products. While for KP very fast

transformation was achieved, EtBP and AcBP were found more resistant to UV irradiation [2]. The photostability of UV filters has been studied mainly to optimize dosage and formulation of products to guarantee long-term protection from UV radiation. Environmental fate has been addressed only recently [7],[9]. In previous experiments we have evaluated photodegradation of the selected benzophenone based PPCPs under the influence of artificial UV light. Using two UV lamps with different emission (low pressure: 254 nm, medium pressure: 265-579 nm) we confirmed extreme photolability of ketoprofen, while its transformation products EtBP and AcBP degraded more slowly, following a pseudo-first-order degradation kinetics. UV filters in general proved to be very photostable, indicating they have the potential of being persistent in the environment [9]. This triggers the need for more research regarding the behaviour of these compounds in the environment.

Our previous photodegradation experiments were performed using artificial UV light in laboratory-controlled conditions with a predetermined range of irradiation wavelengths and UV intensity. The aim of the present study is to investigate the photolytic behaviour of benzophenone based PPCPs under the influence of natural sunlight in order to better understand their environmental fate. This will be achieved by following the removal of the studied compounds in aqueous samples, exposed to solar irradiation in a natural environment.

2 Methods and materials

2.1 Solar irradiation

Photodegradation studies were carried out by exposing 1 L of spiked aqueous solutions of each individual benzophenone with initial concentration of $1 \mu\text{g L}^{-1}$ to sunlight. Samples in 1 L quartz Erlenmeyer flasks were exposed to irradiation in Ljubljana, Slovenia (latitude 46.1, longitude 14.5) in August 2012 for a period of 4 weeks under clear sky conditions with a daily air temperature varying between 12 and 36°C. During exposure period, there were 15 h of sunshine per day and the local sunlight irradiation intensity with a maximum of 932 W m^{-2} [10]. Samples (200

mL) were collected after 1, 3, 5 and 7 days of exposure for ketoprofen and after 1, 2, 3 and 4 weeks for other compounds.

2.2 Analytical procedure

After irradiation, the collected samples (200 mL) were pre-concentrated using solid phase extraction (SPE) with OasisTM Hydrophilic-Lipophilic Balance sorbent. In order to increase volatility and sensitivity of the compounds for further analysis with gas chromatography, they were derivatized. Derivatizing agents, time and temperature of derivatization for each compound are presented in Table 2.

Table 2 : Derivatizing conditions for the investigated compounds.

Compound	Derivatizing agent	Temperature	Time
H-BP, DH-BP, HM-BP, DHM-BP	MSTFA	60 °C	1 h
KP	MTBSTFA	60 °C	1 h
BP, EtBP	PFBHA	60 °C	15 h
AcBP		60 °C	1 h

MSTFA: N-methy-N-(trimethylsilyl) trifluoroacetamide

MTBSTFA: N-(tert-butyltrimethylsilyl)-N-methyltrifluoroacetamide

PFBHA: O-(2,3,4,5,6-pentafluorobenzyl)hydroxylamine hydrochloride

Separation and identification of the compounds were achieved using an HP 6890 (Hewlett-Packard, Waldbronn, Germany) gas chromatograph fitted with a single quadrupole mass selective detector (GC-MSD). Injection was performed in the splitless mode at 250°C. The MS operated in EI ionisation mode at 70 eV. For instrumental control and data processing Chemstation software was used.

3 Results and discussion

The duration of exposure to sunlight and sampling frequency were determined based on previous results of irradiation with artificial UV light and the available literature. Due to previously determined low photostability of ketoprofen, we predicted shorter irradiation periods for ketoprofen than for the remaining compounds. Nevertheless, after 24 h of exposure, the concentration of ketoprofen

was below the limit of detection, indicating ketoprofen degrades rapidly in the environment under the influence of sunlight. While its degradation product EtBP showed higher stability when irradiated with UV lamps, solar irradiation resulted in undetectable amounts of EtBP after only 1 week. Due to rapid degradation of KP and EtBP, the degradation kinetics was impossible to determine. The experiment should be repeated for KP and EtBP with shorter exposure times and more frequent sampling in the future. Ketoprofen's transformation product AcBP proved to be more photostable during the 4 week period, hence we evaluated the degradation kinetics. The concentration of AcBP in aqueous solution decreased exponentially with reaction time indicating the reaction follows a pseudo-first-order kinetics (Figure 1). This is a second-order reaction in which one of the reactants (water in our case) is present in such great amounts that its effect is not seen. The reaction then appears to be dependent on concentration of the compound alone, allowing the approximation to pseudo-first-order reaction. This can be expressed by the following equation:

$$c_t = c_0 e^{-kt} \quad (1)$$

where c_t represents the concentration at time t , C_0 is the initial concentration, k is the degradation rate constant and t is the reaction time.

Pseudo-first-order kinetics plots of natural logarithms of concentration versus time yield straight lines, which is described by the following equation:

$$\ln c_t = -kt + \ln c_0 \quad (2)$$

Half-lives were calculated using the equation:

$$t_{1/2} = \ln 2 / k \quad (3)$$

The degradation rate constant for AcBP was found to be 0.0534 days^{-1} with the half-life of 12.98 days.

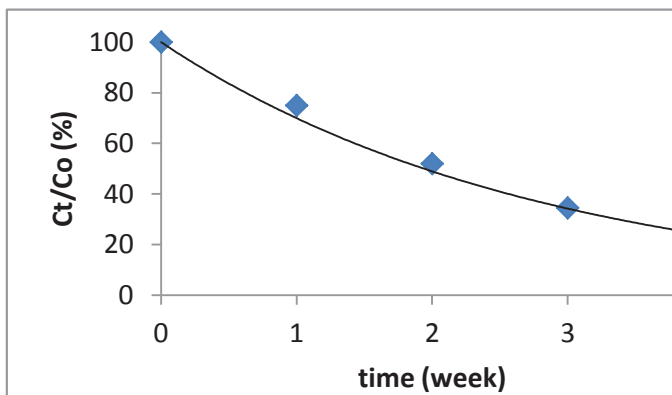


Figure 1 : Photodegradation of AcBP during 4 weeks of solar irradiation.

UV filters H-BP, HM-BP and DHM-BP showed similar behaviour when exposed to sunlight. All three remained unchanged after 2 weeks of irradiation. After 3 weeks, their concentration decreased a little and finally, after 4 weeks removal reached 41 %, 43 % and 38 % for H-BP, HM-BP and DHM-BP, respectively. From these data, the degradation kinetics was not possible to determine. In contrast, photodegradation of BP and DH-BP followed a pseudo-first-order kinetics during the 4 week period of irradiation. The course of their degradation is presented in Figures 2 and 3. For BP we determined a degradation rate constant of 0.0523 days^{-1} and a half-life of 13.25 days. Similar behaviour showed DH-BP with a degradation rate constant of 0.0561 days^{-1} and a half-life of 12.36 days.

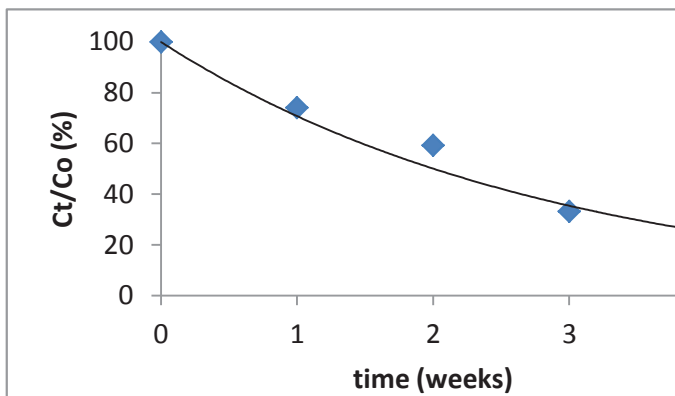


Figure 2 : Photodegradation of BP during 4 weeks of solar irradiation.

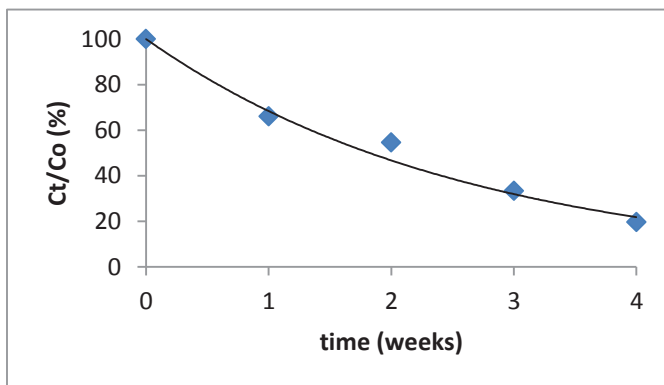


Figure 3 : Photodegradation of DH-BP during 4 weeks of solar irradiation.

The results showed that even though benzophenone based compounds have similar chemical structure, they are expected to undergo different changes in the environment. We can assume that different functional groups are responsible for different photolytic behaviour of benzophenones, where ketoprofen is the most photolabile and UV filters are more resistant to irradiation. Photostability of the investigated compounds was determined in the following order: DHM-BP > H-BP > HM-BP > BP > DH-BP > AcBP > EtBP > KP. Photolytic behaviour of the benzophenones under the influence of sunlight was found to be similar to

photodegradation experiments with artificial UV lamps, although due to different UV intensity and wavelengths of irradiation, a direct comparison cannot be made.

4 Conclusion

The low photostability of ketoprofen and its degradation products EtBP and AcBP indicates the need for further research into the formation and toxicity of stable transformation products formed during UV exposure of these compounds. Also, the high photostability of the investigated UV filters points to their potential of being persistent in the aquatic environment. Therefore, our further research will be oriented towards evaluating various environmental processes, such as adsorption and biological degradation that determine the fate and behaviour of these compounds in the environment

References:

- [1] K. Pestotnik, T. Kosjek, E. Heath. Transformation Products of Personal Care Products: UV Filters Case Studies. In: Lambropoulou DA., Nollet LML. Transformation Products of Emerging Contaminants in the Environment. Analysis, Processes, Occurrence, Effects and Risks. John Wiley & Sons, Inc., In Press, 2013.
- [2] T. Kosjek, S. Perko, E. Heath, B. Kralj, D. Žigon. Application of complementary mass spectrometric techniques to the identification of ketoprofen phototransformation products. *Journal of Mass Spectrometry*, 46:391-401, 2011
- [3] C. Tixier, H.P. Singer, S. Oellers, S.R. Müller. Occurrence and fate of carbamazepine, clofibrac acid, diclofenac, ibuprofen, ketoprofen, and naproxen in surface waters. *Environmental science & technology*, 37(6):1061-1067, 2003
- [4] D.L. Giokas, A. Salvador, A. Chisvert. UV filters: From sunscreens to human body and the environment. *Trends in Analytical Chemistry*, 26(5):360-374, 2007
- [5] D.A. Lambropoulou, D.L. Giokas, V.A. Sakkas, T.A. Albanis, M.I. Karayannis. Gas chromatographic determination of 2-hydroxy-4-methoxybenzophenone and octyldimethyl-*p*-aminobenzoic acid sunscreen agents in swimming pool and bathing waters by solid-phase microextraction. *Journal of Chromatography A*, 967:243–253, 2002
- [6] T. Poiger, H.R. Buser, M.E. Balmer, P.A. Bergqvist, M.D. Müller. Occurrence of UV filter compounds from sunscreens in surface waters: regional mass balance in two Swiss lakes. *Chemosphere*, 55:951-963, 2004
- [7] R. Rodil, M. Moeder, R. Altenburger, M. Schmitt-Jansen. Photostability and phytotoxicity of selected sunscreen agents and their degradation mixtures in water. *Analytical and Bioanalytical Chemistry*, 395: 1513-1524, 2009
- [8] A.J.M. Santos, M.S. Miranda, J.C.G. Esteves da Silva. The degradation products of UV filters in aqueous and chlorinated solutions. *Water Research*, 46(10):3167-3176, 2012
- [9] K. Pestotnik, T. Kosjek, U. Kranjc, O. Bajt, E. Heath. Photodegradation of benzophenones by UV treatment. In *Slovenian chemical days 2012*, Portorož, Slovenia, 2012
- [10] <http://meteo.arso.gov.si/>; accessed daily between 1-31th of August 2012

For wider interest

Pharmaceuticals and personal care products (PPCPs) are a diverse group of compounds used as therapeutic drugs or consumer products for use on the human body (e.g. skin care, dental care and hair care products, sunscreen agents, soaps and cleaners, insect repellents, fragrances and flame retardants). They are produced in large quantities throughout the world and their consumption continues to rise. Consequently, these compounds enter the environment globally. In recent years there has been an increasing concern regarding the presence and effects of PPCP residues in the environment. Among numerous PPCPs this study is focused on benzophenone based compounds that include a pharmaceutical (ketoprofen), its phototransformation products and UV filters. Since photodegradation of PPCPs caused by solar irradiation is an important natural elimination process, we evaluated the behaviour of the selected benzophenones exposed to natural sunlight. Results confirmed low photostability of ketoprofen, while UV filters are more stable, which is in agreement with their use in sunscreens and other products. The results of photodegradation will provide a better understanding of the cycling and fate of these compounds in the environment.



Stability of mercury compounds at high temperatures

Matej Sedlar^{1,3}, Majda Pavlin^{2,3}, Sani Bašič¹, Milena Horvat^{2,3}

¹ Esotech, d.d.

² Department of Environmental Sciences, Jožef Stefan Institute, Ljubljana, Slovenia

³ Jožef Stefan International Postgraduate School, Ljubljana, Slovenia

milena.horvat@ijs.si

Abstract. Combustion of fossil fuels is the main anthropogenic source of mercury. The efficiency of methods for removing mercury from coal syngas or flue gases mainly depends on the chemical forms of mercury. Despite the fact that temperature fractionation is a common approach to defining mercury species in solid samples, the accuracy of known results is still questionable.

For developing the method of temperature fractionation, a home-made apparatus was used, in which known mercury compounds, pure or mixed with SiO₂, were heated by a slow increase of temperature (approximately 2.2 °C min⁻¹) to 800 °C in a flow of either nitrogen or air. Released elemental mercury was detected by an atomic absorption spectrometry technique. The results showed that not only the type of carrier gas, but also the substrate affected the number and size of the peaks and the temperature at which elemental mercury was released.

Keywords: Mercury, temperature fractionation, speciation, pure mercury compounds

1 Introduction

Mercury is a global pollutant that originates from both natural and anthropogenic sources. The greatest anthropogenic source of mercury is industry, where approximately 45 % of global anthropogenic mercury emissions come from fossil fuel combustion [1]. Due to the global nature of mercury pollution, a new legally binding convention will be adopted in 2013 with the main aim of reducing anthropogenic emissions [2]. Considerable measures have already been taken to remove mercury from flue gases of coal combustion or gasification [3]. Until now, no efficient method has been implemented in industry to remove mercury from flue gas at elevated temperatures due to the instability of mercury, its compounds and of its trapping or complexation at higher temperatures.

Generally mercury can occur in flue gas in three different forms, namely as elemental mercury ($\text{Hg}(0)$), particulate (Hg_p), and oxidized mercury (Hg(I) , Hg(II)) [4]. Mercury is found only as $\text{Hg}(0)$ at temperatures above 650 °C. However, when the temperature begins to decrease, mercury is transformed to the oxidized state (Hg(I) , Hg(II)). This form of mercury reacts with other molecules in the gas to form different mercury compounds; the dominant mercury compound depends on the temperature of the gas itself. A knowledge, of which mercury compounds are present during the cooling of gases, is necessary to develop a process for the efficient removal of mercury.

The aims of this study were to observe and understand the behaviour of different mercury species at higher temperatures, exposed to different conditions, and to discover at which temperatures mercury is released from specific mercury compounds. With this in view, sets of experiments were conducted based on the pyrolytic technique. This served to calibrate the method for subsequent comparison with other solid samples, observed in further experiments.

Up to the present, much work has been done to develop an optimal method for mercury fractionation. Different methods for mercury fractionation [5],[6], [7], have resulted in varying results. Taking these inconsistencies into consideration, we developed a method for mercury fractionation which would provide reliable results for the temperatures at which different forms of mercury are released from solid

samples. To calibrate the method two sets of experiments were conducted: the first set included only pure mercury compounds, while the second set included different pure mercury compounds mixed with quartz powder. This served for comparison to other more complex matrixes that will be studied in future work.

2 Methods and materials

Apparatus: The apparatus used for temperature fractionation was a home-made device. As presented in Figure 1, it consisted of a gas cylinder (1) for a supply of carrier gas (nitrogen or air), a flow meter (2) for flow adjustment normally about 1 L min⁻¹, and a quartz tube, which was placed in an electric tube furnace (3). The quartz boat used for samples (4) was carefully positioned in the first quartz tube in the middle of the electric tube furnace which was linearly heated from room temperature to 800°C at a heating rate of approximately 2.2 °C min⁻¹. The second quartz tube was filled with quartz wool (5) kept heated at 800 °C by a small electric furnace (6) to ensure the transformation of all volatile Hg compounds to elemental mercury and to retain any particles that might be released from the sample. A Lumex pyrolysis unit (7) (Pyro 915+) provided additional decomposition of any remaining volatile mercury compounds that could interfere with the atomic absorption measurements [8]. Elemental mercury was detected by a Lumex Ra-915+ atomic absorption detector, based on Zeeman correction (8), which was connected directly to a computer (9) for data collection. A trap containing H₂SO₄–KMnO₄ solution (10) was connected to the exhaust from the Lumex Ra-915+ to retain Hg(0) in solution by oxidation and to quantitatively trap recover mercury released from the sample. This was used to assess the mass balance. Two parameters were controlled; the temperature of the sample at which the maximum of the mercury release peak was obtained, and the peak height/area.

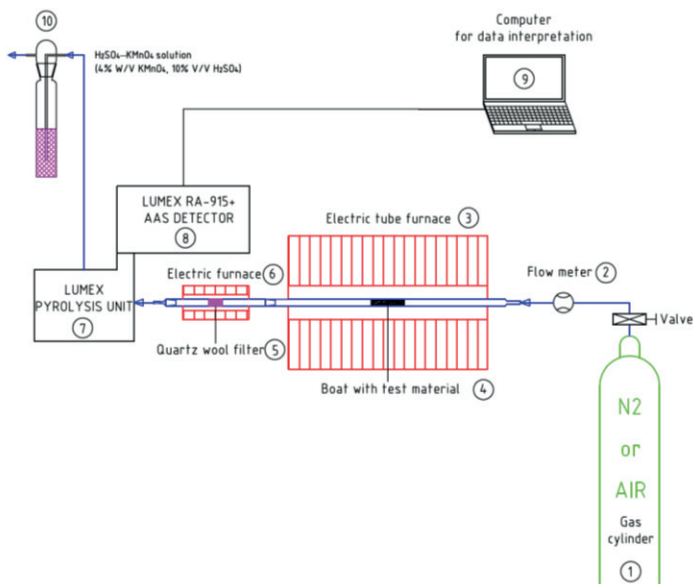


Figure 1: Scheme of the measuring line.

The RA-915+ Mercury Analyser with PYRO-915+ pyrolyser was developed for direct mercury determination (no pre-treatment procedures required). Using the RA-915+ spectrometer with background correction and the PYRO-915+, two-chamber catalyt atomizer allows direct mercury analysis of complex-matrix samples [8].

Sample preparation: Nine different mercury compounds were chosen; HgCl₂, Hg₂Cl₂, HgS, Hg₂SO₄, HgSO₄, HgSe, HgF₂, HgO-Red and HgO-Yellow. Experiments were performed with pure mercury compounds and mercury compounds mixed with SiO₂ powder. In the latter case the compounds (1-4 mg) were mixed with about 5 g of SiO₂ powder. The mixture was carefully homogenized by mixing in zirconia containers in a planetary mill with zirconia balls. Homogenization was done in three sequences, each of 10 min, in order to prevent heating of the contents. The homogeneity of the prepared mixtures was checked by acid digestion of 10 mg sub-aliquots, followed by cold-vapour atomic absorption spectrometry (CVAAS) based on reduction with SnCl₂ [9]. Six independent analyses were made and it was shown that the homogeneity was better than 2.5 %, except for HgSe and HgCl₂ which were approximately 6 and 8 %. After the homogenization

process a sample aliquot 9-30 mg mixture with SiO₂, was transferred to the quartz boat.

In the case of pure substances, pre-treatment was not required. Samples were weighed (< 200 µg) on a Mettler Toledo AE 240 S micro balance, with uncertainty of 0.01 mg. A mass balance assessment by trapping and analysis of mercury in the permanganate solution was made to evaluate the completeness of mercury release during heating.

3 Results and discussion

For better comparison of the experiments, results are shown as graphs of temperature versus the relative intensity of the released mercury. The mercury compounds were intercompared according to the type of carrier gas and the temperature at which mercury was released as a peak from the pure compound and from its mixture with SiO₂.

The thermograms of mercury compounds can be divided into three groups, depending on the number of peaks observed. The first group contained mercury compounds with only one thermal peak. These were HgS, Hg₂Cl₂, HgCl₂, and both HgO compounds (red and yellow). The second group consisted of mercury compounds that formed more than one peak, depending on the conditions (HgF₂, Hg₂SO₄ and HgSO₄). The third group consisted of the mercury compound HgSe which showed no effect on released peak depending of experimental conditions.

The mercury compounds in the first group showed one distinctive mercury peak. The carrier gas and the presence of matrix (SiO₂), have a great impact on the release temperature. Pure mercury compounds show variations in their thermograms solely due to the use of a different carrier gas. It was evident that the maximum of the release peak usually occurred at a lower temperature when purging mercury compounds with nitrogen. A similar situation was found when testing mercury compounds mixed with SiO₂. The most important finding was that mercury compounds from first group mixed with SiO₂, displayed their maximum peak at

different temperature from the pure compound. This reflects the effect of the substrate on these mercury compounds, probably by chemical interaction.

The most typical characteristic of this group of mercury compounds is the HgS thermogram, where nitrogen was used as carrier gas (Figure 2). On this thermogram, the peaks were separated into two temperature ranges. The first range of temperature at which release of mercury occurred extends from 150 to 350 °C with the peak maximum at a temperature of around 300 °C, while the second extends from 225 to 500 °C with a peak maximum temperature of around 340 °C. The difference in temperature behaviour was due to the substrate SiO₂ mixed with HgS in the case of the first temperature range. Evidently quartz affected the temperature at which mercury was released from the HgS sample.

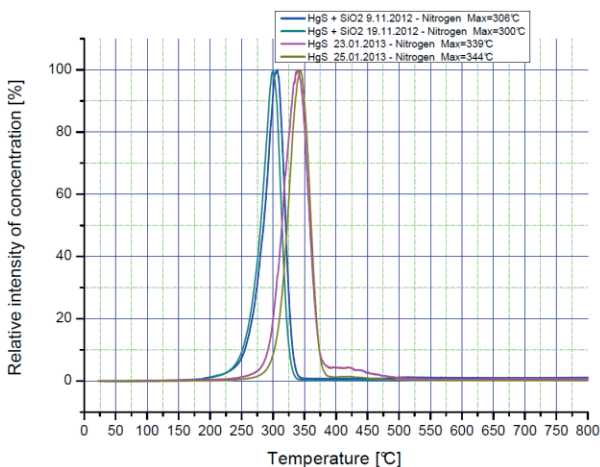


Figure 2: Thermogram of HgS, purged with nitrogen

As we have already mentioned above, the second group of results consisted of mercury compounds mixed with SiO₂ and those without (pure mercury compounds) that showed more than one peak when purged with nitrogen or air. The pure compounds of this group formed much smoother peaks than the same compounds mixed with SiO₂. This indicated that SiO₂ has some interaction with mercury compounds, just like with those from the first group. When comparing pure HgSO₄ to its mixture with the substrate, it was noticed, that the pure compound released

only one main peak while HgSO_4 mixed with quartz released several, no matter which carrier gas was used.

In general, mercury compounds released peaks earlier when purged with nitrogen, except for pure Hg_2SO_4 , which displayed its maximum peak at about the same temperature when purged with nitrogen and air.

The thermogram of HgF_2 where nitrogen was used as carrier gas is presented as an example (Figure 3). As seen on the thermogram, pure HgF_2 formed repeatable peaks at around 480 °C. Peaks also occurred at lower temperatures, but the temperatures of these peaks were not so repeatable. The most repeatable was the range of temperature in which mercury was released. This range extended from 170 °C to 550 °C for all samples of pure HgF_2 . When observing HgF_2 mixed with SiO_2 a degree of repeatability could also be noticed. Peaks of mercury from HgF_2 samples mixed with silica substrate could be observed in the range from room temperature to 370 °C. From this data, interactions of HgF_2 with the silica are clearly evident.

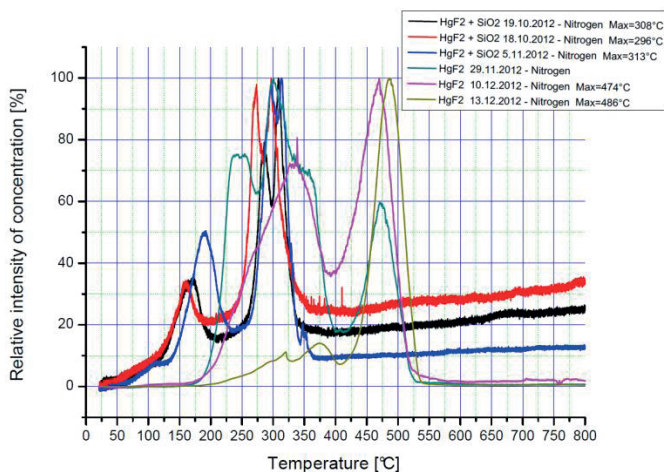


Figure 3: Thermogram of HgF_2 , purged with nitrogen

In the third group, only one mercury compound could be found, which showed no effect of carrier gas or substrate on the peaks released at elevated temperatures. This mercury compound is HgSe .

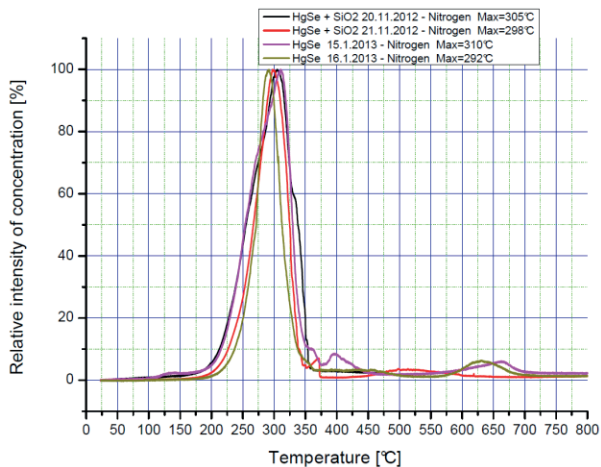


Figure 4: Thermogram of HgSe, purged with nitrogen

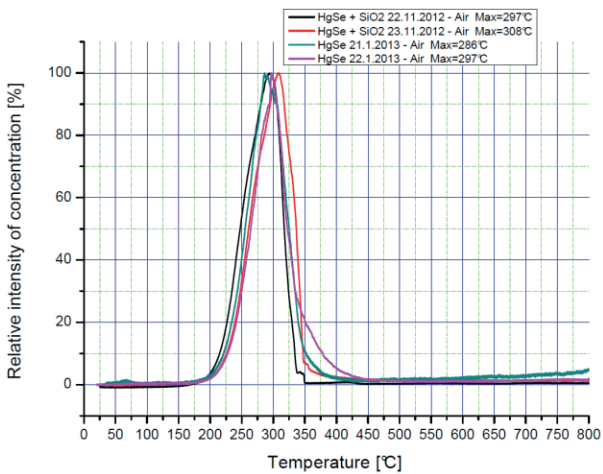


Figure 5: Thermogram of HgSe, purged with air

4 Conclusion

As seen from the experiments conducted during this study, it is necessary to understand the reactions of mercury compounds occurring at higher temperatures. It was shown that the carrier gas and its flow rate, as well as the SiO₂ substrate, and the material that is in contact with the samples affects the release of mercury. This is witnessed in the heights and shapes of the peaks, as well as their number and the breakdown temperature of the mercury compounds. These processes are not fully understood as yet. The mercury compounds most affected by these factors are particularly the sulphates and the fluoride.

Further fractionation experiments will include mixtures of mercury compounds with different substrates, designed to resemble complex matrices such as coal, gypsum, limestone, and materials used for adsorption at higher temperatures. Further investigation of the method's potential for separation and quantification of different mercury compounds in solid materials will be conducted.

References:

- [1] E. G. Pacyna, et al. Global emission of mercury to the atmosphere from anthropogenic sources in 2005 and projections to 2020. *Atmospheric Environment*, 44:2487–2499, 2010
- [2] UNEP. Global Mercury Assessment 2013: Sources, Emissions, Releases and environmental Transport. <http://www.unep.org/PDF/PressReleases/GlobalMercuryAssessment2013.pdf>, 2013.
- [3] R. Monterroso, M. Fan, M. Argyle. Coal gasification and Its Applications. Oxford, U.K., Elsevier Inc.:248–289, 2011
- [4] T. Okano. High Temperature Mercury Oxidation Kinetics via Bromine Mechanisms. *Degree of Master of Science, Faculty of the Worcester Polytechnic Institute*, 2009
- [5] H. Biester and C. Scholz. Determination of Mercury Binding Forms in Contaminated Soils: Mercury Pyrolysis versus Sequential Extractions. *Environ. Sci. Technol.*, 31:233–239, 1997
- [6] M. A. Lopez-Anton, et al. Analysis of mercury species present during coal combustion by thermal desorption. *Fuel*, 89:629–634, 2010
- [7] G. Luo, et al. Identifying modes of occurrence of mercury in coal by temperature programmed pyrolysis. *Proceedings of the Combustion Institute*, 33:2763–2769, 2011
- [8] S. Sholupov, et al. Zeeman atomic absorption spectrometer RA-915+ for direct determination of mercury in air and complex matrix samples. *Fuel Processing Technology*, 85:473–485, 2004
- [9] H. Akagi and H. Nishimura. Speciation of mercury in the environment. In *Advances in mercury toxicology*. T. Suzuki, N. Imura, T.W. Clarkson, New York, USA, Plenum Press:53–76, 1991

For wider interest

The aim of this study was to calibrate a method for temperature fractionation which would provide an understanding of the chemical reactions of different mercury compounds at elevated temperatures. This would serve as a comparison to other solid samples that contain different mercury compounds, and be applicable to pyrolysis processes involving flue gases and release and trapping of mercury at high temperatures.

The experiments conducted showed that many factors, such as the type of carrier gas, the substrate and the heating rate, affect the release of mercury. These effects can be seen in the temperature of mercury release and in the number of peaks. Our findings raise questions about the decomposition of complex matrices releasing mercury and their temperature comparability with pure mercury compounds.

Further fractionation experiments will include mixtures of mercury compounds with different substrates, designed to resemble complex matrices for which temperature fractionation may provide useful information (for example coal, gypsum, limestone, and materials used for adsorption at higher temperatures). We shall also further investigate the potential of the method for separation and quantification of different mercury compounds (or fractions) present in solid materials, especially coal.

Molybdenum coordination compounds as precursors for the preparation of MoS₂

Gleb Veryasov, Adolf Jesih

Department of Inorganic Chemistry and Technology, Jožef Stefan Institute,
Ljubljana, Slovenia

gleb.veryasov@ijs.si

Abstract. New approach for preparation of molybdenum sulphides was explored. Application of coordination molybdenum compounds, e.g. Mo(CO)₄bipy, Mo(CO)₃Toluene, Mo(CO)₅pyrrolidine, [Mo(CO)₅]₂piperazine and Mo(CO)₄piperidine₂ for the synthesis of MoS₂ provided active materials with different morphologies and surface areas. Sulphidization under different temperatures allowed obtaining sulphides with surface area up to 40 m²/g, which is high value in comparison to literature data on unsupported MoS₂ catalysts. Sulphides with highest surface areas were chosen for catalytic activity tests in methanation and hydrogenation reactions.

Keywords: Molybdenum disulphide, catalysis, molybdenum coordination compounds

1 Introduction

Molybdenum disulphide is a potential catalyst for methanation process because it is unaffected by sulphur impurities [1,2]. Catalytic activities of molybdenum sulphide and its compounds, namely carbides, oxides, nitrides and sulphides in CO and CO₂ methanation processes were investigated by different research groups. In 1981 M. Saito and R. B. Anderson [3] established the row of activity of these materials by CO₂ methanation with H₂, A. J. Frank *et al.* investigated methanation of CO with H₂S [4]. However, experimental results showed low activity of molybdenum sulphide in methanation, which can be explained by the shape or specific surface area of the material; therefore modification of MoS₂ is a promising way to improve this catalysts. B. K. Miremadi and S. R. Morrison reported preparation of unusually

active MoS₂ for hydrogenation of CO to methane by exfoliation of starting MoS₂ powder with n-buthyllithium and subsequent processing with water [5].

In current work we explored new technique for the preparation of molybdenum disulphide with relatively high surface area from molybdenum coordination compounds, containing organic ligands. The suggestion was that thermal removal of an organic ligand with simultaneous sulphidization should lead to a high surface area of product, which should lead to a higher amount of active sites on catalyst surface and high catalytic activity. Sulphidization under different temperatures allowed to obtain sulphide with surface area as high as 40 m²/g, which is very high value in comparison to literature data on unsupported MoS₂ catalysts. Samples surface was studied using scanning electron microscopy (SEM).

2 Experimental part

For preparation of starting complex compounds molybdenum hexacarbonyl (98%), α,α' -bipyridine and molybdenum pentachloride (95%), all supplied by Sigma-Aldrich, were used. Solvents were pre-dried over calcium hydride or phosphorous pentoxide. Characterization of samples was performed on Jeol Field Emission SEM 7600 and by Micromeritics Gemini VII 2390 surface area analyzer.

Preparation of complex compounds

Mo(CO)₆/Toluene

Compound was prepared by refluxing molybdenum hexacarbonyl in anhydrous toluene under argon atmosphere for three days [6]. In a typical preparation Mo(CO)₆, 0.57 g, (2.16 mmol) was placed into Schlenk flask equipped with Liebig's condenser. Then, 40 ml of anhydrous toluene, dried above phosphorous pentoxide, were added. Continuous flow of Ar was kept all the time. Flask was covered with alumina foil, placed into bath with glycerin, on the open end of Liebig's condenser mineral oil bubbler was attached and flow of Ar was stopped. Mixture was refluxed for three days. Bubbling of forming CO indicated the reaction progress. After bubbling stopped, compound was rapidly filtered through glass porous filter to remove molybdenum formed, in case the decomposition occurred. Flask containing filtrate was again covered with alumina foil. Gradual removal of toluene on vacuum line resulted in formation of the product in a shape of fine crystals. Yield: 0.5g (1.84 mmol, 85%). Elemental analysis: found C 46.32 H 2.22 N 7.75 calcd. C 46.16 H 2.20 N 7.69

Mo(CO)₄bipy

1.04 g of $\text{Mo}(\text{CO})_6$ (3.94 mmol) and 0.7 g of bipyridine (4.49 mmol) (molar ratio 1:1.14 $\text{Mo}(\text{CO})_6$:bipyridine) were placed into 100 ml glass flask, covered with 30 ml heptane and refluxed for 3 hours. After that compound was filtered and washed several times with small portions of heptane. Yield: 0.9 g (2.47 mmol, 64%). Elemental analysis: found C 43.7 H 3.0 calcd C 44.1 H 2.94 [7]

$[\text{Mo}(\text{CO})_5]_2$ piperazine

1.134 g of $\text{Mo}(\text{CO})_6$ (4.3 mmol) and 0.74 g of piperazine (8.6 mmol) (molar ratio 1:2 $\text{Mo}(\text{CO})_6$:piperazine) were placed into 100 ml glass flask, covered with 40 ml heptane and refluxed for 3 hours. After that compound was filtered and washed several times with small portions of heptane. Yield: 0.94 g (1.68 mmol, 78%). [8]

$\text{Mo}(\text{CO})_4$ piperidine

1.995 g of $\text{Mo}(\text{CO})_6$ (7.56 mmol) and 10 ml of piperidine (0.1 mol) (excess of piperidine) were placed into 100 ml glass flask with 30 ml heptane and refluxed for 4 hours. After that compound was filtered and washed several times with small portions of heptane. Yield: 2.694 g (7.12 mmol, 94%). [8]

$\text{Mo}(\text{CO})_4$ pyrrolidine

2.391 g of $\text{Mo}(\text{CO})_6$ (9.1 mmol), 10 ml of pyrrolidine (0.122 mol) (molar ratio 1:1.14 $\text{Mo}(\text{CO})_6$:pyrrolidine) and 35 ml of heptane were placed into 100 ml glass flask and refluxed for 3 hours. After that compound was filtered and washed several times with small portions of heptane. Yield: 2.794 g (8.68 mmol, 100%). [8]

Preparation of sulphides

Molybdenum coordination compounds were placed in quartz boat into quartz tube and sulphidized in a gas mixture with composition $\text{Ar}/\text{H}_2/\text{H}_2\text{S} - 96\%/2\%/2\%$. Sulphidization was carried out at two different temperatures, at 800 °C and 400 °C at a flow rate of 60 ml/min. Sulphides obtained were characterized by Scanning Electron Microscopy (SEM), BET surface area measurement.

3 Results and discussion

SEM images of sulphides obtained are shown in Figure 1, surface area data is summarized in Table 1. All the coordination compounds used, except $\text{Mo}(\text{CO})_4$ bipy for sulphidization are found to be hard to operate with at high sulphidization temperature (800 °C). In these conditions decomposition is a prior process to sulphidization, leading to transfer of sample all around the tube and following

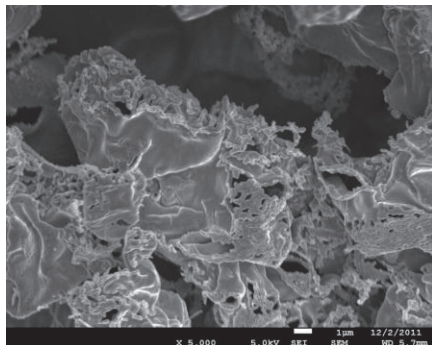
formation of MoS₂ film, or even Mo(CO)₆ crystals, what was observed in case of Mo(CO)₃Toluene.

Sulphide, obtained from Mo(CO)₃Toluene form developed and rough structure with surface area of 4 m²/g. Sulphidization of [Mo(CO)₅]₂piperazine leads to formation of ball-like MoS₂ with above a micron size and with the biggest surface area out of the group of sulphides investigated.

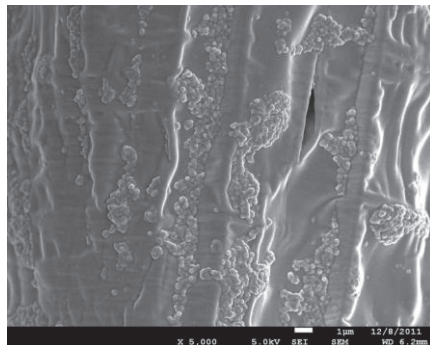
Mo(CO)₅pyrrolidine is an extremely sensitive compound, yield of sulphidization was very low, so that we were not able to measure surface area on the sample obtained. Mo(CO)₄bipy formed a very strong interconnected fibers of MoS₂, however, the sample prepared at 800° contained carbon. Mo(CO)₄piperidine₂ gives layered structure with a number of empty space in-between of layers. [Mo(CO)₅]₂piperazine form ball-like structure with empty space inside the spheres, which makes possible further improvement of the specific surface area obtained by ball opening.

Table 1. Specific surface areas of sulphides obtained

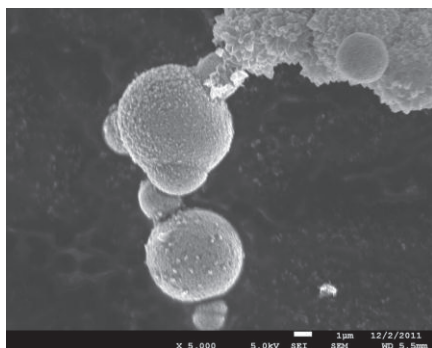
Starting material	Specific surface area/ m ² g ⁻¹
Mo(CO) ₃ Toluene	4
[Mo(CO) ₅] ₂ piperazine	39
Mo(CO) ₄ piperidine ₂	7
Mo(CO) ₄ bipy (at 800°C)	38



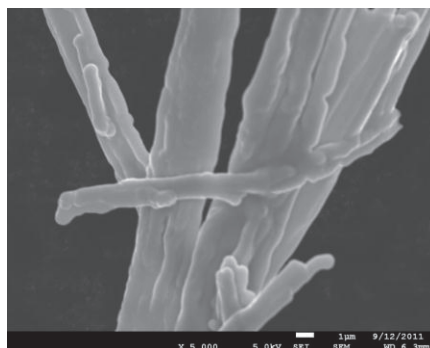
$\text{Mo(CO)}_4\text{piperidine}_2$



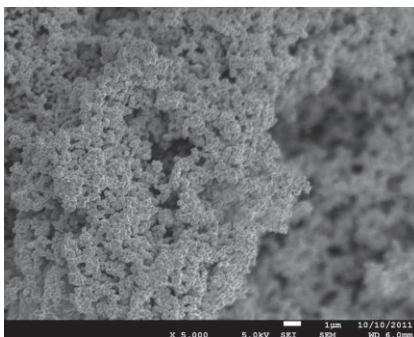
$\text{Mo(CO)}_4\text{bipy (800}^\circ\text{C)}$



$[\text{Mo(CO)}_5]_2\text{piperazine}$



$\text{Mo(CO)}_5\text{pyrrolidine}$



$\text{Mo(CO)}_3\text{Toluene}$

Figure 1. SEM images of sulphidization products at magnification of 5000

References:

- [1] M. Saito and R. B. Anderson, *Journal of Catalysis*, 63, 438-446, 1980
- [2] G. A. Mills and F. W. Steffgen, *Catalysis Reviews*, 8, 159-210, 1973
- [3] M. Saito and R. B. Anderson, *Journal of Catalysis*, 67, 296-302, 1981
- [4] A. J. Frank, H. A. Dick, J. Goral, A. J. Nelson, M. Gratzel, *Journal of Catalysis*, 126, 674-676, 1990
- [5] B. K. Miremedi and S. R. Morrison, *Journal of Catalysis*, 103, 334-345, 1987
- [6] W. Strohmeier, *Chemische Berichte*, 94, 3337-3341, 1961
- [7] S.S. Braga, A. C. Coelho, I. S. Gonçalves, F. A. Almeida Paz, *Acta Crystallographica*, E63, 780-782, 2007
- [8] G. W. A. Fowles and D. K. Jenkins, *Inorganic Chemistry*, 3(2), 257-259, 1964

For wider interest

Molybdenum materials and especially molybdenum disulphide, MoS₂, are widely applied in petroleum refraction and as lubricants in machines. The main advantage of this material is its stability against sulphur poisoning which diminish catalysts activity and is a serious industrial problem. However, just a small part in MoS₂ structure (it has layered structure) has catalytic activity, which results in low activity due to small amount of active sites.

Current work aims improvement of the catalytic activity of MoS₂ within new approaches of preparation.

Simulation of *mer*-[MoBr₃Py₃] Raman spectrum by DFT method

Gleb Veryasov, Dmitry Morozov, Adolf Jesih

Department of Inorganic Chemistry and Technology, Jožef Stefan Institute,
Ljubljana, Slovenia

University of Jyväskylä, Department of Chemistry & Nanoscience Center, Finland,
Jyväskylä

gleb.veryasov@ijs.si

Abstract. We applied DFT method to simulate *mer*-[MoBr₃Py₃] Raman spectrum, using B3LYP functional, cc-PVDZ basis set and pseudo potentials for bromine and molybdenum atoms to take into consideration relativistic effects of heavy atoms; simulated Raman spectrum is compared to the recorded spectrum.

Keywords: Molybdenum compound, DFT, Raman spectroscopy.

1 Introduction

Monomeric halo-pyridine molybdenum complexes are known for significant period of time - first references relate to the year 1931, when Rosenheim and co-workers described synthesis of two MoX₃Py₃ compounds (X = Br, Cl; Py=pyridine) [1] by the reaction of molybdenum trihalides with boiling pyridine. Interaction of (NH₄)[MoX₅ · H₂O] with boiling pyridine gives the only product - *mer*-[MoX₃Py₃], while dilution of pyridine with methanol results in formation of side product with the total amount up to 20%, which was found to have formula [MoX₄Py₂][MoX₂Py₄] [2]. Oxidation of this compound by bromine results in precipitation of *trans*-[MoX₂Py₄]Br₃ [Error! Bookmark not defined.,3]

Switching to ionic complexes of molybdenum(III) halides, containing pyridine as a ligand, *trans*-PyH[MoBr₄Py₂] and *trans*-NH₄[MoBr₄Py₂] · H₂O, Cs[MoBr₄Py₂], LH[MoBr₄Py₂] (L= 4-methylpyridine, 4-pic; 2,2'-bipyridyl, bipy) obtained within cation exchange was reported [4]. Reactions between (PyH)₃MoX₆ (X = Cl, Br) and pyridine results in formation of *trans*-(PyH)MoCl₄Py₂ and *trans*-(PyH)₂MoBr₄Py₂.

Trans-(Py)₂HMoCl₄Py₂ can be obtained from the cold solution of *trans*-(PyH)MoCl₄Py₂ in pyridine. *Trans*-(Py)₂HMoX₄Py₂ decompose at room temperature to *trans*-(PyH)MX₄Py₂ [5].

In 1974 crystal structure of MoCl₃Py₃ and cell parameters of MoBr₃Py₃, calculated from a powder pattern, assuming that the compound should be isostructural to MoCl₃Py₃ were reported by Brenčič [6].

First data about MoI₃Py₃ refer to year 1966 [7]. Djordjević et. al. prepared molybdenum(III) iodide by heating of molybdenum hexacarbonile with iodine in evacuated and sealed ampoule and examined it in reaction with boiling pyridine.

2 Experimental part

2.1 Chemicals and instrumentation

Preparation of MoBr₃Py₃ has been performed within two approaches - in boiling pyridine and at room temperature.

Synthesis in boiling pyridine was made as described elsewhere [Error! Bookmark not defined.]. Molybdenum tribromide (500 mg, 1.49 mmol) was placed into a glass flask with 20 ml anhydrous pyridine and refluxed for 3 hours with following hot filtration in order to remove small amount of residual MoBr₃. To hot filtrate HCl was added to a weak-acid reaction and immediately formed precipitate was filtered and washed with ethanol. Collected product was dried in vacuo. Yield is 350 mg (0.61 mmol, 41%).

Raman spectra was measured on compound on Horiba Jobin-Yvon LabRAM HR High Resolution Raman Spectrometer with internal laser 633 nm and power of 1,7 mW with total 100 scans.

2.2 Computational details

All calculations were performed using DFT with B3LYP functionals [8-9]. All computations were performed carried out using GAMESS(US) program package [10]. We used cc-pVDZ basis set as well known for correlated methods. First initial geometry of mer-[MoBr₃Py₃] was optimized, this gived us minimum energy points from which vibration spectra should be calculated. Then Forces Constants matrix (also known as Hessian matrix), which is matrix of the second derivatives of energy by all coordinates, was calculated. Normal modes frequencies were evaluated by diagonalization of Force Constants matrix. Raman activities (S_i) were converted to

Raman intensities (I_i) using following relationship from the intensity theory of Raman scattering [11-13]:

$$(1) \quad I_i = \frac{f(\nu_0 - \nu_i)^4 S_i}{\nu_i \left[1 - \exp\left(-\frac{h c \nu_i}{k T}\right) \right]}$$

Where ν_0 – is the exciting frequency (cm^{-1}) and ν_i – is the vibrational wave number of the i -th normal mode (cm^{-1}).

For the simulated spectra plots Doppler broadening was used with a bandwidth at half height of peak 15 cm^{-1} .

3 Results and discussion

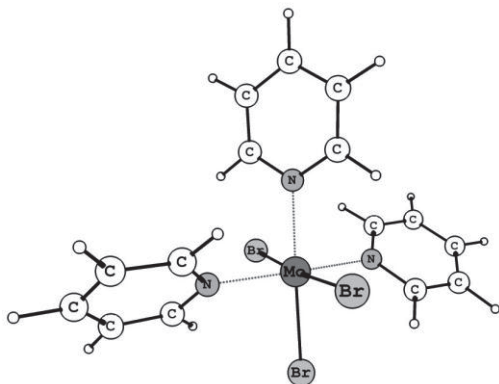


Figure 1. Molecular structure of *mer*-[MoBr₃Py₃]

Molecular structure of the title compound is represented in Figure 1. Computed Raman spectrum was found to be in a good correlation (see Fig. 2) with the experimental one after normalization of Raman shifts by a factor 1.006938 (calculated from the positions of the most intensive band in spectra). Bands appeared above 500 cm^{-1} are of a little interest since they appear from pyridine ligand and their discussion was omitted, all bands in between $100 \text{ cm}^{-1} - 500 \text{ cm}^{-1}$ are listed in Table 1.

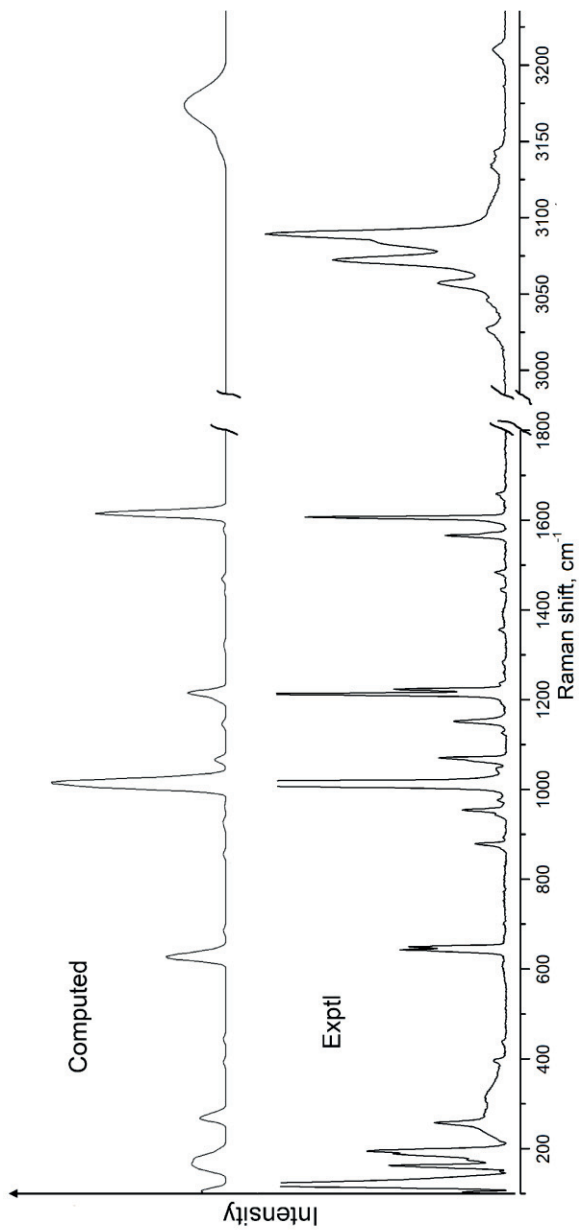


Figure 2. Computed and recorded Raman spectra of $mer\text{-}[\text{MoBr}_3\text{Py}_3]$

Table 1. Bands appeared in spectra below 500 cm^{-1} with assignments

Computed		Experimental		Assignments
Raman shift, cm^{-1}	I, rel.	Raman shift, cm^{-1}	I, rel.	
102	0.15	104	0.03	Py wagging
106	0.03	119	0.19	Py wagging
149	0.08	149	0.01	Py wagging
152	0.01			Py wagging
154	0.07			Py wagging
162	0.11	163	0.07	Py wagging
165	0.07			Mo-N stretching
171	0.03			Mo-Br stretch & Py wagging
176	0.14	176	0.03	Mo-N breathing
184	0.07	188	0.07	Py wagging
195	0.04	194	0.09	Py wagging
264	0.17	258	0.04	Mo-N stretching
276	0.08			Mo-Br stretching
388	0.01			oop ring deformation
393	0.01	396	0.01	oop ring deformation
438	0.00			oop ring deformation
439	0.01	440	0.01	oop ring deformation

4 Conclusions

We simulated Raman spectrum of $\text{mer-[MoBr}_3\text{Py}_3]$ using DFT/B3LYP/cc-PVDZ method with pseudo potentials on molybdenum and bromine atoms. Computed spectrum was found to be in good correlation with experimental one. Band assignment was performed.

References:

- [1] A. Rosenheim, G. Abel, R. Lewy, *Zeitschrift für anorganische und allgemeine Chemie*, 197, 189-211, 1931
- [2] J. V. Brenčić, L. Golič, I. Leban, and R. Rotar, *Zeitschrift für anorganische und allgemeine Chemie*, 622, 2124-2128, 1996

- [3] J. V. Brenčič, A. N. Chernega and R. Rotar, *Acta Chimica Slovenica*, 46(2), 155-160, 1999
- [4] J. V. Brenčič, B. Čeh, I. Leban, B. Modec, R. Rotar, *Zeitschrift für anorganische und allgemeine Chemie*, 4, 796-800, 1993
- [5] J. V. Brenčič, B. Čeh, I. Leban, *Zeitschrift für anorganische und allgemeine Chemie*, 7, 212-220, 1986
- [6] J. V. Brenčič, *Zeitschrift für anorganische und allgemeine Chemie*, 403, 218-224, 1974
- [7] C. Djordjević, R. S. Nyholm, C. S. Pande, and M. H. B. Stiddart, *J. Chem. Soc (A)*, 16-17, 1966; D. Becke, *Journal of Chemical Physics*, 98, 5648-5652, 1993
- [8] C. Lee, W. Yang, R. G. Parr, *Physical Reviews B*, 37, 785-789, 1998
- [9] M. W. Schmidt, K. K. Baldrige, J. A. Boatz, S. T. Elbert, M. S. Gordon, J. J. Jensen, S. Koseki, N. Matsunaga, K. A. Nguyen, S. Su, T. L. Windus, M. Dupuis, J. A. Montgomery, *Journal of Computational Chemistry*, 14, 1347-1363, 1993
- [10] P. L. Polavarapu, *Journal of Physical Chemistry*, 94, 8106-8112, 1990
- [11] G. Keresztury, Raman spectroscopy: theory, in: J. M. Chalmers, P. R. Griffiths (Eds.), *Handbook of Vibrational Spectroscopy*, vol. 1, Wiley, 2002.
- [12] G. Keresztury, S. Holly, J. Varga, G. Besenyey, A. Y. Wang, J. R. Durig, *Spectrochimica Acta A*, 49, 2007 and 2019, 1993

For wider interest

Molybdenum materials and especially molybdenum disulphide, MoS₂, are widely applied in petroleum refraction and as lubricants in machines. The main advantage of this material is its stability against sulphur poisoning which diminish catalysts activity and is a serious industrial problem. However, just a small part in MoS₂ structure (it has layered structure) has catalytic activity, which results in low activity due to small amount of active sites.

Current work aims improvement of the catalytic activity of MoS₂ within new approaches of preparation.

Karakterizacija mleka in sira z uporabo stabilnih izotopov lahkih elementov (C, N in O) v Sloveniji

(prispevek dodiplomske študentke)

Urša Vežjak, Kanduč Tjaša¹, Nives Ogrinc¹

¹ Odsek za znanosti o okolju, Institut "Jožef Stefan", Ljubljana, Slovenija

nives.ogrinc@ijs.si

Povzetek. V prispevku so predstavljeni prvi rezultati izotopske sestave kisika, ogljika in kisika v kravjem mleku, ovčjem in kozjem mleku in siru v Sloveniji. Analizirali smo 31 vzorcev kravjega mleka iz meseca marca, junija, septembra ter 43 decembrskih vzorcev v letu 2012. Analize na ovčjem mleku so potekale na 75 vzorcih v maju, juniju, juliju in na 25 vzorcih sira iz maja 2012. $\delta^{13}\text{C}$ vrednosti v kravjem mleku se spreminjajo od $-28,5$ do $-13,6$ ‰, medtem ko se $\delta^{15}\text{N}$ vrednosti spreminjajo od 3,5 do 6,7 ‰. $\delta^{13}\text{C}$ vrednosti v mleku ovc in koz se spreminjajo od $-29,3$ do $-24,6$ ‰, medtem ko se $\delta^{15}\text{N}$ vrednosti spreminjajo od 1,4 do 7,5 ‰. Enak razpon $\delta^{13}\text{C}$ in $\delta^{15}\text{N}$ smo zasledili v ovčjih in kozjih sirih. Razlike v izotopski sestavi C, N in O so v različnih prehranjevalnih navadah krav, ovc in koz in odvisni od klimatskih in področnih razlik izvora mleka.

Ključne besede: mleko, sir, stabilni izotopi, ogljik, dušik, kisik, prehranjevalne navade

1 Uvod

Mleko in mlečni izdelki predstavljajo pomemben del vsakdanje prehrane. V Sloveniji uživamo predvsem kravje mleko in sir, v manjši meri pa tudi kozje in ovčje mleko in proizvode iz njih, vendar so ti cenovno dražji in bolj podvrženi različnim potvorbam. Masna spektrometrija za analizo izotopov lahkih elementov (IRMS), ki temelji na meritvah vsebnosti stabilnih izotopov proizvoda ali specifične komponente proizvoda, je ena izmed najbolj inovativnih tehnik za opisovanje in

nadzor kakovosti in pristnosti proizvodov, hrane in tudi mleka in mlečnih izdelkov. Z analizo relativne izotopske sestave ogljika, dušika in kisika v mleku in mlečnih izdelkih lahko sklepamo na prehrano živali [1, 2], okoljske pogoje [3, 4] in geografsko poreklo [1, 5].

Izotopska sestava kisika in vodika v živalskih tkivih sta primarno odvisna od izotopske sestave zaužite vode, medtem ko je izotopska sestava ogljika in dušika odvisna od vrste tal in prehranjevalnih navad. Nadalje na $^{15}\text{N}/^{14}\text{N}$ razmerje v mleku in kazeinu poleg prehrane vplivajo še drugi faktorji kot so tla, vlaga, oddaljenost od morja in gnojenje [1, 3, 6]. Vsebnost ^{18}O v mleku je odvisna od krme in vode, ki so jo živali zauživale [1, 5] in pogojena s klimatskimi in geografskimi značilnostmi nekega območja, kot so temperatura, vlažnosti, padavine, oddaljenost od morja ter geografska dolžina in širina [5]. Zato lahko iz rezultatov razmerja ^{18}O in ^{16}O razberemo geografsko poreklo vzorcev.

Glavni namen predlaganega dela je vzpostaviti bazo podatkov o izotopski sestavi pristnega, slovenskega mleka, s pomočjo katere bomo lahko določili potvorjenost mleka in s tem zaščitili potrošnika in dobro ime slovenske mlekarske industrije. Pri tem smo se osredotočili na vzorce kravjega, ovčjega in kozjega mleka in sirov iz različnih geografskih področij v Sloveniji in ugotavljali vpliv klimatskih in področnih razlik na izotopsko sestavo mleka.

2 Materiali in metode

2.1 Vzorčevanje

Mesečno smo zbirali vzorce nehomogeniziranega mleka, ki so nam ga dostavljale štiri slovenske mlekarne: Ljubljanske mlekarne, Pomurske mlekarne, Vipavske mlekarne in Mlekarna Planika iz petih regij po Sloveniji (alpska, dinarska, sredozemska, panonska in Celjska regija - ta se je priključila naknadno). Vzorce mleka smo takoj zamrznili in hranili pri $-20\text{ }^{\circ}\text{C}$ do izvedbe analiz. Vzporedno z vzorci mleka smo vzorčili tudi podzemne vode iz 4 različnih lokacij: Murske Sobote, Gore (Kobarid), Zadloga in Postojne. Analizirali smo 31 vzorcev kravjega mleka iz meseca marca, junija, septembra ter 43 decembrskih vzorcev v letu 2012.

Obdobje laktacije pri ovcah in kozah je sezonsko, zato je analiza potekala na 75 vzorcih v maju, juniju in juliju ter na 25 vzorcih sira iz maja 2012.

2.2 Analize

Izotopsko sestavo oziroma razmerje med težjim in lažjim izotopom v spojini izražamo z vrednostjo- δ , ki predstavlja relativno razliko izotopske sestave raziskovanega vzorca (vz) glede na izbrani standard (st), in jo izražamo v promilih (‰):

$$\delta A = [(R_{vz} - R_{st})/R_{st}] \cdot 1000 \quad (1)$$

V enačbi 1 pomeni A težji izotop elementa (^{13}C , ^{15}N , ^{18}O), vrednost R pa je razmerje med izotopi ($^{13}\text{C}/^{12}\text{C}$, $^{15}\text{N}/^{14}\text{N}$, $^{18}\text{O}/^{16}\text{O}$). Za ogljik je privzet karbonatni standard fosila *Belemnite* *Americana* iz kredne formacije *PeeDee* v Južni Karolini (PDB – *Pee Dee Belemnite*), za dušik zračni dušik (AIR), za kisik pa je privzet standard povprečne morske vode (SMOW – *Standard Mean Ocean Water*) na globini enega metra pri temperaturi 25 °C.

Metoda za določevanje vrednosti $\delta^{18}\text{O}$ temelji na izmenjavi izotopov kisika med vodo v mleku in CO_2 . Meritve izotopske sestave kisika v vzorcih vod smo izvedli na masnem spektrometru *Isoprime* (GV Instruments) s preparativnim nastavkom *Multiflow* za tekoče vzorce. Pri meritvah v vzorcih vode uporabljamo laboratorijske standarde, ki so interno umerjeni na mednarodne: V-SMOW ($\delta^{18}\text{O} = 0,0$ ‰), GISP ($\delta^{18}\text{O} = -24,8$ ‰), in SLAP ($\delta^{18}\text{O} = -55,5$ ‰). Za interni laboratorijski standard uporabljamo morsko vodo s povprečno vrednostjo $\delta^{18}\text{O} = -0,4 \pm 0,1$ ‰ in vodovodno vodo s povprečno vrednostjo $\delta^{18}\text{O} = -9,5 \pm 0,1$ ‰.

Iz mleka smo izolirali kazein. V 50 ml centrifugirko smo dodali 30 ml nehomogeniziranega mleka in centrifugirali pri 3200 x g 10 min. Med tem se je zbrala mlečna maščoba na vrhu vodotopnih spojin, proteini pa v obliki peleta na dnu. Maščobo smo postrgali z vrha in s filter papirjem obrisali ostanke maščobe. Vzorcju smo znižali pH na 4,3 z 1 M HCl. Pri tem so se kazeini oborili in oblikovali so se krpicam podobni skupki. Vzorec smo centrifugirali (3200 x g, 10 min), 1 x sprali z MQ vodo in 1 x z raztopino petrol eter:eter v razmerju 2:1. Po centrifugiranju smo vzorec liofilizirali.

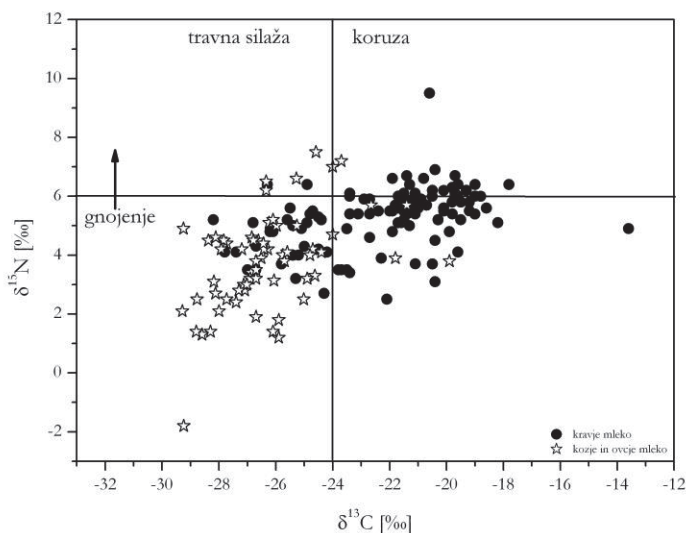
Sir smo naribali (4 g) in vzorcem dodali mešanico petrol etra:etil etra v razmerju 2:1, ter centrifugirali na 3700 x g za 10 minut. Supernatant smo odlili ter postopek ponovili še dvakrat. Izoliran kazein smo sprali z vodo ter ga liofilizirali.

Posušen vzorec smo zatehtali v kositrne kapsule in določili $\delta^{13}\text{C}$ in $\delta^{15}\text{N}$ vrednosti na izotopskem masnem spektrometru za določevanje razmerja stabilnih izotopov lahkih elementov (IRMS) Europa Scientific 20-20 s preparativnim nastavkom za trdne in tekoče vzorce ANCA-SL. Za spremljanje pravilnosti in natančnosti meritev smo za ogljik uporabili referenčne standarde IAEA-NBS (oil), IAEA-CH-3, IAEA-CH-6 s sledečimi $\delta^{13}\text{C}$ vrednostmi $-29,7 \pm 0,2 \text{ ‰}$, $-31,8 \pm 0,2 \text{ ‰}$ in $-24,7 \pm 0,2 \text{ ‰}$. Za dušik pa IAEA-N-1 ($\delta^{15}\text{N} = +0,4 \pm 0,2 \text{ ‰}$) in IAEA-N-2 ($\delta^{15}\text{N} = +20,3 \pm 0,2 \text{ ‰}$). Ponovljivost meritev znaša $\pm 0,1 \text{ ‰}$ za $\delta^{18}\text{O}$ $\pm 0,2 \text{ ‰}$ za $\delta^{13}\text{C}$ in $\pm 0,3 \text{ ‰}$ za $\delta^{15}\text{N}$.

3 Rezultati in diskusija

Meritve izotopske sestave kisika v zimskih in spomladanskih mesecev (januar-aprila) kažejo, da je izotopska sestava mleka v povprečju za 2 ‰ višja od sestave podzemne vode na raziskanem področju. Najnižjo izotopsko sestavo v mleku okrog $-11,4 \text{ ‰}$ zasledimo na Dolenjskem pri Žužembergu (v marcu 2013) in Bohinju na Gorenjskem. Izotopska sestava podzemne vode se spreminja med $-9,1$ (Zadloška voda, v februarju) in $-7,2 \text{ ‰}$ (Zadloška voda, v juniju). V mesecu maju pa je razlika v $\delta^{18}\text{O}$ vrednostih podzemne vode in mleka večja v povprečju za 3,7 ‰. Višjo izotopsko sestavo kisika smo določili v vzorcih mleka v mesecu juniju. Vrednosti se spreminjajo med $-3,6$ in $0,3 \text{ ‰}$. Velikost obogatitve s težjim ^{18}O izotopom glede na podzemno vodo je posledica metabolizma krave, ki se sezonsko spreminja in prehranjevalnih navad. Podrobnejša razlaga rezultatov bo možna, po daljšem vzorčevalnem obdobju. Prav tako smo opazili razlike v vrednostih $\delta^{18}\text{O}$ v mleku iz različnih geografskih področij. Opazili smo statistično signifikantno razliko v obogatitvi mleka z ^{18}O med Primorskimi in celinskimi področji, ki jo lahko razložimo z okoljskimi in ekofiziološkimi faktorji, ki vplivajo na izotopsko sestavo vode in posledično mleka.

V mesecu marcu, juniju, septembru in decembru smo izvedli tudi meritve izotopske sestave ogljika in dušika v kazeinu. Zasledili smo velik razpon med $\delta^{13}\text{C}$ in $\delta^{15}\text{N}$ vrednostmi med različnimi geografskimi področji, kar je grafično prikazano na sliki 1. $\delta^{13}\text{C}$ vrednosti se spreminjajo med $-28,5$ in $-13,6 \text{ ‰}$, medtem ko se $\delta^{15}\text{N}$ vrednosti spreminjajo med 3,5 in 6,7 ‰.



Slika 1. Spreminjanje izotopske sestave ogljika in dušika v kazeinu izoliranem iz mleka. $\delta^{13}\text{C} > -24 \text{ ‰}$: pretežni del prehranjevanja s koroza ; $\delta^{15}\text{N} > 6 \text{ ‰}$: uporaba organskih gnojil pri pridelavi hrane oziroma pri gnojenju pašnika.

Razlike v izotopski sestavi C so posledica različnih prehranjevalnih navad krav. Izkazalo se je, da koroza predstavlja pomemben del prehrane večini krav na Slovenskem, medtem ko se s travno silažo v glavnem prehranjujejo krave na Tolminskem in Postojnskem.

$\delta^{13}\text{C}$ vrednosti v mleku ovc in koz se spreminjajo med $-29,3$ in $-24,6 \text{ ‰}$, medtem ko so $\delta^{15}\text{N}$ vrednosti med $1,4$ in $7,5 \text{ ‰}$. Ti rezultati nakazujejo, da se ovce in koze prehranjujejo v glavnem s pašo in travno silažo. V enem od vzorcev, pa smo zasledili višjo $\delta^{13}\text{C}$ vrednost $-22,7 \text{ ‰}$, ki nakazuje manjši prispevek koroze pri hranjenju. $\delta^{15}\text{N}$ vrednosti, ki so višje od 6 ‰ nakazujejo uporabo organskih gnojil pri pridelavi hrane oziroma pri gnojenju pašnika.

Enako izotopsko sestavo smo zasledili pri ovčjih in kozjih sirih. Z raziskavami bomo nadaljevali tudi v letu 2013.

Zahvala

Delo poteka v okviru CRP projekta V4-1108 z naslovom »Uporaba specifičnih metod za ugotavljanje in preprečevanje potvorb mleka in mlečnih izdelkov«, ki ga financirata Slovenska raziskovalna agencija (ARRS) in Ministrstvo za kmetijstvo in okolje (MKO). Zahvaljujemo se Ljubljanskim mlekarnam, d.d., Pomurskim mlekarnam, d.d., Mlekarni Vipava d.d., Mlekarni Planika predelava mleka d.o.o. in mlekarni Čeleia za redno, mesečno dostavo vzorcev slovenskega mleka in podzemnih vod. Prav tako se zahvaljujemo Kmetijskemu gozdarskemu zavodu Nova Gorica za vzorčevanje kozjega in ovčjega mleka.

Literatura

- [1] L. Bontempo in sod. H, C, N and O stable isotope characteristics of alpine forage, milk and cheese. *International Dairy Journal*, 23: 99-104, 2012.
- [2] F. Camin in sod. Influence of dietary composition on the carbon, nitrogen, oxygen and hydrogen stable isotope ratios of milk. *Rapid communications in mass spectrometry*, 22: 1690-1696, 2008.
- [3] F. Camin in sod. Application of multielement stable isotope ratio analysis to the characterization of French, Italian, and Spanish cheeses. *Journal of Agricultural and Food Chemistry*, 52: 6592-6601, 2004.
- [4] R. Crittenden in sod. Determining the geographic origin of milk in Australasia using multielement stable isotope ratio analysis. *International Dairy Journal*, 17: 421-428, 2007.
- [5] L.A. Chesson in sod. Hydrogen and oxygen stable isotope ratio in milk in United States. *Journal of Agricultural and Food Chemistry*, 58: 2358-2363, 2010.
- [6] F. Camin in sod. H, C, N and S stable isotopes and mineral profiles to objectively guarantee the authenticity of grated hard cheeses. *Analytica Chimica Acta*, 711: 54-59, 2012.

Za širši interes

Rezultati raziskav podpirajo razvoj sistema za monitoring prehrabnenih proizvodov in razvoj metod za izvajanje kontrole živil. Z možnostjo dokazovanja avtentičnosti mleka in mlečnih izdelkov v prehrabnenih izdelkih bodo pristojni organi zaščitili in zavarovali kakovost teh proizvodov hkrati pa tudi zaščitili potrošnika pred morebitnimi potvorbami.

Fatty acid composition as a tool for determination of geographical origin and authenticity of milk and dairy products

(undergraduate student contribution)

Adrián Vicent¹, Marinka Petrišič¹, Marijan Nečemer², Nives Ogrinc^{1,*}

¹ Department of Environmental Sciences, Jožef Stefan Institute, Ljubljana, Slovenia

² Department of Low and Medium Energy Physics, Jožef Stefan Institute, Ljubljana, Slovenia

*nives.ogrinc@ijs.si

Abstract. Dairy products are in considerable high demand; therefore, there is a temptation to economic adulteration on these products. Authenticity and determination of geographical origin of these products are becoming an important issue for providers and consumers. Calculation of fatty acid ratios can be relevant indication for that purpose. Milk samples from four different dairying regions in Slovenia were collected; fatty acids were extracted as methyl esters (FAME) and analysed by GC-FID. Statistical analyses of these samples show a clear differentiation between geographical provenance, and differentiation in ruminant provenance. In addition the first results indicated that adulteration of sheep and goat milk with up to 1% of added cow's milk can be identified employing the described methodology.

Keywords: milk, cheese, dairy product, adulteration, geographical origin, fatty acids, FAME, GC-FID.

1. Introduction

Dairy products are important for human consumption due to their high content in vitamin D, vitamin A, calcium, magnesium, zinc, and protein among others; milk is one of the most nutritionally-complete foods in the nature. As a result, these products are used extensively and thus vulnerable to economic adulteration. Food adulteration and fraud profit has been practised from historical times. For that reason authenticity of dairy products is an important issue [1, 2]. Fatty acids in ruminants are derived from anaerobic fermentation of carbohydrates by the microorganisms present in these animals. Around 200 different fatty acids can be found in cow's milk, most of them at trace levels. The composition of fatty acids in

ruminant's milk depends on the season following the changes in rumen's food [3]. Depending to specific conditions, dairy products can be labelled characterising their origin [4, 5]. The regions where these dairy products come from can be designed for products with protected designation of origin (PDO) or protected geographical indication (PGI). A common theme of food authentication studies is the requirement for a database of genuine samples to which the sample can be compared to establish its authenticity. The same database could be further used for geographical origin determination. For effective data processing, the large number of independent measured parameters is needed. Parameters can be then statistically evaluated in order to identify key tracers that differentiate the regions or countries of interest.

The aim of this work is to determine fatty acid composition of milk and cheese from cow, sheep and goat provided from several farms from different regions of Slovenia, with the purpose to identify patterns that allow us to find differences according to geographical origin for cow's milk; difference between goat, sheep and cow milk; as well as the determination of goat or sheep milk adulteration with cow's milk.

2. Materials and methods

Sampling. Cow, goat and sheep milk samples for fatty acid determination from different farms in different locations in Slovenia were collected, stored in plastic containers and frozen before the analysis. All together around 200 samples were collected. The geographical areas employed for cow's milk origin determination were: Alpine, Dinaric, Mediterranean and Pannonia. To study the difference between goat, sheep and cow milk, samples were collected in June 2012. Finally, for the identification of adulteration, mixtures of milk of different adulteration percentage were produced in a laboratory experiment; adulteration of goat and sheep milk with 10, 5, 2.5, 1 and 0.5% of cow's milk were analysed. Each sample was analysed in duplicate.

Analysis. After extraction of milk fat from milk samples with dichloromethane, we proceeded with esterification of fatty acids. Fatty acids methyl esters (FAME) were obtained from the milk fat samples by transesterification with sodium methylate. The samples were then purged with nitrogen, capped and put into the oven at 90°C

for 10 min. Afterwards, sample vials were cooled to room temperature; BF₃-methanol solvent was added to complete the reaction and placed again into the oven for another 10 minutes at 90°C. After cooling, distilled water and hexane were added to the reaction vial to extract the FAMEs. The determination of fatty acids was carried out by gas chromatography with flame ionisation detection (GC-FID), with the use of a Agilent 6890N Network GC System gas chromatograph equipped with a 30-m capillary column (Omegawax320 (Supelco) Fused Silica 0.32mm x 0.25µm), with split ratio of 30:1. The carrier gas was helium at a flow rate of 1 ml/min. The temperature program for the analysis was from 185 to 215°C. The fatty acids were identified by comparison with Standard FAME Mix. 37 Comp. (Supelco).

Statistical analysis: The statistical calculations were obtained using the StatistiXL statistical software package (1.8) and Statistica 7. Basic statistics included analysis of variance (ANOVA) and Kruskal–Wallis one-way analysis of variance by ranks (Kruskal–Wallis test). Multivariate analysis involved linear discriminant analysis (LDA).

3. Results and discussion

Geographical Origin

It was possible to differentiate milk from different geographical origin based on fatty acid composition using LDA. The results are shown in Fig. 1. The separation was high up to 99.7%. The calculation showed that parameters that mainly contributed to the separation were C20:4n-6; C20:3n-6; C17 and C18:3n-3. For the fatty acid content in cow's milk with respect to geographical origin function 1 explained 97.6% of the total variance and function 2 the rest, 2.1%.

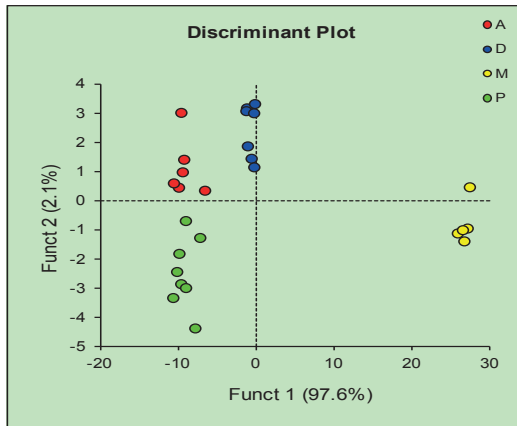


Figure 1: Linear discriminant score plots of fatty acid content in cow's milk with respect to geographical origin: A - Alpine, D - Dinaric, M – Mediterranean, P – Pannonia.

Differences between goat, sheep and cow's milk

Fatty acid composition differs between goat, sheep and cow milk. Goat milk contains more medium saturated chain fatty acids (C6:0 – C14:0) comparing to cow milk. The most abundant fatty acids are C6:0, C8:0 and C14:0 comprising around 20% of all fatty acids in goat milk. C14:0, C16:0 and C18:1 are the most abundant fatty acids in sheep milk.

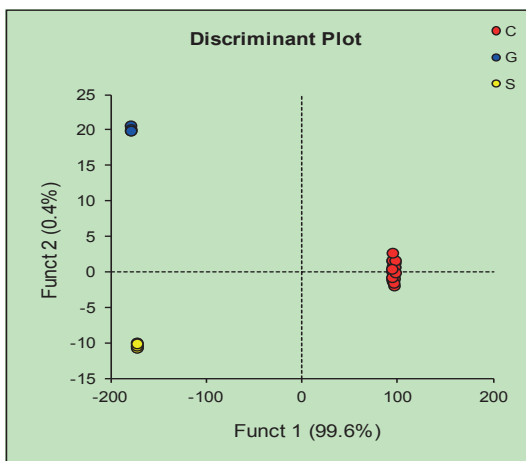


Figure 2: Linear discriminant score plots of fatty acid content in sheep's, goat's and cow's milk with respect to animal origin: C-cow, G-goat, S-sheep

The statistical analysis indicated that the fatty acid content in milk with respect to different animal origin function 1 explained 99.6% of the total variance and function 2 the rest, 0.4% (Fig. 2). The calculation showed that parameters that mainly contributed to the separation were C20:0; C10:0 and C22:1n9. The analysis of variance (ANOVA) was also tested on all fatty acids content in sheep, goat and cow milk. The data were normally distributed and variances were homogeneous only in three cases comprising C16:0, C20:0 and C23:0. The ANOVA analysis showed differences among three milk origin. Post-hoc Duncan test show that in all three cases cow milk was statistically different from sheep and goat.

Adulteration

The preliminary results of sheep and goat milk with addition of 10, 5, 2.5, 1 and 0.5% of cow milk were analysed with ANOVA and Kruskal-Wallis. In the case of sheep milk only C16:1 (ANOVA) was statistically significant ($P = 0.0058$) to discriminate adulteration. But other statistical analysis of variance (Levene test) indicated that variance was not homogeneous. In the case of goat milk C11:0 ($P =$

0.0348), C12:0 (P = 0.0348) and C18:1n9 (P = 0.0348) were statistically significant by Kruskal-Wallis test to discriminate adulteration with cow milk down to 1%. Further investigation is needed in order to define more precisely to which % the adulteration with cow milk could be detected.

4. Conclusions

The present study represents the first report on the fatty acid composition with respect to the geographical origin. It was found that the month of production also influenced the composition of fatty acids in cow milk. Thus, it is important to determine fatty acid composition at least two times per year in summer and winter. The adulteration of sheep and goat milk with cow milk needs further investigation.

Acknowledgement

The work was performed within the project V4-1108 entitled “The use of specific methods for determination and prevention of adulteration of milk and dairy products” financially supported by Slovenian Research Agency and Ministry of Agriculture and the Environment. We thank Ljubljanske mlekarne, d.d., Pomurske mlekarne, d.d., Mlekarna Vipava d.d., Mlekarna Planika predelava mleka d.o.o. and Mlekarna Celeia for supplying monthly cow samples and Kmetijski gozdarski zavod Nova Gorica for supplying goat and sheep milk. The research was additionally supported by Leonardo da Vinci program by the grant given to A. Vicent.

References

- [1] M.J. DENNIS; *Recent developments in food authentication*. Analyst 123 (1998) 151R-156R.
- [2] D.C.E. ROBERTS; *Food Authenticity*. British Food Journal, Vol.96 No.9 (1994) pp.33-35.
- [3] V. STIBILJ, M. K. RAJŠP; *Determination of fatty acids composition of winter consumer and UHT milk samples in Slovenia*. Biotehniški fak. V Ljubljani. Kmetijstvo. Zootehnika, 70 (1997).
- [4] R. KAROUI, J. DE BAERDEMAEKER; *A review of the analytical methods coupled with chemometric tools for the determination of the quality and identity of dairy products*. Food Chemistry 102 (2007) 621-640.
- [5] M. COLLOMB, U. BÜTIKOFER, R. SIEBER, B. JEANGROS, J.-O. BOSSET; *Composition of fatty acids in cow's milk fat produced in the lowlands, mountains and highlands of Switzerland using high-resolution gas chromatography*. International Dairy Journal 12 (2002) 649-659.

For wider interest

Food authenticity and traceability of origin have been given high priority in the recent years. Due to their high nutrient content milk and dairy products represent an important part in the healthy balanced diet. As they are in considerable demand and relatively expensive, they are vulnerable to adulteration or false denomination. Strategies to detect adulteration include also fatty acid composition. Information available through this research should be used to increase the transparency of milk and dairy products supply chain and provide information related to authenticity.

Uporaba izotopov pri raziskavah podzemnih vod

Janja Vrzel^{1,3}, Nives Ogrinc^{2,3}

¹ Institut za ekološki inženiring d.o.o., Maribor, Slovenija

² Odsek za znanosti o okolju, Institut Jožef Stefan, Ljubljana, Slovenija

³ Mednarodna podiplomska šola Jožefa Stefana, Ljubljana, Slovenija

janja.vrzel@iei.si, nives.ogrinc@ijs.si

Povzetek. Voda v naravi kroži v t. i. globalnem vodnem ciklu, tekom katerega je najpomembnejše spreminjanje njenih agregatnih stanj in posledično tudi njene izotopske sestave. Le-ta je značilna za posamezne vode, kar s pridom izkoriščamo za reševanje hidrogeoloških in tudi biogeokemijskih problemov. V hidrogeokemiji se za karakterizacijo vode najbolj množično uporabljajo vodikovi in kisikovi izotopi, kot osnovni gradniki molekule vode. Viri onesnaženj pa se ugotavljajo z uporabo ostalih lahkih stabilnih izotopov (¹³C, ¹⁵N in ³⁴S). Velikokrat nas zanima tudi starost vode, pri čemer se poslužujemo nizko radioaktivnih izotopov, kot so ³H, ¹⁴C, ³⁶Cl in ⁸¹Kr. S pomočjo izotopov tako lahko ocenimo ranljivost podzemnih vod na onesnaženja in izvore onesnaženja, kar pripomore k boljšemu upravljanju z vodnimi viri.

Ključne besede: izotopi, hidrogeokemija, karakterizacija podzemne vode, onesnaženje

1 Uvod

Hidrogeokemija je relativno mlada veda, s širokim spektrom uporabnosti, kar potrjuje tesna povezava hidrosfere, biosfere, atmosfere in litosfere. Posluhuje se naravnih izotopov v hidrosferi in predstavlja nepogrešljivo orodje pri študiju hidrodinamike in ogroženosti pred onesnaženjem. Reševanje hidroloških problemov z izotopi je izvedljivo, ker le-ti nosijo informacije o starosti, izvoru in stopnji obnovljivosti podzemne vode. Pridobivanje tovrstnih informacij pa zahteva sistematično večletno zbiranje podatkov [5] s čimer se ukvarjajo svetovne organizacije, ki se zavedajo pomena pitne vode za človeka. Tako mednarodna

agencija za atomsko energijo (International Atomic Energy Agency - IAEA) iz Avstrije razpolaga z dvema bazama podatkov o vsebnosti izotopov, in sicer v padavinah in rekah: Mednarodna mreža o izotopski sestavi padavin in rek (GNIP in GNIR) [6].

Izotopi so atomi istega elementa, ki imajo v jedru enako število protonov, število nevtronov in posledično mase pa se razlikuje. V naravi ostajata dve vrsti izotopov, to so stabilni in radioaktivni izotopi. Stabilni so tisti, ki ne razpadajo, njihove koncentracije pa se spreminjajo zaradi t. i. frakcionacije. Gre za proces, ki poteče zaradi številnih fizikalnih, kemijskih in bioloških procesov, tekom katerih prihaja do karakterističnih izotopskih sprememb. Eden iz med procesov, pri katerem pride do frakcionacije vodikovih in kisikovih izotopov je izhlapevanje vode. Pri tem se voda obogati s težjimi izotopi (^{18}O , ^2H) oz. osiromaši z lažjimi (^{16}O , ^1H).

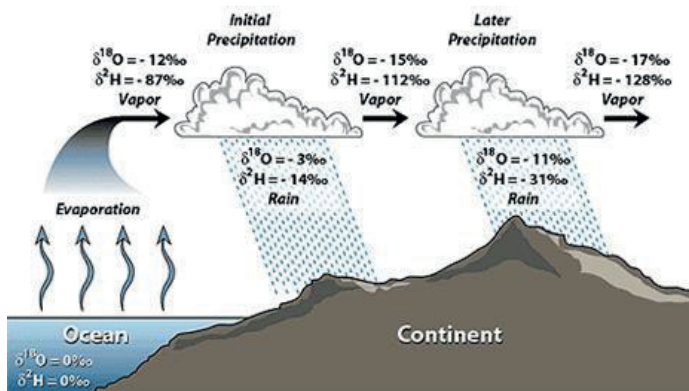
Izotopsko sestavo lahkih elementov (H, O, C, N, S) v vzorcu podajamo z δ -vrednostmi v promilih (‰) izraženo z:

$$\delta A = \left(\frac{R_{vz} - R_{std}}{R_{std}} \right) R_{std} \cdot 1000 \quad (1)$$

kjer A pomeni težji izotop (^2H , ^{13}C , ^{15}N , ^{18}O , ^{34}S), δ -vrednost predstavlja relativno razliko razmerij ($^2\text{H}/^1\text{H}$, $^{13}\text{C}/^{12}\text{C}$, $^{18}\text{O}/^{16}\text{O}$, $^{15}\text{N}/^{14}\text{N}$, $^{34}\text{S}/^{32}\text{S}$) stabilnih izotopov v vzorcu (vz) glede na določen standard (std). Ti standardi so točno določene homogenizirane naravne spojine [1]. Njihova izotopska razmerja so čim bolj podobna povprečni razširjenosti določenega izotopa v naravi [3]. δ -vrednost vsakega standarda je definirana z vrednostjo 0 ‰. Pozitivne vrednosti pomenijo, da vsebuje vzorec več težkega izotopa kot standard, negativne pa, da ga je manj. Za kisik in vodik je privzet standard SMOW (Standard Mean Ocean Water), za ogljika V-PDB (Vienna Pee Dee Belemnite), za dušik atmosferski zrak (AIR) in za žveplo CDT (Cañon Diablo Triolite).

Od kje je pritekla voda v vodonosnik in kakšna je bila njena pot do točke vzorčenja se ugotavlja z vodikovimi in kisikovimi izotopi, ki sestavljajo molekulo vode (H_2O). Spoznanje, da voda ni povsod enaka, ampak se razlikuje v izotopski sestavi, je omogočilo njeno identifikacijo v različnih okoljih. Vrednosti $\delta^2\text{H}$ in $\delta^{18}\text{O}$ v

padavinah so namreč karakteristične glede na zemljepisno širino, oddaljenost od morja, nadmorsko višino in letni čas [5]. Slika 1 prikazuje spreminjanje izotopske sestave atmosfirske vlage in padavin od oceana proti notranjosti kontinenta. Na drugi strani nam izotopska sestava dušika ($\delta^{15}\text{N}$) in žvepla ($\delta^{34}\text{S}$) omogoča določevanje izvorov onesaženja vodnih virov z nitrati in sulfati [4], ker se izotopske sestave posameznih virov med seboj razlikujejo. Tako se $\delta^{15}\text{N}$ vrednosti v nitratu, ki izvira iz sintetičnih mineralnih gnojil spreminja v območju med -3 in $+3$ ‰, medtem ko imajo nitrati, ki izvirajo iz organskih gnojil, $\delta^{15}\text{N}$ vrednosti med $+10$ in $+25$ ‰. Izotopska sestava ogljika ($\delta^{13}\text{C}$) pa nam pomaga pri raziskavah kroženja ogljika, določanja njegovih izvorov in nastanka metana.



Slika 1: Spreminjanje izotopske sestave atmosfirske vlage in padavin od oceana proti notranjosti kontinenta (Vir: <http://www.gns.cri.nz>).

Pri proučevanju vodnih sistemov so poleg stabilnih izotopov nepogrešljivi tudi podatki, ki jih dobimo z analizo radioaktivnih izotopov. Koncentracije radioaktivnih izotopov se spreminjajo zaradi radioaktivnih razpadov. Ti nosijo informacije o starosti vode, zato jih običajno podajamo v letih. Tiste najmlajše (do 30 let) se določajo s ^3H in $^3\text{H}/^3\text{He}$ metodama [7], nekoliko starejše (≤ 50.000 let) s ^{14}C ter najstarejše s ^{81}Kr (50.000–1.000.000 let) in ^{36}Cl (100.000–1.000.000 let). Pri interpretaciji rezultatov omenjenih analiz je hidrogeološko znanje nepogrešljivo [5].

Najnovejše interpretacije izotopskih analiz, tako geokemijskih kot hidrodinamskih, se poslužujejo moderne računalniške opreme, kot je na primer računalniški program

FeFlow. Gre za dobro preizkušen in zanesljiv program, ki omogoča tridimenzionalno simulacijo toka in transportnih procesov v poroznih snoveh. Program od uporabnika zahteva visok nivo znanja hidrogeologije in geokemije [2].

1.1 Primer uporabe izotopov pri študiju podzemnih vod na Ljubljanskem polju

Trenutno potekajo raziskave, tako površinskih kot podzemnih voda, na Ljubljanskem polju, ki predstavlja glavni vir pitne vode za slovensko prestolnico in njeno okolico. Predmet raziskav je ugotoviti odnos med površinskimi in podzemnimi vodami. Glavno orodje teh raziskav so analize stabilnih in radioaktivnih izotopov, s katerimi smo določili izotopsko sestavo podzemne vode, padavin in vode v reki Savi ter njihovo starost. S tem projektom smo tako locirali napajalna območja in pripomogli k boljšemu razumevanju nastanka podzemne vode, njene dinamike in ranljivosti zaradi onesnaženja.

Vzorčenje podzemne vode je potekalo na štirih lokacijah, ki se nahajajo severovzhodno od Ljubljane (Kleče, Hrastje in Jarški prod in Brest), in sicer v obdobju enega hidrološkega cikla 2010–2011. V istem obdobju so potekala mesečna vzorčenja padavinske vode in vode iz reke Save. Ob vsakem vzorčenju so bili *in-situ* izmerjeni fizikalni parametri (T , pH in prevodnost), v laboratoriju pa na zbranih vzorcih naslednje izotopske analize : $\delta^2\text{H}$ in $\delta^{18}\text{O}$ v vodi, $\delta^{15}\text{N}$ in $\delta^{18}\text{O}$ v nitratu in ^3H in $^3\text{H}/^3\text{He}$ (Slika 3).



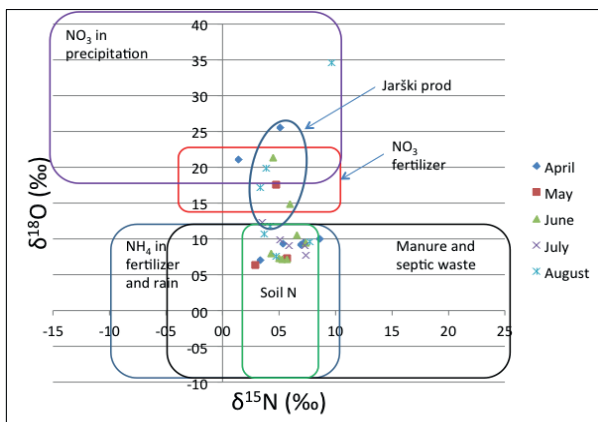
Slika 2: Vzorčenje podzemne vode za $^3\text{H}/^3\text{He}$ analizo.

2. Rezultati

$\delta^2\text{H}$ in $\delta^{18}\text{O}$ analize so pokazale, da vodonosnik napajata dva vira, in sicer padavinska voda ter voda iz reke Save. Padavine prispevajo največji delež vode v vodarnah Kleče, Hrastje in Jarški Prod. Slika 2 prikazuje dokaj zahtevno vzorčenje podzemne vode za $^3\text{H}/^3\text{He}$ analizo.

Glede na rezultate $^3\text{H}/^3\text{He}$ analiz, je najstarejša voda prisotna v vodarni Brest na Ljubljanskem Barju. Zadrževalni čas je bil ocenjen na 40 let, kar nakazuje, da je to področje najmanj ranljivo za onesnaženje. Starejše vode so prisotne tudi v Klečah s starostjo 1.000–10.000 let, vendar je njen delež manjši, ocenjen je na 10 %. Stara voda v Hrastju in Jarškemrodu ni prisotna, ampak le mlajša voda, katere starost je ocenjena v Hrastju na 8–7 let in v Jarškemrodu na 2–7 let.

Analize $\delta^{15}\text{N}$ in $\delta^{18}\text{O}$ v nitratih (NO_3^-) so pokazale (Slika 2), da je z nitrati najbolj onesnažena podzemna voda v Hrastju, kjer sta največja vira nitrata (63 %) kanalizacija in gnojevka, nekoliko manjši delež nitrata (23%) je prisoten zaradi mineralnih gnojil, najmanjši delež (13%) pa je nastal v atmosferi. Med najbolj ranljivo območje spada okolica vodarne Jarški Prod in sicer, zaradi kratkega zadrževalnega časa vode. Tukaj so povišane koncentracije nitrata v podzemni vodi, ki je sestavljena iz padavin (70 %) in savske vode (30%), posledica poljedelstva in spiranja nitrata iz tal. Na podlagi izotopske masne bilance so bili prav tako ocenjeni posamezni prispevki nitrata na lokacijah Hrastje in Kleče. Ugotovili smo, da je glavni izvor nitrata v Hrastju kanalizacija (približno 63 %), za 23 % nitrata so vzrok mineralna gnojila, medtem ko je doprinos s padavinami ocenjen na 13 %. Viri nitrata v Klečah pa so nekoliko drugačni. Tam je največ nitrata naravnega izvora, ki se spira v podzemno vodo iz tal (50%) in poljedelstva (40%) ter nekoliko manj zaradi njegovega izvora v sami atmosferi (10%).



Slika 3: $\delta^{15}\text{N}$ in $\delta^{18}\text{O}$ vrednosti v nitratu v podzemni vodi na Ljubljanskem polju.

Zaključek

Hidrogeokemija je veda, ki nam je v veliko pomoč pri vedno boljšem razumevanju mehanizma vodnega sistema, kar nam je uspelo doseči tudi z raziskavami na Ljubljanskem polju. Te kažejo na precejšnjo ranljivost Ljubljanskega vodonosnika, še posebej v okolici Jarškega Proda. Vodonosnik napajajo predvsem padavine, vir manjšega deleža podzemne vode pa predstavlja reka Sava. Starost teh vod je dokaj majhna, medtem ko smo manjše deleže starejših vod zasledili le v Klečah in v Brestu. Upamo, da bodo te raziskava spodbudile slovenske organizacije, katerih naloga je skrb za pitno vodo, k še večjemu in bolj intenzivnemu ozaveščanju ljudi o pomenu čiste pitne vode.

References:

- [1] H. Craig. Isotopic Standards for Carbon and Oxygen and Correction Fractors for Mass spectrometric Analysis of Carbon Dioxide. *Geochemica et Cosmochimica Acta*, 12(1-2): 133–149, 1957.
- [2] DHI-WASY. *FeFlow 6.1, Fine Element Subsurface Flow & Transport Simulations System, User Manual*. DHI-WASY GmbH, 2012.
- [3] M. H. Engel in S. A. Macko (ed.). *Organic Geochemistry: principles and application*. Plenum, 1993.
- [4] C. Kendall in D. H. Doctor. Stable Isotopes Application in Hydrologic Studies. V: *Treaties on Geochemistry*, Vol. 5: 319–364, 2003.
- [5] W. G. Mook. *Environmental Isotopes in the Hydrological Cycle, Principles and Applications. Vol. 1*. UNESCO-IAEA, 2001.
- [6] T. Vitvar, P. K. Aggarwal in A. L. Herezeg. Global Network is Launched to Monitor Isotopes in Rivers. *Eos Transactions, American Geophysical Union* 88(33): 325–332, 2007.

[7] USGS. $^3\text{H}/^3\text{He}$ Dating Background. <http://water.usgs.gov/lab/3h3he/background/>, 2013.

For wider interest

V naravi obstajata dve vrsti izotopov, stabilni in radioaktivni. V hidrologiji največ uporabljamo stabilne izotope lahkih elementov H, O, C, N in S, od radioaktivnih pa ^3H , ^{14}C , ^{36}Cl in ^{81}Kr . Vrednosti $\delta^2\text{H}$ in $\delta^{18}\text{O}$ v padavinah so namreč karakteristične glede na zemljepisno širino, oddaljenost od morja, nadmorsko višino in letni čas [5]. Na drugi strani nam izotopska sestava dušika ($\delta^{15}\text{N}$) in žvepla ($\delta^{34}\text{S}$) omogoča določevanje izvorov onesnaženja vodnih virov z nitrati in sulfati [4], ker se izotopske sestave posameznih virov med seboj razlikujejo. Izotopska sestava ogljika ($\delta^{13}\text{C}$) pa nam pomaga pri raziskavah kroženja ogljika, določanja njegovih izvorov in nastanka metana.

Pri proučevanju vodnih sistemov so prav tako nepogrešljivi podatki, ki jih dobimo z analizo radioaktivnih izotopov. Ti nosijo informacije o starosti vode, kar pa omogoči oceno ranljivosti vodonosnika.

Z raziskavami na Ljubljanskem polju, smo določili izotopsko sestavo in starost podzemnih in površinskih voda, kar je omogočilo lociranje napajalnega območja tega vodonosnika. S tem smo pripomogli k boljšemu razumevanju nastanka podzemne vode, njene dinamike in ranljivosti zaradi onesnaženja.

Informacijske in komunikacijske tehnologije
(Information and Communication Technologies)

Sensor as a Service using the VESNA Sensor Platform

Adnan Bekan^{1,2}, Carolina Fortuna¹, Matevž Vučnik^{1,2}, Mihael Mohorčič^{1,2}

¹Department of E6, Jožef Stefan Institute, Ljubljana, Slovenia

²Jožef Stefan International Postgraduate School, Ljubljana, Slovenia

adnan.bekan@ijs.si, carolina.fortuna@ijs.si,
matevz.vucnik@ijs.si, miha.mohorcic@ijs.si

Abstract. In this paper we propose a system architecture for wireless sensor networks (WSNs) that makes various types of sensors, sensor data and metadata, discoverable, accessible and controllable over the Internet. This architecture is able to provide sensor as a service functionality using standard communication protocols on the Internet and WSN side. We describe the components of the proposed architecture and then we provide the reference implementation based on the VESNA sensor platform equipped with the open source Contiki OS and its standard protocol stack for constrained devices. We also provide initial performance evaluation of the WSN part of the proposed system architecture.

Keywords: VESNA, Contiki OS, uIP, IPv6, RPL, CoAP, Sensors

1 Introduction

Sensor platforms are typically low power devices equipped with a variety of sensors that are able to interact with the physical world. Furthermore, these devices are able to interconnect with each other and to communicate with the outside world over the Internet [2].

Due to the rapid development of sensor platforms, the currently available platforms are becoming more sophisticated in terms of CPU, memory, energy efficiency and connectivity. As a result, nowadays small, low power devices are able to support embedded operating systems with standardized communication protocols such as IP that are typical for legacy networks. As a result, wireless sensor networks (WSNs) can be created that enable direct interaction with each device in network and thus

“convert” various sensors to software services [1]. The sensors can in such case be requested remotely to deliver meta-data or data to the users.

Usually the size of the metadata is relatively large, but it needs to be retrieved less often than the actual sensor measurements. The data typically take less space but requires frequent transmissions. In order to allow outside users access to rich meta-data and enable them to configure several aspects of sensor devices such as data acquisition strategies in seamless fashion, we propose using the “sensor as a service” concept relying on available standard based protocols such as uIPv6¹ and CoAP². This approach enables the transition from the traditional closed dedicated WSN deployments to a heterogeneous ecosystem of “smart” devices and appliances equipped with sensors and communication interfaces constituting the Internet of Things (IoT).

This paper is structured as follows. Section 2 presents the system architecture. In Section 3 we discuss reference implementation aspects of proposed service oriented system on the VESNA sensor platform. In Section 4 we provide initial performance evaluation of the WSN part of the proposed architecture in terms of packet loss and average response time. Finally, Section 5 concludes the paper.

2 System architecture

The architecture of the system for rich meta-data and data acquisition we propose in this paper is depicted in Figure 1. The proposed system architecture is divided in two main blocks. The first block refers to the clients or consumers of sensor data and meta-data. These consumers are most often HTTP clients making requests. The second block refers to the data providers which are the sensor nodes that sense the environment and perform the data acquisition task. In our architecture, these two blocks can be connected using standards based hierarchical communication architecture. The hierarchical communication architecture achieves adaptation steps from the full-fledged Internet standards to equivalent sensor network standards optimized for constrained devices, in particular to uIPv6 and CoAP. The Internet’s

¹ [wikipedia.org/wiki/UIP_\(micro_IP\)](http://wikipedia.org/wiki/UIP_(micro_IP))

² datatracker.ietf.org/doc/draft-ietf-core-coap/

protocol stack is converted to the equivalent sensor network stack by low power gateways.

By making each sensor node a directly addressable and accessible network entity, the system provides an easy way for discovering, controlling and invoking services from the sensor network. Users can interact with the system at high level of abstraction using standards based communication technology that blends with the existing stack used by the Internet (HTTP/TCP/IP).

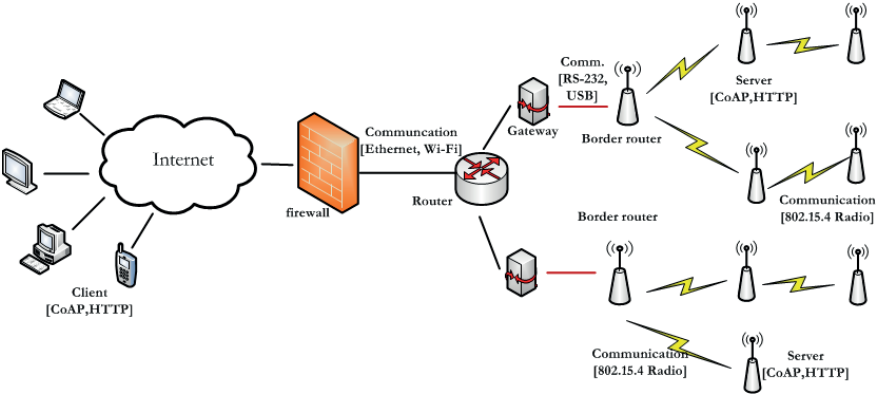


Figure 1: System architecture

3 Reference implementation of the system architecture

The reference implementation of the system architecture introduced in this paper and depicted in Figure 1 includes state of the art hardware and software components.

3.1 Hardware

The networking device that connects the network of sensors to the internet is implemented using the computer (Hermes) that acts as a IPv6 router for sensor networks inside the JSI network and allows every sensor platform in network to be reached using the devices unique public static IPv6 address.

The gateway that does the conversion between various protocols is based on the Raspberry Pi³ with 700 MHz ARM processor, 512 Mbytes of RAM with Wi-Fi and Ethernet module. The ability of a client device in the Internet to communicate with sensor platforms is enabled by the gateway together with the border router that is based on the VESNA⁴ sensor platform.

The sensor network is also based on the VESNA sensor platform which was developed by the SensorLab at Jožef Stefan Institute, Slovenia. VESNA is equipped with ARM Cortex-M3 microprocessor with 32 bit core and maximum frequency of 72 MHz, flash memory of 1 MB and SRA of 96 kB. This platform can host various modules for sensing and radio communication. In the reference implementation we used the VESNA SNE-SENS extension module featuring 11 sensors and the VESNA SNR-MOD radio module with the Atmel ATRF212 radio chip based on IEEE 802.15.4 standard.

3.2 Software

The most distinctive software component of this reference implementation compared to traditional WSNs refers to the embedded software running on the sensor platforms that allows standard based communication stacks for constrained devices. A suitable candidate that meets our requirements is the ContikiOS⁵, which is a minimalistic operating system intended for low power devices. We used uIP TCP/IP stack depicted in Figure 2 that supports IPv6 network with the 6LoWPAN⁶ adaptation layer that does header compression and fragmentation of packets so that smaller chunks fit in the 802.15.4 frame.

The embedded application uses CoAP [2], a low power application protocol designed for constrained networks such as 6LoWPAN and for M2M (machine to machine) applications.

³ raspberrypi.org

⁴ sensorlab.ijs.si/hardware.html

⁵ www.contiki-os.org

⁶ wikipedia.org/wiki/6LoWPAN

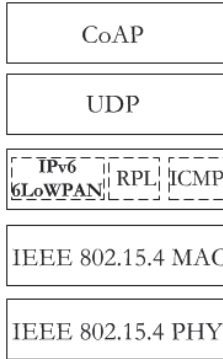


Figure 2 : uIPv6 based communication stack

One of the main advantages of CoAP protocol is its similarity to the HTTP protocol allowing simple translation and communication between these two protocols.

Finally to expose each sensor platform through specific RESTful⁷ handlers to higher protocol layers and to have good overview of the network we used Raspbian⁸, an operating system based on Debian optimized for the Raspberry Pi hardware. In order to enable tunnelling of IPv6 packets through RS-232 we used tunslip, a tool from ContikiOS. This type of system architecture can handle several CoAP clients at the same time unlike system limited to one user per time slot.

Developing the network with uIPv6 naturally allows every device in the network to have unique IPv6 address and to be part of the Internet cloud. Additionally, with CoAP protocol power-efficient communication is achieved.

⁷ wikipedia.org/wiki/Representational_state_transfer

⁸ raspbian.org

4 Initial Evaluation of the proposed system architecture

In this section we describe experiments that were performed on the experimental sensor network consisting of up to 5 sensor platforms to provide an initial quantification of the scalability and performance of the system. To this end we evaluated the performance of the WSN part of the system in terms of packet loss and average RTT (round-trip time) when increasing the number of sensor platforms connected in a network. In this experiment each sensor platform (server) established end-to-end communication with client which simultaneously sent 1000 packets per platform, each packet consisting of 32 bytes. Results of this experiment are shown in Figure 3.

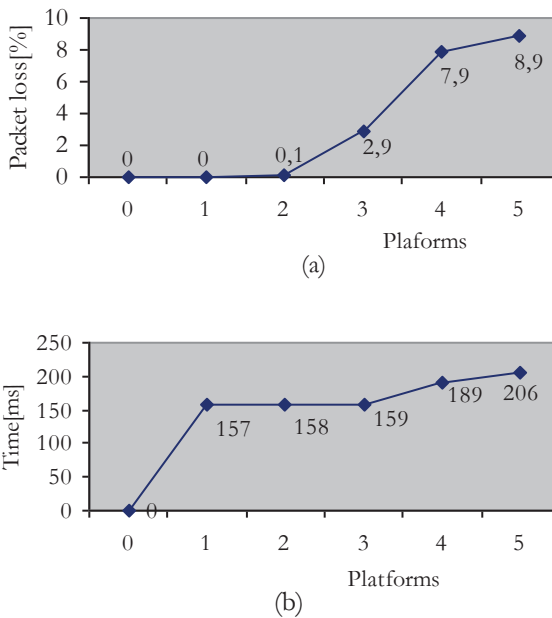


Figure 3 (a) Packet loss, (b) Average RTT

As can be seen from Figure 3, the initial results indicate that the packet loss grows exponentially with the number of sensor platforms that are added to the experiments while the average RTT seems to have a more linear growth.

The packet loss results could be improved by adding a proper antenna to the radio board which is now only a simple wire.

5 Conclusion and future work

In this paper we proposed an architecture that makes various types of sensors, sensor data and metadata, discoverable, accessible and controllable over the Internet. This architecture is able to provide sensor as a service functionality and was demonstrated using the VESNA sensor platform. First we described the components of the proposed architecture and then we provided reference implementation and an initial performance evaluation of the architecture. The described reference implementation is based on the VESNA sensor platform and the open source Contiki OS with its available standard protocol stack optimised for constrained devices yet providing easy and full interoperability with the legacy TCP/IP protocol stack in the Internet.

References:

- [1] J.King, R.Bose, S.Pickles, A-Helal, S.V.Ploeg, J.Russo. Atlas: A Service-Oriented Sensor Platform. In *Proceedings of the Local Computer Networks*, IEEE 31st Conference, Tampa, Florida, USA, 2006
- [2] Jean-Philippe Vasseur, A. Dunkels. *Interconnecting Smart Objects with IP*, 2010.
- [3] M.Kovatsch, S.Duquennoy, A.Dunkels. A Low-Power CoAP for Contiki. In *Proceedings of the Mobile Adhoc and Sensor Systems (MASS)*, IEEE 8th International Conference, Valencia, Spain, 2011.

For wider interest

A wireless sensor platform is the basic building block of sensor network and it typically hosts a microprocessor, one or more sensors and a communication module. A sensor platform is thus capable to measure a physical quantity, perform some processing and communicate with other nodes in the network and with remote servers in the Internet using wireless technologies.

In our system, we are using a sensor platform called VESNA. VESNA is a modular platform for wireless sensor networks developed at the SensorLab, Jožef Stefan Institute, Slovenia. It is suitable both as a development environment as well as a final solution for a large variety of application areas.

Using VESNA in combination with ContikiOS and CoAP allows easy control and invocation of services in the sensor network over the Internet by calling RESTful handlers. The advantage of the CoAP protocol is that it is similar to the HTTP protocol, which allows simple translation and communication between these two protocols.

One advantage of this system architecture is that every node in sensor network has a unique IPv6 address which can be used for interconnection with platforms and sensors. Another advantage of this architecture is that such network can simultaneously handle more users than more primitive types of sensor networks.

Estimation of Human Energy Expenditure Using Inertial Sensors and Heart Rate Sensor

Božidara Cvetković^{1,2}, Mitja Luštrek^{1,2}

¹ Department of Intelligent Systems, Jožef Stefan Institute, Ljubljana, Slovenia

² Jožef Stefan International Postgraduate School, Ljubljana, Slovenia

boza.cvetkovic@ijs.si, mitja.lustrek@ijs.si

Abstract. This paper presents a method for estimation of human energy expenditure during normal daily activities as well as sports activities using wearable inertial sensor attached to the person's thigh and chest as well as feasibility analysis of this method to be used as an application on an average smartphone. This is done by using one inertial sensor attached to the person's thigh (standard smartphone placement) and performing feature selection that selects only relevant attributes with low computational complexity that can be processed on smartphone and still keep high estimation accuracy. In addition to that, we tested a combination of thigh inertial sensor with heart rate monitor, usually worn by athletes, to collect more relevant data and gain on accuracy.

Keywords: human energy expenditure, physical activity, embedded smart phone sensors, wearable sensors, regression

1 Introduction

Mobile devices are used for almost everything these days from talking and texting to event scheduling, daily life monitoring, finding direction, etc. Two of the reasons for such a fast success of the mobile devices and mobile applications are the embedded sensor and their significant improvement with each new model that appears on the market and availability and ease of development. Average smart phone has a rather powerful processing unit. It comes with variety of sensors, for example global positioning system (GPS), camera, proximity sensor, ambient light sensor, gyroscopic sensor and accelerometer. The accelerometer measures the movement

acceleration and is therefore the most interesting in terms of analysis of human physical activity, more precisely the human energy expenditure, which is a focus of this paper.

Over the years, research in medical field has shown that a sufficient amount of physical activity can have a positive impact on one's health and well-being regardless of age [1][2][3] and that the physical inactivity is one of the leading causes of death worldwide [4]. Although this is widely accepted as a fact, only small amount of population has regular or sufficient exercise. Key reason for this is the limited time, due to the fast pace of life. If one was able to measure amount of performed physical activity during the regular day and present the difference according to the sufficient physical activity, than this could serve as a motivation for the person to do additional exercise and reach the daily goal. Most importantly, the amount of physical activity can be also used to monitor one's diet, either being healthy individual or someone who suffers from dietary disease. This raises a question; How can we measure the amount of physical activity.

Cost of physical activity is usually expressed in a unit referred as metabolic equivalent of task (MET), where 1 MET is defined as energy expended at rest. MET range is from 0.9 (sleeping) to 23 (running at 22.5 km/h). There are several methods used to reliably estimate energy expenditure. Direct calorimetry [6] measures the heat produced by human body while exercising. This is the most accurate method of estimating human energy expenditure, however it can be used only in a controlled environment such as laboratory. Indirect calorimetry [7] measures the amount of carbon dioxide production and oxygen consumption during rest and steady-state exercise. This method can be used outside the laboratory, however it cannot be used in everyday life since its usage requires a breathing mask. Doubly labelled water [7] is a gold standard, it measures the amount of exhaled carbon dioxide by tracking its amount in water which is labelled by deuterium and oxygen-18. This method can be used in everyday life, however it measures the energy expended over longer periods of time and is rather expensive. And finally, the most affordable system is using wearable inertial sensors or other wearable sensors that are moderately accurate and reliable. These can be used in everyday life and the estimation can be done over shorter periods of time.

This paper presents a method for estimation of human energy expenditure during normal daily activities as well as sports activities using wearable inertial sensor attached to the person's thigh and chest as well as feasibility analysis of this method to be used as an application on an average smartphone. This is done by using one inertial sensor attached to the person's thigh (equivalent to pocket, the standard smartphone placement) and performing feature selection that selects only relevant attributes with low computational complexity that can be processed on smartphone and still keep high estimation accuracy. In addition to that, we tested a combination of thigh inertial sensor with heart rate monitor, usually worn by athletes, to collect more relevant data and gain on accuracy. The heart rate monitor contains one more inertial sensor and can be easily connected to smartphone.

The rest of the paper is structured as follows. Section two presents the related work; Section 3 presents the hardware and the method. Section 4 contains the experiment and the results and finally the Section 5 concludes the paper.

2 Related Work

Estimation of energy expenditure is an interesting domain for mobile application development, according to the number of applications that can be found on application markets of individual operating systems. These applications can be divided into two categories; those that use accelerometer sensors and estimate energy expenditure based on number of steps the user does over one day [12]; and those that use embedded accelerometers to estimate the intensity of the performed activity, thus estimate the expended energy, for example MyFitnessCompanion [13]. Pedometers can be used only to detect the ambulatory activities such as walking or running and not their intensity. MyFitnessCompanion app can detect the intensity since it uses the accelerometers but it has one major shortfall, the user has to define which activity will be performed. Estimation of energy expenditure is afterwards based on the predefined energy estimation value taken from the Compendium of physical activities [14].

Most methods that use artificial intelligence techniques to estimate energy expenditure using wearable sensors seek linear or nonlinear relations between the

energy expenditure and the accelerometer outputs. The most basic methods use one accelerometer and one linear regression model. The estimation accuracy can be improved by multiple regression models [8] and complex attributes [9]. The regression method by Crouter et al. [10] is currently among the most accurate. It uses one accelerometer attached to the hip. In the first step it classifies a person's activity into sitting, ambulatory activity or lifestyle activity. In the second step it uses a linear regression model for the ambulatory activity and an exponential regression model for the lifestyle activity. Sitting is always considered to have the energy expenditure of 1 metabolic equivalent of task (MET, 1 MET is the energy expended at rest). The weakness of this method is the exclusion of some activities such as cycling, and a larger error for the upper body due to the sensor placement.

This paper will present a method that uses three regression models that are based on the current users' activity. The activity is automatically recognised using the activity-recognition classifier. The recognized activity will also be used as one of the attributes in the energy expenditure regression models

3 Sensors and Data Pre-processing

To develop and test the method for estimation of energy expenditure we used one tri-axial inertial sensor and chest-strap worn by 10 people performing predefined activities. Besides our dedicated sensors each person was using Cosmed the indirect calorimeter [15] to measure actual expended energy.

3.1 Dedicated Sensors and Translation to Embedded Smartphone Sensors

Smartphone contain several sensors one of which is one tri-axial inertial sensor. For the purpose of this research we used simple tri-axial inertial sensor developed by Shimmer [16] attached to the users thigh, mimicking the placement of the smartphone, which would be carried around in the trousers pocket. Inertial sensor is orientation-sensitive; therefore we had to determine the exact orientation for the sake of simplicity. For example, the smartphone has to be carried in the right pocket downwards with screen towards the person's body. Each person wore the inertial

senor the same with a freedom of few centimetres up or down the thigh. The placement and orientation of the Shimmer inertial sensor is shown on Figure 1.



Figure 1. Shimmer inertial sensor attached to the thigh.

In our previous research we have observed that the estimation of the energy expenditure can be improved with heart rate data. For that purpose we used Zephyr chest-strap [17], very popular with athletes, which can be easily connected to the smartphone via Bluetooth. Zephyr chest-strap contains additional tri-axial accelerometer, which can be used to gain on activity-recognition accuracy.

3.2 Data Collection and Data Processing

Data collection

Ten people equipped with our dedicated sensors, inertial and chest-strap, were additionally given a Cosmed indirect calorimeter to measure the real expended energy. The person performed the predefined activities presented in Table 1.

Each activity was performed several times and the duration of the activity is 6 minutes. The range of reference energy expenditure measured by Cosmed is 12 MET.

Table 1. Predefined activities.

Lying	Kneeling
Sitting	On all fours
Standing	Lying doing light exercises
Walking slowly (4 km/h)	Sitting doing light exercises
Walking quickly (6 km/h)	Walking doing light exercises
Running slowly (8 km/h)	Scrubbing the floor
Stationary cycling lightly	Shovelling snow, digging
Stationary cycling vigorously	

Data Processing

The stream of data of ten people was split into 10 seconds windows, each window overlapping with the previous one by one half of its length. For each window 136 attributes were computed, 135 from the acceleration data and one from heart rate. These attributes formed a vector, which was fed into a machine-learning algorithm to train a regression model. To reduce calculation complexity, since the goal is to run the method on a smartphone, we performed feature selection using ReliefF method [18]. The feature selection method returned the attributes in the ranked order. The selection of attributes was performed as follows. Each attribute was removed one-by-one from the entire set starting with the one with lowest rank score. After each removal the regression was tested using cross-validation. This was performed 10 times for each person. The point where the accuracy started decreasing rapidly was chosen for the selection point leaving 23 attributes.

Descriptive example of selected attribute would be: Interquartile range of sorted magnitudes, where magnitude values are sorted and the result is a difference between the magnitude value at $\frac{3}{4}$ and the $\frac{1}{4}$ of the window, squared sum of the signal values, different amplitudes of signal, sum of absolute values, velocity, sum of impacts, mean values, average heart rate, prevalent activity, etc.

In our previous research we have observed that when using only one regression model for all activities result in higher estimation error in case of running and cycling [19]. Based on this finding we divided the data in three sets: running set, cycling set

and rest of the activities set. The activity-recognition classifier was taken from our previous research [19]. Regression model was build for each set, to be used for particular recognised activity.

4 Experiment and Results

The experiment was done using data of ten people performing activities as described in Section 3.2. For each person we trained three regression models Weka suite [20] and six regression algorithms: M5PRules, M5P, REPTree, MultiLayer Perceptron. Linear Regression and SMOReg. The results were validated using leave-one-person-out approach. We have validated each regression model; for running activity; cycling activity; and for all other activities with algorithms presented in Table 2.

We have chosen the best performing algorithm per set for our final application using the dedicated sensors with possibility to transfer the method to the smartphone. The best performing algorithm is SMOReg, for other activities and MLP for running and cycling activities. The mean absolute error for this combination is 0.65 MET.

Table 2. Mean absolute error in MET per regression model with six machine-learning algorithms.

	M5PRules	M5P	REPTree	Linear Regression	MLP	SMOReg
Other activities	0.55	0.54	0.55	0.58	0.86	0.52
Running activity	0.94	0.96	1.02	0.98	0.78	0.99
Cycling activity	0.78	0.99	0.74	0.98	0.66	0.87

5 Conclusion

The paper presents low computational complexity method for estimation of human energy expenditure. The focus of the paper is to develop a method that can be easily transferred and used on an average smartphone.

Presented method uses three regression models. Separate model is used for running activity, separate is used for cycling activity; and separate is used for all other activities. The regression models were built ten times on data of 9 people using several machine-learning regression algorithms and evaluated on 1 person using leave-one-person-out approach.

Accurate estimation of energy expenditure and its integration into the device that can interact with the user, can have positive impact on quality of life of each individual, regardless of age and health state.

References:

- [1] World health Organization, HEPA, <http://www.euro.who.int/>
- [2] S. B. Cooper, S. Bandelow, M. L. Nute, J. G. Morris, M. E. Nevill. The effects of a mid-morning bout of exercise on adolescents' cognitive function, *Mental Health and Physical Activity*, 5 (2):183-190, 2012.
- [3] M. Hamer, E. Stamatakis. Objectively assessed physical activity, fitness and subjective wellbeing, *Mental Health and Physical Activity*, 3(2): 67-71, 2010.
- [4] H.W. Kohl 3rd, C.L. Craig, E.V. Lambert, S. Inoue, J.R. Alkandari, G. Leetongin, and S. Kahlmeier. The pandemic of physical inactivity: global action for public health, *The Lancet*, 380:294–305, 2012.
- [5] J. Speakman. *Doubly labelled water: Theory and practice*, Springer, 1997.
- [6] P. Webb, J. F. Annis, and S. J. Troutman Jr.. Energy balance in man measured by direct and indirect calorimetry, *American Journal of Clinical Nutrition*, 33: 1287–1298, 1980.
- [7] J. A. Levine. Measurement of Energy Expenditure, *Public Health Nutrition*, 8(7A):1123–1132, 2005.
- [8] D. P. Heil. Predicting activity energy expenditure using the actual activity monitor, *Research quarterly for exercise and sport*, 77:64–80, 2006.
- [9] C. V. Bouten, K. R. Westerterp, M. Verduin, and J. D. Janssen. Assessment of energy expenditure for physical activity using a triaxial accelerometer, *Medicine and science in sports and exercise*, 26:1516–1523, 1994.
- [10] S. E. Crouter, K. G. Clowers, and D. R. Bassett. A novel method for using accelerometer data to predict energy expenditure, *Journal of applied physiology*, 100:1324–1331, 2006.
- [11] Y. Jang, M. Jung, J. Kang, and H. K. Chan. An Wearable Energy Expenditure Analysis System based on the 15-channel Whole-body Segment Acceleration Measurement, in *IEEE-EMBS 2005, 27th Annual International Conference of the IEEE*, 2005.
- [12] ACCUPEDO, <https://play.google.com/store/apps/details?id=com.corusen.accupedo.te>
- [13] D. Mark, P. Cristiano, N. Chris, M. Mounir. User Adoption of Mobile Apps for Chronic Disease Management: A Case Study Based on myFitnessCompanion®, *Impact Analysis of Solutions for Chronic Disease Prevention and Management*. LNCS 7251, pp 42-49, 2012.
- [14] B. E. Ainsworth, W. L. Haskell, M. C. Whitt, M. L. Irwin, A. M. Swartz, et al.. Compendium of physical activities: An update of activity codes and MET intensities, *Medicine and Science in Sports and Exercise*, 32:498–516, 2000.
- [15] Cosmed, <http://www.cosmed.com>
- [16] Shimmer, <http://www.shimmer-research.com>

- [17]Zephyr, <http://www.zephyr-technology.com>
- [18]I. Kononenko. Estimating Attributes: Analysis and Extensions of RELIEF. European Conference on Machine Learning, 171–182, 1994.
- [19]Solar, Héctor, Fernández, Erik, Tartarisco, Gennaro, Pioggia, Giovanni, Cvetković, Božidara, Kozina, Simon, Luštrek, Mitja, Lampe, Jure. A non invasive, wearable sensor platform for multi-parametric remote monitoring in CHF patients. Health and Technology 2013, pp 1-11, Springer.
- [20]M. Hall, E. Frank, G. Holmes, B. Pfahringer, P. Reutemann, and I. H. Witten. The WEKA Data Mining Software: An Update, *in SIGKDD Explorations*, 11(1):10–18, 2009.

For wider interest

Mobile devices are used for almost everything these days from talking and texting to event scheduling, daily life monitoring, finding direction, etc. Two of the reasons for such a fast success of the mobile devices and mobile applications are the embedded sensor and their significant improvement with each new model that appears on the market and availability and ease of development. Average smart phone has a rather powerful processing unit and it comes with variety of sensors, for example global positioning system (GPS), camera, proximity sensor, ambient light sensor, gyroscopic sensor and accelerometer, being the most interesting in terms of analysis of human physical activity, more precisely human energy expenditure which is a focus of this paper.

Over the years, research in medical field has shown that a sufficient amount of physical activity can have a positive impact on one's health and well-being regardless of age and that the physical inactivity is one of the leading causes of death worldwide. Although this is widely accepted as a fact, only small amount of population has regular or sufficient exercise. Key reason for this is the limited time, due to the fast pace of life. If one was able to measure amount of performed physical activity during the regular day and present the difference according to the sufficient physical activity, than this could serve as a motivation for the person to do additional exercise and reach the daily goal. Most importantly, the amount of physical activity can be also used to monitor one's diet, either being healthy individual or someone who suffers from dietary disease. This raises a question; How can we measure the amount of physical activity.

This paper presents a method for estimation of human energy expenditure during normal daily activities as well as sports activities using wearable inertial sensor attached to the person's thigh and chest as well as feasibility analysis of this method to be used as an application on an average smartphone.

Potential Usage of Smartphone Inertial Sensors in Healthcare Applications

Hristijan Gjoreski^{1,2}, Simon Kozina^{1,2}, Matjaž Gams^{1,2}, Mitja Luštrek^{1,2}

¹ Department of Intelligent Systems, Jožef Stefan Institute, Ljubljana, Slovenia

² Jožef Stefan International Postgraduate School, Ljubljana, Slovenia

hristijan.gjoreski@ijs.si, simon.kozina@ijs.si,

matjaz.gams@ijs.si, mitja.lustrek@ijs.si

Abstract. The increasing availability of the smartphones on one hand and the necessity to improve healthcare on the other hand, are encouraging the development of smartphone healthcare applications. In this paper an idea of transforming the smartphone into a healthcare device capable of recognizing everyday activities and detection of fall events is presented. This approach firstly use inertial sensors data as an input, then the data is preprocessed and segmented, and finally artificial intelligence methods are applied which recognize the user's activity and detect a fall event. The thorough evaluation of the methods showed that it is possible to achieve satisfactory performance for both tasks using only one inertial sensor embedded in a smartphone.

Keywords: Smartphone, inertial sensors, artificial intelligence, machine learning, activity recognition, fall detection.

1 Introduction

Production of mobile phones is in constant increase. Currently, more than 85% of the world population owns a mobile phone [1]. This shows that in a very short time, mobile devices will become easily accessible to virtually everybody. In recent years, the number of smartphones, which are a new generation of mobile phones, is in constant increase. In 2012, 1 billion smartphones were in use and this number is expected to be doubled in the next 3 years [2]. Smartphones, in contrast to the basic telephones, are offering many features such as multitasking and the deployment of a variety of sensors: inertial, compass, GPS, light, pressure etc.

The intelligent use of these sensors is the basis to many applications. In recent years, studies in the Ambient Intelligence (AmI) field have shown that body-worn sensors, especially the inertial ones, give rich information about the user. This information can be used in many healthcare applications: automatic recognition of daily activities, detection of alarming situations (fall), step counters, energy expenditure estimation, etc. The early studies in this area were conducted by using intrusive body-worn sensors and were not applicable for everyday use. Later, with the increasing accessibility and miniaturization of sensors and microprocessors, the intrusiveness reduced significantly. Finally, when these sensors were introduced in the smartphones, a whole new era for practical usage has started. By applying intelligent techniques, such as the ones described in this study, any smartphone user can benefit from the rich information that his/hers smartphone sensors can provide.

In this paper, our idea of transforming the smartphone into a healthcare device capable of recognizing activities and detection of fall situations is presented. First, we present the general concept of a smartphone implementation. Then, techniques for sensor data fusion, synchronization and preprocessing are introduced. Next, the methodology for the both healthcare tasks is introduced. Finally, the experimental results achieved for both tasks are discussed.

2 Smartphone Implementation

An overview of the smartphone implementation is given in Figure 1.

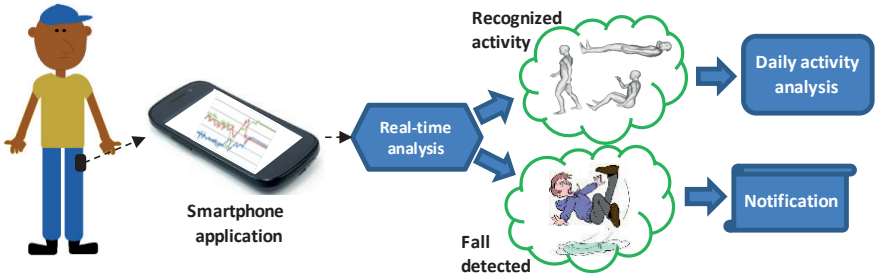


Figure 1. Smartphone implementation overview.

The implementation consists of a smartphone equipped with inertial sensor. A software application on a smartphone implements all the methods described in this paper. The application uses the inertial sensor's data from the smartphone as an input and in real-time outputs user's activity and detects fall events. If a fall is detected, an appropriate alarm notification can be triggered e.g. an SMS is sent to the user's predefined contacts. This is especially useful for elderly who live alone and could be, in the case of a fall, stranded for a long time. In the case of the activity recognition (AR), the recognized activities are logged during the whole day and can be later analyzed. The analysis may contain daily activity statistics, comparison between different days and therefore, detection of health-related anomalies.

3 Inertial Sensors

Inertial sensors detect and measure the inertial forces that influence them. When the sensors are attached on a human body, they measure forces of a particular body part. An inertial sensor consists of an accelerometer and a gyroscope. An accelerometer is a sensor that measures the acceleration applied to the sensor and also the constant Earth's gravity. When the accelerometer is at rest, only Earth's gravity is measured. Additionally velocity and sensor orientation can also be estimated. A gyroscope or a gyro is a device for determining or maintaining orientation. It measures the angular velocity and therefore allows more accurate recognition of movement than in devices with only an accelerometer, which was the only inertial sensor in older smartphones.

4 Preprocessing

The data from inertial sensors can contain many erroneous measurements due electromagnetic noise. To reduce the impact of the noise on the data, a band-pass filter (between the frequencies 0.1 to 20Hz) and a low-pass filter (with a cut-off frequency of 1Hz) are used [3]. The band-pass filter has two goals: (1) to eliminate the low-frequency acceleration (gravity) that captures information about the orientation of the sensor with respect to the ground and (2) to eliminate the high-frequency signal components generated by non-human motion and high-frequency noise, thus preserving the medium-frequency signal components generated by dynamic human motion. The band-pass filtered data is used for the extraction of features relevant for dynamic activities, such as walking, running and cycling. The

low-pass filter has the opposite purpose: to eliminate most of the signal generated by dynamic human motion and preserve the low-frequency component, i.e., gravity. In this way the low-pass filtered data contains the sensor-orientation information, which is relevant for the recognition of the static activities (postures), such as lying, sitting, standing and kneeling. These filters provide two streams of filtered data which is further processed in order to extract appropriate features for AR or FD.

Finally, an overlapping sliding-window technique is applied. A window of fixed size (width) moves across the stream of data, advancing by half its length in each step. The data within each window is used in the AR described in the next section.

5 Methodology

Different methodology was used for each of the analyzed tasks. On one side, the method developed for the AR is mainly based on the machine learning and combining classification models with a multi-layer architecture. On the other side, the fall detection methodology is based on the recognized activity and additionally applies context-based reasoning rules to detect a fall situation. The methodology is briefly described in the following sections; more details can be obtained in the provided references.

5.1 Activity Recognition

To recognize the users' activity, the stream of data from the sensors is first segmented into 2-second time windows. We showed in prior work that 2-second windows are a reasonable trade-off between the overall recognition accuracy (increases with window length) and the ability to recognize very short activities (decreases with window length) [4]. To recognize an activity from sensor data three-layer architecture for the AR, i.e., TriLAR [5], is used. The TriLAR architecture consists of the following: (i) a bottom layer, where the data is passed to an arbitrary number of independent AR methods; (ii) a middle layer, where a hierarchical aggregator combines the predictions from the bottom-layer methods; and (iii) a top layer, where a hidden Markov model uses the temporal dependence of activities to remove the spurious transitions between them and produce the final activity.

5.2 Fall Detection

Because of the specificity of the fall detection task, a higher level reasoning about the user's situation is performed. The methodology is based on domain rules which are applied on already processed data in order to reason about the user's situation. In particular, we developed a CoFDILS (Context-based Fall Detection using Inertial and Location Sensors) reasoning schema [6], which uses the context information from the sensors to determine whether a fall has occurred. It exploits three context components: the user's activity, body accelerations and location information. Each of the components is obtained using a separate method. First, the user's activity is recognized using the TriLAR method, explained in the previous subsection. Next, the user's body accelerations are extracted using the changes in the acceleration signal during motion: Acceleration Vector Changes (AVC) [7]. This AVC sums up the differences between consecutive values of the lengths of the acceleration vector and normalizes them. By applying an empirically defined threshold to the AVC value, the movement of a sensor is detected. Finally, the user's location is determined using a location tag attached to the user. In general any technique that can detect the location of smartphone can be used as input in the method. In recent years several examples of successful indoor localization of smartphones were proposed. WIFARER [8] is a smartphone application that provides the location of the phone using the Wi-Fi signals. Another successful indoor localization for smartphones is the LocLizard platform [9] that provides API which can be used in the smartphone application.

To explain the basic principle of the context-based reasoning, let us consider the following example in which a user is lying down quickly on a bed, i.e., a non-fall situation. In this case, the body movement component recognizes a high acceleration. If this component reasons by itself, a wrong decision would be formed: a fall would be detected. If the activity of the user is additionally evaluated, the decision would still be wrong (a high acceleration and lying activity = a typical fast fall). However, when the location of the user is evaluated (the bed), the final decision is corrected into non-fall (quickly lying on the bed). In similar manner, several more rules that reason about the user situation and detect a fall are defined.

6 Experiments

The experiments were performed with wearable sensor equipment consisting of the same types of sensors as the ones included in the smartphones, i.e. inertial sensors.

Because the methods developed are general and can be reused for any type of inertial sensors, we are confident that the main findings are also valid for the smartphone implementation.

6.1 Activity Recognition

6.1.1 Experimental Scenario

A 90-minute, test scenario was designed in cooperation with a medical expert to capture the real-life conditions of a person’s behavior, although it was recorded in a laboratory. The scenario was performed by ten volunteers. It was divided into three groups: exercising activities, elementary activities and everyday-life activities. The scenario included ten elementary activities (the percentage of instances per class): standing (16%), sitting (11%), lying (22%), on all fours (10%), kneeling (6%), bending (standing leaning) (3%), walking (15%), running (5%), cycling (10%) and transition (going down and standing up) (2%). These activities were selected as they are the most common elementary, everyday-life activities.

6.1.2 Results

To test the TriLAR architecture, we used the abovementioned dataset. The evaluation technique was leave-one-person-out cross validation. This technique constructs the training model on the data from all the people except one. The remaining person is used to evaluate the accuracy of the trained model. This procedure was repeated for each person (10 times) and the average performance was measured. In Figure 2 results of AR evaluated with the F-measure are shown. F-measure combines the precision and the recall (harmonic mean) of each activity.

Dynamic activities are better recognized than static activities, with two exceptions. The TriLAR architecture is successful at recognizing lying activity as the sensor’s orientation is significantly different than with other activities, but has trouble recognizing the transitional activities as sensor’s movement is similar to other static activities. The static activities, other than lying, are more difficult to recognize because the inertial sensor is not moving and sensor’s position is similar between these activities.

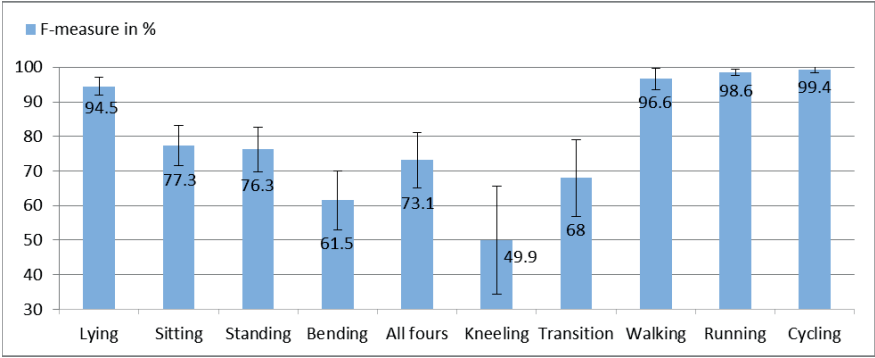


Figure 2. Activity recognition results among different activities.

6.2 Fall Detection

6.2.1 Experimental Scenario

A complex, 15-minute test scenario was specifically designed to investigate events that might be difficult to recognize as falls or non-falls. This scenario was created in consultation with a medical expert. The events in the scenario are listed in Table 1. Because typical fast falls are easy to detect due to high acceleration, only one such fall (1) was included. Three atypical falls not involving high acceleration (2, 3 and 4) were included to test the use of the contextual activity information, i.e., that a person is not expected to sit/lay on the ground (as opposed to the chair/bed). Furthermore, the two events 5 and 6 involve high acceleration and could thus be misclassified as falls by acceleration-based methods. However, the methods that use the activity and location as contextual information should be able to detect that these are non-fall events. An event (7) was included that involves voluntarily lying on the ground, which could mislead the methods that use information other than acceleration. The events 8, 9 and 10 are normal and were included to verify that all the methods work correctly during normal events.

The scenario was recorded by 11 young healthy volunteers (24–33 years, 7 males and 4 females). It was repeated 5 times by each person, resulting in 55 recordings and a total of 550 events for the FD. Testing elderly people was not feasible, because the scenario was too strenuous and risky for them, but the volunteers were advised how to act by the medical expert in order to mimic elderly. Additionally, the data for 3 more people was recorded for tuning the basic parameters, e.g., thresholds, preliminary tests and choosing the best algorithms.

6.2.2 Results

The results achieved by the inertial sensors only and their combination with the location information, are shown in Table 1. In the experiments the location was provided by additional sensor. Because the method requires only rough estimations of predefined locations, we are confident that the smartphone estimations provided by the LocLizard API [9], would be enough for achieving similar performance.

The results show that, if only inertial sensors are used half of the falls with high acceleration can be detected (1). However, the slow falls are almost impossible to be detected with inertial sensors only (2, 3 and 4). During the non-fall, but events with high acceleration (5 and 7), the acceleration is misleading and false alarm is raised. The normal events (8, 9 and 10) are recognized as non-fall events with high performance.

The location is really important for detection of complex fall situations (events from 1 to 4). Compared to the inertial sensors alone approach, the overall performance is improved by 41 percentage points when the location is included. The reason for this is that the inertial sensors are not enough for accurate FD especially not for events that do not include high accelerations (the events 2, 3 and 4). These types of events require additional user information, such as the location.

Table 1. FD results for each fall and non-fall event.

		Inertial		Inertial + Location	
		TR	TL	TR	TL
Fall Events	(1) Tripping – Quick falling	53	45	100	100
	(2) Fainting – Falling slowly	3	0	95	96
	(3) Falling from a chair slowly	3	3	93	93
	(4) Sliding from a chair	5	4	91	93
Non-Fall Fall-like Events	(5) Sit down quickly on a chair	36	36	75	75
	(6) Searching on the ground	100	100	85	86
	(7) Quickly lying down on a bed	56	50	100	100
Non-Fall Normal Events	(8) Sitting normally	95	95	86	87
	(9) Lying normally	100	100	100	100
	(10) Walking	100	100	100	100
Overall F-measure in %		42	40	93	93

The analysis of the performance for the different sensor placements (left or right thigh) shows that there is no significant difference. Therefore, the user can simply choose the placement which is more appropriate to him/her without decreasing the FD performance.

7 Conclusion

The paper presented an idea of transforming a smartphone into a healthcare device capable of recognizing activities and detection of fall situations. Techniques for sensor data fusion, synchronization and preprocessing were introduced. Then, the proposed methodology for the both healthcare tasks was evaluated on two special comprehensive experimental scenarios. The results showed that it is possible to achieve satisfactory performance for the both tasks using only one inertial sensor embedded in a smartphone. In the future, we first plan to finalize the whole smartphone implementation, extensively test it in everyday usage and offer the application to everybody who needs it.

References:

- [1] Ekholm, J., Fabre, S.: Forecast: Mobile data trac and revenue, worldwide, 2010-2015. In: Gartner Mobile Communications Worldwide, 2011.
- [2] Number of Smartphones Around the World Top 1 Billion -- Projected to Double by 2015. <http://finance.yahoo.com/news/number-smartphones-around-world-top-122000896.html>
- [3] E. M. Tapia, Using Machine Learning for Real-time Activity Recognition and Estimation of Energy Expenditure, *Ph.D. Thesis*, Massachusetts Institute of Technology, 2008.
- [4] M. Žbogar, H. Gjoreski, S. Kozina and M. Luštrek, Improving accelerometer based activity recognition. *Proc. 15th Int. Multiconf. Inf. Soc.*, p.p. 167-170, 2012.
- [5] S. Kozina, H. Gjoreski, M. Gams and M. Luštrek, Three-layer Activity Recognition Combining Domain Knowledge and Meta-Classification. *Journal of Medical and Biological Engineering*, Available Online, doi:10.5405/jmbe.1321, 2013.
- [6] H. Gjoreski, M. Luštrek and M. Gams, Context-Based Fall Detection using Inertial and Location Sensors. *Proc. International Joint Conference on Ambient Intelligence. Lecture Notes in Computer Science* vol. 7683, p.p. 1–16, 2012.
- [7] H. Gjoreski, M. Luštrek and M. Gams, Accelerometer Placement for Posture Recognition and Fall Detection. *Proc. The 7th International Conference on Intelligent Environments*, p.p. 47–54, 2011.
- [8] WIFARER smartphone application. <http://www.wifarer.com/>
- [9] LocLizard, API for smartphone indoor localization. <http://api.loc lizard.com/>

For wider interest

Production of mobile phones is in constant increase. Currently, more than 85% of the world population owns a mobile phone. This shows that in a very short time, mobile devices will become easily accessible to virtually everybody. In recent years, the number of smartphones, which are a new generation of mobile phones, is in constant increase. In 2012, 1 billion smartphones were in use and this number is expected to be doubled in the next 3 years. Smartphones, in contrast to the basic telephony, are offering many features such as multitasking and the deployment of a variety of sensors: inertial, compass, GPS, light, pressure etc.

The intelligent use of these sensors is allowing many potential applications. Recent studies have shown that the body-worn inertial sensors give rich information about the user, which can be used in many healthcare applications: automatic recognition of daily activities, detection of alarming situations (fall), step counters, energy expenditure estimation, etc. The early studies in this area were made using intrusive body-worn sensors and were not applicable for everyday usage. When these sensors were introduced in the smartphones, a whole new era for practical usage was has started. By applying intelligent techniques such as the ones described in this study, any smartphone user can benefit from the rich information that his/hers smartphone sensors can provide.

In this paper an idea of transforming the smartphone into a healthcare device capable of recognizing everyday activities and detection of fall events is presented. This approach firstly use inertial sensors data as an input, then the data is preprocessed and segmented and finally, artificial intelligence methods are applied which recognize the user's activity and detect a fall event. If a fall is detected, an appropriate alarm notification can be triggered e.g. an SMS is sent to the user's predefined contacts. This is especially useful for elderly persons who live alone and could be, in the case of fall, stranded for a longer time. In the case of the activity recognition, the recognized activities are logged during the whole day and can be later analyzed. The analysis may contain daily activity statistics, comparison between different days and therefore, detection of health-related anomalies.

Business simulation game – an innovative pedagogical approach in business environment

Andrej Jerman Blažič¹, Tanja Arh¹

¹ Laboratory for Open Systems and Network, Jožef Stefan Institute, Ljubljana, Slovenia

andrejcek@5.ijs.si, tanja@e5.ijs.si

Abstract. The purpose of this paper is to present and discuss the concepts of serious games and their beneficial support in the world of business industries as an innovative pedagogical approach. Serious games have been demonstrated to provoke active learners' involvement through exploration, experimentation, competition and co-operation. These games are used widely outside of formal education systems, for example by the military and within the health and commerce sectors. Business simulation games are considered as effective tools for the empowerment and mediation of business content learning. They act as serious games which contribute to learning through a simulation of real-life situations and business environments. They are especially useful in the area of business management processes and business strategies where they train or educate users. IBM Innov8 v.2 is one example of business simulation games that train and teach the fundamental concepts of business process management in a "risk free" environment.

Keywords: serious games, business simulation games, business process management, e-learning

1 Introduction

It is argued that digital games, including simulations and virtual worlds, have the potential to be an important learning tool because they are interactive, engaging and immersive activities [1]. Serious games therefore are generally held to be applications developed with digital game technology and design principles having training, situation simulation or education while entertaining the user as a prime purpose. Serious gaming is, thus, games that engage users in their pursuit and contribute to

the achievement of a defined purpose other than pure entertainment [2]. They have been seen as good opportunity for supporting learning or training because of their capability to increase visualizations and challenge the learner's creativity [3]. Academia has been studying video games and their use in learning in the last two decades. However the area is still treated as a novel approach in learning in both educational systems: within the universities and within the lifelong learning programs [4]. The search for new positioning of educational games within university programmes is still an issue of discussion as the changing setting of education by use of gaming is becoming slowly a new form of interactive content, worthy of exploration. The »fruits« of game based learning research that resulted in applicable setting are now starting to penetrate in different environments where training or learning is required. Serious computer games have shown that they can gather useful learning content based on known educational material. Today, the term "serious games" is becoming more and more popular. [5]

There are specific training domains where serious games, learning concepts and approaches have shown a high learning value. The main property of serious games usage is the capability to motivate and teach in ways that other methods cannot, a unique solution in the vast area of training issues studied by trainers and researchers [6]. Using the knowledge that has been provided in training classes and at lectures, real situations can be practiced and simulated mainly by training within the gaming environment. Serious games have the potential to significantly improve training and education activities and initiatives.

Business simulation games are part of serious computer games. They "are all about leveraging the power of computer games to captivate and engage end-users for a specific purpose, such as to develop new knowledge and skills in the business environment". However they have been used to recruit staff, improve communication between managers and their far-flung staff, and train employees at all levels. [2]

Nowadays, new employees are being educated passively from PDFs, PowerPoint, or from blackboards in training classes in order to being recruiting to adapt to new challenged workflow. However, virtual environments and 3D gaming bring new

pedagogical approaches that help learners to experience efficient game-based learning methods and gain new skills required for business environment workspace. For the purposes of this article, the IBM Innov8 v.2 game will be presented that helps to bridge the gap in understanding between business leaders and IT teams in an organization.

2 The framework

Serious games as a term has been around for over 40 years. In 1968 Clark C. Abt called his book “Serious Games”. The book described his work in the 1960s in which he examined war-games (where dramatic scenarios were combined with mathematical analysis and the interplay of groups) and simulations to train managers, students, and teachers in educational-curriculum development, school-system planning, industrial management and technological planning and forecasting.

Michael and Chen [2] give the following definition: “A serious game is a game in which education (in its various forms) is the primary goal, rather than entertainment”. It is worth noting that Huizinga [7] defined games as a free activity standing quite consciously outside “ordinary life”, and as being “not serious”-following this definition games cannot be serious. Callois [8] similarly defined games as voluntary, therefore also conflicting with the notion of serious games. This gives a good indication of the kinds of contradictions found in comparisons of the available literature. Serious (computer) games have been demonstrated to provoke active learner involvement through exploration, experimentation, competition and co-operation. They have been seen as a good opportunity for supporting learning processes because of their capability to increase visualizations and challenge student creativity [5]. Academia has been studying video games and their use in the learning environment in the last two decades. However the area is still treated as a novel approach in learning in both educational systems: within the universities and within the lifelong learning programs [6]. According to a 2008 study by the Ewing Marion Kauffman Foundation, a great lecture can improve learning outcomes by 17%, while switching to a different delivery mechanism such as serious gaming can improve learning outcomes by 10%.

3 Business simulation games

As a part of serious computer games, business simulation games support training and learning that is focused on management of economic processes. They are presented as a training technique in which participants consider sequence of problems and take decisions. The main component is simulation which is based on sequential decision-making exercise structured around a hypothetical model of the operations of an organization. Being a simulation game, the participants can select different decisions without any fear for a real loss to the organization in case participants make mistakes. Participants can select actions and can have experience regarding the consequences of those actions. The learners/users are using their newly acquired skills and knowledge by applying them to a competitive challenge provided within the business game [9].



Figure 1: A screenshot of The business game at PIXELearnig (a virtual business environment)

Business simulation games help to model the realities of the business world by simulating basic – and in some cases advanced – business theories and practices in controlled game environments. Because they simulate the real-world system, they can often be used as a teaching method executive education as well [10]. The benefits of business simulations are in the possibilities the users to experience and test themselves in situations before encountering them in real life, give them the chance to experiment and test hypotheses. Within the business simulations offered

within a serious game, subjects seem much more “real” to the users or learners than when taught passively from PDFs, PowerPoint, or from blackboards. Extensively business game simulations in professional world are used for training workers in the financial industries and management, where the study of the economic models can be carried out with some of the available business games. Business simulations have been used as well as in experiments, such as those done by Donald Broadbent who has studied learning and cognition. Those studies have revealed how people often have an attitude for mastering systems without necessity to comprehend the underlying principles [10].

The usage of business simulation games brings benefits such as: they permit users to experience and test themselves in situations before encountering them in real life, they permit users to experiment with business variable hypotheses and test them. The subjects in the game seem more “real” to the users than when taught passively in the training classes or lectures [11].

4 INNOV8 game

The INNOV8 v.2, also known as the IBM business process management simulation game is a role-playing game that simulates business process management (BPM) in a 3D virtual environment. The IBM self-oriented architecture (SOA) team originally created the game to help educate potential SOA clients dealing with project team leaders. It takes players through the entire lifecycle of discovery, collaboration, optimization, and innovation of a fictional company’s business processes. It gives both IT and business players an excellent introduction to BPM, from learning the anatomy of a model, to how one might optimize the model and make a company more profitable. Players, for example, learn how to eliminate waste while managing a “green” supply chain or improve customer service and maximize profits while running a call centre. IBM offers Innov8 v.2 and associated materials for free to schools and IBM intends to make the new release freely available for businesses as well. The 2.0 version was released on May 2009. While early versions of the game were available only on CD using original call centre service scenario (players develop more efficient ways to respond to customers), IBM is delivering Innov8 v.2 via web download with two additional scenarios: *smarter traffic* (players evaluate existing traffic patterns and re-route traffic based on incoming metrics) and *smarter supply chains*

(players evaluate a traditional supply chain model, balance supply and demand and reduce environmental impact) in order to reflect a new level of intelligence required for future, high-value job opportunities.

4.1 The overview – smart customer service

The game starts on the very first moment when a player takes a role of a female virtual character named *Logan* that has been hired by After Inc. The game features a fictional call centre agency, which has a process model that is functioning sub-optimally. The player must discover the current model, find out why it is under-performing and then optimize it to meet the demands of the market.

Players have to achieve three main levels: process discovery and process modelling, collaboration driven simulation and iterative process improvement, and real-time business management.



Figure 2: A screenshot of virtual business meeting. (Players use drag-and-drop graphic to design their business process diagram)

The game allows players to visualize how technology and related business strategies affect an organization's performance. Together, players can map out business processes, identify bottlenecks and explore 'what if' scenarios in an experiential learning environment. Players have the opportunity to play with different variables and see how their changes vary the outcome, preparing them for the day they need to make real decisions. Players use drag-and-drop graphics to advance through the game. Since main parts of the game are taking place in 3D environment, the game gives the very impressions of the “first-person-shooter”- like game play. Some parts of the game, which even has virtual characters in a shape of heroes and villains, use “Second Life-like” graphics. While different tasks and levels are completed, the game tries to “force” the players to make decisions as they seek more efficient ways to manage a call centre and respond to customers. The game comes to an end when the business meeting takes place. At the meeting a player has to play with different variables of business modelling and see how player’s changes vary the outcome.



Figure 3: A screenshot of simulation business model (Players can play with different variables to test their outcome, before put the model in “life”)

75% of CEOs surveyed by IBM cited education and the lack of qualified candidates as the issues that will have the greatest impact on their business over the next three years. With a growing number of jobs and professions requiring a combination of technology and business skills, INNOV8 can be an effective way of developing this new, hybrid skill set. A recent study also found that 56% of IBM customers cited lack of skills, mainly individuals with a blending of IT technical understanding and business process acumen, as the leading inhibitor to service oriented architecture (SOA), a \$65 billion market opportunity. INNOV8 will help students and young professionals develop these crucial skills [12].



Figure 4: A screenshot of virtual environment of Innov8 v.2 (a virtual female character called Logan, which is guided by a player)

5 Conclusion

Business simulation games are tools, they can help us explore and understand issues, and train for various circumstances. They based on the use of the computer and internet capabilities are a reality and they are expected to be the default tool in many areas in the future. Due to their limitations or functionalities many of them will be adapted or re-modeled [13]. IBM itself not only uses games for internal training but has made part of its training programme a commercial product. Whether these games can be classified as serious, or advertainment - they require the use of IBM solutions to achieve answers, they are popular. Their game, INNOV8 v.2, has been downloaded by 1.000 schools worldwide and more than 100 universities worldwide have built custom curriculum using the serious game to help students learn about business process management. The research on modern students' education methods and techniques has proven that education based on practical usage of knowledge and training in a target activity environment is the most effective way of learning and educating [1]. Depending on the discipline, an environment can have real character, that is, it exists in reality or a virtual character, and that is, it comes into being through simulation of real phenomena. It can be claimed that Business Simulation Games are perceived as an interesting and desired form of gaining experience that can be used in later professional practice [14]. There are many Business Simulation Games that meets challenges of learning and training in

business environment. In this case IBM Innov8 v.2 shows its example. But different Business Simulation Games simulate different business situations, thus, each game can serve its purpose. Overall, the potential of Business Simulation Games as learning tools will increase given the improving underlying technology, availability of kit, increasing interaction techniques, software's ability to process data, and the increase in gamers [15].

References:

- [1] M. Ulicsak, M. Wright. *Games in Education: Serious Games, A Futurelab Literature Review*. Futurelab. Innovation in education, 2010.
- [2] D. Michael, S. Chen. *Serious Games: Games that educate, train, and inform*. Boston, MA.: Thomson Course Technology, 2006.
- [3] J. B. Hauge, J.C.K.H. Riedel, (2011). State of the Art of Serious Games for Business and Industry. *17th International Conference on Concurrent Enterprising*, Achen, Germany 2011.
- [4] J. Aleckson: *Definitions: Serious Games and Game Based Learning*, January 19. 2009. <http://managingelearning.com/2009/01/19/definitions-serious-games-game-based-learning/> (Accessed December, 2012)
- [5] M. Pivec. Editorial: Play and learn: potentials of game-based Learning. *British Journal of Educational Technology*, 38(3): 387–393, 2007
- [6] D. Michael, S. Chen. Serious Games in Defence Education: A report into the potential educational. *Benefits of Education*, 61(3): 1-95, 2005.
- [7] J. Huizinga. *Nature and Significance of Play as a Cultural Phenomenon*,” Beacon Press, 1955
- [8] R. Cailliois. *Man, Play, and Games*. New York: Schocken Books. 1971
- [9] B. Keys, J. Wolfe. (1990). The Role of Management Games and Simulations in Education and Research. *Journal of Management*, 16(2): 307-336, 1990.
- [10] G. M. Farkas. *Social Software in Libraries: Building Collaboration, Communication, and Community Online*. Information Today, Inc. 2007.
- [11] C. Hogarth, M. Robin. *Educating Intuition*. University of Chicago Press. 2001
- [12] Matt Berry IBM Media Relations 2007. Available at: <http://www-03.ibm.com/press/us/en/pressrelease/22549.wss> (Accessed Januar 10, 2013)
- [13] R. S. Bernard. Characterizing Business Games Used in Distance Education. *Developments in Business Simulation and Experimental Learning*, Vol 22, 2006.
- [14] M. Wawer, M. Milosz, P. Muryjas, M. Rzemieniak, M. (2010). Business Simulation Games in Forming Students’ Entrepreneurship. *International Journal of Euro-Mediterranean Studies*, 3 (1): 49-73, 2010.
- [15] JiSC, 2007. Game-based learning: JiSC. Available at: www.jisc.ac.uk/publications/briefingpapers/2007/pub_gamebasedlearningBP/pub_gamebasedlearningBP_content.aspx (Accessed December 12, 2010).

For wider interest

My research is based on serious games and their innovative approach in lifelong learning processes. As a matter of fact, people tend to absorb more easily information they acquire through interactive channels and while they respond to a challenge in a competitive and entertaining environment. From that viewpoint, game technology can give enhance existing learning approaches and training methodologies. The gaming technology is a vast area and has numerous challenges to be explored in order to support efficient learning and training.

Time-window selection for optimal generalization with noise variance reduction in ecological data

Vladimir Kuzmanovski^{1,2}, Marko Debeljak^{1,2}, Sašo Džeroski^{1,2,3}

¹ Department of Knowledge Technologies, Jožef Stefan Institute, Ljubljana, Slovenia

² Jožef Stefan International Postgraduate School, Ljubljana, Slovenia

³ Centre of Excellence for Integrated Approaches in Chemistry and Biology of Proteins, Ljubljana, Slovenia

vladimir.kuzmanovski@ijs.si

Abstract. Due to the imperfect human ability to observe a real world processes, the raw measured environmental data contains unobservable non-systematic errors that are further transferred as noise in the observed data. In addition, the raw environmental data are never exactly representative of the real world processes that have been observed. On the other hand, for obtaining a quality performance of the analyses of those data, such systematic anomalies or noise need to be explored and considered in a proper way. In this paper we demonstrated an approach for noise (non-systematic error) reduction implemented in the domain of ecological data. The described approach employed stochastic optimization algorithm, in order to delimit dataset into subsets by defining time-window that is representative for a time period under consideration. The results of case study of La Jaillière (France) experimental site shows that defining time-window and optimizing its length increases the performance of the data analyses by reducing the noise caused by some non-systematic and non-measured variable that influence the value of the observed variable over time.

Keywords: Time-window, Noisy data, Optimization, Genetic Algorithm, Data Mining, Model Trees

1 Background & Objectives

Obtaining a quality experimental data from real world environment is almost impossible due to the fact that the human ability for observing a real world process is not perfect [1]. Consequently, analysts of measured environmental data face additional problem because the observations are never exactly representative of the real world processes that have been observed. Therefore, analysis of environmental data has to explore such anomalies in the data and consider them in a proper way. Roughly, it can be conceptualized as:

$$\text{Measured Value} = \text{True Value} \pm \text{Error}$$

The Error is a combined expression of the inherent variation in the process that has been observed and numerous factors that interfere with the measurements (e.g. systematic error related to calibration of the instruments used for data collection, unmeasured systematic variable that affects the observed variable and cannot be measured with the available instruments, etc.). Furthermore, both produce unexplained variation of observed variable, which is generalized as noise. Types of noise are present to almost any real world problem, but it's not always known [2].

In data mining, the presence of noise in empirical data reduce the performance of learned model in terms of model accuracy, time in building a model, and the size of the model. Therefore we need to find out how much the noise in data translates into uncertainty (in ability to approximate the real value of the observed variable).

Statistics literature proposes sampling methods for noise explanation and reduction in case of numerous sources of noise and normal distribution of the experimental errors. It is defined by the central limit theorem and it provides a theoretical basis for making assumption of normally distributed error structure in experimental measurements [3].

Because the experimental error is never exactly normal distributed in experimental measurements, we have implemented an optimization approach for noise reduction in time based experimental data that does not require any assumptions related to distribution type of the experimental error. Namely, we are looking for optimal time-window length for delimiting of dataset into subsets that will reduce the noise and will be representative for a real world process that we are observing. We used optimization approach by implementing evolutionary algorithm for time-window

length and machine learning algorithm's parameter optimization. The evaluation of candidate solutions was performed by solving a machine learning problem. It is a problem of predicting daily outflow of drained water (target, output) on a field level from measured meteorological data and data for agricultural practices performed on the fields (input). The case-study takes into account fields within the study area of La Jaillière, located in western France.

2 Materials & Methods

The data we used in our analyses are from the experimental site La Jaillière, run by the technical institute ARVALIS - Institut du Végétal. It is situated at the southern end of the Armorican massif in western France. The site has been dedicated to the study of the influence of agricultural management practices on water quality since 1987. It is a reference site for the European Commission FOCUS working group [4]. The La Jaillière site is considered as a representative of the agricultural regions in Europe with shallow silt clay soils. The climate at the site is of oceanic type. The mean annual precipitation of 717 mm is evenly distributed along the year (monthly values between 40 and 62 mm). The mean annual potential evapotranspiration is 712 mm (meteorological station of La Jaillière, 1987-2012).

The site contains fields divided into north and south parts. Each part contains blocks of fields. Each block is used for a different type of experimental analyses. In our study, we have included data from 11 fields. The surface area of each plot is from 0.34 to 1.08 ha, and is cultivated following a traditional winter wheat/corn crop rotation. Most of them are equipped with an independent tile drainage system (for drainage type water collection) and/or run off traps consisting in metal cuttings at field edges to collect runoff water. A methodological precaution concerns the establishment of drainage trenches between the fields to avoid water to pass from one field to another. The tile drains are located at the depth of $d = 0.9$ m below the soil surface, with a spacing of 10 m [5].

The Arvalis team, in charge of the experimental site of La Jaillière, collect all the data about the agricultural practices (tillage, sowing, fertilizing and pesticides application dates), the amount of water flows and the concentration of the water solution (mineral and active substances) in the surface waters (drainage and runoff). All these data are collected in the PCQE (Pratiques Culturelles et Qualité des Eaux) database. The data are stored for each plot separately for 24 campaigns (1987-2011).

The optimization approach for noise reduction evaluates the predictive performance of data subsets constructed by last sequential campaigns. The number of last sequential campaigns defines the time-window which slides through time for each new campaign. We used genetic algorithm (GA) for predictive performance optimization and time-window definition. GA is search heuristics based on the mechanics of natural selection and natural genetics, and mimics the process of natural evolution. As such, they represent an intelligent exploitation of a random search within a defined search space to solve a problem [6]. GA's have been developed by John Holland at the University of Michigan in late 1960's. Their domain of utilization is very large, a review of their implementations and some application domains are given by De Jong [7], Goldberg [8], Eiben [9].

GAs are modeled on the principles of the evolution through natural selection, employing a population of individuals that undergo selection in the presence of variation. Variation is achieved by inducing operators such as mutation and recombination (crossover). A fitness function is used to evaluate individuals. The success of reproduction depends on their fitness. When setting up a GA it is important to define the representation of chromosome (mapping from genotype to chromosome), fitness function and algorithm parameters, i.e. population size, mutation and crossover rates, and stopping criteria.

In our experimental design we have used binary representation of the chromosomes and population size of 30 chromosomes in one evolution. In a single binary chromosome we have mapped two parameters that need to be explored and optimized: number of years that will define the time-window, and minimal number of instances – parameter of M5P algorithm for inducing model trees [10]. Furthermore, we take 10 % of chromosome's length as mutation rate and 80% as crossover rate. Stopping criteria was defined as 100 evolutions (generations). As fitness function we used Index of Agreement [11]:

$$d = 1.0 - \frac{\sum_{i=1}^N (O_i - P_i)^2}{\sum_{i=1}^N (|P_i - \bar{O}| + |O_i - \bar{O}|)^2} \quad (1)$$

where N is number of instances and \bar{O} is a mean of the observed values.

Namely, the Index of Agreement (d) is standardized measure of the degree of model prediction error and it overcomes the insensitivity of correlation-based measured to differences in the observed and model-predicted values [12]. Its values vary between 0 and 1. A value of 1 indicates a perfect match, and 0 indicates no agreement at all. The evaluation of chromosomes, from the population, converges in solving machine learning problem for accurately predicting outflow of drained water on a field level based on input data. The models are learned with M5P algorithm for inducing model trees [10]. Finally, the average of performances of individual models learned for all campaigns between 1987+($i+1$) and 2011, (where i is a time-window length written in the chromosome that has been evaluated) gives the evaluation of particular chromosome.

3 Results & Discussion

The optimization process was employed for estimating the optimal time-window length. Since, the initial population is randomly determined, we run the optimization process 10 times. Figure 1 shows the stability performance of the optimal solutions, over 10 runs of the optimization process. It shows that the performances of the optimal solution in each run reach the same value, which means that the optimization process did not get into a local optimum, but reach the global optimum.

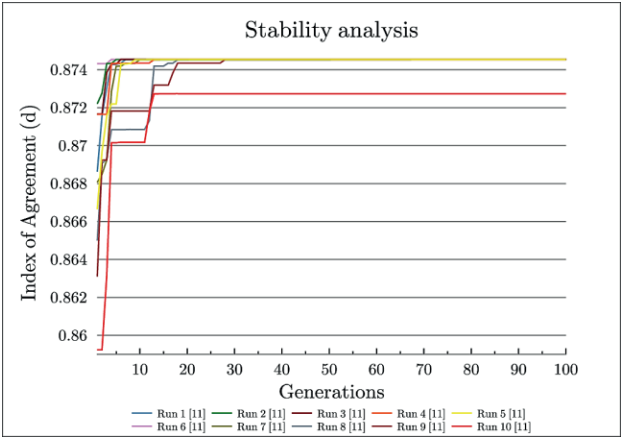


Figure 1: Stability analysis for all 10 runs. Except trajectory of 10th run, all converge in a single point.

	8 years	11 years	All data
Min. number of instances	610-612	618-619	1580-1850
Index of Agreement (d)	0.870	0.879	0.865
Std. Deviation of d	0.27	0.23	0.27

Table 1: Best solutions discovered by the optimization approach within 10 runs, presented with minimal number of instances in a leaf (algorithm parameter that has been optimized), Index of Agreement (model comparison metric used for evaluation of candidate solutions) and standard deviation of the Index of Agreement

The best solutions that were discovered in all ten optimization runs are presented in Table 1. Namely, time-window length of 8 years was found as most optimal in only one run, while in the rest of the optimization processes most dominant was length of 11 years. Therefore, both are given and considered for further evaluation.

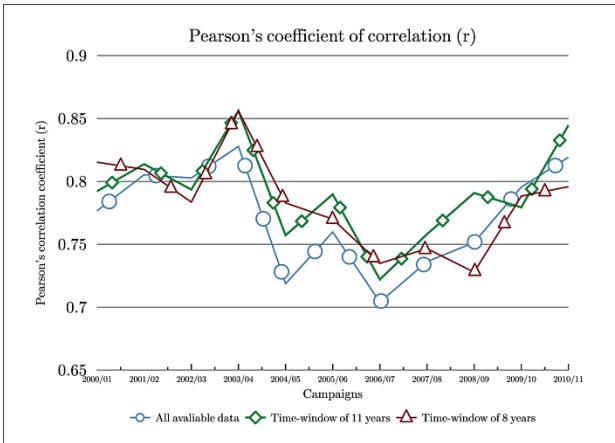


Figure 2: Correlation coefficients of models learned from time-window of 8 and 11 years compared to performance of learned model from all available data.

For final analysis of the performances of the given optimal solutions, we have tested the models for each campaign, starting from 2000/2001. Namely, we have learned models for each campaign, taking 8 and 11 years as time-window, and finally compared them with the models learned from a complete dataset (all campaigns

since 1987/1988 to 2010/2011). The model’s performances (Correlation Coefficient and Index of Agreement) are presented in Figure 2 and Figure 3.

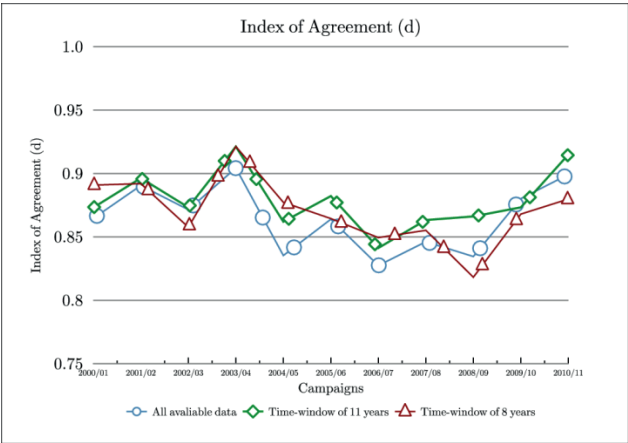


Figure 3: Index of Agreement of models learned from time-window of 8 and 11 years compared to performance of learned model from all available data.

The Figure 3 shows that the time-window of last sequential 11 years perform better than models learned on the complete data in 10 of 11 test campaigns. On the other hand, time-window of 8 years outperform time-window of 11 years in 3 campaigns (2000/01, 2004/05 and 2006/07). Furthermore, we analyzed the correlation coefficients of learned models, since the Index of Agreement as performance metric is not a widely used. The ratios of correlation coefficients between models learned on a different time-window lengths and complete dataset are almost the same as previously discussed. Therefore, the time-window of 11 years improves the learned models for predicting field’s outflow of the drained water the most. In addition, although the performances of the different time-window length are very close to each other, the optimization approach and defining a time-window for noise reduction in the domain of ecological modeling can guarantee that the noise caused by different micro- environmental and climatic changes (e.g. changes of the landscape by creating buffer zones or natural change in surrounding’s vegetation, changes in micro-climate, etc.), as well as changes in agricultural practices over time periods (e.g. changes of tillage practices and crop rotation planning) will be diminished. Finally, this approach will have additional advantages when lazy (e.g. k-

Nearest Neighbours, Lazy Bayesian Rules, etc.) and instance-based methods for classification and regression will be used, since they are instance-based methods and don't build a model.

4 Conclusion

In this paper we demonstrated an approach for noise reduction implemented in the domain of ecological data. The described approach employed stochastic optimization algorithm, Genetic Algorithm (GA) – widely used evolutionary algorithm, in order to delimit dataset into subsets by defining time-window that is representative for a time period under consideration. The GA's criterion for optimization was maximization of Index of Agreement [11] as a performance metric of learned model by M5P algorithm for inducing model trees [10]. The results of case study of La Jaillière (France) experimental site shows that defining time-window and optimizing its length increases the performance of the learned model for prediction or classification by reducing the noise caused by some non-systematic and non-measured variable that influence the value of the target variable over time. Finally, this approach has additional advantages when lazy learning methods for classification and prediction will be applied, since they are instance-based and don't build a model.

References:

- [1] C. A. Peters. Statistics for analysis of Experimental data. Chapter in *Environmental Engineering Processes Laboratory Manual*, AEESP, Champaign, Illinois, 2001.
- [2] J. Han and M. Kamber. *Data Mining: Concepts and techniques*. Morgan Kaufmann Publishers, 2000.
- [3] R. Durrett. *Probability: Theory and examples, 4th Edition*. Cambridge University Press, 2004.
- [4] FOCUS. FOCUS - surface water scenarios in the EU evaluation process under 91/414/EEC. SANCO/4802/2001-rev2, 2001.
- [5] F. Branger, S. Debionne, P. Viallet, I. Braud, M. Vauclin. Using the LIQUID framework to build an agricultural subsurface drainage model. In *Proceedings of the 7th International Conference on Hydroinformatics*, Nice, France, 2006.
- [6] M. Mitchell. *An introduction to genetic algorithms*. Cambridge, MA: MIT Press, 1996.
- [7] K. A. De Jong. *An analysis of the behaviour of a class of genetic adaptive systems*, PhD Thesis. University of Michigan, 1975.
- [8] D. E. Goldberg. *Genetic algorithms in search, optimization, and machine learning*. Addison-Wesley, 1989.
- [9] A. E. Eiben. Genetic algorithms with multi-parent recombination. In *Proceedings of the International Conference on Evolutionary Computation. The Third Conference on Parallel Problem Solving from Nature*, Jerusalem, Israel, 1994.
- [10] J. Quinlan. Learning with continuous classes. In *Proceedings of 5th Australian Joint Conference on Artificial Intelligence '92*, Tasmania, Australia, 1992.
- [11] C. J. Willmott. On the validation of models. *Physical Geography*, 2(2):184-194, 1981.
- [12] D. R. Legates and G. J. McCabe. Evaluating the use of "goodness-of-fit" measures in hydrologic and hydroclimatic model validation. *Water Resources Research*, 35(1):233-241, 1981.

For wider interest

In this paper we demonstrated an approach for noise reduction implemented in the domain of ecological data. The described approach employed stochastic optimization algorithm, Genetic Algorithm (GA), in order to delimit dataset into subsets by defining time-window that is representative for a time period under consideration. The optimization means finding most optimal solution regarding the defined fitness function. In addition, the term stochastic describes that the process of optimization takes in account the uncertainty by including randomness. The results of case study of La Jaillière (France) experimental site shows that defining time-window and optimizing its length increases the performance of the learned model, which can be used for prediction or classification, by reducing the noise caused by some non-systematic and non-measured variable that influence the value of the target variable over time. Finally, this approach has additional advantages when lazy learning methods for classification and regression will be applied since they are instance-based and don't build a model. Namely, these methods consider the whole training set during prediction. Therefore, the bigger the train dataset is, the longer it lasts.

Gene function prediction for *Solanum tuberosum* from time-series gene expression data

Jurica Levatić^{1,2}, Živa Ramšak^{1,3}, Tjaša Stare³, Dragi Kocev¹, Kristina Gruden³, Sašo Džeroski^{1,2}

¹ Department of Knowledge Technologies, Jožef Stefan Institute, Ljubljana, Slovenia

² Jožef Stefan International Postgraduate School, Ljubljana, Slovenia

³ Department of Biotechnology and Systems Biology, National Institute of Biology, Ljubljana, Slovenia

jurica.levatic@ijs.si

Abstract. In this study, we employed machine learning techniques to predict the biological functions of genes. Gene function annotation still remains one of the key challenges in modern biology. Such knowledge is essential for the understanding of complex biological systems. Machine learning models were trained on time-series microarray gene expression data, measured for 17,318 *Solanum tuberosum* (potato plant) genes capturing the response of the plant to viral attack. Preliminary verification of de-novo predicted gene functions, performed by our biological collaborators, indicates promising results. This suggests that combining data mining with the microarray expression data and the GoMapMan ontology of gene functions has the potential to elucidate new unknown actors in the potato defense against pathogens and improve the knowledge on the functions of these unknown actors.

Keywords: gene function prediction, *Solanum tuberosum*, potato, hierarchical multi-label classification

1 Introduction

Functional genomics is the field of science concerned with using the vast amount of genomic data (e.g., DNA-sequence microarray-derived expression levels) in order to describe the functions and interactions between genes and proteins. A central task of functional genomics is to establish the functions of genes, i.e., to assign the specific biological or biochemical functions (roles) to genes for which this information is unknown. Traditionally, this is done by conducting wet-lab experiments. However, this

laborious job has been recently approached from another perspective: Gene function prediction can be considered as a classification problem, where machine learning techniques can generate predictions of gene functions and guide laboratory experiments in the annotation process. With recent advances in high-throughput biotechnologies, such as the measurement of time course gene expression profiles with microarrays, large amounts of biological data are generated at high rate. These data are a rich source of information for deducing and understanding gene functions, and are readily used by the machine learning community. In particular, gene expression data have been successfully used for inferring functions of genes, assuming that genes with similar expression patterns have similar biological function [1].

Utilizing machine learning techniques for predicting the functions of genes is currently an important and popular topic, where various techniques have been applied, such as Bayesian networks [2] or Support Vector Machines [3]. This problem has been recently approached from the perspective of *hierarchical multi-label* classification (HMC) [3, 4]. The HMC paradigm deals with classification problems where each instance can have more than one class (multiple labels) and classes are organized in a hierarchical fashion (an example that belongs to some class automatically belongs to all of its superclasses).

The task of gene function prediction is intrinsically a HMC task, since (1) each gene can have more than one function and (2) classes (gene functions) are typically organized in a hierarchy. Promising results from recent studies [3, 4] show that a HMC approach could be particularly suitable for the problem of gene function prediction. Better performance (in terms of classification accuracy, model complexity and computational efficiency) can be achieved with approach designed to deal with the task of HMC directly than by converting the HMC problem into the form convenient for common machine learning algorithms: Inducing a separate model for each class, thus ignoring the hierarchical structure. The objective of our work is to develop a predictive model for the annotation of potato genes by using time-series gene expression data that capture the response of the plant to viral attack in the context of hierarchical multi-label classification (HMC).

The remainder of the paper is organized as follows. The microarray gene expression data are presented in Section 2, followed by a description of the classification methods

and the evaluation measures in Section 3. The experimental results are presented in Section 4. Finally, the conclusions are given in Section 5.

2 Microarray gene expression data

The technique of DNA microarrays is capable of monitoring the expression levels of thousands of genes simultaneously. Usually, the same set of genes is monitored under different experimental conditions (e.g., diseased vs. healthy organism). The aim is to identify the genes that are most active in performing the functions of the living organism which are the subject of interest, such as the immunological response triggered by virus infection.

2.1 Description of the dataset

Potato Oligo Chip Initiative (POCI) microarrays were used to perform gene expression analysis of 37,865 genes in potato leaves. The dataset consists of time series of gene expression level measurements capturing the potato plant response to viral attack. The measurements were taken under six different conditions, considering two different potato varieties, upper and lower leaves, and healthy/infected plants. Each expression pattern is a sequence of 6 (bottom leaves) or 9 (upper leaves) data points, i.e., measurement of gene expression level at days: 0, 1, 3, 4, 5, 7 (bottom leaves) and additionally at days 8, 9 and 11 for upper leaves. In total, each gene is described with 42 numerical features.

The target, i.e., the biological function of a gene, takes values from the GoMapMan Ontology tree [5], which is an extension of the plant-specific MapMan [6] ontology. Particular values of the target (classes) correspond to specific paths in the GoMapMan tree. For example, two genes can be assigned the classes *Photosynthesis/lightreaction/ATP synthase* and *Photosynthesis/photo-respiration/glycolate_oxidase*, the hierarchical structure of which is illustrated in Figure 1. Each gene can have multiple functions that correspond to paths in the ontology tree, hence this is a ‘multi-label’ hierarchical classification problem.

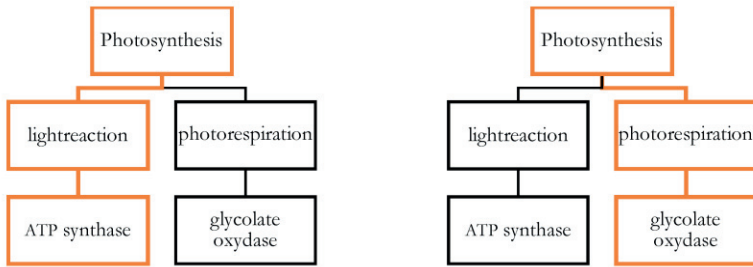


Figure 1. The class values of two example genes, coming from the hierarchical tree structure of the GoMapMan Ontology [5].

Of the 37,865 genes in the dataset, 17,318 have known annotations and were used to train classifiers. For the remaining 20,547 genes, no annotation is known. Ultimately, these are the genes to which we aim to apply the developed classification models and predict their biological function.

The genes with known annotation can belong to 838 different classes. The frequency of these classes ranges from 0.2352 to 0.0001, with many small, less frequent classes (Fig. 2). Such a setting with a large number of classes with an imbalanced distribution

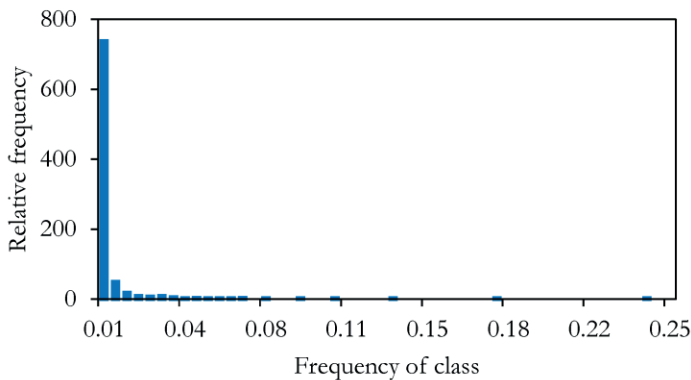


Figure 2. The histogram of class frequencies shows that the distribution of gene functions (classes) is very imbalanced. The majority of classes have low frequencies, which poses a difficulty for most machine learning algorithms.

is typical for the task of gene function prediction. This poses an additional difficulty for machine learning algorithms, which are often biased towards frequent classes. Bearing

in mind that small, infrequently occurring classes (i.e., biological functions) are often the ones the biological community is most interested in, the former issue is especially relevant.

3 Classification methods and evaluation measures

3.1 Decision trees for hierarchical multi-label classification

Gene function prediction is intrinsically a hierarchical multi-label classification problem; therefore, it is natural to choose machine learning methods capable of dealing with this type of classification task. We used decision trees for HMC, as implemented in CLUS decision tree and rule learning system [4]. In particular, we build ensembles of decision trees (CLUS-HMC ENS) [7]. Ensembles of decision trees were successfully used before to predict functions of genes [7].

The ensemble is a set of predictive models, where the prediction for a new instance is obtained by combining the predictions of all base models: A set of diverse predictive models (making different errors on new examples) achieves better predictive performance than its individual members. There are several ways to build an ensemble of trees, such as Bagging or Random Forests, both of which are implemented in CLUS-HMC ENS. In this work, we used the Random Forest [8] approach. The predictions from such a random forest of HMC trees come in the form of probabilities for each of the classes in the hierarchy: A threshold is applied to make specific class predictions.

3.2 Evaluation measures

In functional genomics, it is often the case that individual classes have a few positive instances, that is, typically only a few genes have a particular function. Since the size of the class is not necessarily correlated to its interestingness (i.e., small classes can be more interesting than large ones), we are more interested in correctly classifying positive instances than correctly classifying negative instances. In other words, we want to predict that a gene has a certain function rather to predict that it doesn't. In such a setting, common evaluation measures, such as accuracy or ROC curves, can give overly optimistic evaluation because they reward correctly classified negative instances.

In this work, we opted to use measures based on precision-recall curves (PR curves), obtained by varying the classification threshold. We believe these measures are more

suitable with respect to the earlier discussion, and, besides that, allow evaluation of the models independent from a classification threshold. Precision and recall are defined as follows:

$$Prec = \frac{TP}{TP + FP} \quad (1)$$

$$Rec = \frac{TP}{TP + FN} \quad (2)$$

where TP, FP and FN are the numbers of true positives, false positives and false negatives, respectively. A PR curve is the plot of the model's precision as a function of its recall when varying the classification threshold from 0 to 1. As in the case of ROC curves, the area under the precision-recall curve (AUPRC) is used to summarize PR curve into the single numerical value convenient for comparison of performance among different models.

4 Experimental results

In this section, we present the experimental results. We trained the ensembles of HMC trees on the dataset consisting of gene expression data for 17,318 genes with known annotations. For model evaluation, we used the procedure of 10-fold cross validation. The parameter settings for CLUS-HMC ENS were as follows: The size of the random forest was set to 100 trees and the number of attributes to consider in each internal tree node to $\lfloor \log_2 N \rfloor + 1$, where N is the total number of attributes (i.e., gene expression measurements per gene, $N = 42$).

By examining class-wise predictive performances (Fig 3.), we can make several observations. Notably, a certain heterogeneity in class-wise performance exists, i.e., some classes are modelled considerably better than others, with an overall trend of increase of per-class AUPRC with class frequency. A large number of less frequent biological functions could not be predicted correctly. However, we can make a considerably large selection of those classes for which the random forest of the trees was quite successful. In Table 1, we present the top 10 most-accurately modelled classes (with largest AUPRC). For practically relevant predictions, the application of our predictive model should be narrowed down from the entire set of 838 possible

biological functions in the training set, to the classes where the model yields good performance.

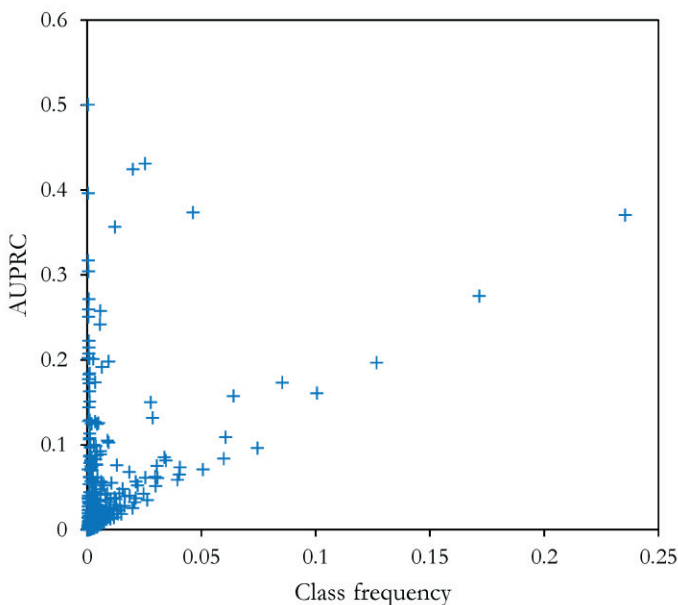


Figure 3. The class-wise AUPRC vs. class frequency plot reveals several characteristics of the results. Overall, the frequent classes are modelled better, but a considerable number of smaller classes are also modelled successfully.

The predictions for the genes with the known function were inspected to select an appropriate value of the classification threshold (i.e., the threshold applied to probability score given by the CLUS-HMC ENS) relevant for biological functions. Different thresholds seem to be appropriate for different classes. For most, however, 0.3 seems to be reasonable, not introducing too many false positives or false negatives among the predicted functions of genes.

We applied the developed model to generate functional predictions for 20,547 genes for which their biological role is unknown. The predictions were submitted to our biological collaborators at National Institute for Biology for verification. Their preliminary inspection revealed that the selected threshold works really well for

predicting the function of genes assigned to the ‘biotic stress’ and partially for the ‘photosynthesis’ classes. These are the processes that change the most after viral infection: Thus, the experimental dataset contained information mostly related to these classes. On the other hand, the selected threshold doesn’t work so well with the ‘RNA’ class. This suggests that, to get best results, the thresholds for the individual classes should be optimized relative to the precision-recall curve.

Table 1. Top 10 classes most-accurately predicted by the random forest ensemble. Some paths in the class hierarchy are predicted better than others, namely classes with ‘protein’ or ‘photosynthesis’ at their root function hold 6 among the top 10 positions. Note that ‘/’ represents a new hierarchy level.

Class	Frequency	AUPRC
Minor CHO metabolism/myo-inositol/InsP synthases	0.0002	0.51
Photosynthesis	0.0199	0.42
Protein/synthesis/misc ribosomal protein	0.0252	0.42
Signalling/receptor kinases/legume-lectin	0.0002	0.40
Protein	0.2352	0.37
Protein/synthesis	0.0463	0.37
Photosynthesis/lightreaction	0.0120	0.34
Photosynthesis/calvin cycle/RPE	0.0003	0.29
RNA	0.1715	0.27
minor CHO metabolism/trehalose/TPP	0.0004	0.26

5 Conclusions

Characterizing gene functions has become one of the major challenges in the post-genomic era. The traditional approach for the assessment of biological function of genes includes laborious and time-consuming wet-lab experiments. However, machine learning techniques can generate predictions of gene functions and guide laboratory experiments in the annotation process. In particular, hierarchical multi-label classification approaches are suitable for solving such task. In this work, we used decision tree ensembles for HMC as implemented in CLUS system to develop a model

for potato gene function prediction. The results exhibit heterogeneous class-wise performance, but a considerable selection of biological functions where random forests of HMC trees was successful can be made. We applied the learned model to predict biological function for 20,547 potato genes with unknown function. Preliminary inspection by domain experts confirmed that the model can yield correct predictions of certain biological functions. However, to obtain more accurate results, the classification threshold in CLUS-HMC ENS should be optimized for each individual class.

In the future we plan to continue the collaboration with the biologists at the National Institute for Biology with the aim of using machine learning techniques to help elucidate biological knowledge about immune response processes in potato. Furthermore, we expect that the predictions should improve if more experimental data is used to learn the models, such as information about functional domains (INTERPRO) presence in the genes.

References:

- [1] X. Zhou, M. C. J. Kao, and W. H. Wong. Transitive functional annotation by shortest-path analysis of gene expression data. In *Proceedings of the National Academy of Sciences*, 99(20):12783–12788, 2002.
- [2] O. G. Troyanskaya, K. Dolinski, A. B. Owen, R. B. Altman, and D. Botstein. A Bayesian framework for combining heterogeneous data sources for gene function prediction (in *Saccharomyces cerevisiae*). In *Proceedings of the National Academy of Sciences*, 100(14):8348–8353, 2003.
- [3] Z. Barutcuoglu, R. E. Schapire, and O. G. Troyanskaya. Hierarchical multi-label prediction of gene function. *Bioinformatics*, 22(7):830–836, 2006.
- [4] C. Vens, J. Struyf, L. Schietgat, S. Džeroski, and H. Blockeel. Decision trees for hierarchical multi-label classification. *Machine Learning*, 73(2):185–214, 2008.
- [5] GoMapMan Ontology Tree. <http://www.gomapman.org/ontology>, 2013
- [6] MapMan. <http://mapman.gabipd.org>, 2013
- [7] L. Schietgat, C. Vens, J. Struyf, H. Blockeel, D. Kocev, and S. Džeroski. Predicting gene function using hierarchical multi-label decision tree ensembles. *BMC bioinformatics*, 11(1):2, 2010.
- [8] L. Breiman. Random forests. *Machine learning*, 45(1):5–32, 2001.

For wider interest

Deoxyribonucleic acid or DNA can be considered as a book of life, where all the information needed for the development and functioning of living beings is written. The smallest meaningful sentences of this book are called genes. Genes are the blueprints for building essential ingredients of life and hold the genetic traits passed to offspring.

One of the central challenges of modern biology is to understand the biological roles of particular genes in the organism. For example, certain genes determine the colour of our eyes, while some of them are included in the immunological response to viral infection. Such functions can be determined experimentally, but this is time-consuming, laborious and expensive task. However, on the other hand, machine learning techniques can be used to guide laboratory experiments. Such methods can learn from experimental biological data and predict the biological functions of genes. We used measurements of expression levels for 17,318 potato genes, following response of plants to viral attack, to build computational model for potato gene function prediction. With the learned model, we generated predictions for 20,547 potato genes with previously unknown biological function.

Preliminary inspection of the predictions by a domain experts showed that we were able to correctly predict certain biological functions, mainly the ones which change the most after viral infection. We can conclude that machine learning approaches have the potential to improve the knowledge about potato defence against pathogens and plant genetics in general.

Network Coding Aware Routing for Performance Boost in Wireless-Mesh-Networks

Erik Pertovt^{1,2}, Kemal Alić^{1,2}, Aleš Švigelj^{1,2}, Mihael Mohorčič^{1,2}

¹ Department of Communication Systems, Jožef Stefan Institute, Ljubljana, Slovenia

² Jožef Stefan International Postgraduate School, Ljubljana, Slovenia

erik.pertovt@ijs.si

Abstract. Network Coding (NC) is a novel technique for enhancing the performance of Wireless Mesh Networks (WMNs) by increasing the network throughput. NC aware routing further increases the possibility of benefiting from NC procedures; traffic is routed taking into account new coding opportunities identified along the path, resulting in further increase of network throughput. In this paper, a new NC aware routing metric is proposed in which congested nodes are detected using the nodes coding gain (CG) to prevent the network saturation. The results show that the proposed NC aware routing avoids node congestion, thus enabling higher network traffic loads compared to the conventional routing metrics used in combination with NC.

Keywords: Network coding, network coding aware routing, network coding aware routing metric, congestion, wireless mesh networks.

1 Introduction

In Wireless Mesh Networks (WMNs), nodes connect through multi-hop wireless links forming a wireless access/backbone network [1]. In order to improve the performance in multi-hop WMNs, various mechanisms can be used. Among the promising mechanisms, which have gained an increased attention in the past years, is network coding (NC). Instead of using “classical” receive and forward mechanism for packets in intermediate nodes, NC combines multiple received packets either from the same or from different traffic flows into one encoded packet and then forwards it to the next hops or destinations thus increasing the network capacity. In wireless networks, NC exploits the broadcast nature of the wireless medium, where nodes can overhear packets which are not destined to

them, resulting in new coding opportunities, which enable combining even more packets together. A practical NC procedure, referred to as COPE, was proposed in [2] and is widely used as a reference for NC in wireless mesh networks. It opportunistically transmits two or more encoded packets. Encoding is done based on the information available in the transmitting node on which packets neighbouring nodes have already received through opportunistic listening. However, further benefits and therefore the true potential of NC in the network layer can only be achieved by strong collaboration with routing procedure, rather than performing routing and coding independently [3, 4]. By applying NC aware routing [5], paths with more coding opportunities can be discovered, yielding modified routes along which more packets are being coded together. This results in using less bandwidth compared to NC unaware routing for transferring the same amount of traffic from source to destination. On the other hand, the information on node's coding successfulness can be used to prevent the saturation at the bottleneck nodes in the network, as more coding does not necessarily result in higher network throughput.

In this paper, a novel routing metric is proposed to prevent congestion at bottleneck nodes based on the coding successfulness of nodes and links. The novel metric is based on adopted expected transmission count (ETX) metric, which is a commonly used metric in WMN, and has showed good results also in combination with NC aware routing [6, 7]. Since the resulting procedure avoids links and nodes where congestion might occur we refer to it as congestion-avoidance coding-aware routing.

The rest of the paper is structured as follows. In Section 2, we first propose a new NC aware routing metric, which exploits the node and link coding gains (CGs) for preventing congestions. In Section 3, the new metric is evaluated using simulation. In particular, we compare COPE NC procedure with the proposed NC aware routing metric to the reference COPE with NC unaware ETX routing metric. In Section 4, we drew the conclusions and outline the future work.

2 Congestion-Avoidance Coding-Aware Routing

NC aware routing can be used for discovering additional coding opportunities and congestion avoidance. In this section, we propose a NC aware routing based on congestion-avoidance coding-aware routing metric. ETX based metric enhanced with the link CG and node CG information avoids routes with congested nodes, which indicate the presence of network bottlenecks.

Based on results, presented in [8], we designed a novel additive metric defined as follows:

$$Cost_{ij} = \begin{cases} ETX_{ij} + \left(\frac{g_{ij} + g_{ji}}{2} - G_{thr} \right) & , G_j \geq G_{thr} \\ ETX_{ij} & , G_j < G_{thr} \end{cases} \quad (1)$$

where $Cost_{ij}$ is metric cost for a link connecting the sender i to the receiver j , as shown in Figure 1. ETX [9] is the well-known expected transmission count metric, which reflects the effect of link loss ratios. It is defined as:

$$ETX_{ij} = \frac{1}{d_{ij} \cdot d_{ji}} \quad (2)$$

where d_{ij} is probability of successful packet transmission from the sender i to the receiver j , and d_{ji} is probability that acknowledgement for the received packet (from the receiver j) has been successfully received at node i . G_j is the measured CG [2, 8] of node j , defined as the ratio between the number of source packets $N_{S,j}$, routed by the node j without coding, and the number of packets $N_{C,j}$, required to send source packets with coding:

$$G_j = \frac{N_{S,j}}{N_{C,j}} \quad (3)$$

Based on the definition of G_j , we define the measured CG for the link ij as a ratio between the number of source packets $n_{S,ij}$, which are transmitted from the

sender i to the receiver j , and the number of packets $n_{C,ij}$ required to transmit all the source packets $n_{S,ij}$ from the sender i to the receiver j using NC:

$$g_{ij} = \frac{n_{S,ij}}{n_{C,ij}} \quad (4)$$

Similar, the measured link CG for link ji is denoted by g_{ji} .

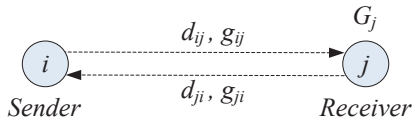


Figure 1: Link between nodes i and j with reference terms.

Parameter G_{thr} is a constant value and at this point has to be tuned for a particular network – the choice of this value is based on the results of node CG and experience with a variety of previous simulations. It represents the boundary from which the effect of the link and node CGs affect on the proposed routing metric calculation. If G_j is lower than G_{thr} , the proposed metric cost of a link ij is equal to ETX_{ij} . If G_j is higher or equal to G_{thr} , additional term is added to ETX_{ij} , which represents the influence of measured CGs on links ij and ji . With this, nodes with high G and links with higher g , will be disfavoured.

In [8], high G of a node indicates that the node is handling a very high traffic and can become or already is congested, while nodes with lower G can still handle more traffic. Therefore, a portion of traffic routed through nodes with high G should be redirected to nodes with lower G , possibly lower than G_{thr} , in order to distribute the load more evenly across the network. When G of a node is too high (G of a node higher than G_{thr}), we distinguish also between different node links regarding the coding gain information. We indirectly consider the traffic intensity from the observed node j to its neighbour i via g_{ji} and the traffic intensity from the neighbour i to the observed node j via g_{ij} . With the latter, we consider also

the intensity of the neighbour congestion, which should also be kept low; a neighbour of node j (i.e., node i) with high traffic (high g_{ij}) should avoid using the link ij to a congested node more than a neighbour i with low traffic (low g_{ij}).

The proposed metric determines wireless link costs, which are then used by the routing algorithms such as Dijkstra and Bellman-Ford algorithms to find the shortest paths between various source-destination pairs.

3 Simulation Parameters and Performance Evaluation

In this section, we present the simulation results for different routing metrics using random topology shown in Figure 2. We compare the performance of COPE using the proposed NC aware metric and COPE using ETX metric. In addition, the results for reference scenario (ref. sc.), where NC is not used, are presented. Simulations were conducted in the WMN NC simulation model [10], developed in the OPNET Modeler [11] simulation tool.

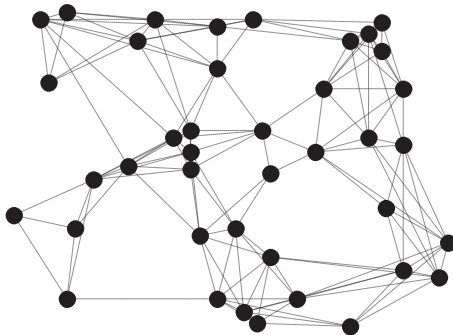


Figure 2: Network topology with 40 wireless nodes.

The investigated network consists of 40 wireless nodes placed on 1 km x 1 km. Each node transmits at 2 Mbit/s. Wireless connections established between neighbours, which are represented in the network topology as wireless links, are graphically presented in Figure 2 with dashed lines between nodes. Packet delivery probabilities of wireless links are between 70% and 100% meaning that packets can get lost during transmissions. Moreover, packets on wireless links are delayed due

to propagation through wireless medium. All nodes have the same configuration representing homogeneous network. Traffic load is generated on all nodes with the same intensity using exponential distribution of inter-arrival times and constant packet lengths (i.e., 10 kbit). Destination nodes are selected using uniform probability distribution among all network nodes. Every simulation run took 330 seconds and results were collected during 250 seconds of steady traffic conditions – from the 70th second to 320th second. Routing was performed using Dijkstra algorithm and routing tables were updated every 30 seconds from the 10th second on. Following initial investigation the preliminary results shown in this paper were obtained for G_{thr} in (1) set to 1.25, for each wireless node in the network. More detailed investigation of the impact of this parameter is planned as future work.

In Figure 3, the average packet delay (between source and destination nodes) and the network goodput in dependency of network load are presented for three scenarios: a) COPE NC procedure with the proposed NC aware ETX-based routing metric, b) COPE NC procedure with NC unaware ETX routing metric, c) no-NC scenario (ref.sc.) with ETX routing metric. The network goodput is the application level throughput and represents the amount of useful data delivered by the network per unit of time, while the network throughput accounts also other traffic from lower layers below the application layer such as protocol overheads and any retransmission.

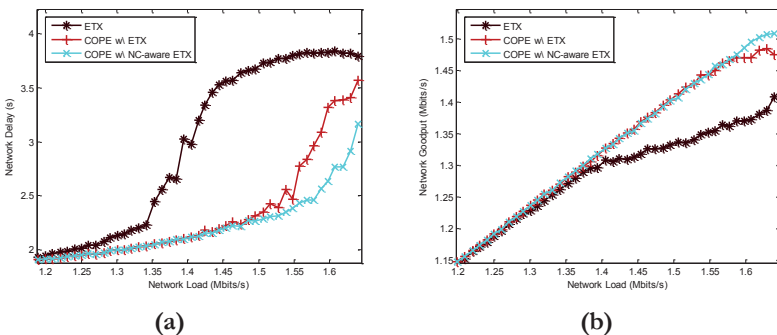


Figure 3: Network delay (a) and goodput (b) in dependency of network load for different routing scenarios.

The results show that COPE with the proposed NC aware routing metric can handle the highest given traffic load, while ref. sc. without NC can handle the lowest load. The proposed congestion-avoidance coding-aware routing metric also reduces network delay. The benefit of using this metric becomes notable with loads higher than 1.5 Mbit/s. By increasing the load, the difference becomes even more notable. Figure 4 indicates the measured CG G for each node during the 9th and 10th routing table update. The cases are for COPE with ETX in Figure 4.a and COPE with the proposed NC aware metric in Figure 4.b. We can see that the node in the middle of the graph has the highest G . It is also the bottleneck of the network. Moreover, this node has higher G with ETX metric. This is because the congestion on the node is detected with the proposed NC aware metric based on the too high G of the node compared with G of other nodes in the network. A part of the traffic traversing this node is thus put on other routes, which do not cross the congested node. With this, the node is released from such high traffic, which caused the congestion and network saturation.

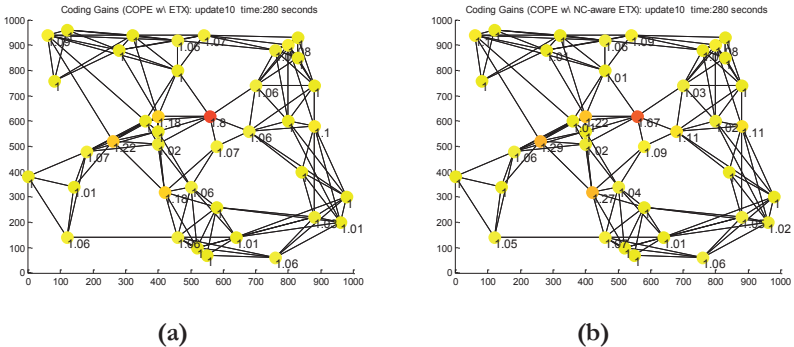


Figure 4: Measured CG G for each node: (a) COPE with ETX metric, (b) COPE with the proposed NC aware metric.

We can conclude that NC aware routing notably improves the NC procedure performance. We also showed that the accurate use of NC information in strong collaboration with routing, to prevent congestions in the network, improves the overall network performance.

4 Conclusion and Further Work

In this paper, we have proposed a novel congestion-avoidance coding-aware routing metric in order to redirect load from nodes handling the highest loads to nodes handling less load, yet still making use of identified network coding opportunities. The proposed metric is based on the measured CG information. The results show that NC supported by NC aware routing in WMN networks further improves the network performance compared to NC unaware routing. This exhibits in increased network throughput and lower average packet delays. Our future work is focusing on further investigation of the proposed NC aware routing metric. Special attention will be given to such traffic redirection that will create or improve coding opportunities. Proposed metric should re-route traffic that is likely to code rarely and should prefer traffic that is likely to get coded along the route.

References:

- [1] I. F. Akyildiz, X. Wang, "A survey on wireless mesh networks," *IEEE Communication Magazine*, vol. 43, no. 9, pp. S23-S30, September 2005.
- [2] S. Katti, H. Rahul, W. Hu, D. Katabi, M. Médard, and J. Crowcroft, "XORs in the Air: Practical Wireless Network Coding," *IEEE/ACM Transactions on networking*, vol. 16, June 2008.
- [3] E. Pertovt, K. Alič, M. Mohorčič, A. Švigelj, "ETX-based Metrics and Adapted Routing Algorithms for Network Coding," in *20th Electrotechnical and Computer Science Conference (ERK 2011)*, Portorož, Slovenija, September 2011.
- [4] J. Le, JCS Lui, D-M. Chiu, "DCAR: distributed coding-aware routing in wireless networks," *IEEE Transactions on Mobile Computing*, vol. 9, no. 4, pp. 596-608, April 2010.
- [5] M. A. Iqbal, B. Dai, B. Huang, A. Hassan, S. Yu, "Survey of network coding-aware routing protocols in wireless networks," in *Journal of Network and Computer Applications*, vol.34, no. 6, pp. 1956-1970, August 2011.
- [6] L. Yifei, S. Cheng, X. Qin, T. Jun, "ICM: a novel coding-aware metric for multi-hop wireless routing," *5th International Conference on Wireless Communications, Networking and Mobile Computing (WiCom '09)*, September 2009.
- [7] B. Ni, N. Santhapuri, Z. Zhong, S. Nalakuditi, "Routing with opportunistically coded exchange in wireless mesh networks," *IEEE workshop on wireless mesh networks (WiMesh '06)*, September 2006.
- [8] K. Alič, E. Pertovt, A. Švigelj, "Network topologies and traffic distribution evaluation for network coding," *IARA Netware 2012*, Roma, Italy, August 2012.
- [9] D. S. J. De Couto, D. Aguayo, J. Bicket, R. Morris, "A high-throughput path metric for multi-hop wireless routing," *9th ACM International Conference on Mobile Computing and Networking (MobiCom '03)*, San Diego, California, September 2003.
- [10] K. Alič, E. Pertovt, A. Švigelj, "Simulation environment for network coding," in *Mosharaka International Conference on Communications, Networking and Information Technology (MICCNIT 2011)*, Dubai, UAE, 2011.
- [11] OPNET web page, available at <http://www.opnet.com/>, accessed May 2010.

For wider interest

Wireless mesh networks are typical representatives of wireless access/backbone networks, where nodes such as wireless (WiFi) routers, are highly connected to each other through multi-hop wireless links enabling access to the Internet. Various mechanisms exist to improve the performance in multi-hop wireless mesh networks. Among the promising mechanisms, which have gained an increased attention in the past years, is wireless network coding. Network coding enabled node combines multiple packets from the same or from different traffic flows into one encoded packet and forwards it to the next node along the way to the destination, where original packets are recovered making use of several encoded packets, thus increasing the network capacity. In wireless networks, network coding exploits the broadcast nature of the wireless medium, where nodes can overhear packets which are not destined to them, resulting in new coding opportunities, which enable combining even more packets together. Further benefits and therefore the true potential of network coding in the network layer can be achieved with routing metrics and algorithms that are aware of coding opportunities that arise when an individual path is selected as a route. Applying network coding aware routing, paths with more coding opportunities can be discovered resulting in modified routes where more packets are being coded together, thus using even less bandwidth compared to network coding unaware routing for transferring the same amount of traffic from source to destination. On the other hand, the information on node's coding successfulness can be used to prevent the congestion at the bottleneck nodes in the network as more coding does not necessarily result in better network throughput. Therefore, we propose a novel congestion-avoidance coding-aware routing metric. It routes packets so as to avoid congested nodes based on the information of measured node coding gain, assuming that higher coding gain may indicate that traffic on that node is too high and node should be avoided. Using computer simulation we show that the proposed metric with network coding performs better than the existing (conventional) coding-unaware ETX routing metric with network coding.

Learning bagged models of dynamic systems

Nikola Simidjievski^{1,2}, Ljupco Todorovski³, Sašo Džeroski^{1,2}

¹ Department of Knowledge Technologies, Jožef Stefan Institute, Ljubljana, Slovenia

² Jožef Stefan International Postgraduate School, Ljubljana, Slovenia

³ Faculty of Administration, University of Ljubljana, Slovenia

nikola.simidjievski@ijs.si

Abstract. In this paper, we present an ensemble learning method for modeling dynamic systems. The method is a combination of the bagging approach to ensemble learning and the approach of inductive process modeling of dynamic systems. We illustrate the use of the proposed method on the task of modeling phytoplankton growth in Lake Bled.

Keywords: dynamic systems, dynamic modeling, equation discovery ensembles, bagging, aquatic ecosystems

1 Introduction

Experts construct mathematical models to describe and predict the behavior of dynamic systems under various conditions. Such models are often formulated as ordinary differential equations (ODEs), which describe the change of the state of the system over time. Constructing a model is a cascade process using knowledge and measured data about the observed system and integrating these together with the laws of nature into an understandable pattern. Two major paradigms for constructing models of dynamic systems exist: (1) theoretical (knowledge-driven) and (2) empirical (data-driven) modeling. In the first approach, domain experts derive a mathematical (ODE) model structure of a system, the parameters of which are calibrated using the measured data. The second approach uses the measured data to search for the best combination of model structure and parameters which most adequately fits the task. This paradigm is used by machine learning approaches to modeling dynamic systems.

Within the area of computational scientific discovery, equation discovery systems [1] have emerged that use observation data to determine both the model structure and parameter values. The state-of-the-art equation discovery techniques [6] integrate both the theoretical and the empirical approaches to modeling dynamic systems. They use process-based domain knowledge, which describes the entities and processes that may occur in the particular system. The ability to use such knowledge has proven to be the key factor for the success of such systems.

Another machine learning paradigm that we draw upon is the paradigm of ensemble learning. In machine learning, ensemble learning methods [3] build combinations of multiple predictive models (ensembles) to maximize the predictive performance of the system. An ensemble learning method is a supervised learning technique which combines several base models and improves the overall predictive outcome representing a single model and minimizes the over-fitting of the data. Ensembles are employed mostly in the context of solving classification and regression tasks. In this paper, we focus on adapting them to the task of modeling dynamic systems. To the best of our knowledge ensembles of dynamic system models have not yet been considered in the machine learning community and addressed in this context.

We adapt the traditional approach to ensemble learning, i.e. bootstrap aggregation [4], to solve the task of learning ensembles of dynamic models from observation data. We also aim to evaluate the performance of this kind of ensembles of ODE models in comparison to “classical” individual ODE models. The individual models and the components of the ensembles derived with the process-based modeling automated approach. The remainder of this paper is organized as follows. Section 2 describes the bootstrap aggregation ensemble learning algorithm and its adaptation to the context of building ensemble models of dynamic systems. Section 3 gives an introduction to automated modeling of dynamic systems, focusing on inductive process modeling and recent contribution in this area, i.e., the ProBMoT system. Section 4 describes the experimental setup and discusses the results of the experimental evaluation. For the experimental evaluation, a case study from the domain of modeling aquatic ecosystems domain is considered, where the aim is modeling phytoplankton concentration in Lake Bled, Slovenia. Finally, Section 5 summarizes the conclusions of this paper.

2 Bagging of ODE models

Several practical and theoretical studies clearly state that an ensemble of models gives better performance than the best single model [2]. While ensembles of models for other machine learning tasks are widely used [3], learning ensembles of ODE models has not been considered. So far several approaches can be considered to address this challenge, using state-of-the-art techniques for learning different models from different data samples. For example, such approach considers using contiguous sections of the observed data with randomly selected starting points and duration. Adapting existing sampling methods requires more care and it is discussed below.

BAGGING (Bootstrap aggregation) [4] developed by Breiman et.al is one of the first and simplest ensemble learning techniques. This technique uses bootstrap sampling. Data instances are sampled uniformly with-replacements to obtain bootstrap replicates of the training data. Each base model is learned from one bootstrap replicate. The models are combined afterwards by averaging the output (regression) or by voting (classification). This method successfully overcomes the over-fitting problem, but is not useful for linear models or in general with base models that only changes a little for small changes in the training data. Bagging has no memory, and can be parallelized to handle different replicates on different CPUs, which performance-wise is very useful [11].

Unlike the traditional methods for data sampling, where part of the data is used for training the different models, which are combined into an ensemble afterwards; here we consider time point error weighting as a method for sampling. The classical approach of generating bootstrap samples for a building ensemble models for common classification task, includes generating samples from random data instances in the training set. By uniformly sampling with replacements, it is very likely that some of the instances will repeat, and there of generating m different training sets with size same as the original training set. Furthermore, every sample is used in the learning algorithm, thereof learning m different model classifiers which will participate in the ensemble.

On the other hand, our approach differs in the sampling process from the classical approach. Mainly, for performing bagging, we choose uniformly random time points

from the time series, and by assigning weights to each of them we are adapting the technique of generating bootstrap replicas in the context of time-series. The values in the weighting set vary in the interval from 0 to any positive integer, as long as the sum of the values in the set normalizes to the size of the dataset. By using this technique we can emphasize different time-points, thus replicating the effects of bootstrap replicas. In the learning phase this technique is used along with a particular objective function Weighted Root Mean Squared Error (WRMSE):

$$WRMSE = \frac{1}{\sum_{t=0}^n w_t} * \sqrt{\frac{\sum_{t=0}^n w_t * (y_t - \hat{y}_t)^2}{n}} \quad (1)$$

, where y_t and \hat{y}_t denote the observed and simulated values of the system variables, n denotes number of time-points in the observed data, w_t denote the weight at time point t . More precisely, penalizing (encouraging) different time points from each bootstrap replica.

3 Inductive Process Modeling & ProBMoT

Equation discovery is a machine learning sub-field, which by using observations, aims to determine the scientific laws that govern the dynamics of a given system and induce them in form of equations. Moreover, Inductive Process Modeling (IPM) [5] is an equation discovery approach, which takes into consideration the domain-knowledge along to the observations, and thus producing an explanatory process-based model. These models consist of two basic components: entities and processes. The entities represent the state/subject of the system, whereas the processes represent the interaction between the entities thus modeling the system dynamics.

From the mathematical point of view, the entities represent the variables involved in an interaction represented by the processes, which results in a set of differential and algebraic equations. This set of equations is the model of the dynamic system. The domain-knowledge is embodied in a form of a library of generic entities and generic processes that represent vague concepts of the particular domain. A search is performed through all possible model variants described in the library, resulting in a set of candidate models. Each candidate model is then used in the process of estimating parameter values. In this step, each of the candidate models is simulated

with a set of parameter estimates. The set for which the simulated trajectory is most adequate to the observed data is chosen to be the model parameters. Each of the models is sorted by their estimation function, i.e. sum of squared errors (SSE), and the model with the minimal error/best fit is chosen as an output of the algorithm.

ProBMoT [6] is software tool for complete modeling, parameter estimation and simulation of process-based models. ProBMoT follows the basic IPM paradigm and employs domain-specific modeling knowledge formulated in a library. Overlooking the definition of specific model structures, conceptual models are formulated from these templates, representing an abstraction of a whole class of models. Significantly, the main feature of the ProBMoT is the use of more specific constraints and rules which gives the ability of constructing more feasible models by allowing another (higher) level of conceptualization of the domain knowledge. The conceptual models are significant due to their transparency to the domain experts and the ubiquity among domains. Generating conceptual models, represents a task which involves spatial segregation of a system into a variety of discrete fragments (layers) with a different role in the system, as well as aggregation or differentiation among layer. These models define the system as set of components related between them, where each connection represents rule or an exchange of information, giving more logical representation of the modeled system. Using this approach, candidate models are created by applying all possible substitution rules that will represent descendant functional processes from the lowest level of the hierarchy.

The parameter estimation process is based on meta-heuristic optimization framework jMetal 4.3. [7] that implements a number of global optimization algorithms [8], this is to, avoid the fast convergence to a local-optimum when using local optimization algorithms. For simulating the candidate ODE models, ProBMoT employs the CVODE solver from SUNDIALS [9].

Basically, the process of parameter estimation resembles the one in IPM and follows the least-square approach for parameter identification, and tends to optimize a variety of quantitative objective functions. The most competitive advantage of the ProBMoT is the implementation of custom quantitative objective functions such as sum of squared errors (SSE), mean squared error (MSE), root mean squared error

(RMSE) and weighted RMSE (WRMSE) used for generating ensembles. Moreover this process has the ability to adapt to scenarios when models should be fitted on multiple observation datasets. This means, every chosen set of parameter estimates most sufficiently corresponds to every of the observation datasets. This process can be considered as a multi-objective optimization problem, but for most cases we translate it into a single-objective. The parameter set to be fitted can also include the initial values of the system.

In order to adequately meet the purpose of learning ensemble models of ODEs additional modifications of the ProBMoT were made. Basically, by tempering with the learning data, ProBMoT is able to generate diverse sets of output models which are considered as the members of the ensembles. Each of the models is fitted using the WRMSE function during the learning phase. The simulations of the member models are then combined into one by techniques such as averaging or weighted median, which represents the output of the ensemble model. The output model is again evaluated with the RMSE error function, thus providing a comparable measure of the performance of the ensemble to the single models in the evaluation process.

4 Experimental Evaluation

In this paper we address the task of learning ensemble models of nonlinear dynamic systems in the domain of aquatic ecosystems. More precisely, our case study is modeling the food-web dynamics of Lake Bled in Slovenia. The model includes three ecological variables represented as ordinary differential equations, i.e. phytoplankton concentration, dissolved phosphorus and zooplankton concentration. According to Atanasova et. al. [10] the dynamics of this ecosystem are severely complex, thus modeling this kind of system and obtaining acceptable results has proven to be a challenging task.

To completely reveal the effects of ensembles of ODE models and additionally to minimize the complexity of the modeled system, we focus on modeling just phytoplankton concentration, whereas the other two variables are assumed to be exogenous.

4.1 Datasets

The datasets used for these experiments were obtained from the Slovenian Environment Agency. The measurements consist of physical, chemical and biological data for the years from 1996-2002. All data was depth-averaged for the upper ten meters of the lake. Measurements were performed with a monthly frequency, and interpolated with cubic spline algorithm, thus obtaining supposable daily measurements. Each of the datasets consists of around 300 time points. For our experiment we used the datasets 1996-2001 for training the models and the 2002 dataset for evaluation.

4.2 Experimental setup

Using the process-based modeling formalism of ProBMoT we define a specific library describing the entities and processes involved in the dynamics of phytoplankton concentration variance. The library used is deduced from the complete library of aquatic ecosystem presented in [10], resulting in total of 128 candidate models. For the parameter estimation procedure we used Differential Evolution with rand/1/bin strategy, 1000 evaluations over a population space of 50 individuals. Our problem stated 20 parameters and 1 initial value eligible for estimation. We perform two experiments. In the first, we train single and use this as a baseline. In the second, we train an ensemble using the proposed bagging method with ten replicas and averaged output.

To evaluate the performance of the ensembles for this experiment we used the following setup, similar to the learning curve analysis, used in machine learning. At each iteration, we train a model on a combination of train data sets corresponding to measurements in the period from 1996-2001. The train model is then evaluated on a single data set corresponding to the 2002 measurements. In the first iteration, we use 2001 dataset for training. In each consequent iteration, we add one more preceding year to the combination of data sets used in the previous iteration (see the first column of Table 1). The performance of the models was evaluated using RMSE qualitative comparison.

4.3 Results

Table 1 summarizes the RMSE values for both the single model and ensemble model evaluation. As is stated before, several learning iterations were used for obtaining the Learning Curve (Figure1), each of them on a different subset of the training set. The results show the evaluation from the best models obtained. Mainly, presented here are the predictions from the best models in each iteration of the single model scenario, respectively only best models were considered in the process of generating the ensemble output. The ensemble output is generated, by averaging the predictions of each of the ten bootstrap replicas.

Table 1. Comparison of the test errors of a single model and an ensemble model obtained with bagging ten models

Train datasets (year)	Test dataset (year)	Single model	Ensemble Bagging/10/Average
'01	2002	1.252	2.359
'00,'01	2002	0.951	0.977
'99,'00,'01	2002	1.618	1.510
'98,'99,'00,'01	2002	1.624	1.536
'97,'98,'99, '00,'01	2002	1.672	1.635
'96,'97,'98,'99,'00,'01	2002	1.695	1.677

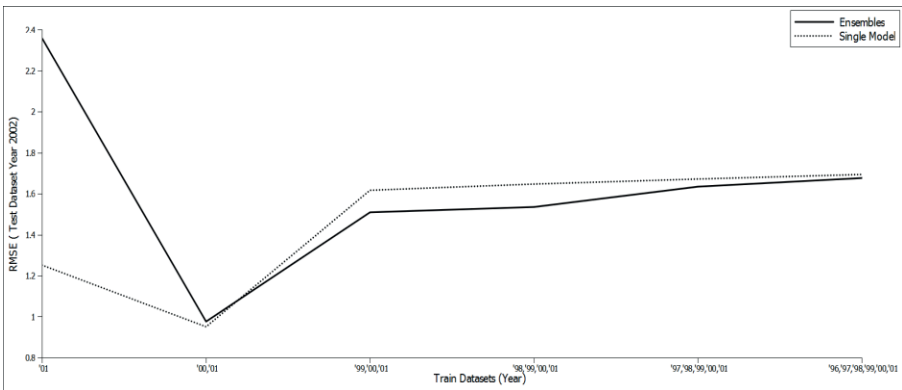


Figure 1. Learning Curve - Test errors of a single model and a bagged ensemble of ten models

4.4 Discussion

The results of the experiments show that the ensemble model performs slightly better on the given test data set than the single model. This slight increase in predictive performance comes at the cost of substantial increase in computational complexity.

This imposes two possible directions for improving the ensemble approach. We can overcome the high computational complexity of the ensemble approach by developing a parallel implementation which will bring the time required to build the ensemble close to the time required to build a single model. Second, we consider focusing on improving the ensemble model accuracy. According to Kuncceva et.al [12], model diversity can be a key-factor of the performance of the ensembles. Having this in mind, we will consider a different technique for sampling the training data. Instead of selecting random time points, we can select random time windows consisting of several contiguous time points. This sampling approach will preserve the dynamics present in the input data which is lost when sampling with random time points.

The shape of the learning curve can be explained by the fact that the complexity of the problems by year varies, i.e., the observation data sets are of different lengths and the dynamics of the modeled state differs from year to year. An interesting phenomenon that can be spotted from this experimental setup, is adding additional training data beyond the second year does not improve the predictive performance. Adding just one preceding year is sufficient for improving the performance of both the ensemble model and the single model on this particular case study.

These results uncover important characteristics of the ensembles approach. Moreover, they clearly point to important directions for future improvement of the performance of this methodology.

5 Concluding remarks and Further work

We address the task of learning ensembles of ordinary differential equation models of aquatic ecosystem dynamics. To this end, we extend the state-of-the-art approach for inductive process modeling. In particular, we adapted the ProBMoT, tool for automated process-based modeling, to the ability for generating diverse set of ODE models and their combination to an ensemble model. Additionally, we added the ability of leaning ODE models with custom designed objective functions and optimization techniques. These modifications are used to properly generate ensembles of dynamic models and evaluate their performance.

The case study considered is a model of phytoplankton growth in the Lake Bled in Slovenia, a complex nonlinear dynamic process part of the food-web dynamics of the lake. Our concern was generating an ensemble of diverse ODE models with the adapted bagging technique. The model considers one ecological variable from multiple observation data sets. Having this in mind, we considered a learning curve evaluation scenario. In summary, the results of our study show that ensemble models slightly improve the overall predictive performance.

The following possible directions for further work have been identified. First, the development of a methodology for increasing the diversity of the generated models by investigating different techniques for sampling the training set. Second, studying the model selection methods as a possible direction for improving the performance of the ensembles. In addition, experiments on other ecological domains can be performed, thus reaffirming the conclusions drawn in this paper. Moreover, adapting other state-of-the-art ensemble techniques in the context of ODE models, such as boosting, are to be investigated. Finally, we intent to examine domains other than ecological, thus extend the generality of our approach.

References:

- [1] L.Todorovski and S.Dzeroski. Integrating Domain Knowledge in Equation Discovery, *Computational Discovery of Scientific Knowledge* vol. 4660, (Springer Berlin, Heidelberg, 2007), pp. 69-97.
- [2] G. Seni and J.Elder. *Ensemble Methods in Data Mining: Improving Accuracy Through Combining Predictions*. Morgan and Claypool Publishers, 2009.
- [3] O.Okun, G. Valentini and M.Re. *Ensembles in Machine Learning Applications* vol. 373, Springer, 2011.
- [4] L.Breiman. Bagging predictors. *Machine Learning* 24, 2 (1996a), pp. 123-140.IPSSC
- [5] W.Bridewell, P.Langley, L.Todorovski and S.Dzeroski. Inductive Process Modeling. *Machine Learning* 71 (2008), pp. 1-32.
- [6] D. Cerepnalkoski, K.Taskova, L. Todorovski, N.Atanasova and S. Dzeroski. The influence of parameter fitting methods on model structure selection in automated modelling of aquatic ecosystems. *Ecological Modelling* 245:136-165,2012
- [7] J.J.Durillo and A.J.Nebro. jMetal: A Java framework for multi-objective optimization. *Advances in Engineering Software* 42:760-771,2011
- [8] R.Storn and K.Price. Differential Evolution: A simple and efficient heuristic for global optimization over continuous space. *Journal of Global Optimization* 11(34),341-359, 1997
- [9] S.Cohen and A.Hindmarsh. CVODE, a stiff/nonstiff ODE solver in C. *Computers in Physics*,10:138-143,1996
- [10] N.Atanasova, L.Todorovski, S.Dzeroski, S. Reker-Remec, F.Reckangel and B.Kompare. Automated modelling of a food web in Lake Bled using measured data and a library of domain knowledge. *Ecological modelling*, vol 194. no.1-3,pp.37-48, 2006
- [11] B. Panda, J. Herbach, S. Basu and R. Bayardo. PLANET: Massively Parallel Learning of Tree Ensembles with MapReduce. In *Proceedings of International Conference on Very Large DataBases (VLDB 2009)*, pages 1426-1437, Lyon, France, 2009.
- [12] L.Kuncheva and C. Whitaker. Measures of diversity in classifier ensembles. *Machine Learning*, 51, pp. 181-207, 2003

For wider interest

“A model of a system is a tool used to answer questions about the real systems without having to do an experiment” – Lennart Ljung

Engineers and mathematicians construct mathematical model to describe and predict the behavior of real dynamic systems under various conditions. These kinds of models normally are formulated with ordinary differential equations (ODEs), which represent a change of the state of the system over time. This process can either be theoretical or empirical. In the theoretical approach, experts use their knowledge of the domain to derive a mathematical equation of some process in the nature. On the other hand, the empirical paradigm uses measured data and tries to find the model that best fits the observed data in a trial and error process. This paradigm has been recently used to develop machine learning approaches to constructing ODE models from observed data. The state-of-the-art approaches have emerged that combine both the domain-knowledge and measured data to identify both the model structure and the values of the models parameters.

Our research is concerned with extending the existing machine learning paradigms of automated modeling towards learning ensembles of ODE models. Our primary objective is adapting the existing and developing new techniques for combining ODE models, thus improving the descriptive and predictive performance of nonlinear and chaotic dynamic systems.

Pharmacokinetic model for the evaluation of a proposed drug delivery system

Maja Somrak¹, Miha Moškon¹, Dušan Vučko¹, Boštjan Pirš², Miha Mraz¹, Roman Jerala^{3,4}

¹ Faculty of Computer and Information Science, University of Ljubljana, Slovenia

² Faculty of Medicine, University of Ljubljana, Slovenia

³ National Institute of Chemistry, Ljubljana, Slovenia

⁴ Centre of excellence ENFIST, Ljubljana, Slovenia.

maja.somrak@gmail.com

Abstract. We developed a multi-compartment pharmacokinetic model for the evaluation of a proposed therapy with *in situ* production of biological drugs from implanted microencapsulated engineered mammalian cells. We identified crucial drug processes in the body, determined significant compartments and calculated additional drug-specific parameters according to the available studies. We modified the model in consistence with drug administration or delivery system to compare potential therapy with conventional treatments. Results enable us to evaluate effectiveness, predict the degree of side effect occurrence and to calculate the required dosages.

Keywords: pharmacokinetics, physiologically based multi-compartment model, therapy evaluation, drug delivery system, biological drugs

1 Introduction

Drug discovery and development is both very expensive and time consuming. To predict results of drug kinetics in the body, it is useful to incorporate computer simulation, which provides for simpler and faster option than *in vivo* research. Because of complex physiological mechanisms and an extensive set of biological parameters that cannot be accurately measured for either ethical or technical reasons, computer models are basic approximations of actual pharmacokinetic processes. Consequently, drug trials cannot be substituted with computer simulation,

nevertheless they can provide valuable benefits. Simulation can accelerate trials by reducing the number of required tests and support further development.

For the purpose of testing the new drug delivery system, we implemented a physiologically based pharmacokinetic (PBPK) model for *in situ* biological drug production. Pharmacokinetic model is a mathematical model, based on system of ordinary differential equations to describe essential drug kinetics. Generally, we simulate drug absorption, distribution, metabolism and elimination from the body.

To construct a physiologically plausible model, we took into account the relevant biological parameters and based the simulated processes on actual physiological mechanisms.

The model was tested for two biological drugs, interferon alpha and anakinra, for treating hepatitis C and ischaemic heart disease, respectively. In the proposed new drug delivery system, the therapeutic proteins are being produced in microencapsulated cells at a constant rate, which can be initiated by chemical reagents. Implanting these drug-producing cells into the affected tissue would allow for constant *in situ* production of the biological drug. The proposed type of application should maintain steady concentration levels, with relatively higher local concentration comparing to other organs and tissues. To evaluate such drug delivery system we have to compare results of perspective therapy with standard treatments that are currently used in clinics.

2 Derivation of multi-compartment physiologically based model

Physiologically based model is constructed of compartments, which represent specific organs of the body. The modeled compartments were selected upon drug and tissue specifics. Relevant organs are represented separately, while less significant tissues are merged together on the basis of common characteristics [10].

For interferon, we constructed three final models - two for standard treatments and a third one for a prospective therapy with drug-producing microencapsulated cells. The fundamental design is the same in all models; they are only modified for particular entry points of the drug and the corresponding absorption or production kinetics (Figure 1).

Mathematical models were implemented and tested using Matlab.

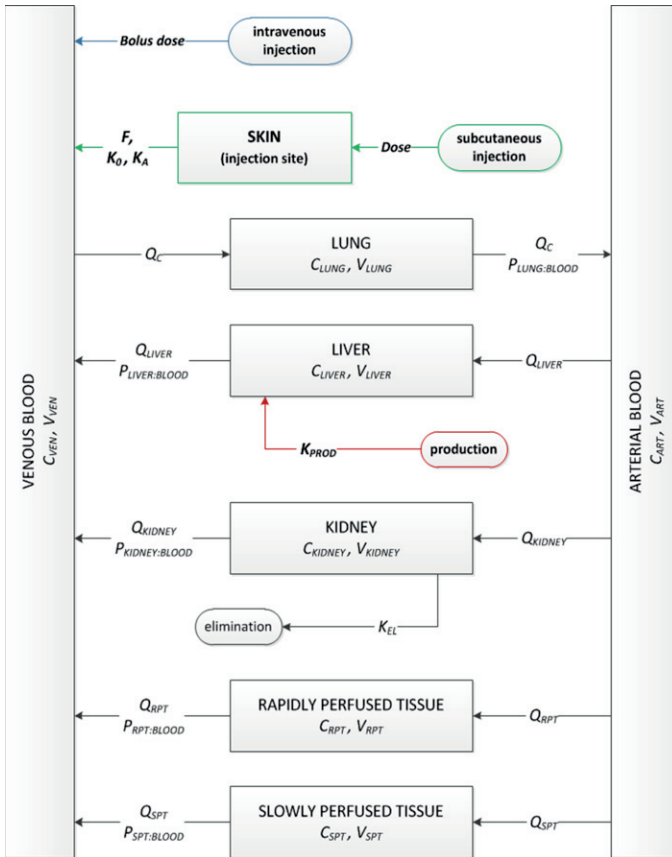


Figure 1: Diagram of multi-compartment pharmacokinetic model, modified for three different interferon therapeutic regimens. Basic model, presented by gray blocks, remains the same, the difference is in drug administration and delivery, where various scenarios are represented with colored blocks. The blue block corresponds to standard intravenous injection and the green block to another conventional approach, subcutaneous administration. The red block is used in simulating drug production at target site, in this case inside the liver.

Parameters

Compartments are defined with set of parameters that fall into one of the following categories:

Species specific parameters

are representative of the species as a whole. These parameters are organ blood flows (Q_i) and volumes (V_i).

Individual specific parameters

include body weight (BW), cardiac output (QC), varying percents of tissue volumes (e.g. percent body fat). Values can range substantially among individuals, depending on factors such as age, sex, renal function, activity level and diet. Values used in our simulation are typical of an adult male, weighing 70 kg, with mean cardiac output and normal renal function.

Chemical specific parameters

are drug absorption and elimination half-lives ($t_{1/2}$), elimination rate (K_{EL}) and derived partition coefficients ($P_{BLOOD:TISSUE}$). One of the most critical elements in pharmacokinetic modeling is the uncertainty of values of the partition coefficients, which denote how the drug is distributed through bodily tissues. Coefficients have a complex dependence on solubility, permeability, pH, binding affinity of the drug to the receptor and other parameters or mechanisms, which are not easily measurable or fully understood.

Chemical and route of administration (ROA) specific parameters

need to be accurate as possible for the model to produce relevant results for later comparison between different types of drug administration. The parameters that were known were dose and dose regimen, bioavailability (F) and absorption rate constants for first-order (K_A) and zero-order (K_0) absorption. By calculating the area under the curve of concentration in target tissue over time for standard treatments, we determined desired drug production rate (K_{PROD}). The optimal drug production allows local concentration to remain just above the calculated therapeutic level.

General mass-balance equations

Essential kinetics are described with a system of ordinary differential equations, some of which are presented on current page.

The first equation describes the change in concentration over time in non-eliminating tissue (1). It has the same form for both rapidly and slowly perfused tissues. Each compartment is then described with its distinctive values for blood flow, concentration and partition coefficient. Since the liver metabolism of both therapeutic proteins is negligible, we can use the same form of equation for the liver as well (2). For the lung equation (3), we have to consider that venous and not arterial blood flows into the tissue.

$$\frac{\delta C_{tissue}}{\delta t} = \frac{Q_{tissue}}{V_{tissue}} * \left(C_{arterial} - \frac{C_{tissue}}{P_{blood:tissue}} \right) \quad (1)$$

$$\frac{\delta C_{liver}}{\delta t} = \frac{Q_{liver}}{V_{liver}} * \left(C_{arterial} - \frac{C_{liver}}{P_{blood:liver}} \right) \quad (2)$$

$$\frac{\delta C_{lung}}{\delta t} = \frac{Q_{lung}}{V_{lung}} * \left(C_{arterial} - \frac{C_{lung}}{P_{blood:lung}} \right) \quad (3)$$

For the kidneys, we have to include the elimination of the drug into the calculation (4).

$$\frac{\delta C_{kidney}}{\delta t} = \frac{Q_{kidney}}{V_{kidney}} * \left(C_{arterial} - \frac{C_{kidney}}{P_{blood:kidney}} \right) - \left(k_{el} * \frac{C_{kidney}}{V_{kidney} * P_{blood:kidney}} \right) \quad (4)$$

In the equation describing the change of concentration in venous blood (5), there is a sum of blood flows from multiple compartments. These include liver, kidney, rapidly and slowly perfused tissue. Blood flow from the lung is accounted for in the equation for the arterial blood compartment (6).

$$\frac{\delta C_{venous}}{\delta t} = \frac{1}{V_{venous}} * \left(\sum \left(\frac{Q_i * C_i}{P_{blood:i}} \right) - Q_{venous} * C_{venous} \right) \quad (5)$$

$$\frac{\delta C_{arterial}}{\delta t} = \frac{1}{V_{arterial}} * \left(\sum \left(\frac{Q_{lung} * C_{lung}}{P_{blood:lung}} \right) - Q_{arterial} * C_{arterial} \right) \quad (6)$$

Modeling pharmacokinetic processes

The accurate absorption and production estimation is important, since this is the main distinguishable part of different types of administration.

In the intravenous administration, dose is bolus and drug enters the system completely, without including any absorption processes. For subcutaneous injection we have to account for two stage absorption, absorption at saturation which follows zero-order kinetics (7) and subsequent first-order absorption that is proportional to local concentration (8). Production is mathematically equivalent of continuous infusion (9).

$$\frac{\delta C}{\delta t} = \frac{k_0}{V} \quad (7)$$

$$\frac{\delta C}{\delta t} = \frac{k_a * (1 - F_z) * D}{V} \quad (8)$$

$$C_{ss} = \frac{K_{PROD}}{K_{EL} \cdot V} \quad (9)$$

Distribution is not a single process, but a complex system of mechanisms, which relies considerably on the properties of the drug as well. For this reason, distribution is often modeled indirectly with the use of partition coefficients. Calculating these values is not entirely reliable, but represents an estimate. Even a choice of different measurement methods can produce varying results. We took into account different studies [2,7,16] and fitted data to minimize deviations from measurements.

The elimination constant for the kidneys was determined by curve fitting to the obtained data [4,8,11]. Additional curve fitting was used to correct absorption [4,11].

3 Results

The simulations were made for interferon subcutaneous (SC) and intravenous (IV) delivery and for local drug production. We compare concentration-time profile of standard subcutaneous therapy (dose of 3 MU, 3 times per week) and concentration-time course of hypothetical therapy with localized production in Figure 2. Overlapping graphs reveal that in case of SC administration there are substantial fluctuations of concentration, which are rather undesirable. High concentration peaks are accountable for side effects, periods of concentration lower than therapeutic contribute to lower effectiveness of the therapy. With the proposed

delivery system it appears that constant production and elimination balances the concentration on a steady level. Changing the amount of drug-producing cells, we are able to increase or decrease the overall production and reach a level, where concentration stays inside the therapeutic window at all times, but remains sufficiently low to minimize the systemic side effects.

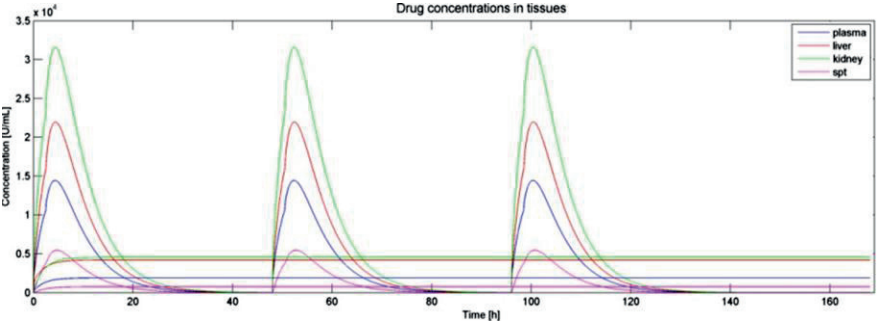


Figure 2: Simulation results for interferon alpha – subcutaneous administration graph (visible high peaks of concentration) overlapped with proposed local drug production therapy graph (steady and low concentration levels).

When the drug is produced at the target site, concentration levels between target tissues and other organs are inclined in favour of the target tissue - although kidneys show a substantial uptake of the drug in subcutaneous administration, the relative difference between kidney and liver concentrations are smaller with localized therapy. Target tissue composition and perfusion influence drug localization, which is even more evident in simulation case of anakinra production inside the damaged myocard.

3 Conclusion

Predicting therapy effectiveness in drug development is an interesting and useful practice that can aid in designing drug trials. Although computer modeling is merely an approximation of the real pharmacokinetic mechanisms, it produces satisfactory results. We have implemented models for the simulation of new drug delivery system and tested it for two study cases. For each therapeutic, we built a model for

the proposed therapy and an additional reference model for the design confirmation and treatment comparison. The obtained results predict distinct concentration-time profiles and high degree of drug localization. If we compare results to standard therapies, we can conclude that the proposed therapy has several advantages, which would make it more effective (drug concentration does not fall below the therapeutic level), more patient friendly (no need for the repetitive injections and reduced side effects due to the absence of high concentration peaks) and equally efficient at lower cumulative drug amounts. By calculating the desired production level, we can further determine the required amount of microencapsulated cells that would need to be implanted into the affected tissue to produce the required amount of therapeutic protein.

However, obtained results are estimates, which at least for now, cannot be validated using data, obtained from real applications of such therapy. The reason is the fact that development of the delivery system for this kind of therapy has not yet reached the phase of clinical trials. Nevertheless, the results of pharmacokinetic simulation are very informative and important as first evaluations of a proposed therapy. In this context, the prediction of therapy outcomes can provide the basis for decisions about further implementation of the new drug delivery system for therapy.

With this in mind, we believe we have attained the initial purpose of pharmacokinetic simulation. In the future, we could improve the models by simulating receptor binding and other distribution-affecting processes separately and further include subcompartments to simulate kinetics at a lower level, which would help us gain a detailed insight and improved evaluation.

Acknowledgements

The work presented in this paper is a part of the project “Switch IT: Inducible Therapeutics” which team Slovenia presented at International Genetically Engineered Machine (iGEM) 2012 synthetic biology competition.

References:

[1] “Switch IT: Inducible Therapeutics” project of team Slovenia on International Genetically Engineered Machine (iGEM) 2012 synthetic biology competition: <http://2012.igem.org/Team:Slovenia>

- [2] Bohoslawec, O., Trown, P. W., and Wills, R. J. (1986) Pharmacokinetics and tissue distribution of recombinant human alpha A, D, A/D(Bgl), and I interferons and mouse alpha-interferon in mice. *Journal of Interferon Research* 6, 207-13.
- [3] Cawthorne, C., Prenant, C., Smigova, a, Julyan, P., Maroy, R., Herholz, K., Rothwell, N., et al. (2011) Biodistribution, pharmacokinetics and metabolism of interleukin-1 receptor antagonist (IL-1RA) using [18F]-IL1RA and PET imaging in rats. *British journal of pharmacology* 162, 659–72.
- [4] Chatelut, E., Rostaing, L., Grégoire, N., Payen, J. L., Pujol, a, Izopet, J., Houin, G., et al. (1999) A pharmacokinetic model for alpha interferon administered subcutaneously. *British journal of clinical pharmacology* 47, 365–71.
- [5] Dahlén, E., Barchan, K., Herrlander, D., Højman, P., Karlsson, M., Ljung, L., Andersson, M., et al. (2008) Development of Interleukin-1 Receptor Antagonist Mutants with Enhanced Antagonistic Activity In Vitro and Improved Therapeutic Efficacy in Collagen-Induced Arthritis. *J. Immunotoxicol.* 5, 189-99.
- [6] Hall, J. E. (2010) *Guyton and Hall Textbook of Medical Physiology: with STUDENT CONSULT Online Access, 12e (Guyton Physiology)* (p. 1120). Saunders.
- [7] Johns, T. G., Kerry, J. A., Veitch, B. A. J., Johns, T. G., Kerry, J. A., Veitch, B. A. J., Mackay, I. R., et al. (1990) Pharmacokinetics, Tissue Distribution, and Cell Localization of [35 S] Methionine-labeled Recombinant Human and Murine α Interferons in Mice. *Cancer Res.* 50, 4718–23.
- [8] Kim, D.C., Reitz, B., Carmichael, D. F., Bloedow, D. C. (1995) Kidney as a major clearance organ for recombinant human interleukin-1 receptor antagonist. *Journal of Pharmaceutical Sciences* 84, 575–580.
- [9] Lavoie, T. B., Kalie, E., Crisafulli-Cabatu, S., Abramovich, R., DiGioia, G., Moolchan, K., Pestka, S., et al. (2011) Binding and activity of all human alpha interferon subtypes. *Cytokine* 56, 282–9.
- [10] Levitt, D. G., Schoemaker, R. C. (2006) Human physiologically based pharmacokinetic model for ACE inhibitors: ramipril and ramiprilat. *BMC clinical pharmacology* 6, 1.
- [11] Marcellin, P., Boyer, N. (2003) Transition of care between paediatric and adult gastroenterology. Chronic viral hepatitis. *Best Pract Res Clin Gastroenterol.* 17, 259-75.
- [12] Mescher, A. (2009) *Junqueira's Basic Histology: Text and Atlas, 12th Edition* (p. 480). McGraw-Hill Medical.
- [13] Mrhar A. (1983) Računalniška simulacija nelinearnih farmakokinetičnih modelov pri razvoju optimalnih zdravil (Computer simulation of nonlinear pharmacokinetic models for development of optimal drugs), Ph.D. Thesis
- [14] Roferon-A (Interferon alfa-2a, recombinant), Hoffmann-La Roche Inc.
- [15] Roy, A., Georgopoulos, P. G. (1997) Mechanistic Modeling of Transport and Metabolism in Physiological Systems Towards a Framework for an Exposure and Dose Modeling and Analysis System.
- [16] Thitinan, S., McConville, J. T. (2009) Interferon alpha delivery systems for the treatment of hepatitis C. *International journal of pharmaceutics* 369, 121–35.

For wider interest

Typical pharmacological therapy comprises regular applications of drugs into the body, which cause high fluctuations of drug concentration and wide distribution of drug throughout the body. An advanced therapy based on synthetic biology would consist of the localized continuous production of biological drugs which should lead to reduced systemic side effects and lower total amount of required drug. In order to evaluate the efficacy of new type of therapy, we utilized pharmacokinetic modeling for comparison of different therapeutic regimens.

Mathematical model relies on experimentally determined parameters and physiological mechanisms affecting drugs inside the human body. In simulation, the outcomes of the key drug processes, through which every drug passes inside the body, are calculated. The result of modeling is the concentration time course for each of the selected organs and tissues, which determines the efficacy and side effects of the therapy.

Simulation results serve as a basis for therapy evaluation and comparison. It is possible to use the model for calculation of additional parameters, e.g. necessary dose adjustments for patients with renal dysfunction or the required amount of implanted microcapsules for the new cell-based therapy.

We obtained very informative and encouraging results, regardless of the fact, that computer model is only an approximation of the real and complex processes. While simulation cannot substitute clinical trials, it can definitely benefit and improve drug development process, save time, expenses and other resources.

Semi-automatic construction of pattern rules for translation of natural language into semantic representation

Janez Starc^{1,2}, Dunja Mladenić^{1,2}

¹Artificial Intelligence Laboratory, Jožef Stefan Institute, Ljubljana, Slovenia

²Jožef Stefan International Postgraduate School, Ljubljana, Slovenia

janez.starc@ijs.si

Abstract.

The paper presents an approach to constructing pattern rules that enable transforming text into semantic representation. We propose a semi-automatic approach to pattern rule construction based on machine learning methods. To make the translation of text into semantic representation faster and more productive, our approach allows the user to select a document and construct pattern rules for it in a semi-automatic way by using automatically suggested parts of pattern rules each consisting of a textual pattern with the corresponding logical pattern. Frequent and coherent textual patterns are suggested as well as concepts from the selected ontology that may be used in the logical pattern. To help the user to evaluate a pattern rule, rules are applied on all documents to obtain semantic expressions. Preliminary testing of the developed system shows that the proposed approach is promising.

1 Introduction

A lot of text is published online every day and there is an increasing demand to store the knowledge contained in text into some kind of a knowledge base. We look at the problem of translating text into semantic representation. Developing methods for this problem would represent progress in machine reading, which is automatic, unsupervised understanding of text [1]. The translation can be done with rules that map fractions of text to the semantic expressions representing knowledge captured in the text fractions that can be later added to the selected ontology. One approach to construct such rules is to learn them automatically with machine-learning methods. Lately, semi-supervised learning methods were successful in relation extraction [2] [3]. These methods require little human effort, but they do not achieve perfect precision. They can be used just on type of relations that have a lot of redundant mentions in text. These methods usually yield relations that have a

predicate and few simple arguments. We argue that this linear structure is not sufficient to capture all the semantic phenomena from text. On the other hand, manual construction of rules can overcome the disadvantages of automatic machine-learning methods, but takes a lot of human effort, which we try to reduce by automatically suggesting parts of pattern rules.

In this paper, we present a semi-automatic approach for constructing pattern rules. The approach reduces the time of construction by assisting the user. It suggests different parts of the rule. The user investigates one document at the time for possible rules. The approach follows the macro-reading paradigm [4], meaning that it is not necessary to extract all facts from the selected document. The system also assists the user by applying the constructed rule on the document collection that the user has provided and constructs the list of all semantic expressions for this rule. The proposed approach can be used on text written in any natural language as long as the necessary natural language processing tools are provided.

2 Approach

In this section, we will present our approach to semi-automatic pattern rule construction. First, we will present the preprocessing step, where textual data is transformed in the required form and generalized. Then, we will define pattern rules and describe how different parts of them are suggested.

2.1 Dataset generalization

Our approach operates on textual data processed by natural language processing tools. Sentence and word splitters are mandatory. Tools, such as lemmatizer, part-of-speech tagger, named-entity recognizer, dependency parser are needed to construct additional layers, which are used for generalization. The structure of the processed data is presented on Figure 1. There should be one corpus for each natural language. The documents are split into sentences. Sentences are split into tokens. There are several layers for each tokenized sentence: lexical tokens, lemmas, part-of-speech tags, named entities. During the processing additional layer is generated – generalized tokens. In the process of generalization each generalized token is assigned a value from another layer. One possible generalization is presented in

Figure 2. If a token is a named-entity, then the generalized token will be the type of the named entity. If part-of-speech tag of the token represents a number (e.g. CD tag), then the generalized token will be assigned a tag *[Number]*. Otherwise, the generalized token is the same as lexical token. These tokens are called basic tokens for the rest of the paper.

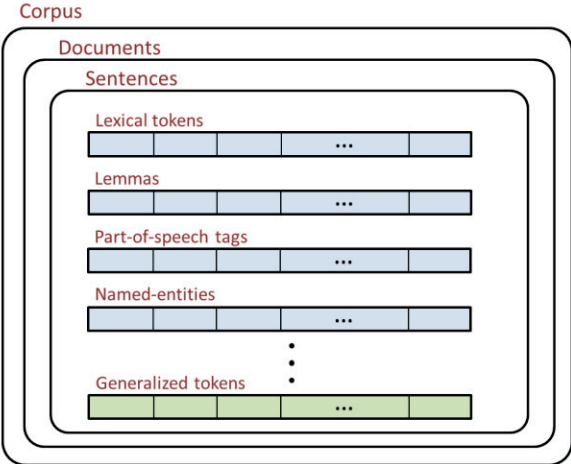


Figure 1: The structure of the processed textual data

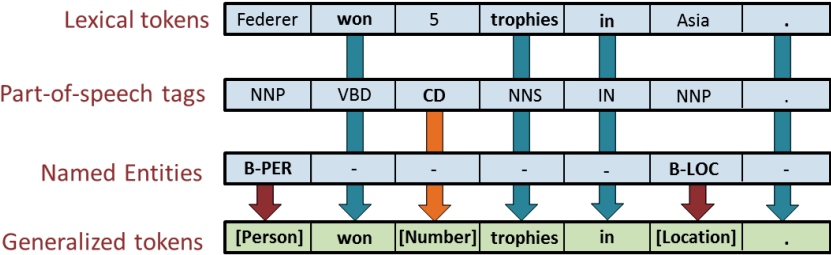


Figure 2: The process of generalization

2.2 Definition of pattern rules

A pattern rule that we aim to construct consists of a textual pattern, a logical pattern, and argument mappings. The textual patterns consist of fixed words, and empty slots, which serve as arguments of the pattern (see Figure 4 for an example of a pattern). Thus, many different fractions of text match with textual patterns. The

arguments of textual patterns are generalized tokens. They are connected with arguments of the logical pattern via argument mappings. When the rule is applied the arguments of logical pattern are filled with arguments from the textual pattern, and the logical pattern becomes a semantic expression that may be a potential addition to the ontology. The static parts of the logical patterns, i.e., predicates, constants, should already be defined in the ontology to integrate well with it. An example of pattern rule is presented on Table 1.

2.3 Pattern rule suggestion

To construct rules faster and better, user can use textual and logical pattern suggestions. Textual patterns that will be suggested are selected using two criteria. Rules that produce many expressions are preferred. Thus, textual patterns that are more frequent are likely to be suggested. Since patterns are distributed according to the power law [5], it is possible to produce *many* expressions with a *small* number of rules, which have very frequent textual patterns. The following procedure is used to compute the frequencies of patterns. All possible n-grams (substrings) of the generalized sentence are considered as patterns. Long patterns (more than 8 tokens) are not counted, because counting them would require a lot of memory. In addition, these patterns are not frequent and may be split on several patterns.

The other criteria for suggesting is *coherence*. Textual patterns that are more likely to produce valid expressions are desired. To measure the coherence we used *specific correlation - sc* [6].

$$sc(pat) = \log\left(\frac{p(pat)}{\prod_{i=1}^n p(pat_i)}\right) \quad (1)$$

Where $p(pat)$ is the probability of the pattern – pat ; $p(pat_i)$ is the probability of the i -th token in the pattern; and n is the length of the pattern. This measure rewards the patterns, whose tokens frequently co-occur together. Deeper research on identifying good textual patterns has been done in [7].

On the other hand, concepts from the target ontology are suggested to help the user constructing logical patterns. The suggested concepts are concepts from the ontology that are denoted by the basic words from the lexical pattern.

3 Implementation

In this section, we will demonstrate the implementation of our approach that we developed. The graphical user interface of the implementation consists of several panels, which we present in the following sections.

3.1 Document selection panel

In the beginning, the user selects the language and number of his choice (see Figure 3). After the user clicks the *Get Document* button, the selected document will appear in the Document panel.

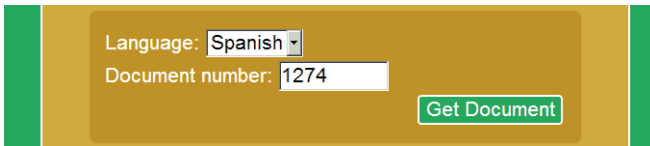


Figure 3: Document selection panel

3.2 Document panel

The selected document is shown in this panel. The last part of document panel is depicted on Figure 4. Each sentence is in its own paragraph. Plain text is in *black* color. Parts that are in *orange* or *green* represents patterns. If the user moves the mouse over such pattern, the statistics of the pattern will appear in a hint box near the pattern (Figure 4, Figure 5).

The parts of text that are orange, match with patterns suggested by the system. These patterns occur in the corpus more times than a predefined threshold; they include at least one non-basic token; and have a higher specific correlation than other patterns which overlap with them. The parts of text that are green have already pattern rules defined for them. Consequently, the corresponding expression is already constructed and presented in the hint box, like the one on Figure 5.

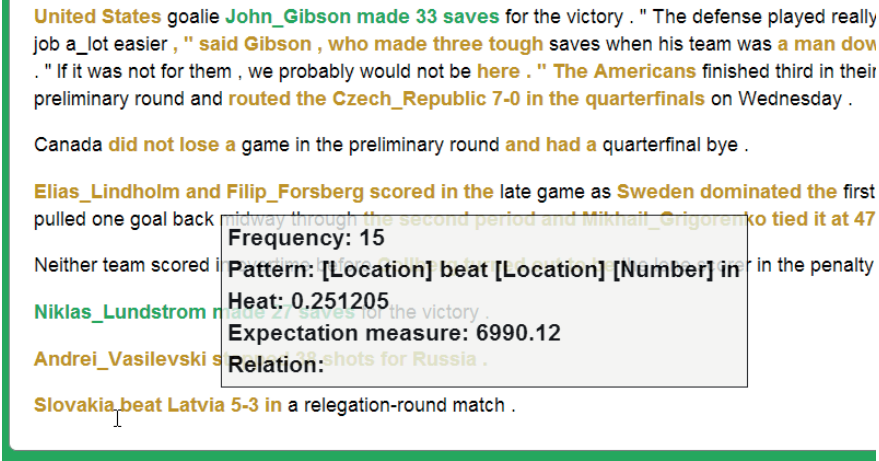


Figure 4: The bottom part of the document panel. The statistics box is displayed for text: *Slovakia beat Latvia 5-3*

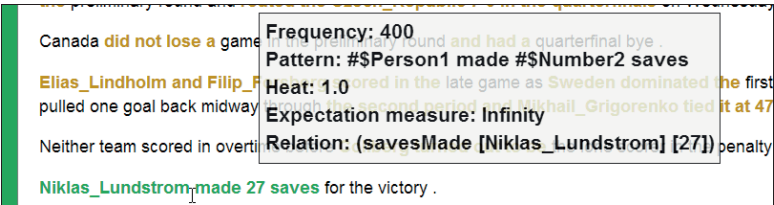


Figure 5: Applied pattern rule on *Niklas_Lunstrum made 27 saves*

3.3 Pattern rule panel

This is the panel, where the user constructs pattern rules (Figure 7). To construct a rule, a valid textual pattern needs to be in the lexical pattern box. This can be achieved either by clicking on the orange fraction of text, or by selecting some text and dragging it the lexical pattern box. In both cases, the system generalizes the text to become a pattern. The frequency of the pattern is calculated and displayed above. In the same moment, a generic pattern is displayed in the logical pattern box, for example (*predicate %1% %2%*). Each argument in the lexical pattern box starts with # \$ and ends with its serial number. To construct argument mappings, the user must define arguments in the logical pattern by stating their serial number encapsulated

with percentage characters, for example %1%. The user constructs the logical pattern with concepts from the ontology. In the suggestions box, the system suggests few concepts from the ontology that might be included in the logical pattern. When the rule is complete, the user clicks on the button *Save rule*. The system applies the rule on all documents and reports the number of matches. The matches in the current document become highlighted in green.

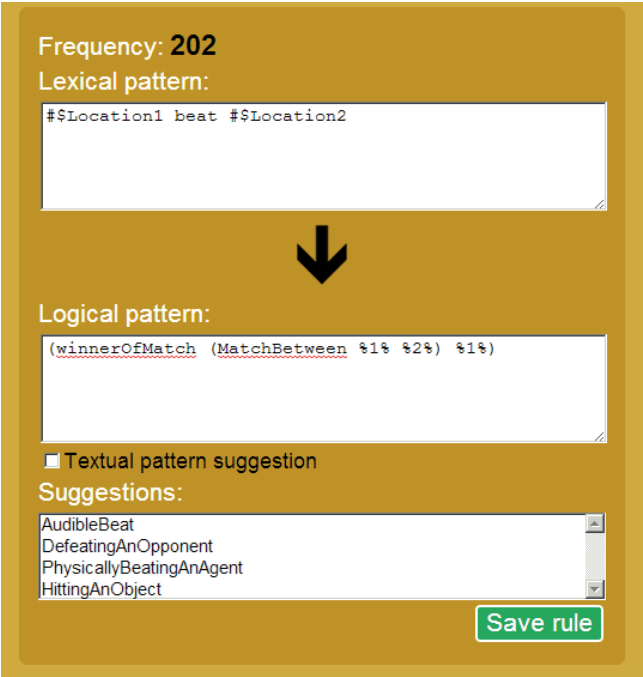


Figure 6: Pattern rule panel

4 Preliminary testing

In this section, we present the preliminary testing of our system. We took about a month of English, Spanish and Catalan news articles from Web Newsfeed [8]. For each language, four articles talking about corruption in Spain were selected. Using these articles, several pattern rules were constructed with our system. In this experiment, we took OpenCyc as the target ontology. All the constants that are not arguments were already defined in OpenCyc. We present a rule that was created with

our system, on Table 1. The rule is made for Catalan language and extracts information about events, where a certain person received a certain amount of money. The rule was applied three times. One of the three expressions is stated in the bottom part of the table.

Table 1 - Pattern rule representing “person received money” information for Catalan language

Lexical pattern	Logical pattern	Times applied
#Person1 rebien #Money2 euros	(#\$thereExists ?EVENT (\$and (#\$isa ?EVENT #\$MoneyTransfer) (#\$moneyTransferred ?EVENT (#\$Euros %2%)) (#\$beneficiary ?EVENT %1%)))	3
Expression		
(#\$thereExists ?EVENT (\$and (#\$isa ?EVENT #\$MoneyTransfer) (#\$moneyTransferred (#\$Euros 9900)) (#\$beneficiary ?EVENT [Álvarez_Cascos])))		

5 Conclusion

We have proposed and implemented an approach for semi-automatic construction of pattern rules. The output of the approach is a list of pattern rules that can be used on any document and a list of semantic expressions that are the result of the application of the constructed rules on the underlying corpus. The suggestions of textual and logical patterns, allows the user to quickly create good pattern rules, which was also tested on the presented implementation.

In further research, we would like to improve the process of suggesting pattern rules. One possible direction that we would like to investigate is by exploiting machine learning approaches to information extraction and using deeper natural language tools. The suggestions of textual patterns can be improved by combining the specific correlation with part-of-speech tags and dependency trees. Later semantic expressions will be automatically added to the ontology. In this way, ontological constraints might help to reject the false expressions.

Acknowledgements

This work was supported by Slovenian Research Agency and the ICT Programme of the EC under XLike (ICT-STREP-288342).

References:

- [1] O. Etzioni, "Machine reading of web text," in *Proceedings of the 4th international conference on Knowledge capture - K-CAP '07*, 2007.
- [2] Agichtein, E. and Gravano, L., "Snowball: Extracting relations from large plain-text collections," in *Proceedings of the fifth ACM conference on Digital libraries*, 2000.
- [3] Etzioni, O. and Cafarella, M. and Downey, D. and Kok, S. and Popescu, A.M. and Shaked, T. and Soderland, S. and Weld, D.S. and Yates, A., "Web-scale information extraction in knowitall:(preliminary results)," in *Proc. of the 13th international conference on World Wide Web*, 2004.
- [4] Tom M. Mitchell and Justin Betteridge and Andrew Carlson and Estevam R. Hruschka Jr. and Richard C. Wang, "Populating the Semantic Web by Macro-Reading Internet Text," in *{Proceedings of the 8th International Semantic Web Conference (ISWC 2009)}*, 2009.
- [5] W. B. a. T. J. M. Cavnar, "N-gram-based text categorization," *Ann Arbor MI*, vol. 48113, no. 2, pp. 161--175, 1994.
- [6] T. V. d. Cruys, "Two multivariate generalizations of pointwise mutual information," in *DiSCo '11 Proceedings of the Workshop on Distributional Semantics and Compositionality*, 2011.
- [7] J. Starc and B. Fortuna, "Identifying good patterns for relation extraction," in *Proceedings of 15th Multiconference on Information Society*, 2012.
- [8] Trampus, Mitja and Novak, Blaz, "The Internals Of An Aggregated Web News Feed," in *Proceedings of 15th Multiconference on Information Society*, 2012.

For wider interest

Imagine computers being able to read understand and memorize a large encyclopedia like Wikipedia. This means that they would be able to answer any question regarding the read text and provide explanation for it. This is the goal of a subfield of artificial intelligence called machine reading. By the definition, it is automatic, unsupervised understanding of text [1]. The aim of our research is to make progress towards machine reading.

To be able to fulfill machine reading, computers must store the read data in a language they understand. We will call it semantic language. An example sentence in semantic language would be *(placeOfBirth TigerWoods CypressCalifornia)*, which in our language means that Tiger Woods was born in Cypress, California. Computers need to know all the components of a semantic language sentence before memorizing it. This is called the background knowledge.

Text is translated into semantic language with pattern rules. These rules consist of textual and semantic pattern. Textual pattern connects with different portions of text that have similar meaning. Semantic pattern becomes a semantic sentence after applying the rule. There are two ways to acquire pattern rules. Either have them constructed manually or learn them with machine-learning methods. The first way is very expensive in terms of human labor. There are an enormous number of rules to be produced, and it takes time for a human to learn producing rules. On the other hand, machine-learning methods need less human involvement, but suffer from inaccuracy.

We built an interface, which allows a human to develop good rules in a fast way. This is done by suggesting him frequent and coherent textual patterns. Additionally, it suggests concepts from background knowledge that are likely to form the semantic pattern. The user constructs a rule on a selected document. When a new rule is constructed, the system searches all the documents for possible applications of the rule. In the future, we will add machine-learning methods to our system and make it simpler to use, thus it will be available for wider audience.

Automated modeling of Rab5–Rab7 conversion in endocytosis

Jovan Tanevski^{1,2}, Ljupčo Todorovski³, Sašo Džeroski^{1,2}

¹ Department of Knowledge Technologies, Jožef Stefan Institute, Ljubljana, Slovenia

² Jožef Stefan International Postgraduate School, Ljubljana, Slovenia

³ Faculty of Administration, University of Ljubljana, Slovenia

jovan.tanevski@ijs.si, ljupco.todorovski@fu.uni-lj.si,
saso.dzeroski@ijs.si

Abstract. Inductive process modeling (IPM) is an approach to equation discovery that can be used to induce models of dynamical systems. We apply IPM to the task of modeling the conversion of Rab5 domain proteins to Rab7 domain proteins, a key process in endocytosis. We first introduce a formal representation of the domain knowledge for modeling this process. We then present the design of the experiments and the obtained results. We finally compare our results with those present in the literature.

Keywords: inductive process modeling, structure identification, parameter estimation, systems biology, endocytosis.

1 Introduction

Equation discovery is a machine learning approach used to discover scientific laws and models in the form of equations from observations [1,2]. Inductive process modeling (IPM) is a knowledge and data driven approach based on equation discovery principles [3,4]. IPM combines domain specific knowledge, listing constituent entities and interactions between them (processes), both described in a formal language, and observations in the form of time-series data in order to induce explanatory models of dynamic systems. Process models correspond to (ordinary) differential equation (ODE) models. The IPM approach performs both structure identification and parameter estimation by using the provided knowledge and data. In this paper, we apply the IPM approach to modeling a dynamical system in the domain of systems biology.

A recent paper by Del Conte-Zerial et al. [5], presents a mathematical model of the dynamics of a particular endocytosis process, the conversion of Rab5 domain proteins to Rab7 domain proteins, which occurs during endosome maturation. The authors propose a Rab5–Rab7 conversion model based on extensive comparative analysis of a number of model structures and different kinetic laws. In a follow-up paper Tashkova et al. [6] addresses the task of parameter estimation of a single Rab5–Rab7 conversion model structure and shows the utility of several parameter estimation methods under a range of observation scenarios considering endocytosis data of different completeness and accuracy of interpretation.

In this paper, we generalize the results of [6], by integrating the proposed parameter estimation methods within IPM (in a recently developed IPM tool ProBMoT [7]), to automatically explore the space of candidate model structures considered by Del Conte-Zerial et al. [5]. We conjecture that IPM can reproduce the model structure obtained following the manual comparative analysis.

We first formulate the modeling knowledge (Section 2) for the task at hand. We then, run ProBMoT on this domain knowledge and the data used by Del Conte-Zerial et al. [5] and Tashkova et al. [6]. We present our results and compare them with the results of the manual modeling experiment in Section 3. We give a summary of our work and propose directions for further work in Section 4.

2 Process-Based Knowledge for Modeling Endocytosis

IPM takes at input time-series data about the dynamic behavior of the observed system and modeling knowledge in terms of a library of template model components – entities and processes. In the case of modeling endocytosis, entities correspond to protein domains, while processes refer to interactions among the protein domains. In order to develop the library of knowledge for this domain we used the modular formulation of the Rab5–Rab7 conversion from [5], which can be represented as a system of ordinary differential equations (ODEs) given in Equation 1.

$$\begin{aligned}
\frac{dr_5}{dt} &= K_1 - (k_1 + GEF_5(R_5 + R_7))r_5 + GAP_5(R_5, R_7)R_5 \\
\frac{dR_5}{dt} &= GEF_5(R_5 + R_7)r_5 - GAP_5(R_5, R_7)R_5 \\
\frac{dr_7}{dt} &= K_2 - (k_2 + GEF_7(R_5 + R_7))r_7 + GAP_7(R_5, R_7)R_7 \\
\frac{dR_7}{dt} &= GEF_7(R_5 + R_7)r_7 - GAP_7(R_5, R_7)R_7
\end{aligned} \tag{1}$$

In Equation 1, variables r_5 and r_7 represent the concentrations of GDP-bound (passive state) Rab5 and Rab7 domain proteins, while R_5 and R_7 represent the concentrations of GTP-bound (active state) proteins. Parameters K_i and k_i represent GDI association rates and GDI dissociation fluxes. The Rab5–Rab7 interactions labeled with *GEF* represent activating reactions, while the *GAP* interactions represent inhibitory reactions.

Del Conte-Zerial et al. [5] considered different functional forms for modeling the GEF and GAP interactions. The combinations of the different functional forms result in different model structures. Figure 1 provides a graphical representation of the general model structure considered by Del Conte-Zerial et al. [5].

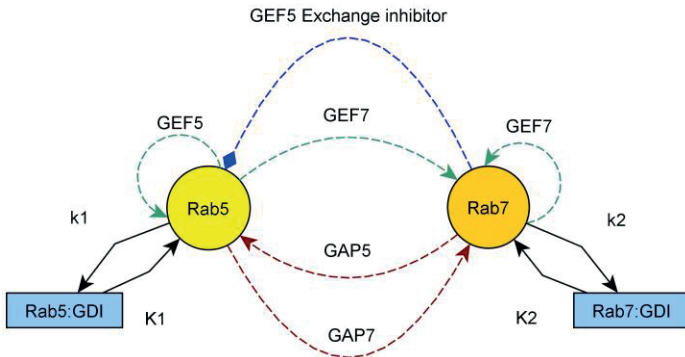


Figure 1 Graphical representation of the Rab5–Rab7 interaction model.

The dashed lines represent hypothetical interactions that are result of different combinations of the considered (optional) interactions, while the solid lines are non-optional interactions. The green arrow lines correspond to activation reactions which

increase the conversion from GDP-bound (passive) to GTP-bound (active) states, the red arrow lines correspond to the increase of hydrolysis from GTP-bound to GDP-bound states, and the blue line with rectangle ending represents an inhibitory reaction which decreases the conversion from GDP-bound to GTP-bound states of the corresponding Rab domain proteins.

Table 1 Part of the developed library of domain knowledge. Definition of a template entity, the root process and one template process.

```

template entity Protein {
vars:
  GDP_bound_state_conc {range:<0,2>}, GTP_bound_state_conc {range:<0,2>},
  GEF, GAP, t;
consts:
  GDI_dissociation_flux {range: <0.001, 4>}, GDI_association_rate {range: <0.001, 4>};
}
template process Root(p1 : Protein, p2: Protein) {
consts:
  td {range: <50,150>};
processes:
  GDI_GDP_membrane_interaction(p1), GDI_GDP_membrane_interaction(p2),
  GEFProcess(p1,p2), GEFCombined(p1,p2), GAPPProcessPlus(p1,p2),GAPPProcess(p2,p1);
equations:
  td(p1.GDP_bound_state_conc) = -p1.GEF * (p1.t / (p1.t+td))*p1.GDP_bound_state_conc
    + p1.GAP * p1.GTP_bound_state_conc,
  td(p1.GTP_bound_state_conc) = p1.GEF * (p1.t / (p1.t+td))*p1.GDP_bound_state_conc
    - p1.GAP * p1.GTP_bound_state_conc,
  td(p2.GDP_bound_state_conc) = -p2.GEF * p2.GDP_bound_state_conc
    + p2.GAP * p2.GTP_bound_state_conc,
  td(p2.GTP_bound_state_conc) = p2.GEF * p2.GDP_bound_state_conc
    - p2.GAP * p2.GTP_bound_state_conc;
}
template process GEFProcess(p1: Protein, p2: Protein){
consts:
  ke {range:<0.001,4>}, kf{range:<0.001,4>}, kg{range:<0.001,4>},
  km{range:<0.001,4>}, ki{range:<0.001,4>};
}
template process Exchange_inhibition : GEFProcess {
equations:
  p1.GEF=ke*p1.GTP_bound_state_conc/(km*(1+p2.GTP_bound_state_conc/ki) +
    p1.GDP_bound_state_conc);
}
// ...

```

Table 1 presents a fragment of the ProBMoT library for inductive process modeling of endocytosis. It contains a single template entity protein that corresponds to the both protein domains of Rab5 and Rab7. The variables of the protein template correspond to the concentrations of the active-state and passive-state proteins. Furthermore, the root process template specifies the general form of the conversion model from equation 1, where the interaction processes correspond to the interactions from Figure 1. Finally the library contains specifications of all kinetic rate law alternatives considered for modeling individual reactions in Del Conte-Zerial et. al. [5] considered in their work.

For example, the *Exchange_inhibition* rate law is one modeling choice for the GEF5 interaction (i.e., GEF5 arrow in Figure 1), which is considered as one possible alternative of a more general *GEFProcess*. The latter has a few more sub-processes in the library, not listed in Table 1, that correspond to other possibilities for modeling the GEF5 interaction. All other processes in the library are described in a similar hierarchical manner. The *GEFCombined* interaction process contains the possible alternatives for the GEF7 interaction. The *GAPProcess* interaction process contains the possible alternatives for the GAP7 interaction and the *GAPProcessPlus* interaction process contains the possible alternatives for the GAP5 interaction.

3 Modeling Endocytosis with ProBMoT

The process-based knowledge in the form of library of template entities and processes provides alternatives for modeling individual endocytosis processes. Using the library and a general specification of the entities and processes involved in the Rab5–Rab7 conversion, ProBMoT enumerates all candidate model structures. The enumeration results in 126 candidate structures. Del Conte-Zerial et al. [5], consider only a subset of 54 structures and omit others. Note that ProBMoT automates the structure identification task and allows us to perform a complete experiment, where all 126 structures are considered.

Obtaining a complete model from the enumerated structure requires estimation of the parameter values. To this end, we use Differential Evolution as a parameter fitting method, which was configured according to the settings reported in [6]. The parameter ranges were set to the interval $[0, 2]$ for the initial values of the system

variables (r_5 , R_5 , r_7 , and R_7), to $[10^{-3}, 4]$ for all the other model parameters, and to $[10^3, 10^5]$ for the output scaling parameter (see below). Each model for each candidate parameter set in the process of parameter estimation is evaluated using the available data and the output of the model simulation. The parameter estimation is guided by an objective function based on root mean squared error (RMSE). The objective function for evaluating a model m is defined as in equation 2.

$$RMSE_{Objective}(m) = \sum_{i=1}^2 \sqrt{\frac{1}{N} \sum_{j=1}^N (x_i[j] - y_i[j])^2}, \quad (2)$$

In equation 2 $x_i[j]$ and $y_i[j]$ denote the simulated and measured (respectively) value of the observed variable i at time point j , and N denotes the number of the measurement time points in the dataset.

The data provided for the experiment is real time-series of measurements from Del Conte-Zerial et al. [5]. The data was collected from 3 independent experiments (28 time courses), scaled and averaged. The data consists of 10571 time points on the interval $[-5, 330]$ seconds. The measured time-series for Rab5 and Rab7 concentrations were manually aligned, so the conversion switch point is at time point 0. Due to the limitation of the measurement equipment, only total concentration of the Rab5 and Rab7 domain proteins can be observed. Therefore, the observed values at each time point correspond to r_5+R_5 and r_7+R_7 . To deal with the limited observations and their scale, we define the model output as $K^*(r_5 + R_5)$ and $K^*(r_7 + R_7)$, where K denotes a scaling parameter. Additionally, we used the transformation $t \leftarrow t + 828.56$ on the time points from the data shifting the conversion point to the real time so that our model simulations can be directly compared to the measured data [5, 6].

Figure 2(a) provides a graphical representation of the best ranking model structure according to its RMSEObjective value given the data. It has an error of 3040.08. Note at this point that the error range for all the 126 candidate models is pretty narrow and many alternative model structures have errors comparable and only slightly higher than the best model. The mean error of all 126 candidate model

structures is 3841.65 with a standard deviation of 1022.12. Moreover, the mean error of the first 100 models is 3411 with the deviation of 201.34.

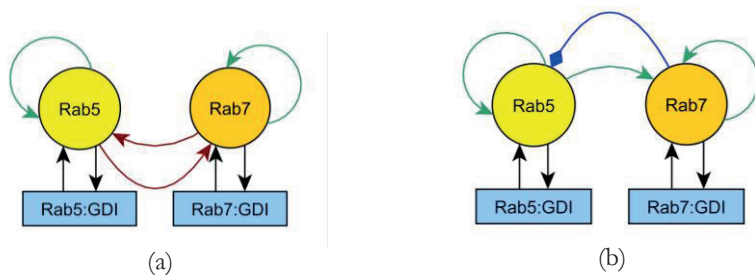


Figure 2 (a) the best model structure according to its RMSEObjective value, (b) the model structure reported by Del Conte-Zerial et al.

Figure 2(b) presents the structure of the model reported by Del Conte-Zerial et al. [5]. This cut-out switch model structure has an error of 3735.98 and ranks 93rd according to its RMSEObjective value given the measured data. Structurally the models contain equal number of interactions between the protein domains, but the types of the interactions are different. In the best ranking model, complex GAP5 and GAP7 interactions are present which increase of hydrolysis from GTP-bound to GDP-bound states. The GEF interactions in this model are comprised only of auto-activation of the corresponding protein domains. On the other hand, complex GAP interaction are not present in the model reported in [5] and the complex GEF interactions are inhibiting the conversion of GDP-bound to GTP-bound states of the Rab5 domain (GEF5) on one hand, and increase the exchange of GDP-bound to GTP-bound states of the Rab7 domain (GEF7) on the other.

Despite the observed error, rank and the difference in the structures and the types of the interactions, the best ranking model and the model reported in [5], lead to similar simulated dynamics that fits well to the measured data as shown in Figure 3, where Model 97 denotes best ranked model found by ProBMoT according to its RMSEObjective value, while Model 12 denotes the model reported in [5].

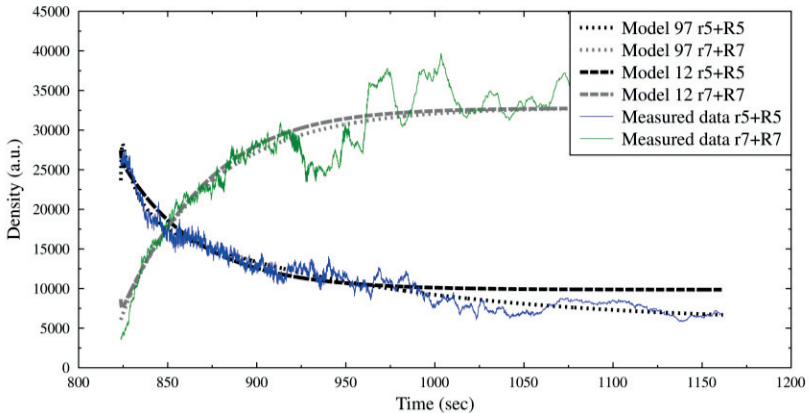


Figure 3 Dynamics of the total concentration of the protein domains of Model 97 and Model 12 compared to the measured data

Using RMSE based function as only objective function guiding the parameter estimation results in a situation where discriminating between model structures can be impossible without using an additional criterion which captures complex dynamical behavior. Additional criteria which complement the information about the fit to the measured data gained by this objective function should be considered especially when dealing with scenarios with limited observability in which the measured data does not capture the complex events and the expected behavior in sufficient detail. One such criterion, used in [5], is based on performing bifurcation and phase plane analysis. Only after model structure passes certain criteria related to these analyses, the comparison with the measured data is being made for the final model selection.

4 Summary and further work

We encoded process-based knowledge for modeling endocytosis and used IPM-based tool ProBMoT to model a particular endocytosis process of Rab5–Rab7 protein domain conversion. We compared the obtained models with the results from manual modeling experiments reported in [5].

The best model obtained with ProBMoT differs in error and structure from the model reported in [5]. However, we also found out that range of errors obtained for

different candidate structures is pretty narrow. We can conclude from the experiments that the objective function based on squared error, used for parameter estimation, might not be sufficient for discriminating among the model structures when modeling endocytosis. Going beyond the use of this kind of error measures as only criterion for optimization is one possible direction for further work. The integration of information gained by performing analysis of the complex dynamical behavior on the candidate models within the IPM approach, like in [5], might improve our method and result in better discrimination among model structures. These findings give direction to further work in the process of automated modeling of endocytosis and the further development of the IPM approach.

Finally, the Rab5–Rab7 conversion, although important, is only one phase of the whole endocytosis process. The IPM approach can be also used to gain knowledge about the dynamics of other parts of the endocytic pathway, knowledge that can be used to develop a complete explanatory model of endocytosis.

References:

- [1] P. Langley, H. Simon, G. Bradshaw, J. Zytkow: *Scientific Discovery: Computational Explorations of the Creative Processes*. MA: The MIT Press, 1987
- [2] S. Džeroski, L. Todorovski. Discovering dynamics. In *Proceedings of the Tenth International Conference on Machine Learning*, 97-103, 1993
- [3] W. Bridewell, P. Langley, L. Todorovski, S. Džeroski. Inductive process modelling. *Machine Learning*, 71:109_130, 2008
- [4] S. Džeroski, L. Todorovski. Encoding and using domain knowledge on population dynamics for equation discovery. In: *Logical and Computational Aspects of Model-Based Reasoning*, 227-247, 2002
- [5] P. Del Conte-Zerial, L. Bruschi, J.C Rink, C. Collinet, Y. Kalaidzidis, M. Zerial, A. Deutsch. Membrane identity and GTPase cascades regulated by toggle and cut-out switches. *Molecular Systems Biology*, 4(206), 2008
- [6] K. Taškova, P. Korošec, J. Šilc, L. Todorovski, S. Džeroski. Parameter estimation with bio-inspired meta-heuristic optimization: modeling the dynamics of endocytosis *BMC Systems Biology*, 5(159), 2011
- [7] D. Čerepnalkoski, K. Taškova, L. Todorovski, N. Atanasova, S. Džeroski. The influence of parameter fitting methods on model structure selection in automated modeling of aquatic ecosystems. *Ecological Modelling*. 245:136-165, 2012

For wider interest

Our work focuses on artificial intelligence approaches to modeling dynamical systems. In particular, we work on development and application of tools for inductive-process modeling. These tools take as input knowledge formalized as library of model components for modeling dynamical systems in a particular domain of interest and time-series data about the behavior of the observed system. They integrate knowledge transformation methods from artificial intelligence with standard simulation and parameter estimation methods from system identification to automate the process of establishing a model of the dynamical system at hand.

While most of the inductive-process modeling applications have been in the domain of ecology, our interests are towards using them in context of system and synthetic biology. The work presented in this paper is an application of the IPM approach to the domain of systems biology. It describes the entire process of automating a manual experiment from the literature. The challenges and the findings to which we come across during the various application scenarios, like the one presented in this work, provide us with directions towards the further development of the approaches and towards the goal of providing tools that improve the ease and the efficiency of the task of modeling

Analysing Financial Vocabulary Using a New Semantic Subgroup Discovery System Hedwig

Anže Vavpetič^{1,2}, Petra Kralj Novak^{1,2}, Nada Lavrač^{1,2}

¹ Dept. of Knowledge Technologies, Jožef Stefan Institute, Ljubljana, Slovenia

² Jožef Stefan International Postgraduate School, Ljubljana, Slovenia

anze.vavpetic@ijs.si

Abstract. Subgroup discovery (SD) aims at finding statistically interesting subsets of objects (typically encoded as symbolic rules) for a chosen property of interest. In this paper, we present a newly developed semantic subgroup discovery system Hedwig, which exploits the ontological background knowledge to construct subgroup describing rules as well as to effectively guide the search procedure via top-down induction. We demonstrate the effectiveness of our system with an application in a financial domain: we search for interesting vocabulary patterns that accompany credit default swap (CDS) trend reversal for the financially troubled country of Portugal over a collection of over 8 million news articles collected in year and a half period. Our experiments yielded two interesting news topics that accompany CDS trend reversals of Portugal. We also provide several directions for further work.

Keywords: semantic data mining, subgroup discovery, ontology, text mining, credit default swap, financial crisis

1 Introduction

This paper addresses the task of subgroup discovery (SD), first defined by Klösgen [3] and Wrobel [8]; SD is commonly described as being in the intersection of predictive and descriptive data mining as it is used for descriptive tasks although the rules are induced from class-labelled data. The goal of SD is to find subgroups of individuals that are statistically interesting according to some property of interest for a given population of individuals.

The process of exploiting formal ontologies within the process of data mining is called Semantic Data Mining (SDM) [7]. In this paper, we present a new semantic subgroup discovery system named Hedwig, which searches for subgroups with descriptions constructed from the given ontological vocabulary (including any provided binary relations). Additionally, the traversal of the search space is effectively guided by the structure of the ontology. The most relevant related work in exploiting ontologies in data mining includes [6] and [9]. In [6], the SEGS system was introduced and the gene ontology was used to find enriched gene sets from microarray data, and in [9] an ontology of Computer Aided Design elements and structures was used to find frequent design patterns.

In this paper, we present the results of applying the newly developed system Hedwig to get insight into the vast amount of news articles collected over the last year and a half as part of the EU projects FIRST and FOC. We seek for insight in the financial domain; more specifically we investigate the vocabulary related to the European sovereign debt crisis used in news articles and financial blogs. We investigate the relationship between the financial market perception of a financial entity and the articles mentioning the financial entity. As a measure of market perception, we use the credit default swap (CDS) price. In essence, CDS is insurance for country bonds and reflects the market expectation that the issuer will default. The higher the CDS price, the more likely it is that that country will be unable to repay its debt [10]. Portugal is the focus of our investigation as an example of a financially troubled country.

In [2], the authors have employed SD techniques for a related problem. They have induced indicators of systemic banking crises by looking at past crises in the period 1976-2007. Rather than looking at news articles and relating them to the CDS prices, they have used 105 publicly available features. Their main result is that demographic indicators are the most important: the percentage of the active population in connection to the annual percentage of money growth and the male life expectancy are especially crucial.

The main contribution of this paper is the new semantic data mining system named Hedwig, which is presented with its premiere application in understanding financial

news. Another contribution is the first insights into the relationship between the European sovereign debt crisis vocabulary and the CDS price trends.

The paper is structured as follows. Section 2 describes the novel Hedwig semantic SD system. Section 3 describes the data preparation stage and experimental setup. Section 4 presents the experimental results. Section 5 gives directions for further work and concludes the paper.

2 Methodology

This section describes the newly developed Hedwig semantic subgroup discovery system. Compared to standard subgroup discovery algorithms, Hedwig uses domain ontologies to guide the search space and formulate generalized hypothesis. Existing semantic subgroup discovery algorithms are either specialized for a specific domain [6] or adapted from systems that are not aware of the hierarchical structure of ontologies [7]. Hedwig overcomes these limitations as it is designed to be a general purpose semantic subgroup discovery system.

Let us first explain the notation. We represent rules as first-order logic expressions. For example, the rule:

Max(X) \leftarrow **Country**(X), **Before**(X,Y), **comp_NESTLE_S_A**(Y). [50, 10],

where variables X, Y represent input examples (in our case days), is interpreted as follows. An above average co-occurrence of some country – with Portugal – on a day that is followed by an above average co-occurrence of the Nestle company is true for 50 input examples, which are also known as coverage. 10 out of those belong to the desired target class **Max** (also known as support). Note the convention that lowercase predicates (e.g., **comp_NESTLE_S_A**) represent specific instances, while capitalized predicates represent classes, i.e. sets of specific instances (e.g., the predicate **Country** subsumes instances like **cou_Portugal** or **cou_Slovenia**).

In order to search for interesting subgroups, we employed the algorithm provided in Figure 2. The algorithm uses beam search, where the beam contains the best N rules found so far. The search starts with the default rule which covers all input examples.

```

function induce():
    rules = [default_rule]
    while improvement(rules):
        foreach rule in rules:
            rules.extend(specialize(rule))
        rules = best(rules, N)
    return rules

function specialize(rule):
    specializations = []
    foreach predicate in eligible(rule.predicates):
        # Specialize by traversing the subclassOf hierarchy
        for subclass in subclasses(predicate):
            new_rule = rule.swap(predicate, subclass)
            if can_specialize(new_rule):
                specializations.add(new_rule)
    if rule != default_rule:
        # Specialize by adding a new unary predicate to the rule
        new_predicate = next_non_ancestor(eligible(rule.predicates))
        new_rule = rule.append(new_predicate)
        if can_specialize(new_rule):
            specializations.add(new_rule)
    if rule.predicates.last().arity == 1:
        # Specialize by adding new binary predicates
        specializations.extend(add_binary_predicate(rule))
    return specializations

```

Figure 2: Pseudo code of the Hedwig semantic SD algorithm.

In every iteration of the search, each rule from the beam is specialized via three operations:

1. Replace the rule's predicate with a predicate that is a sub-class of the previous one, e.g., $\text{City}(X)$ is specialized to $\text{Capital}(X)$.
2. Append a new unary predicate to the rule, e.g., $\text{Max}(X) \leftarrow \text{City}(X)$ is specialized to $\text{Max}(X) \leftarrow \text{City}(X)$, $\text{Company}(X)$.
3. Append a new binary predicate, thus introducing a new existentially quantified variable, e.g.: $\text{Max}(X) \leftarrow \text{City}(X)$ is specialized to $\text{Max}(X) \leftarrow \text{City}(X)$, $\text{Before}(X, Y)$.

Rule induction via specializations is a well-established way of inducing rules, since every specialization either maintains or reduces the current number of covered examples. A rule will not be specialized once its coverage is 0 or falls below some

predetermined threshold. After the specialization step is applied to each rule in the beam, a new selection of the best scoring N rules is made. If no improvement is made to the collection of rules, the search is stopped. In theory, our procedure supports any rule scoring function. Currently we implemented the popular SD scoring functions WRAcc [4], χ^2 [5] (for discrete target classes), and Z-score [1] (for ranked examples).

The system Hedwig, which implements the above algorithm, supports ontologies and examples to be loaded as a collection of RDF triples (a graph). The system automatically parses the RDF graph for the *subClassOf* hierarchy, as well as any other user-defined binary relations. Hedwig also defines a namespace of classes and relations for specifying learning examples to which the input must adhere.

3 Data preparation

This section presents the data and the data preparation stage needed to apply our methodology. Three sources of data were used: text from news and blogs, CDS prices and a domain ontology.

We started with a large database of annotated news articles (over 8 million), which were acquired over the last year and a half (period from 2011-10-24 to 2013-01-13) as part of the FIRST and FOC EU projects. Among other properties of each article (e.g., title and URL), the most important ones for our task is the information about which entities from a pre-defined European Sovereign Debt vocabulary appear in the given article (e.g., entities like “Portugal” or “Angela Merkel” or “austerity”). These entities (counting over 6000) are part of a larger domain ontology which consists of several class hierarchies, e.g., the Euro crisis vocabulary, companies and banks, and geographical data.

We decided to focus our experiment on Portugal, as it is representative as a financially troubled country in the analysed period. Therefore the news articles were filtered to include only the articles mentioning Portugal. The preparation stage consisted of two steps. The first step involved counting the number of times Portugal occurs together with every other entity of interest (around 6000 entities) for each day of the collected history of articles. The second step involved selecting only

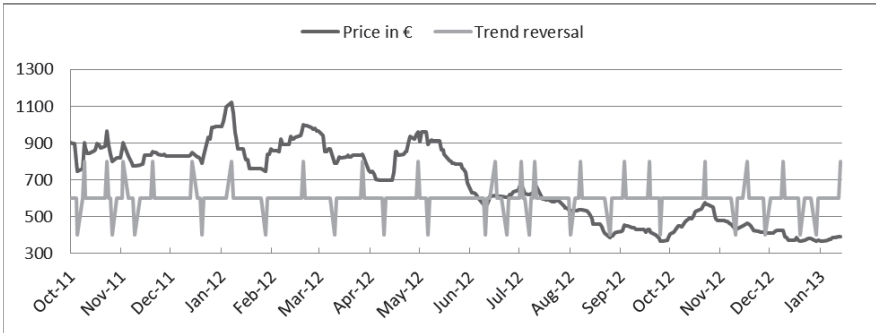


Figure 1: Portugal CDS prices and trend reversals between October 2011 and January 2013. Upward spikes indicate local maxima, while downward spikes indicate local minima.

the significant co-occurrences as example features. Each day represents one learning example and each example is described by the presence or absence of a certain entity that co-occurred with Portugal on that day. To filter out uninformative entities, we kept only the entities with a co-occurrence frequency at least 1.5 times greater than the average co-occurrence frequency over all days.

The target attribute for each example (day) was computed from the CDS prices of Portugal and has three possible values that indicate the significant local extremes in the CDS price timelines: ‘max’ or ‘min’ if the local extreme was reached, respectively, or ‘steady’ if there was no change in the trend (Figure 1). These steps yielded a dataset of 337 examples, each with an average of 282 features (ranging between 35 and 761).

The processed news and blogs articles, the CDS local extremes and the domain ontology were encoded as a set of RDF triples which were input to the Hedwig system.

4 Financial use case

In our experiment, we focused on finding subgroups for two target classes which represent trend reversals: the local maximum (‘max’) represents the date when the CDS price started to decrease and the local minimum (‘min’) the opposite. In both

cases, we used the WRAcc SD rule score, a beam width of 100, minimum coverage of 5 examples and the maximum number of predicates per rule of 6.

For the case of CDS price reaching the maximum (target class ‘max’), the best scoring subgroup was:

$$\text{Max}(X) \leftarrow \text{reg_Western_Europe}(X), \text{Angela_Merkel}(X), \\ \text{glo_austerity}(X), \text{glo_recession}(X). [28, 7]$$

For the case of CDS price reaching the minimum (target class ‘min’), the best scoring subgroup was:

$$\text{Min}(X) \leftarrow \text{Index}(X), \text{comp_GALP_ENERGIA}(X), \\ \text{Loan_Term}(X), \text{glo_fiscal_stimulus}(X). [43, 8].$$

The first rule indicates that Portugal CDS prices reaching a local maximum are characterized by increased frequency of the following entities co-occurring with Portugal: Western Europe regions, Angel Merkel, and the terms ‘austerity’ and ‘recession’. We should point out that a local maximum in a country’s CDS price indicates that from that day on, the market expectation that the country will default decreased. Conversely, the second rule tells us that when the CDS price reach a local minimum, we can notice an increased frequency of (stock) index terms, Portugal’s corporation of natural and renewable energy companies (Galp Energia), loan terms and ‘fiscal stimulus’. These results show that the higher the CDS prices, the more the sovereign debt vocabulary is used. When CDS prices are low, a more general financial terminology is used.

5 Conclusions

The newly developed semantic subgroup discovery system Hedwig was presented, which overcomes the limitations of existing semantic subgroup discovery systems. Compared to standard subgroup discovery, novelties of this paper are the exploitation of the ontology to generalize over the entities, while also using of the user-provided binary relations and using the *subClassOf* relation to guide the search procedure. We are performing a comprehensive study to show the comparison of the new system with the related work.

We employed Hedwig for analysing news articles about Portugal during the last year and a half. Using co-occurrence frequencies of entities appearing together with Portugal, a domain ontology linking the entities into a formal hierarchy, and a history of Credit Default Swap (CDS) prices, we induced subgroups describing prominent entities appearing at times of CDS trend reversals (either upward or downward). The extracted subgroup descriptions give us a clear indication that the news article content does indeed reflect the CDS prices. Having this information, we are encouraged to proceed with building a model for CDS trend reversal prediction. For this purpose, we plan to include additional information about the entities (e.g., TF-IDF weights) and extra-textual information (not only the pre-defined ontological entities) into the input data. Additionally, we will employ several classification algorithms and compare them.

Acknowledgments

This work was supported by the Slovenian Research Agency [grants P-103 and P-04431] and the EU projects FIRSST and FOC. We would like to thank Igor Mozetič for his help with conceiving the experiment and interpreting the results.

References

- [1] M. H. DeGroot and M. J. Schervish. *Probability and Statistics*, chapter 8, 9. Addison-Wesley, 2002.
- [2] D. Gamberger, D. Lučanin, T. Šmuc. Descriptive Modeling of Systemic Banking Crises. In *Proceedings of Discovery Science 2012*, Lyon, France, 2012, Springer, LNCS, vol. 7569, pp. 67-80
- [3] W. Klösgen. *Advances in knowledge discovery and data mining*. American Association for Artificial Intelligence, Menlo Park, CA, USA, 1996
- [4] N. Lavrač, B. Kavšek, P. A. Flach, L. Todorovski: Subgroup Discovery with CN2-SD. *Journal of Machine Learning Research* 5: 153-188, 2004
- [5] K. Shimada, K. Hirasawa, J. Hu. Class Association Rule Mining with Chi-Squared Test Using Genetic Network Programming. In *Proceedings of IEEE International Conference on Systems, Man and Cybernetics*, Taipei, Taiwan, pp. 5338-5344, 2006
- [6] I. Trajkovski, N. Lavrač, and J. Tolar. SEGs: Search for enriched gene sets in microarray data. *Journal of Biomedical Informatics*, vol. 41, pp. 588–601, 2008
- [7] A. Vavpetič and N. Lavrač. Semantic Subgroup Discovery Systems and Workflows in the SDM-Toolkit. *The Computer Journal* 56(3): 304-320 first published online June 4, 2012 doi:10.1093/comjnl/bxs057, 2013

- [8] S. Wrobel. An algorithm for multi-relational discovery of subgroups. In *Proceedings of the 1st European Conference on Principles of Data Mining and Knowledge Discovery*, Trondheim, Norway, pp. 78–87. Springer, 1997
- [9] M. Žáková, F. Železný, J. A. García-Sedano, C. M. Tissot, N. Lavrač, P. Kremen and J. Molina. Relational data mining applied to virtual engineering of product designs. In *Proceedings of the 16th International Conference on Inductive Logic Programming*, Santiago de Compostela, Spain, pp. 439–453, Springer, 2006
- [10] J. Hull, M. Predescu, and A. White. The relationship between credit default swap spreads, bond yields, and credit rating announcements. *Journal of Banking & Finance*, Vol. 28, No. 11., pp. 2789-2811, Elsevier 2004.

For wider interest

Our work was stimulated by our collaboration in the Forecasting Financial Crises (FOC) EU project. The topic of the FOC project is to understand and possibly forecast systemic risk and global financial instabilities.

In our work we started from a large collection of web news articles from a variety of internet sources and focused on answering the following question: what is the main vocabulary (e.g., countries, persons, companies) that is used in the news when certain financial events occur? More specifically, we focused on a troubled Eurozone country, Portugal, and the trend changes in its Credit Default Swap (CDS) prices which reflect the risks to the lending of money to the country in question. The higher the CDS prices, the higher the chances of the country failing to repay its debts.

In the paper, we introduce a novel system Hedwig that was used for the previously described task. We report the main vocabulary occurring in news together with Portugal at the time when its CDS price reached a global extreme (a local minimum or maximum). In the long term, we intend to induce models for actually predicting the future CDS trend changes based on the contents of the current news articles.

Nanoznanosti in nanotehnologije (Nanosciences and Nanotechnologies)

Hidrotermalna sinteza fotokatalitične prevleke iz TiO_2 na aluminiju

Anže Abram^{1,2}, Goran Dražič^{1,2,3}

¹ Department for Nanostructured Materials, Jožef Stefan Institute, Ljubljana, Slovenia

² Jožef Stefan International Postgraduate School, Ljubljana, Slovenia

³ National Institute of Chemistry, Laboratory for materials electrochemistry, Ljubljana, Slovenia

anze.abram@ijs.si

Povzetek. Titanov dioksid (TiO_2) je zaradi svojih fotokatalitičnih lastnosti postal pomemben material v tehnologijah čiščenja zraka ter odpadne in pitne vode. Izrazite fotokatalitične lastnosti kaže v obliki delcev nanometerskih dimenzij. Veliko nanomaterialov je zdravju škodljivih, zato se njihovi uporabi v obliki nanoprahov ter suspenzij izogibamo, saj tako najlažje vstopajo v telo. Raziskali smo možnost priprave trdno vezane obloge anataznega TiO_2 filma na aluminijevi podlagi, pripravljene po postopku hidrotermalne sinteze iz titanovega izopropoksida ($\text{Ti}(\text{OCH}(\text{CH}_3)_2)_4$) v vodnem mediju. Sinteza je potekala pri različnih temperaturah, od 100° do 200°C , in različno dolgo. Za karakterizacijo sem uporabil rentgensko praškovno difrakcijo, vrstično ter presežno elektronsko mikroskopijo z elementno analizo, mikroskop na atomsko silo ter UV/VIS spektrometer za določanje spremembe koncentracije organske spojine (kofeina) po obsevanju vzorcev z UV svetlobo. Izkazalo se je, da poleg anataznih nanodelcev na površini kristalizira predvsem bemit ($(\gamma\text{-AlO}(\text{OH}))$). Površina kaže fotokatalitske lastnosti.

Ključne besede: fotokataliza, TiO_2 , titanov dioksid, aluminij, čiščenje odpadnih vod, hidrotermalna sinteza, tanki filmi, plasti, ekologija

1 Uvod

Nanodelci ter z njimi povezana tehnologija lahko že sami po sebi predstavljajo ekološki in zdravstveni izziv. V naravi so prisotni od nekdaj, vendar je njihovo uporabo potrebno omejiti, saj so zaradi lahkega vnosa v telo skozi dihala ali kožo zdravju škodljivi. Vpliv nanodelcev titanovega dioksida na zdravje je v zadnjih letih še posebno raziskano zaradi njegove množične uporabe [1,2]. Prav zato je veliko

raziskav usmerjenih v imobilizacijo titanovega dioksida v obliki trdno vezanih prevlek [3]. Preveleke s postopkom reaktivnega naprševanja z magnetom ter plazemskim nanašanjem so se izkazale za učinkovite, a so fotokatalitične lastnosti in kakovost nanosa nezadovoljivi. Tehnika potapljanja (dip-coating) in nanašanja z vrtenjem (spin-coating) se pogosto uporablja za pripravo homogenih prevlek, a so le-te slabo sprijete s podlago in predstavljajo ekološki problem. Močno vezane prevleke po postopku hidrotermalne sinteze [4] pa predstavljajo dobro rešitev za obrabno obstojne prevleke, ki bi zmanjšale vnost nano titanovega dioksida v okolje.

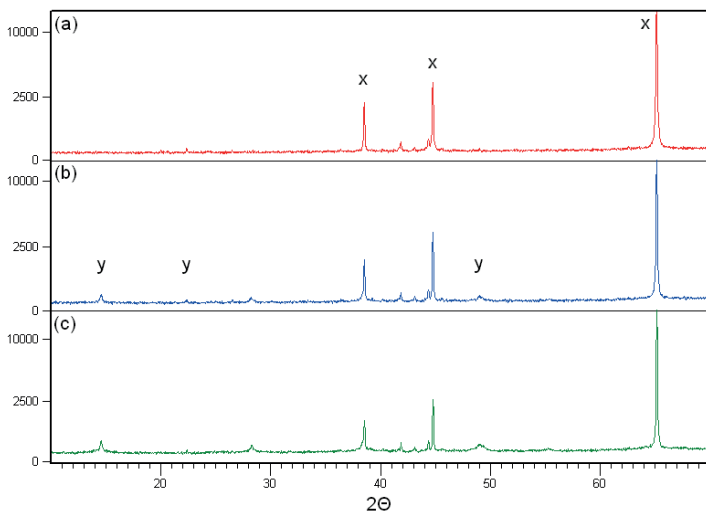
2 Metode in materiali

Hidro- oz. solvothermalna sinteza je metoda kristalizacije iz raztopine pri visokih tlakih in visoki temperaturi pri čemer je topilo voda (hidro-) ali neka organska spojina (solvo-). [5,6] Kristalizacija poteka v avtoklavih; to so jeklene posode ki vzdržijo visok tlak. Reakcijska zmes je hermetično zaprta znotraj njih. Zaradi možnosti korozije in onesnaženja vzorca je raztopina ločena od jeklene posode z inertnim materialom, v našem primeru teflonom. Uporabili smo večnamenski avtoklav brez mešanja pri temperaturah med 100 in 200 °C ter časih do 48 ur in raztopino titanovega izopropoksida ($\text{Ti}(\text{OCH}(\text{CH}_3)_2)_4$) v vodnem mediju pri 50% polnitvi.

Hidrotermalno obdelane vzorce iz pločevine Impol M13 ($\text{AlSi0,2Fe0,6Cu0,4Mn0,39Mg0,36}$) smo karakterizirali z rentgensko praškovno difrakcijo, vrstično ter presevno elektronsko mikroskopijo z elementno analizo, mikroskopom na atomsko silo, določitvijo stičnega kota ter UV/VIS spektroskopijo za spremembe koncentracije organske spojine (kofeina) po obsevanju vzorcev z UV svetlobo.

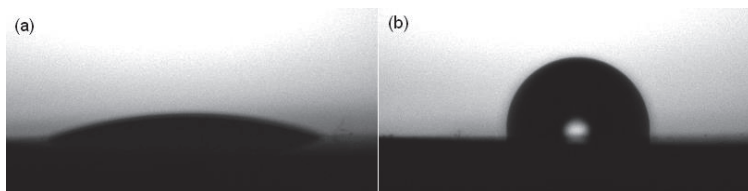
3 Rezultati in diskusija

Rentgenska praškovna analiza je pokazala, da se po hidrotermalni sintezi na površini aluminija pojavi bemit. Pri višjih temperaturah sinteze so vrhovi bemita bolj izraziti. Količina titanovega dioksida na površini je v primerjavi z bemitom majhna in ga zato ni bilo mogoče identificirati prek XRD spektrov (Slika 1).



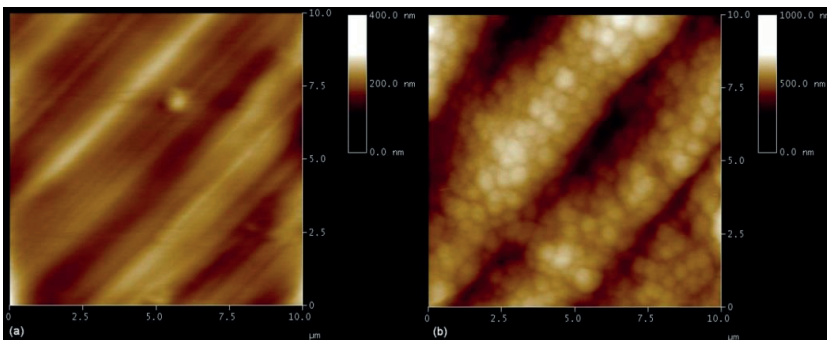
Slika 1: Difraktogrami vzorcev, pripravljenih pri različnih temperaturah. Z »x« so označeni vrhovi aluminija, z »y« pa vrhovi bemita. (a) neobdelana podlaga (b) Hidrotermalno obdelana podlaga, 150 °C, 12h (c) Hidrotermalno obdelana podlaga, 200 °C, 12h

Nano TiO_2 naredi površino po obsevanju z UV svetlobo hidrofilno, kar je prikazano na sliki 2.



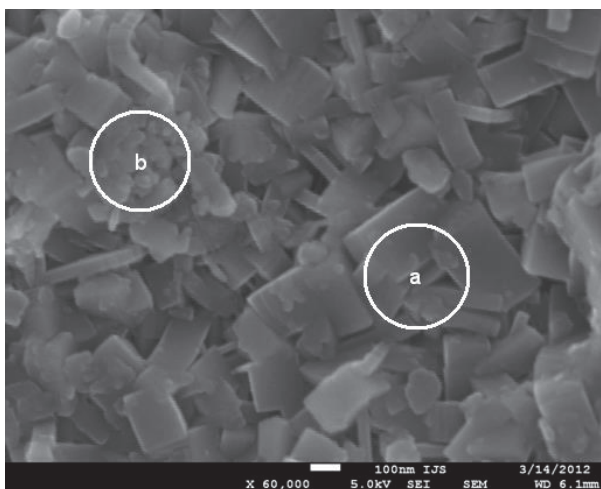
Slika 2: Primerjava stičnega kota na obdelanem in neobdelanem vzorcu po obsevanju z UV svetlobo. (a) Obdelan vzorec, stični kot $\sim 25^\circ$ (b) Neobdelan vzorec, stični kot $\sim 80^\circ$

Na AFM posnetku (Slika 3) so vidne raze na neobdelani podlagi, ki so posledica mehanske obdelave pločevine. Pri obdelanih vzorcih se te ohranijo, na njih pa kristalizira bemit. Povprečna velikost delcev bemita je okoli pol mikrona. Hrapavost vzorcev (Rms) se po obdelavi poveča iz 20 na 80 nm.



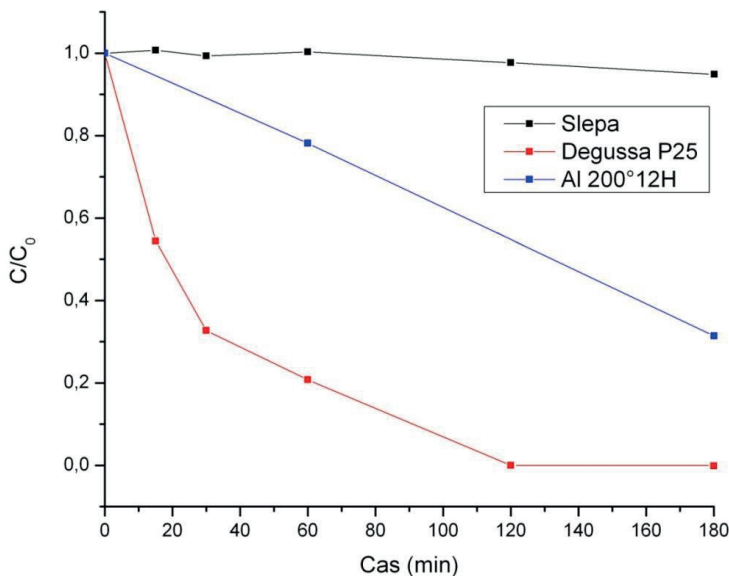
Slika 3: AFM posnetek neobdelanega (a) in hidrotermalno obdelanega vzorca (b)

Iz SEM posnetkov je razvidno, da homogenost nanosa narašča z višjo temperaturo in daljšimi časi sinteze. Pri temperaturi 150 °C in času 12h so TiO_2 delci ujeti med večje kristale bemita (Slika 4).



Slika 4: SEM posnetek hidrotermalno pripravljene vzorca 150 °C, 12 ur.
Med kristali bemita (a) so nanodelci TiO_2 (b), identificirani z EDXS.

Fotokatalitičnost smo dokazali z razgradnjo kofeina. Vzorec je bil postavljen na dno 10 ml reaktorja iz kvarčnega stekla, v kateri je bila 10ppm raztopina kofeina. Reaktor je bil obsevan v sterilizatorju z UV izvorom. Znižanje koncentracije kofeina s časom obsevanja smo določili z UV/VIS/NIR spektrometrom. Na sliki 5 je primerjava hidrotermalno pripravljenega vzorca s kontrolnim vzorcem (slepa proba, kjer ni bilo dodatka TiO_2) ter komercialnim Degussa P25 TiO_2 prahom.



Slika 5: Delež razgradnje kofeina po času za slep vzorec, Degussa P25 in hidrotermalno pripravljena aluminijeva podlaga, 200 °C 12h.

Pokazali smo, da je s postopkom hidrotermalne sinteze možno pripraviti trdno vezano oblogo titanovega dioksida, ki je fotokatalitično aktivna. Poleg titanovega dioksida kristalizira na površini tudi bemit.

Literatura:

- [1] Landsiedel, R., Ma-Hock, L., Kroll, A., Hahn, D., Schnekenburger, J., Wiench, K., & Wohlleben, W. Testing metal-oxide nanomaterials for human safety. *Advanced materials (Deerfield Beach, Fla.)*, 22(24), 2601–27, 2010.
- [2] Gajewicz, A., Rasulev, B., Dinadayalane, T. C., Urbaszek, P., Puzyn, T., Leszczynska, D., & Leszczynski, J. Advancing risk assessment of engineered nanomaterials: application of computational approaches. *Advanced drug delivery reviews*, 64(15), 1663–93, 2012.
- [3] Fujishima, a, Zhang, X., & Tryk, D. TiO₂ photocatalysis and related surface phenomena. *Surface Science Reports*, 63(12), 515–582, 2008.
- [4] Cho, C. H., Han, M. H., Kim, D. H., & Kim, D. K. Morphology evolution of anatase TiO₂ nanocrystals under a hydrothermal condition (pH=9.5) and their ultra-high photo-catalytic activity. *Materials Chemistry and Physics*, 92(1), 104–111, 2005.
- [5] Byrappa, K., Yoshimura, M. *Handbook of hydrothermal technology; A Technology for Crystal Growth and Materials Processing*. Noewich: Noyes Publications and William Anbdrew Publishing, 2001.
- [6] Byrappa, K., & Adschiri, T. Hydrothermal technology for nanotechnology. *Progress in Crystal Growth and Characterization of Materials*, 53(2), 117–166, 2007.

Za širši interes

Eden največjih problemov trajnostnega razvoja je zagotovitev zadostne količine pitne vode v prihodnosti. Poraba vode raste proporcionalno s svetovno populacijo, medtem ko se zaloge hitro zmanjšujejo. V manj razvitih delih sveta dostop do čiste in pitne vode že danes predstavlja velik problem. Prav zato se velik poudarek daje tehnologijam čiščenja zraka in vode, med katerimi svoje mesto v zadnjih letih zasedajo tudi sistemi samočistilnih naprav na osnovi fotokatalize. Fotokatalitski materiali, ki so po navadi v obliki nanometerskih delcev, med obsevanjem z ultravijolično svetlobo (ki je prisotna tudi v sončni svetlobi) tvorijo radikale, ki razgrajajo organske snovi, ki pridejo v stik z organskimi delci. S pravilno pripravo lahko dosežemo samočistilni efekt na cenovno ugoden način, kar je še posebej pomembno za države v razvoju, kjer dostop do drugih tehnologij ni mogoč.

Nanodelci lahko že sami po sebi predstavljajo ekološki in zdravstveni izziv zaradi lahkega vnosa v telo skozi dihala ali kožo. Vpliv nanodelcev titanovega dioksida na zdravje je v zadnjih letih še posebno raziskan zaradi njegove množične uporabe v kozmetiki (sončne kreme). Zato je veliko raziskav usmerjenih v imobilizacijo titanovega dioksida v obliki trdno vezanih prevlek. Obstaja več možnosti priprave takih plasti (plazemsko nanašanje, potapljanje,...), ki pa bodisi ne dajo zadostnih fotokatalitskih učinkov ali pa so prešibko vezani na podlago. Postopek hidrotermalne sinteze predstavlja dobro rešitev za obrabno obstojne prevleke, ki bi zmanjšale vnos nano titanovega dioksida v okolje.

Gre za postopek, pri katerem raztopino s prekursorjem in podlago postavimo v hermetično zaprto posodo in izpostavimo povišani temperaturi, kar posledično poveča tlak v reakcijski posodi. Zaradi istočasnega raztapljanja prekursorja v vodi in obarjanja nanodelcev na površine, ki so v stiku z vodo, se na podlagi tvori tank sloj titanovega dioksida. Tako pripravljene obloge titanovega dioksida na aluminiju so se izkazale za fotokatalitsko učinkovite.

Transformations of alcohols mediated by *N*-halosuccinimides: reactions in solution or under solvent-free conditions

Njomza Ajvazi¹, Stojan Stavber^{2,3}

¹ Jožef Stefan International Postgraduate School, Ljubljana, Slovenia

² Department of Organic and Bioorganic Chemistry, Jožef Stefan Institute, Ljubljana, Slovenia

³ Centre of excellence for integrated approaches in chemistry and biology of proteins

njomzaajvazi@hotmail.com

Abstract. The efficiency of direct conversion of tertiary alcohols to vicinal halohydrins – chlorohydrins and bromohydrins – under green reaction conditions was tested preliminarily on model tertiary benzyl alcohols. Tertiary alcohols were successfully directly halogenated to vicinal halohydrins with *N*-halosuccinimide in organic solvents, aqueous organic solvents (cyclopentyl methyl ether, 2-methyl tetrahydrofuran, acetic acid and acetonitrile) and in aqueous media. The efficiency of the reaction in water was significantly improved in the presence of sodium dodecyl sulphate as the surfactant. Various transformations of alcohols were performed also under solvent-free reaction conditions, in solution or under alkyl alcohol high concentration conditions mediated by catalytic amount of *N*-halosuccinimide. Phenyl substituted alcohols undergo at least three different reaction pathways: transformation to phenyl-substituted alkenes, dimerization and formation of ethers. The type of transformation depends on the reaction conditions and a structure of an alcohol.

Keywords: halogenation; *N*-halosuccinimide; alcohols; etherification; dimerization

1. Introduction

Vicinal halohydrins are extremely versatile building blocks in organic, medical and industrial chemistry and widely used for transformation into epoxides [1] and ketones [2]. Halohydrins can be directly synthesized by functionalization of alkenes to *vic*-halohydrins with a variety of reagents: such as molecular halogens in combination with water [3], *N*-halosuccinimide with water in the presence of β -cyclodextrin [4a], ionic liquid [4b], thiourea [4c], or ammonium acetate [4d].

Furthermore, alkyl aryl ethers are important solvents and synthetic building blocks for the production of fragrances, cosmetics, pharmaceuticals, and dyestuffs [5]. One of the most common methods for the preparation of ethers is the Williamson ether synthesis, which requires the conversion of an alcoholate with alkyl derivatives of Bronsted acids [6], then reductive etherification of aromatic aldehydes with decaborane [7]. However, these synthetic procedures for preparation both vicinal halohydrins and alkyl aryl ethers have several disadvantages: such as multiple step synthesis, toxic and expensive reagents, problematic manipulation, and long reaction time.

In this work various alcohols were transformed by *N*-halosuccinimides into corresponding vicinal halohydrins, ethers, dimers or alkenes under various reaction conditions - reactions in solution, under alkyl alcohol high concentration reaction conditions or under solvent-free conditions. Newly developed methods present a significant contribution from a green chemistry viewpoint, economy of time and reagents.

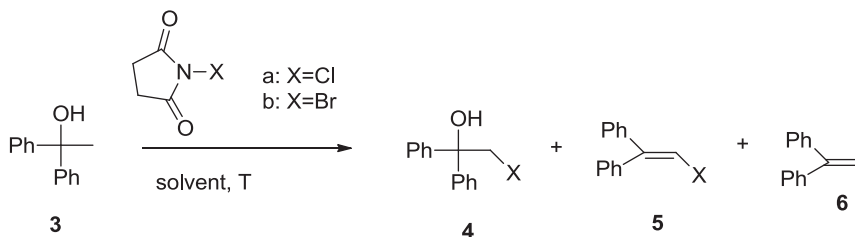
2. Results and discussion

2.1 Halogenation of tertiary alcohols in organic solvents

We chose 1,1-diphenylethanol (3, see Table 1) as a model compound to find the best reaction conditions for its conversion to halohydrins. The reactions were performed using 1 mmol of 1,1-diphenylethanol and 1.1 mmol *N*-halosuccinimide

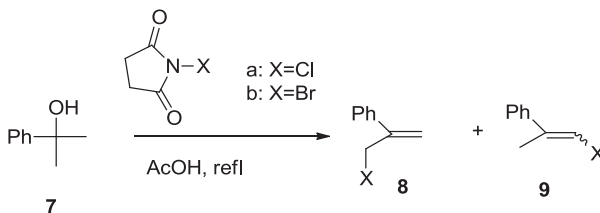
and organic solvents (cyclopentyl methyl ether, 2-methyl tetrahydrofuran, acetic acid or acetonitrile) as the reaction medium. It was found that the reactions gave the mixture of products: 2-halo-1,1-diphenylethanol (4), 1-halo-2,2-diphenylethene (5) and 1,1-diphenylethene (6).

Scheme 1 Transformation of 1,1-diphenylethanol 3 with NCS (*N*-chlorosuccinimide) and NBS (*N*-bromosuccinimide) in organic solvents



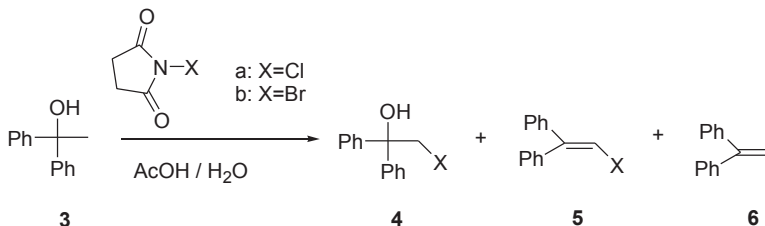
We found that in cyclopentyl methyl ether quantitative conversion of starting material occurred in the case of reaction with equimolar amount of NCS and NBS resulting in the formation of eliminated product (6) as the main product. Also in 2-methyl tetrahydrofuran we observed a high conversion of alcohol to the product (6). In acetonitrile we observed that the conversion of alcohol with NCS is much lower than with NBS. Moreover, NCS causes formation of halohydrin (4) and addition-elimination product (5), while in reaction with NBS halohydrin (4) is the main product. To check a transformation also on some other tertiary alcohols 2-phenyl-2-propanol was treated with NCS and NBS in acetic acid (7, see Scheme 2). In this case both possible addition-elimination products (8) and (9) were formed. We found that in the NCS-mediated reaction the formation of (3-chloro-1-en-2-yl)benzene (8) was predominant, while the reaction with NBS gave (1-bromo-1-en-2-yl)benzene (9) as the main one.

Scheme 2 Transformation of 2-phenyl-2-propanol 7 with NXS in acetic acid ^{a)}



We further studied how the addition of water to the acetic acid reaction media affects the course of the reaction of 1,1-diphenylethanol (3) with NBS or NCS. We observed that when large amounts of water were added, the formation of vicinal halohydrin products were exclusive, while in the case of low relative concentration of water, the addition-elimination process was found to be exclusive.

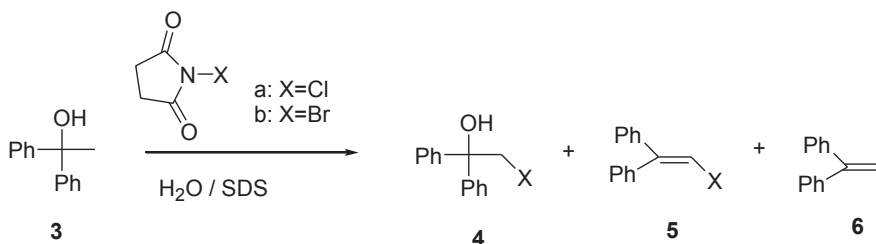
Scheme 3 The influence of addition of water to acetic acid reaction media on the course of the reaction of 1,1-diphenylethanol 3 with NCS and NBS



2.2. Halogenation of tertiary alcohols in water in the presence of a surfactant

Since from green chemistry point of view water is the best substitution for any organic solvent, we checked the course of the reaction of 1,1-diphenylethanol (3) with NXS in pure water. The conversion of starting material after the reaction with NCS was low, while the NBS-mediated transformation gave considerably higher yield. In order to improve efficiency of this transformation we tested if addition of a surfactant has any effect on the course of the reaction. We chose sodium dodecyl sulfate (SDS) as the surfactant.

Scheme 4 The course of the reaction of 1,1-diphenylethanol 3 with NXS in aqueous media in the presence of SDS



From the study of the influence of the concentration of surfactant on conversion of 1,1-diphenylethanol in water with NCS and NBS (presented in figure 1 and 2) was established that the catalytic effect of SDS in the case of NCS-mediated reaction reaches its maximum efficiency at its 3×10^{-3} M concentration, while in the case of NBS-regulated reactions the optimal concentration of SDS was found to be between 3×10^{-3} and 8×10^{-3} M. It was found that the choice of surfactant had a significant influence on the yield and the reaction time; namely, addition of SDS increases the yields and reduces the reaction times.

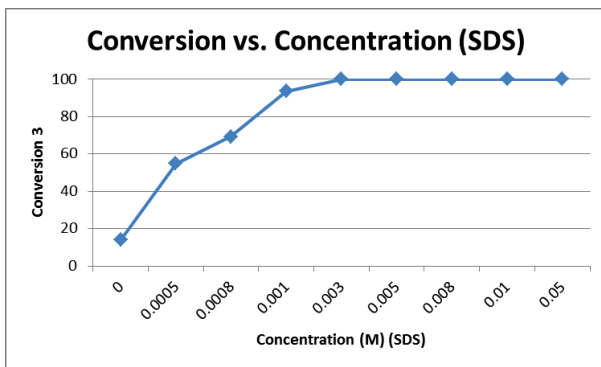


Figure 1 The effect of added amount of SDS surfactant on the efficiency of the reaction of 1,1-diphenylethanol 3 with NCS

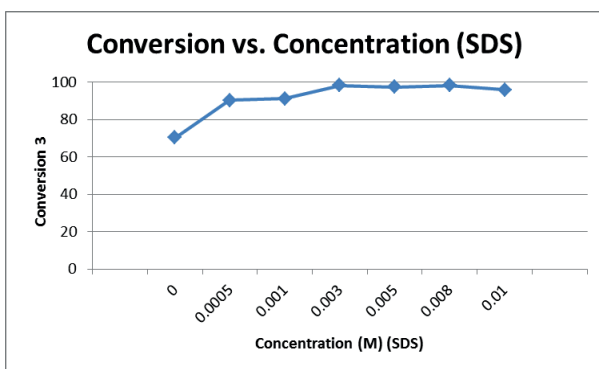
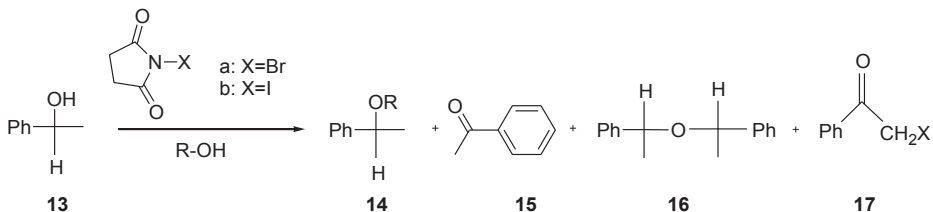


Figure 2 The effect of added amount of SDS surfactant on the efficiency of the reaction of 1,1-diphenylethanol 3 with NBS

Following the principles of green chemistry we further checked the transformation of secondary and tertiary alcohols with catalytic amounts of *N*-halosuccinimides under solvent-free conditions, in solution or in the presence of another alkyl alcohol under high concentration conditions.

Table 1 The catalytic effect of NIS and NBS on conversion of 1-phenylethanol 13 under solvent-free conditions or in solution ^{a)}



Entry	X ^c	R-OH	Conv.(%)	Relative distribution (%) ^b			
				14	15	16	17
1	I	/	91	/	13	78	/
2		MeOH (1ml)	100	82	/	18	/
3	Br	/	37	/	5	32	/
4		MeOH(1mmol)	41	19	4	15	3

^a Reaction conditions: 13 (0.5 mmol), time 5-24h at temp. 49-75°C

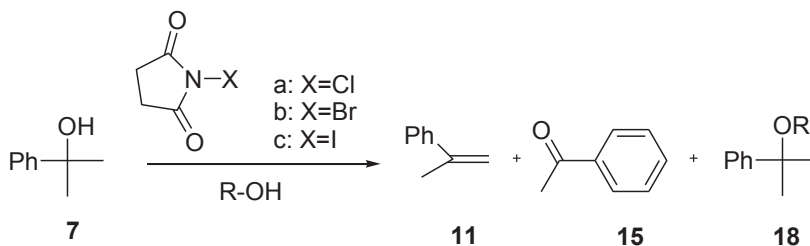
^b Determined from ¹H NMR spectra of the isolated crude reaction mixtures

^c Catalytic amount: 3-5 mol %.

We showed that 1-phenylethanol (13) can be directly converted to methyl ether (14, entry 1) with catalytic amount of NIS in methanol solution. In the case NBS-catalysed reaction, low conversion of the starting material was observed in the presence of another alkyl alcohol under high concentration reaction conditions where methyl ether and dimer were the main products (14, 16 entry 2). We observed that the transformation of 1-phenylethanol catalysed by NIS under solvent-free

reaction conditions was higher than in reaction with NBS and in both cases dimer was the main product (16, entries 1,3)

Table 2 The catalytic effect of NXS on conversion of 2-phenyl-2-propanol **7** under solvent-free conditions or in solution ^{a)}



Entry	X ^c	R-OH	Conv. (%)	Relative distribution		(%) ^{b)}
				11	15	
5	Cl	MeOH (1ml)	100	/	/	100
6		EtOH (5ml)	100	53	/	47
7		PrOH (5ml)	96	74	/	22
8	Br	/	87	66	21	/
9		MeOH (1mmol)	86	/	/	86
10		MeOH (5ml)	100	/	/	100
11		EtOH (1ml)	100	60	/	40
12		PrOH (1ml)	93	62	/	31
13		iPr (1ml)	97	59	/	38
14 ^d	I	MeOH (1mmol)	44	35	3	6
15		MeOH (2ml)	94	/	/	94

^a Reaction conditions: **7** (0.5 mmol), time 18-48h at temp. 50-87°C

^b Determined from ¹H NMR spectra of isolated crude reaction mixtures

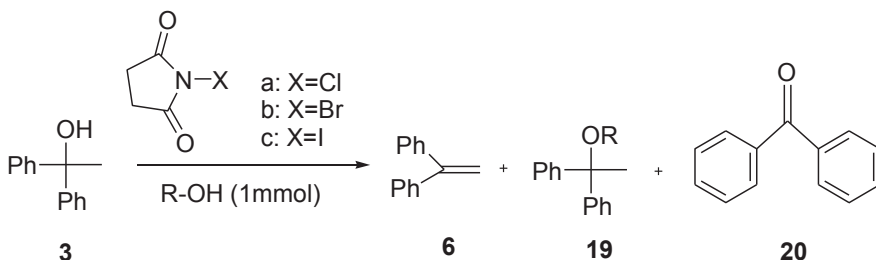
^c Catalytic amount: 0.5-6 mol %

Similarly to 1-phenylethanol we showed that 2-phenyl-2-propanol (**7**) could be directly converted to ether with catalytic amount NXS in solution. This conversion was performed in the presence of another alkyl alcohol under high concentration

reaction conditions where in reaction with NBS we observed the higher conversion of the starting material (entry 9).

We observed that 2-phenyl-2-propanol (7) in reaction in the presence of catalytic amounts of NBS under solvent-free conditions gave mainly the elimination product (11, entry 8).

Table 3 The catalytic effect of NIS and NCS on conversion of 1,1-diphenylethanol 3 under solvent-free conditions ^{a)}



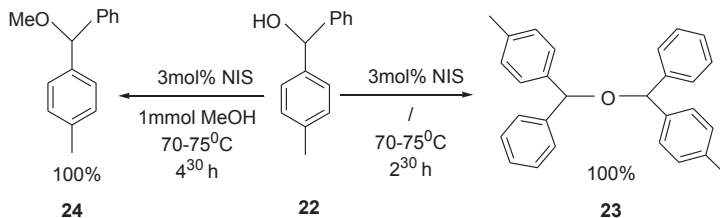
Entry	X	R-OH	Conv.(%)	Relative distribution (%) ^{b)}		
				6	19	20
16	Cl	MeOH	45	25	20	/
17	Br	/	12	12	/	/
18		MeOH	84	50	6	28
19		EtOH	100	68	/	32
20		PrOH	100	100	/	/
21		iPrOH	100	71	/	29
22		tert-BuOH	55	44	/	11
23	I	/	96	96	/	/
24		MeOH	100	88	/	12

^a Reaction conditions: 3 (0.5 mmol), NXS 0.5-5 mol %, time 3³⁰-48h at temp. 60-75°C

^b Determined from ¹H NMR spectra of isolated crude reaction mixtures

We showed that transformation of 1,1-diphenylethanol (3) catalysed by NIS and NBS in the presence of another alkyl alcohol under high concentration reaction conditions gave the elimination product (6, entries 18, 19, 20, 21, 22 and 24) as the main product, while in reaction with NCS the elimination product (6) and ether (19) were main products (entry 16). We observed that 1,1-diphenylethanol (3) in reaction

with NIS (quantitative conversion of the starting material), NBS (low conversion of the starting material) as catalytic amount under solvent-free conditions gave the elimination product (6) as the main product (entries 17, 23).



We showed that the transformation of 4-methylbenzhydrol (22) catalysed by NIS in the presence of another alkyl alcohol under high concentration reaction conditions gave ether (24), while under solvent-free conditions gave dimer (23) as the main products.

3 Conclusions

We showed that tertiary alcohols could be directly converted to vicinal halohydrins using *N*-halosuccinimides as halogenating reagents.

These transformations were successfully performed in the following solvents: cyclopentyl methyl ether, 2-methyl tetrahydrofuran, acetic acid, acetonitrile and water. In all cases vicinal halohydrins were found to be the main products except in the case of the reaction in acetic acid, where the formation of haloalkene was the main process. Transformation of tertiary alcohols to vicinal halohydrin in aqueous media was considerably enhanced and yields improved in the presence of sodium dodecyl sulphate in the amounts around its critical micelle concentration.

Furthermore, we developed a new method for direct conversion of secondary and tertiary alcohols to dimeric ethers catalyzed by *N*-halosuccinimides under solvent-free reaction conditions.

Direct *N*-halosuccinimides catalyzed transformation of secondary and tertiary alcohols into alkyl aryl ethers were performed under alkyl alcohol high concentration reaction conditions or in solution. In the case of 1,1-diphenylethanol (3) dehydration resulting in the 1,1-diphenylethene was observed in the presence of catalytic amounts of *N*-halosuccinimides under solvent-free conditions, while phenyl-substituted secondary and tertiary alcohols under the same conditions gave dimeric products. Phenyl-substituted secondary alcohols under alkyl alcohol high concentration reaction conditions gave alkyl ethers.

So far, we obtained benzyl alkyl ether and we are in a good way to get dialkyl ethers under the same conditions.

4 References:

- [1] M. B. Smith, J. March. *Advanced Organic Chemistry, 5th Edition*. Wiley-Interscience, New York, NY 2001.
- [2] D. Dolenc, M. J. Harej. *Org. Chem.* 67, 312, 2002
- [3] J. H. Rolston, K. J. Yates. *Am. Chem. Soc.* 91, 469, 1969
- [4] (a) M. Narender, M. Somi Reddy, Y. V. D. Nageswar, K. J. Rama Rao. *Mol. Catal. A: Chem.* 10, 258, 2006, ; (b) J. S. Yadav, B. V. S. Reddy, G. Baishya, S. J. Harshavardhan, Ch. Janardhana Chary, M. K. Gupta. *Tetrahedron Lett.* 46, 3569, 2005; (c) B. Das, K. Venkateswarlu, K. Damodar, K. J. Suneel. *Mol. Catal. A: Chem.* 269, 17, 2007; (d) P. A. Bentley, Y. Mei, J. Du. *Tetrahedron Lett.* 49, 1425, 2008
- [5] F. Edgar, T. Jörg. *Org. Process Res. Dev.* 9, 206-211, 2005
- [6] S. Ege. *Organic Chemistry structure and reactivity, 5th Edition*. Houghton Mifflin Co., Boston New York 2004.
- [7] S. H. Lee, Y. J. Park, C. M. Yoon. *Tetrahedron Lett.* 40 6049-6059, 1999

For wider interest Aim of this work is to achieve direct conversion of tertiary alcohols to vicinal halohydrins — chlorohydrins and bromohydrins — under green reaction conditions, i.e. to find a synthetic way that allows us a selective introduction of chlorine and bromine atom into organic molecule in only one step by using less hazardous reagents with lower impact on human health and environment. We showed that tertiary alcohols could be directly converted to vicinal halohydrins using *N*-halosuccinimides. These transformations were successfully performed in the following solvents: *cyclopentyl methyl ether*, *2-methyl tetrahydrofuran*, *acetic acid*, *acetonitrile* and *water*. In all cases vicinal halohydrins were found to be the main products except in the case of the reaction in acetic acid, where the formation of haloalkene was the main process. Transformation of tertiary alcohols to vicinal halohydrin in aqueous media was considerably enhanced and yields improved in the presence of *sodium dodecyl sulphate* in the amounts around its critical micelle concentration. Additionally, we performed these transformations under alkyl alcohols high concentration reaction conditions. Furthermore, we have discovered and developed new method for direct conversion of secondary and tertiary alcohols to dimeric ethers using *N*-halosuccinimides in catalytic amount under solvent-free reaction conditions. Another new method of direct transformation of secondary and tertiary alcohols into alkyl aryl ethers was discovered and developed using *N*-halosuccinimides in catalytic amounts in the presence of another alkyl alcohol under high concentration reaction conditions or in solution. So far, we obtained benzyl alkyl ether and we are in a good way to get dialkyl ethers under the same conditions. These discoveries represent considerable contribution to the green chemical approach to transformations of alcohols into various valuable derivatives.

Electrical and thermal properties of polymer systems with coexisting ferroelectric and relaxor states

Goran Casar^{1,2}, Xinyu Li³, Jurij Koruza^{1,2}, Qiming Zhang³, Vid Bobnar^{1,2}

¹ Jožef Stefan Institute, Ljubljana, Slovenia

² Jožef Stefan International Postgraduate School, Ljubljana, Slovenia

³ Department of Electrical Engineering and Materials Research Institute, The Pennsylvania State University, University Park, Pennsylvania 16802, USA

goran.casar@ijs.si

Abstract. We report dielectric, thermal and electrocaloric investigations of poly(vinylidene fluoride-trifluoroethylene), P(VDF-TrFE) copolymer, irradiated with high-energy electrons. While up to now investigations have mainly focused either on non-irradiated ferroelectric P(VDF-TrFE) or copolymer, irradiated with high doses, which is completely transformed into a relaxor, we concentrate on P(VDF-TrFE) samples, irradiated with low doses. Dielectric investigations, particularly nonlinear dielectric results, and differential scanning calorimetry data clearly evidence that in these samples ferroelectric and relaxor states coexist. It is also shown that large electrocaloric response of P(VDF-TrFE)-based systems is further enhanced in systems with coexisting relaxor and ferroelectric states.

Keywords: relaxor, polymer, nonlinear dielectric spectroscopy, calorimetry.

Polymers, based on polyvinylidene fluoride, PVDF, have played an important role in sensor and actuator applications due to their high piezoelectric effect. Similar high piezoelectric response was found in poly(vinylidene fluoride-trifluoroethylene), P(VDF-TrFE) copolymer, which, contrary to PVDF, spontaneously crystallizes into a polar phase. When P(VDF-TrFE) system is further manipulated either with high-energy electrons irradiation or with additional monomers, all-trans chains in normal P(VDF-TrFE) are converted into nanopolar regions, thus transforming the material into a relaxor system. Relaxor polymers have been proposed for various advanced applications as they possess high strain response, high electric energy density with

fast discharge speeds and large electrocaloric effect [1]. Up to now investigations have mainly focused either on ferroelectric polymers or polymers that are completely transformed into a relaxor. We report dielectric, thermal and electrocaloric investigations of P(VDF-TrFE) copolymer, irradiated with low doses of high-energy electrons using Van de Graaff generator. In addition to linear dielectric investigations and differential scanning calorimetry (DSC), nonlinear dielectric spectroscopy was used in order to clearly show that at lower irradiation doses ferroelectric and relaxor states coexist in the P(VDF-TrFE), which strongly influences some of the materials properties, particularly the electrocaloric response.

Figure 1 shows the temperature dependences of the real, ϵ' , and imaginary, ϵ'' , parts of the complex linear dielectric constant, detected at various frequencies in the ferroelectric P(VDF-TrFE) copolymer and in samples irradiated with 20, 40 and 60 Mrad. In the non-irradiated sample both, ϵ' and ϵ'' , reach a frequency-independent maximum at the paraelectric-to-ferroelectric phase transition temperature. The dielectric maximum temperature becomes more frequency dependent as doses of high-energy electrons increase, and in 60 Mrad sample the temperature of dielectric maximum becomes fully frequency-dependent in the entire frequency range. Such a broad dispersive dielectric maximum is a typical feature of relaxor systems [2].

While a linear relation between polarization P and electric field E is valid only for relatively low electric fields, for higher fields the polarization can be expressed as a power series of E as $P/\epsilon_0 = (\epsilon' - 1)E + \epsilon_2' E^2 + \epsilon_3' E^3 + \dots$. Here, ϵ_2' and ϵ_3' represent the real parts of the second and the third order nonlinear dielectric constants, respectively. ϵ_2' is nonzero only for the macroscopically noncentrosymmetrical systems and is proportional to the net polarization, while ϵ_3' can distinguish between the discontinuous, first order, and continuous, second order ferroelectric phase transition, and the relaxor behaviour [3]. In addition, the dielectric nonlinearity $a_3 = -\epsilon_3' / \epsilon_0^3 \epsilon'^4$ can also distinguish the type of the phase transition and has already been used for the description of the nonlinear properties of relaxors [2].

Figure 2 shows the temperature dependences of the real part of the third order nonlinear dielectric constant in the ferroelectric and irradiated samples. Although the

ferroelectric phase transition in the P(VDF-TrFE) 65/35 mol. % was reported to be of a weakly first order [4], in our case ϵ_3' changes sign at the phase transition

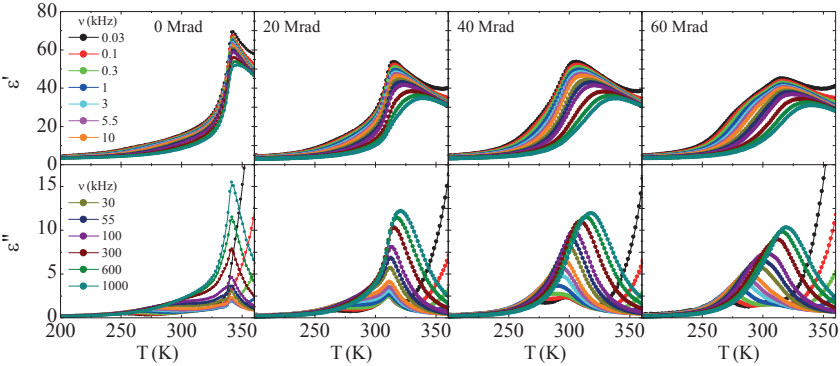


Figure 1: ϵ' and ϵ'' vs. temperature, detected at various frequencies in the ferroelectric and irradiated P(VDF-TrFE) copolymer samples.

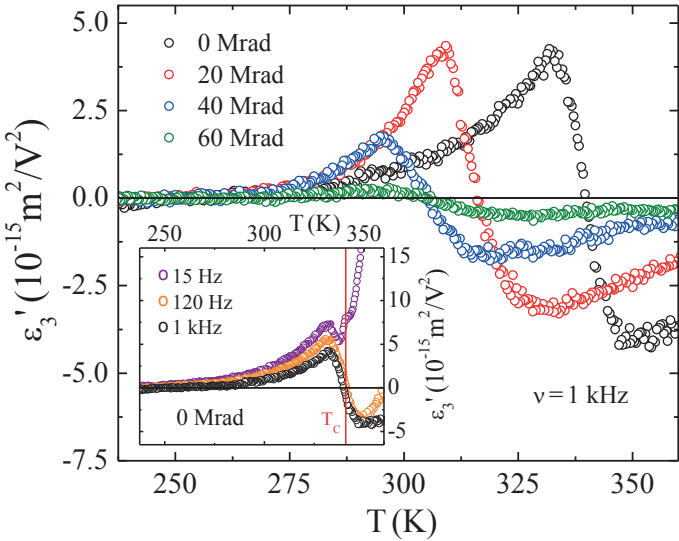


Figure 2: Temperature dependences of the real part of the third order nonlinear dielectric constant in the ferroelectric and irradiated samples. The inset shows response of the ferroelectric sample at different frequencies of the applied signal.

temperature, which is predicted by the Landau theory for the second order phase transitions [3]. This can be either due to the fact that the 65/35 mol. % sample is

very close to the transition type boundary, thus already a small change in the ratio could change the transition type (the 70/30 mol. % copolymer undergoes a second order transition, while for the 56/44 mol. % sample the first order transition was reported [4]), or due to the fact that our samples were uniaxially stretched. The latter seems to be more likely – it is namely known that clamping on a substrate (perhaps via ordering of the polymer chains) changes the type of the phase transition in the P(VDF-TrFE) 70/30 mol. % copolymer films [4].

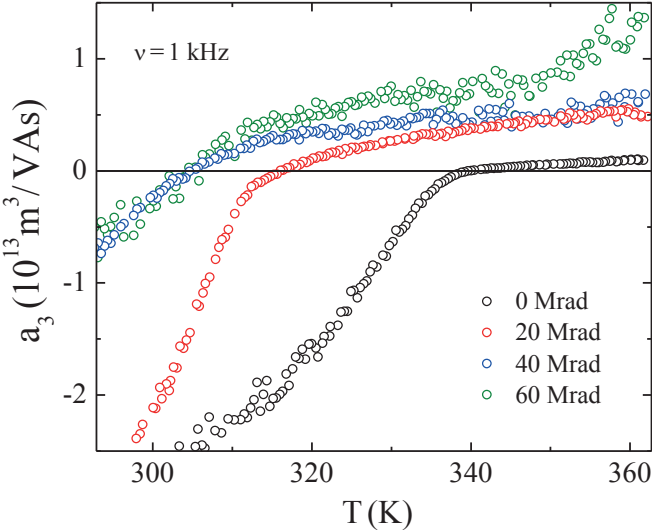


Figure 3: Dielectric nonlinearity a_3 vs. temperature in the ferroelectric and irradiated P(VDF-TrFE) samples.

Figures 2 and 3 clearly reveal that in our samples ferroelectric and relaxor states coexist. While in relaxors ϵ_3' and a_3 are always positive, here both quantities change sign – exactly at T_C as is evident from the inset to Figure 2. $a_3(T)$ also very precisely depicts the decreasing of T_C as a consequence of irradiation. The inset to Figure 2 indicates that the third harmonic response is always positive at low frequencies due to the increasing conductivity contribution at higher temperatures, thus in the main frames of Figures 2 and 3 data detected at 1 kHz are shown. The coexistence of ferroelectric and relaxor states in irradiated samples has additionally been confirmed with DSC experiments. While these investigations have been performed mainly in

order to study the influence of irradiation on the melting peak, the inset to Figure 4 reveals the presence of the ferroelectric phase in irradiated samples.

The electrocaloric effect is related to the change in temperature and entropy when the electric field is adiabatically applied to the material, and is proportional to the degeneracy of the elementary dipolar entities and to the induced polarization [5]. Electrocaloric investigations of P(VDF-TrFE) samples, irradiated with different doses, are presented in Figure 5, which reveals that the response is enhanced in samples, irradiated with 40 Mrad and 20 Mrad, particularly around the ferroelectric transition temperature. Although disorder certainly increases with the dose of irradiation, the electric field apparently more efficiently polarizes the samples with coexisting ferroelectric and relaxor states.

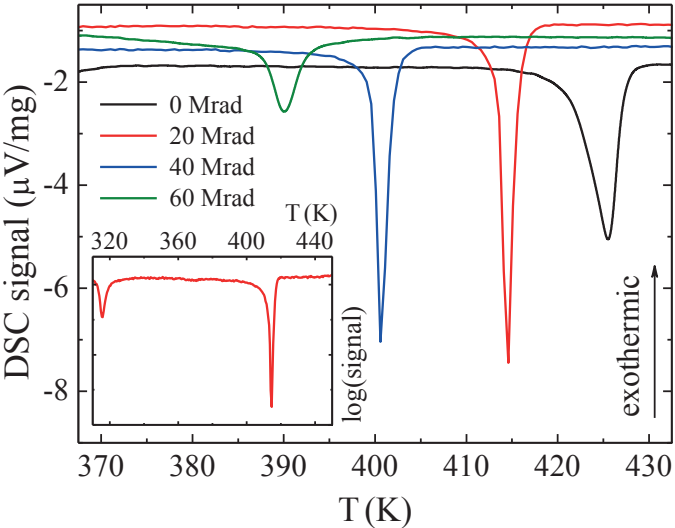


Figure 4: DSC traces of P(VDF-TrFE) in the temperature range around melting peaks. The inset shows the trace of the 20 Mrad sample in a broad temperature range, revealing also a ferroelectric transition peak at around 315 K.

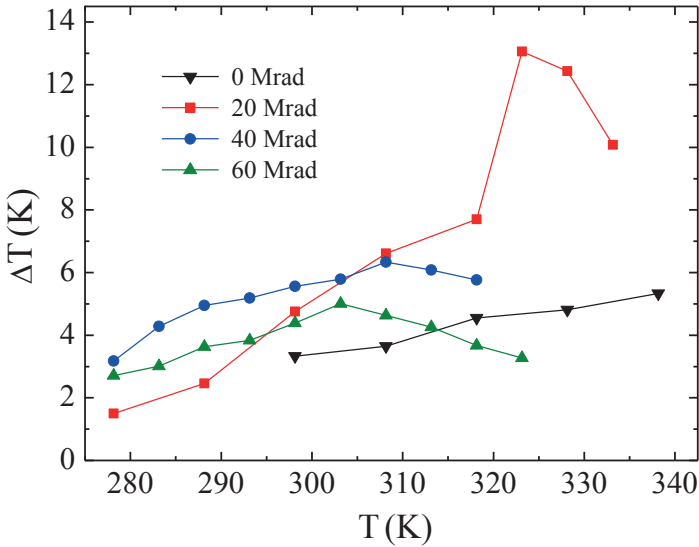


Figure 5: Comparison of the electrocaloric effect in the ferroelectric and irradiated P(VDF-TrFE) copolymer at different temperatures.

References:

- [1] B. Nesse, B. Chu, S. G. Lu, Y. Wang, E. Furman, Q. M. Zhang. Large Electrocaloric Effect in Ferroelectric Polymers Near Room Temperature. *Science*, 321(5890): 821-823, 2008.
- [2] V. Bobnar *et al.*, Crossover from Glassy to Inhomogeneous-Ferroelectric Nonlinear Dielectric Response in Relaxor Ferroelectrics. *Phys. Rev. Lett.*, 84(25): 5892-5895, 2000.
- [3] S. Miga, J. Dec. Non-linear Dielectric Response of Ferroelectric and Relaxor Materials. *Ferroelectrics*. 363(1): 141-149, 2008.
- [4] D. Nordheim, S. Hahne, B. Ploss. Nonlinear dielectric properties and polarization in thin ferroelectric P(VDF-TrFE) copolymer films. *IEEE Trans. Dielect. Elec. Insul.* 19(4): 1175-1180, 2012.
- [5] R. Pirc, Z. Kutnjak, R. Blinc, Q. M. Zhang. Upper bounds on the electrocaloric effect in polar solids. *Appl. Phys. Lett.*, 98(2): 021909, 2011.

For wider interest

Dielectric spectroscopy investigates electrically-induced properties of a material as a function of frequency and/or temperature. Dielectric properties are related to polarizability and thus depends on the structure and molecular properties of a material. That is why it is an useful tool for material characterization and is used in pharmacy, biotechnology and material science. The basic quantity in dielectric spectroscopy is complex dielectric constant ϵ^* , which consists of the real, ϵ' , and imaginary, ϵ'' , part. The real part is related to stored energy within the medium, whereas the imaginary part describes the losses. That is why the dielectric constant is very important in devices for storing electrical energy (capacitors).

Numerous materials are also able to convert the electrical energy into mechanical work (electromechanical effect) or into heat (electrocaloric effect) – note that electrical energy converted into heat in electrocalorics is not due to the electrical current running through it. Such properties of a material can be utilized in many devices such as actuators, sonars, integrated microelectromechanical systems or artificial muscles, which use the electromechanical effect, or in heating/cooling devices of new generation, which use the electrocaloric effect.

Ferroelectrics and relaxors are materials that possess giant electromechanical and electrocaloric effect. Our subject of study was P(VDF-TrFE), a relaxor polymer system. Relaxor polymers in comparison to other inorganic relaxors have some advantages: they have greater electromechanical response, exhibits fast response speeds and can be prepared in variety of shapes. P(VDF-TrFE) is normally a ferroelectric system and becomes relaxor under sufficient doses of high-energy electron irradiation. Up to now investigations were mainly focused either on ferroelectric P(VDF-TrFE) or on polymer, irradiated with high doses of high-energy electrons, which is completely transformed into a relaxor. Our aim was to investigate P(VDF-TrFE), irradiated with lower doses, which was believed to be neither ferroelectric nor completely transformed into a relaxor. In our work we show, by means of dielectric spectroscopy and differential scanning calorimetry, that ferroelectric and relaxor states indeed coexist in P(VDF-TrFE), irradiated with low and moderate doses. In addition we demonstrate how such a coexistence influences some of the materials properties, particularly the electrocaloric response.

Synthesis of superparamagnetic clusters as a carrier for wine fining agents

Peter Dušak^{1,2}, Slavko Kralj¹, Darko Makovec^{1,2}

¹ Department of Materials Synthesis, Jožef Stefan Institute, Ljubljana, Slovenia

² Jožef Stefan International Postgraduate School, Ljubljana, Slovenia

peter.dusak@ijs.si

Abstract. The haze in wines presents a problem for wineries. Phenolic and polyphenolic compounds are one of factors involved in haze formation. To eliminate them, fining agents working on protein-phenol or polyphenol interactions are used. Traditional fining agents for wine making, e.g. egg white, caseinate, etc., can cause allergic reactions by consumers. A possible issue to remove fining agents after fining is their immobilization on superparamagnetic carriers. Superparamagnetic clusters (SCs) were synthesized as fining carriers by controlled heteroagglomeration of nanoparticles (NPs) in aqueous media. For easier analysis two model types of NPs, i.e. silica nanoparticles (SNPs) and superparamagnetic iron oxide nanoparticles (MNPs), and two types of interactions were studied, i.e. electrostatic (EI) and chemical (CI), to form clusters. Better results were observed by CI, which were further used to synthesize SCs, composed of MNPs.

Keywords: fining agents, polyphenols, superparamagnetic clusters, controlled heteroagglomeration, allergens.

1 Introduction

Beverage clearness is an important parameter in beverage industry, especially in winemaking. One of the major problems of bottled wines is their instability, which is seen as a haze [1]. Besides protein factors, the haze formation in wine is caused by the presence of phenolic compounds. Phenolic compounds, i.e. chemically structured as a hydroxyl group bonded to an aromatic ring, can be classified into two groups: basic phenolic compounds and polyphenols [2]. Wine phenolics belong to two main groups, non-flavonoid and flavonoid. They are related to wine colour, e.g.

free anthocyanins [3], astringency, bitterness and oxidative level and also to well-known health beneficial effects as antioxidants, e.g. resveratrol [4].

Polyphenols show a great diversity of structures, ranging from rather simple molecules, with molecular weights of about 100 Da, to polymers of thousands of Da [5]. They can be oxidized by molecular oxygen with side chain amino groups of peptides at alkaline pH to quinines, leading to the formation of protein cross-links [6]. These highly reactive quinines can irreversibly react with the sulfhydryl and amino groups of proteins. The cause of haze in wine is protein-polyphenol interaction [7]. Polyphenols may interact with proteins reversibly and irreversibly [2]. In reversible interactions, usually non-covalent forces such as hydrogen bonding, hydrophobic bonding and van der Waals forces are involved [8], whereas in irreversible interactions, covalent bonds are formed between the polyphenols and proteins [9]. Proteins and polyphenolic compounds can combine to form soluble complexes, held together by weak associations, which can lead to sedimentation [8, 10]. To clarify wine, fining is used as a processing technique.

Fining agents work on a principle of protein-polyphenol interaction. Traditionally used fining agents in wine making are egg white [11], gelatin [11], isinglass, and caseinate [12]. Besides traditional fining agents, synthetic polymers, such as polyvinyl pyrrolidone [13, 14], poly(vinylpyrrolidone) [13], are used to adsorb polyphenols from wine. Some of these fining agents, like caseinate [15] and egg white [16] might cause allergic reactions. To prevent allergic reactions fining agents used to clarify wines or as stabilizers need to be listed on the wine label [17, 18]. The removal of allergenic fining agents from wine presents a challenge for wine manufacturers. A possible issue for this challenge is an immobilization of fining agents, e.g. casein, on an appropriate carrier, that could be easily removed after fining. MNPs are promising materials as a carrier in separation applications because of their ability to be manipulated with an external magnetic field. To disperse the magnetic particles it is beneficial if they are small enough to be in the superparamagnetic state, which is usually below 20 nm. In applications that involve guiding particles in a magnetic-field gradient, assembly into SCs show a distinct advantage over individual superparamagnetic NPs, due to the magnetic force acting on them [19]. As a carrier, a SC can be used. SCs can be prepared by controlled

heteroagglomeration, i.e. agglomeration between oppositely charged particles, of NPs in aqueous suspensions.

In this work the controlled heteroagglomeration of maghemite MNPs in their aqueous suspension was used to prepare SCs. For easier analysis, the interactions between the carboxyl-functionalized magnetic nanoparticles (cMNPs) and the amino-functionalized silica nanoparticles (aSNPs) were studied instead of the interactions between two different functionalized types of MNPs. Finally, the SCs from different functionalized types of MNPs were formed.

2 Experimental work

The cluster preparation was studied by using two model types of functionalized NPs, i.e. aSNPs and cMNPs, which interact by attractive electrostatic interactions (EI) or by chemical interactions (CI). Finally, SCs were prepared by using two types of differently functionalized MNPs.

The superparamagnetic maghemite (γ -Fe₂O₃) NPs were synthesized using co-precipitation from aqueous solutions. The preparation of a stable aqueous suspension of NPs using citric acid as the surfactant has been described elsewhere [20]. The NPs in the stable aqueous suspension were coated with an approximately 4-nm-thick layer of silica by the hydrolysis and polycondensation of tetraethoxysilane (TEOS) in the presence of an alkaline catalyst, NH₄OH [21].

SNPs were received from National Institute of Chemistry. The preparation of SNPs was done by a modified Stöber process described elsewhere [22].

The surfaces of the SNPs and silica-coated MNPs were specifically functionalized, i.e., silane molecules, with amino or with carboxyl terminal functional groups, were grafted onto their surfaces. aSNPs and amino-functionalized magnetic nanoparticles (aMNPs) were functionalized by grafting 3-(2-aminoethylamino) propylmethyldimethoxysilane (APMS) onto their surfaces, as described elsewhere [21], with some modification. In brief, the APMS dissolved in ethanol (100 ml) was added to 100 mL of suspension containing the SNPs (500 mg). The addition of APMS was 5 μ mol calculated per 1 m² of the NP surface. The pH value of the

reaction mixture was set to 11 using NH_4OH . The reaction mixture was then heated to $50\text{ }^\circ\text{C}$ and stirred for 5 h. After ageing, the suspension of functionalized NPs was completely stable. aSNPs and aMNPs were washed and re-dispersed in distilled water.

cMNPs were prepared by grafting pre-synthesized carboxyl silane onto silica-coated MNPs. The carboxyl silane was synthesized by reacting the APMS and succinic anhydride in N, N- dimethylformamide [21].

To study mechanisms that can be applied to synthesize the SCs, the interactions between the two types of the functionalised model NPs were studied. For easier analysis the interactions between the aSNP and cMNPs were studied. The aSNP / cMNPs ratio was set to 1: 89 assuming full coverage of aSNP core with cMNPs. The heteroagglomeration occurred in the suspension due to the attractive EI or CI between the molecules grafted at the nanoparticles' surfaces. Finally, procedures developed for the heteroagglomeration between the model nanoparticles were used to synthesize SCs containing MNPs. Here, the cMNPs were attached onto the aMNP cores. The aMNP / cMNPs ratios of 1: 6 and 1: 12 were used for study.

The EI between the negatively charged cMNPs and the positively charged aSNPs occurred when the suspension of aSNPs was vigorously admixed into the suspension of cMNPs at pH 5.5. The aSNPs / cMNPs ratio was kept constant at 1: 89, whereas the concentrations of cMNPs were different (0.007, 0.07, 0.7 and 60 mg/ml).

The CI between aSNPs and cMNPs or aMNPs and cMNPs was achieved through the covalent bonding between the activated surface carboxyl and amino groups. The carboxyl surface groups of cMNPs were activated using single-step 1-ethyl-3-(3-dimethylaminopropyl)carbodiimide (EDC) coupling protocol [23]. Briefly, the pH of the cMNP suspension was adjusted to 5 with (0.01M) HCl. The calculated amount of 5-fold molar excess of EDC solution was added to the reaction mixture. After 5 minutes of rigorously stirring the calculated amount of aSNPs or aMNPs was added and the pH value was adjusted to 7. The reaction mixture was stirred at room temperature for 2h. The CI between aSNPs and cMNPs were done at two

different concentrations (0.7 and 60 mg/ml) of cMNPs and constant aSNPs/cMNPs ratio. For the synthesis of the SCs with different functionalized MNPs, three different concentrations of cMNPs (0.5, 1 and 2 mg/ml) were used.

The initial suspensions of the functionalized NPs and synthesized clusters in the aqueous suspension were characterized by measuring a zeta (ζ)-potential (Brookhaven Instruments Corporation, ZetaPALS), dynamic light scattering (DLS; Fritsch, ANALYSETTE 12 DynaSizer) and transmission electron microscopy (TEM; JEOL 2010F).

3 Results and discussion

The average particle size of silica-coated MNPs was estimated from TEM images to be 11 ± 3 nm. The amorphous layer of silica appeared to be homogenous and of a fairly constant thickness, close to 4 nm. The specific surface area of the silica-coated MNP was estimated by considering the sizes of the MNP cores and the silica shells (measured from TEM images) to be approximately $100 \text{ m}^2/\text{g}$. The average particle size of SNPs was estimated to be $92 \pm 5 \text{ nm}$, corresponding to a calculated specific surface area of $30 \text{ m}^2/\text{g}$.

The changes in the NPs' surface charge were followed by measurements of the ζ -potential of their aqueous suspensions as a function of pH. Figure 1 shows the changes in the ζ -potential for SNPs, aSNPs, silica-coated MNPs, cMNPs and aMNPs. The silica shows a relatively acidic character, because its structure is terminated with negatively charged -OH surface groups.

Grafting the APMS to the SNPs or silica-coated MNPs provides the positive surface charge of ζ -potential, which is caused by terminal amino groups [21]. The presence of amino groups at the surfaces results in a shift of an isoelectric point (IEP) to a higher pH value of 7.5 in case of silica and silica-coated MNPs. cMNPs with the covalently attached pre-synthesized carboxyl-silane onto their surfaces showed highly negative ζ -potential at pH above IEP at approximately pH 3 due to negatively charged carboxyl groups. The high absolute values of the ζ -potential provided strong electrostatic repulsive forces between the NPs in the suspensions, providing a good colloidal stability at in broad region of pH except close to IEP.

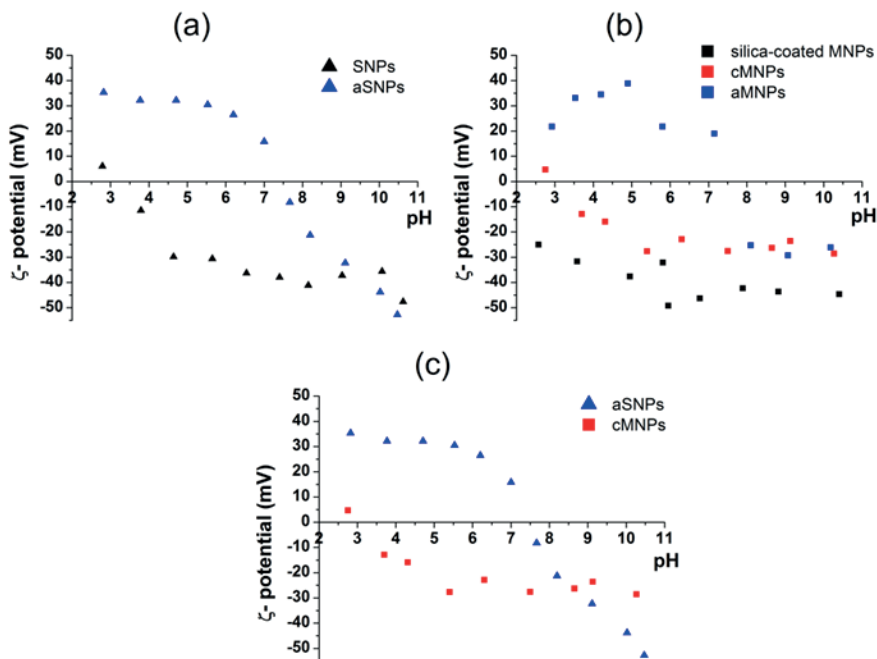


Figure 1: ζ -potential of (a) SNPs, aSNPs, (b) silica-coated MNPs, cMNPs, aMNPs, (c) potential difference between aSNPs and cMNPs.

Distribution of the hydrodynamic diameters (d_H) of NPs in their aqueous suspensions is presented by number-weighted DLS measurements (Fig. 2). aSNPs showed wide size distribution, ranging from 100 to 600 nm, with the peak at around 300 nm (Fig. 2a). The smallest sizes correspond well to the TEM size of the SNPs, whereas the majority of the SNPs were present in the form of small agglomerates.

cMNPs had narrow d_H size distribution (Fig. 2b). The majority of cMNPs had d_H size around 20 nm, in good agreement with the average diameter of cMNPs determined from the TEM images. The good correlation between these two methods indicates that the NPs are well dispersed.

First, the electrostatic interactions were studied in the case of aSNP cores and cMNPs “shell” nanoparticles. EI were done at pH 5.5, where the absolute ζ -potential difference between the two types of NPs is the highest (Fig. 1c). Figures

3a and 3b show clusters of aSNPs and cMNPs formed at lower (0.07 mg/ml) and higher (60 mg/ml) concentration of cMNPs. It is evident that smaller cMNPs were attached to the larger aSNP cores. The coverage of aSNPs with cMNPs was non-uniform. There were large differences in the coverage from aSNP to aSNP, and the individual aSNPs were covered non-homogeneously, usually containing small agglomerates of the cMNPs attached to their surfaces while larger areas were uncovered. Better coverage of the aSNP cores were achieved in the case of the higher (Fig. 3b) compared to lower (Fig. 3a) concentrations of the cMNPs.

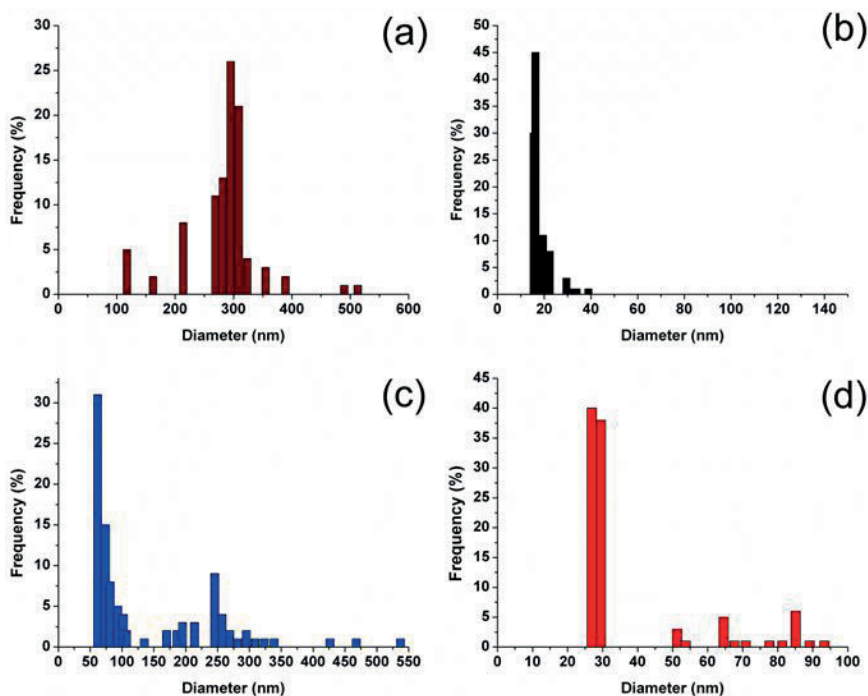


Figure 2: DLS number distribution of (a) aSNPs, (b) cMNPs, clusters formed by (c) EI, (d) SCs.

DLS measurement of the hydrodynamic size distribution of the clusters formed by EI showed two peaks (Fig. 2c). The first peak between 50 and 75 nm was attributed to the cMNPs, whereas the second peak between 150 and 300nm was ascribed to formed clusters. The reason for higher number frequency of the smaller cMNPs

compared to the clusters was the consequence of the fact that not all the cMNPs attached onto the aSNPs.

The chemical bonding of cMNPs onto the aSNPs was much more effective than EI. TEM analysis showed that the SNPs are homogeneously covered by the cMNPs. Each SNP was covered by approximately 20 cMNPs (Fig. 3c). The coverage of aSNPs core was better at higher (60 mg/ml) concentration compared to lower concentration (0.7 mg/ml) of cMNPs. The clusters formed at higher concentration had also larger hydrodynamic size distribution compared to lower concentration of cMNPs (data not shown).

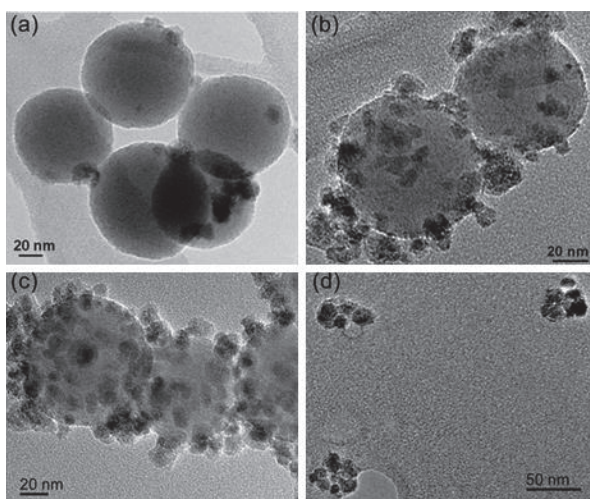


Figure 3: TEM image of (a) EI with 0.007mg/ml, (b) EI with 60mg/ml of cMNPs, (c) CI with 60mg/ml of cMNPs, (d) SCs with ratio 6 and 1mg/ml of cMNPs.

Finally, the SCs were synthesized using heteroagglomeration between aMNPs and cMNPs. At the aMNPs / cMNPs ratio 1: 12 (data not shown), the formed SCs had wide hydrodynamic size distribution (up to 500nm) compared to the ratio 1: 6 (Fig. 2d). The SCs at the higher ratio are more likely to sediment due to gravitation and are difficult to be re-dispersed once the sedimentation accrues. By lowering aMNPs / cMNPs ratio to 1: 6, the hydrodynamic size distribution of formed SCs decreased. Figure 3d shows the SCs synthesized at 1mg/ml of cMNPs and

aMNPs / cMNPs ratio 1: 6. The as-synthesized SCs had size ranging from 50-70 nm estimated from TEM images. This is in good agreement with DLS measurement (Fig. 2d), where the first peak presents individual MNPs and the second peak, i.e. 50- 95 nm presents formed clusters.

4 Conclusions

To prepare the SCs, as carriers for wine fining agents, with an appropriate size for magnetic separation, the synthesis of cluster combining two model types of NPs and two types of interactions in the suspensions, i.e. EI and CI, were studied. By the EI the coverage of aSNPs with cMNPs was non-uniform, whereas covalent CI bonding between amino groups at the surfaces of aSNPs and the activated carboxyl groups at the cMNPs lead to homogeneous coverage. The CI were further used for the synthesis of SCs. The as-synthesized SCs had an appropriate size to be effectively separated after fining by an external magnetic field.

5 Acknowledgments

This work was supported by the Slovenian Research Agency (ARRS). We acknowledge Dr. Marjan Bele from National Institute of Chemistry, Slovenia, for providing us SNPs. The authors also acknowledge the use of equipment in the Center of Excellence on Nanoscience and Nanotechnology – Nanocenter.

6 References

- [1] M. Esteruelas, N. Kontoudakis, M. Gil, M.F. Fort, J.M. Canals, F. Zamora. Phenolic compounds present in natural haze protein of Sauvignon white wine. *Food Research International*, 44(1):77-83, 2011
- [2] T. Ozdal, E. Capanoglu, F.L. Altay. A review on protein-phenolic interactions and associated changes. *Food Research International*, 2013
- [3] J.X. Castillo-Sánchez, M.S. García-Falcón, J. Garrido, E. Martínez-Carballo, L.R. Martins-Dias, X.C. Mejuto. Phenolic compounds and colour stability of Vinhão wines: Influence of wine-making protocol and fining agents. *Food chemistry*, 106(1):18-26, 2008
- [4] M.I. Fernández-Mar, R. Mateos, M.C. García-Parrilla, B. Puertas, E. Cantos-Villar. Bioactive compounds in wine: Resveratrol, hydroxytyrosol and melatonin: A review. *Food chemistry*, 130(4):797-813, 2012
- [5] S. Soares, N. Mateus, V. de Freitas. Interaction of Different Polyphenols with Bovine Serum Albumin (BSA) and Human Salivary α -Amylase (HSA) by Fluorescence Quenching. *Journal of Agricultural and Food Chemistry*, 55(16):6726-6735, 2007

- [6] T. Prodpran, S. Benjakul, S. Phatcharat. Effect of phenolic compounds on protein cross-linking and properties of film from fish myofibrillar protein. *International journal of biological macromolecules*, 51(5):774-782, 2012
- [7] K.J. Siebert. Effects of Protein–Polyphenol Interactions on Beverage Haze, Stabilization, and Analysis. *Journal of Agricultural and Food Chemistry*, 47(2):353-362, 1999
- [8] K.J. Siebert, N.V. Troukhanova, P.Y. Lynn. Nature of Polyphenol–Protein Interactions. *Journal of Agricultural and Food Chemistry*, 44(1):80-85, 1996
- [9] N.G. Kroll, H.M. Rawel, S. Rohn. Reactions of plant phenolics with food proteins and enzymes under special consideration of covalent bonds. *Food Science and Technology Research*, 9(3):205-218, 2003
- [10] E. Haslam. Natural Polyphenols (Vegetable Tannins) as Drugs: Possible Modes of Action. *Journal of Natural Products*, 59(2):205-215, 1996
- [11] A. Oberholster, L.M. Carstens, W.J. du Toit. Investigation of the effect of gelatine, egg albumin and cross-flow microfiltration on the phenolic composition of Pinotage wine. *Food chemistry*, 138(2-3):1275-1281, 2013
- [12] A. Lifrani, J. Dos Santos, M. Dubarry, M. Rautureau, F. Blachier, D. Tome. Development of Animal Models and Sandwich-ELISA Tests to Detect the Allergenicity and Antigenicity of Fining Agent Residues in Wines. *Journal of Agricultural and Food Chemistry*, 57(2):525-534, 2008
- [13] B. Laborde, V. Moine-Ledoux, T. Richard, C. Saucier, D. Dubourdieu, J.-P. Monti. PVPP–Polyphenol Complexes: A Molecular Approach. *Journal of Agricultural and Food Chemistry*, 54(12):4383-4389, 2006
- [14] F. Cosme, I. Capão, L. Filipe-Ribeiro, R.N. Bennett, A. Mendes-Faia. Evaluating potential alternatives to potassium caseinate for white wine fining: Effects on physicochemical and sensory characteristics. *LWT - Food Science and Technology*, 46(2):382-387, 2012
- [15] P. Restani, F. Uberti, R. Danzi, C. Ballabio, F. Pavanello, C. Tarantino. Absence of allergenic residues in experimental and commercial wines fined with caseinates. *Food chemistry*, 134(3):1438-1445, 2012
- [16] P. Rupa, Y. Mine. Immunological comparison of native and recombinant egg allergen, ovalbumin, expressed in *Escherichia coli*. *Biotechnology Letters*, 25(22):1917-1924,
- [17] P. Weber, H. Steinhart, A. Paschke. Investigation of the Allergenic Potential of Wines Fined with Various Proteinogenic Fining Agents by ELISA. *Journal of Agricultural and Food Chemistry*, 55(8):3127-3133, 2007
- [18] J.M. Rolland, E. Apostolou, M.P. de Leon, C.S. Stockley, R.E. O’Hehir. Specific and Sensitive Enzyme-Linked Immunosorbent Assays for Analysis of Residual Allergenic Food Proteins in Commercial Bottled Wine Fined with Egg White, Milk, and Nongrape-Derived Tannins. *Journal of Agricultural and Food Chemistry*, 56(2):349-354, 2007
- [19] A. Ditsch, S. Lindenmann, P.E. Laibinis, D.I.C. Wang, T.A. Hatton. High-Gradient Magnetic Separation of Magnetic Nanoclusters. *Industrial & Engineering Chemistry Research*, 44(17):6824-6836, 2005
- [20] S. Campelj, D. Makovec, M. Drofenik. Preparation and properties of water-based magnetic fluids. *Journal of physics. Condensed matter: an Institute of Physics journal*, 20(20):204101, 2008
- [21] S. Kralj, M. Drofenik, D. Makovec. Controlled surface functionalization of silica-coated magnetic nanoparticles with terminal amino and carboxyl groups. *Journal of Nanoparticle Research*, 13(7):2829-2841, 2010
- [22] M. Bele. Preparation and Flow Cytometry of Uniform Silica-Fluorescent Dye Microspheres. *Journal of Colloid and Interface Science*, 254(2):274-282, 2002
- [23] G.T. Hermanson. *Bioconjugate Techniques*. Academic Press, 2008.

For wider interest

Magnetic particles are promising materials for magnetic carriers, because they can be guided or held on a certain point in a magnetic-field gradient. Magnetic carriers are used in biomedicine, e.g. for drug delivery systems, in biotechnology for separation of products from complex mixture, in food industry for cleaning products from unwanted ingredients, in remediation of water from heavy-metal pollution, etc. In mentioned applications, magnetic particles are dispersed into mixture containing targeted species, e.g. molecules, cells or microorganisms. After the attachment of targeted species onto the magnetic particle, the conjugate is separated from the mixture using an external magnetic field. To disperse magnetic particles it is beneficial if they are small enough to be in superparamagnetic state, which is usually less than 20nm. The use of superparamagnetic nanoparticles is beneficial, because they do not show spontaneous magnetic moments and in contrast to larger ferri/ferromagnetic particles, they do not agglomerate due to magnetic dipole-dipole interactions.

For separation applications used in biotechnology, chemistry and especially in food industry the size of magnetic carriers is very important. In applications that involve guiding particles in a magnetic-field gradient, assembly of superparamagnetic nanoparticles into clusters shows a distinct advantage over individual superparamagnetic nanoparticles, due to much larger the magnetic force acting on them in a magnetic field gradient. Besides the size, the carrier surface has an important role in the separation applications. The carriers' surfaces need to be specifically functionalized, i.e. appropriate functional groups have to be provided at their surfaces to enable specific interactions with the targeted species needed to be separated.

The aim of our work was to study the controlled synthesis of superparamagnetic clusters, with heteroagglomeration, i.e. agglomeration between oppositely charged particles, in aqueous suspensions. These clusters would be further functionalized with a specific species, e.g. molecules, proteins, enzymes, which would interact with specific targeted species. As-prepared superparamagnetic clusters are developed to be used in food and beverage industry to separate allergen species.

Investigation of the structural, optical and electrical properties of Ta₂O₅-rich thin films from solution

Raluca C. Frunză^{1,2}, Martin Strojnik¹, Marko Jankovec³, Marko Topič³,
Barbara Malič¹

¹ Jožef Stefan Institute, Ljubljana, Slovenia

² Jožef Stefan International Postgraduate School, Ljubljana, Slovenia

³ Faculty of Electrical Engineering, University of Ljubljana, Tržaška cesta 25,

Ljubljana, Slovenia

raluca.frunza@ijs.si

Abstract. High-K dielectric Ta₂O₅-based thin films were prepared by Chemical Solution Deposition (CSD) at temperatures not exceeding 400°C. Spin coated thin films on platinized silicon and glass substrates of both pure Ta₂O₅ and the mixed ternary composition Ta₂O₅ – Al₂O₃ – SiO₂ with the Ta:Al:Si = 8:1:1 atomic ratio were investigated. The samples were XRD-amorphous and had flat surfaces. All samples showed high optical transparency in the visible range. Their dielectric permittivity values were in the range from 18 to 27. The mixed oxide samples showed a significant improvement in terms of leakage currents, which were also dependent on the thermal budget of the samples.

Keywords: high-K dielectrics, amorphous materials, sol-gel chemistry

1 Introduction

In the last decades, transparent electronics became one of the most fascinating and fast growing research areas. It aims towards the realization of fully transparent devices, and thus it requires the low cost deposition of semiconducting or dielectric thin films with suitable properties onto the substrates requiring low temperature processing, as glass or even plastic. Among the dielectric materials, tantalum pentoxide (Ta₂O₅) has attracted much interest due to its high refractive index, high relative permittivity (ϵ) and good thermal and chemical stability [1]. As a drawback, the high ϵ (in the range from 20 to 28 for amorphous structure [2]) corresponds to

the low bandgap ($E_g = 4.4$ eV [3]) hence to low bandoffsets between the tantalum pentoxide and Si or other oxides causing high leakage currents [4,5].

New multicomponent dielectrics based on a mixture of Ta_2O_5 (high ϵ , low E_g) and SiO_2 and/or Al_2O_3 (low to moderate ϵ , high E_g) would enable improved transparency and decreased leakage current as compared to the pure Ta_2O_5 , but with a trade-off in permittivity. It is worth noting that the addition of Al_2O_3 and SiO_2 , which are known as glass formers, would stabilize the amorphous phase. Generally the amorphous structure is preferred due to the smoother surface of the material and because it has no grain boundaries, which could act as paths for impurity diffusion and leakage current [3]. Therefore amorphous multicomponent dielectrics based on tantalum pentoxide emerge as promising materials for transparent electronics applications.

In this study, Ta_2O_5 -based thin films from solution were investigated. Samples of both the ternary composition $Ta_2O_5 - Al_2O_3 - SiO_2$ with the Ta:Al:Si = 8:1:1 atomic ratio (further denoted as 8:1:1) and pure Ta_2O_5 (further denoted as Ta) were processed at 300 °C and 400 °C. The samples were characterized from the structural, optical and electrical point of view.

2 Experimental details

The precursors were prepared by alkoxide-based sol gel synthesis. The solutions, all of 0.1M concentration, were synthesized at room temperature in nitrogen atmosphere. For the 8:1:1 composition, each metal precursor was dissolved separately in a suitable solvent, and the obtained solutions were mixed together. The Ta_2O_5 precursor was prepared by dissolving Ta-ethoxide in 2-methoxyethanol (2-MOE). In order to reduce the reactivity of the Ta-alkoxide, diethanolamine (DEA) in the R = 2 molar ratio of DEA over Ta-ethoxide was added. Al-butoxide was also dissolved in 2-MOE. As precursor for SiO_2 the prehydrolyzed solution of Si-ethoxide in ethanol was used. The as-prepared solutions were clear, transparent and stable.

Ta_2O_5 -based thin films were deposited on the substrates by spin coating for 30 s at a controlled speed of 3000 rpm. After each deposition, the films were heated in air on

the hot plates at 150 °C for 2 minutes and at 300 °C or 400 °C for additional 2 minutes. The spinning–heating procedure was repeated ten times. The samples were deposited on both Corning Eagle XG glass substrates and platinized silicon (Pt/TiO₂/SiO₂/Si or shortly Pt/Si) for transmittance measurements and investigation of their electrical properties, respectively.

The microstructure of the thin films deposited both on glass and on Pt/Si was investigated by X-ray diffraction (XRD) using a PANalytical X'Pert PRO diffractometer with Cu K α 1 radiation. The data were collected in the 2 θ range from 10° to 65°, with a step of 0.034° and an exposure time of 100 s per step. The surface morphology of the Pt/Si samples was analyzed by Atomic Force Microscope (AFM), by Asylum Research MFP-3D-S™. A JEOL Ltd. JSM–7600F Field Emission Scanning Electron Microscope (FE-SEM) was used to investigate the fracture surfaces of the films on Pt/Si.

The optical transmittance spectra were measured at room temperature in the spectral range 200–1100 nm using a HP 8453 UV–Vis spectrophotometer and a clean uncoated glass substrate as reference.

Au electrodes of 0.4 mm diameter were sputtered on top of the Pt/Si samples. The electrical measurements were conducted in the as-fabricated metal-insulator-metal (MIM) capacitors. Dielectric permittivity values, ϵ , and loss factor, $\tan \delta$, were measured at room temperature with a driving signal of 50 mV, at the frequency of 1 kHz using a HP 4284A impedance analyzer. The current–voltage (IV) characteristics were measured using a Keithley 2602A system sourcemeter and a HP 16058A test fixture combined setup.

3 Results and discussion

The XRD patterns recorded for the samples deposited both on glass and Pt/Si are shown in Fig. 1. The studied tantalum pentoxide-based thin films exhibited an amorphous structure as evidenced by the absence of diffraction peaks in the investigated 2 θ range.

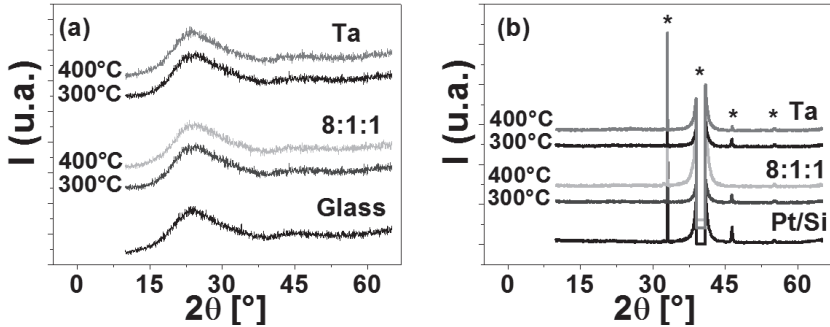


Figure 1: Diffractograms of Ta_2O_5 -based thin films spin-coated on glass (a) and Pt/Si (b). The Pt/Si substrate peaks are denoted by *.

It is known that Ta_2O_5 crystallizes at relatively high temperatures, $600\text{ }^\circ\text{C} - 700\text{ }^\circ\text{C}$ [4]. Moreover, the ternary composition material should exhibit even higher crystallization temperature due to the addition of Al_2O_3 and SiO_2 [6]. Therefore it is expected for samples subjected to temperatures not exceeding $400\text{ }^\circ\text{C}$ to be amorphous.

The surface morphology of the Ta_2O_5 -based thin films was characterized by AFM and the average root mean square (RMS) surface roughness values was about 0.2 nm. All the samples had uniform surfaces without any evident microstructural details. Fig. 2 shows three-dimensional (3D) AFM images of the samples heated at $400\text{ }^\circ\text{C}$ as obtained for the scan area of $1\text{ }\mu\text{m} \times 1\text{ }\mu\text{m}$.

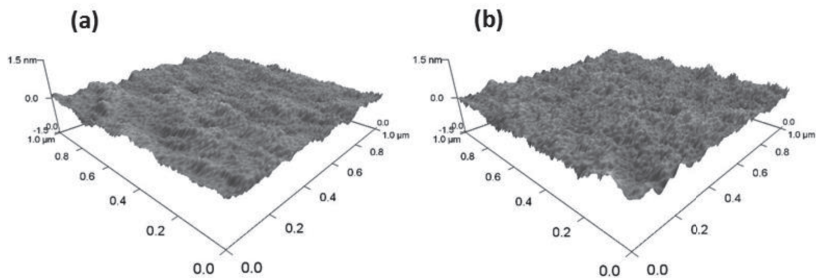


Figure 2: AFM 3D topography of the Ta (a) and 8:1:1 (b) samples deposited on Pt/Si and heated at $400\text{ }^\circ\text{C}$.

The thickness of the samples was determined from the cross-section FE-SEM images and proved to be dependent on the thermal budget, which was related to the process of densification [7]. A considerable decrease of the thickness with the heating temperature was observed from about 180 nm to about 115 nm for the samples heated at 300 °C and 400 °C, respectively, which was attributed to enhanced densification upon heating.

Typical transmittance spectra for the 300–1000 nm range are depicted in Fig. 3.

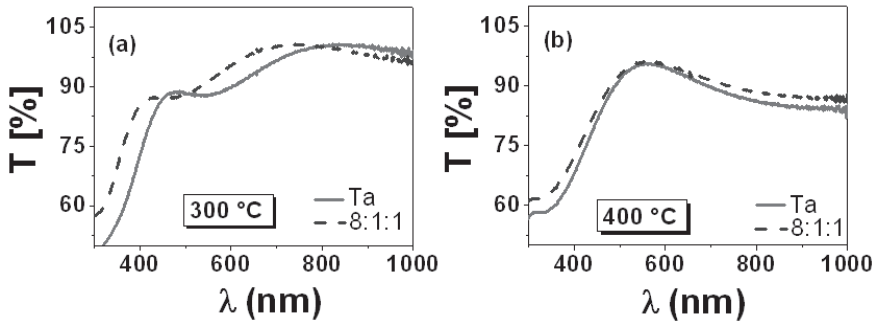


Figure 3: Optical transmittance spectra of the Ta_2O_5 -based thin films deposited on glass and heated at the temperatures of 300 °C (a) and 400 °C (b).

The number of extrema decreases with decreasing thickness [8]. For the given spectral region the 300 °C samples showed two maxima (Fig. 3a), whereas the 400 °C samples exhibited one maximum (Fig. 3b). This is in agreement with the difference in thickness. For both preparation temperatures, the transmittance rises around 300 nm and it reaches values above 65% in the visible region (400-700 nm). The films with the 8:1:1 composition exhibited a slightly higher overall optical transmittance.

The dielectric permittivity and losses of the studied films are depicted in Fig. 4a. For the samples heated at 300 °C the calculated ϵ showed no difference for the two compositions and was about 18. The Ta film heated at 400 °C exhibited the highest dielectric permittivity, a value of 27. The value obtained for the $\text{Ta}_2\text{O}_5 - \text{Al}_2\text{O}_3 - \text{SiO}_2$ film at the same temperature was lower, about 22.

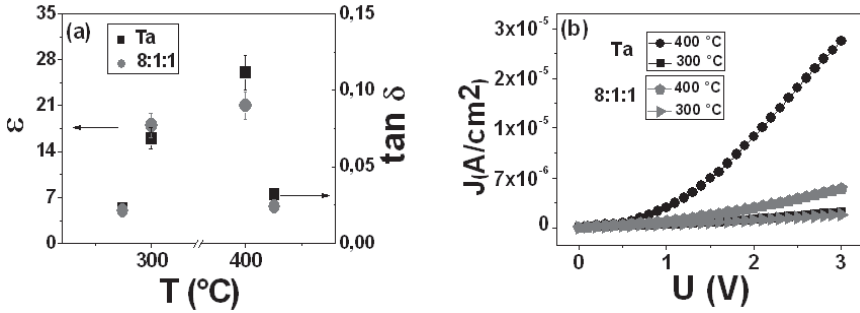


Figure 4: Dielectric properties (a) and room temperature I (V) characteristics (b) of the Ta_2O_5 -based thin films deposited on Pt/Si

For amorphous Ta_2O_5 thin films the permittivity values in the range of 20 – 28 are generally reported [2]. However, Al_2O_3 and SiO_2 exhibit lower values of ϵ than Ta_2O_5 , being respectively 9 and 3.9 [6]. The relative permittivity value roughly follows the linear rule of mixtures with composition [6], and therefore it is straightforward that the Al_2O_3 and/or SiO_2 modified oxides have a much lower ϵ than the pure ones.

In terms of the loss factor, no differences were observed for the two compositions. All the samples exhibited dielectric losses as low as 2.2% when heated at 300 $^{\circ}\text{C}$, and up to 3.2% when heated at 400 $^{\circ}\text{C}$.

The leakage current density versus the applied voltage characteristics for all the samples studied are given in Fig. 4b. The voltage was increased in steps of 0.1 V, and for each point the current was measured after a delay time of 0.1 s. Measurements on the Ta_2O_5 -based thin films indicated that the addition of Al_2O_3 and SiO_2 led to a significant improvement in terms of leakage currents, which are also dependent on the thermal budget of the samples.

Current densities of $10^{-8} - 10^{-7} \text{ A}/\text{cm}^2$ for an applied voltage of up to 3V were reported for metal-insulator-semiconductor (MIS) capacitors of amorphous Ta_2O_5 prepared by sputtering [9]. However, higher values of $10^{-5} - 10^{-6} \text{ A}/\text{cm}^2$ were reported for thin films obtained by CVD and CSD [10,11].

Up to 100 kV/cm, the investigated thin films exhibited ohmic conduction. The $\log(I)$ vs. $\log(V)$ plots (the insets in Fig. 5) were modelled as linear regressions with slopes ranging from 0.92 to 1.30, which are close to the theoretical value of 1 for ohmic conductivity.

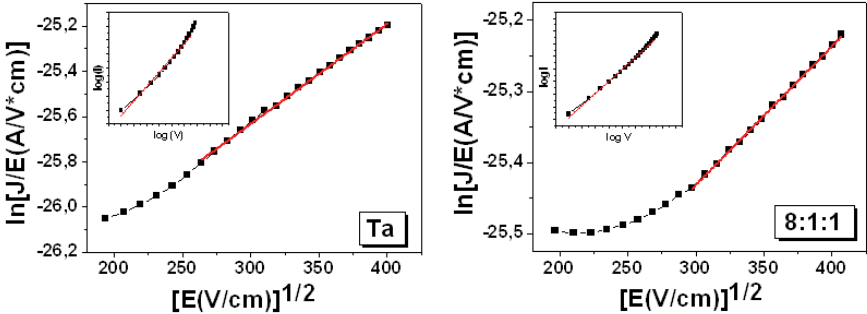


Figure 5: J - E characteristics plotted as $\ln(J/E)$ vs $E^{1/2}$ for the thin films heated at 300 °C. The insets show the $\log V$ vs. $\log I$ plots.

It was reported that the conduction in both amorphous and crystalline tantalum oxide thin films is ohmic at fields lower than 100 kV/cm [12,13], and governed by nonlinear mechanisms at higher electrical fields. In the case of the samples heated at 300 °C, the straight line characteristics of the $\ln(J/E)$ versus $E^{1/2}$ plots (Fig. 5) proved that Poole-Frenkel is the dominant conduction mechanism at high electric fields. Although the 8:1:1 thin film heated at 400 °C showed similar results, the Ta one exhibited highly nonlinear behaviour which might be due to other conduction mechanism.

4 Conclusions

Solution-derived $Ta_2O_5 - Al_2O_3 - SiO_2$ (Ta:Al:Si = 8:1:1 atomic ratio) and Ta_2O_5 thin films on platinumized silicon and glass substrates were processed at the temperatures 300 °C and 400 °C. All films were XRD-amorphous and showed high optical transparency in the visible range. The dielectric permittivity values of the thin films heated at 400 °C were 22 and 27 for the 8:1:1 and the Ta samples, respectively. The samples heated at 300 °C exhibited an ϵ value of about 18 for both compositions. As

compared to the pure Ta₂O₅ thin films, the samples with the mixed composition showed lower leakage within the investigated temperature range. The current-voltage characteristics were ohmic at low applied electric fields and exhibited Poole-Frenkel behaviour at higher applied fields.

Acknowledgements:

We acknowledge the financial support of the Slovenian Research Agency (Young researcher programme, contract number: 1000-10-310134; J2-4173: Oxide-based components for transparent electronics; P2-0105: Electronic ceramics, nano-, 2D and 3D structures). We would like to thank to the Centre of Excellence NAMASTE, which has kindly allowed us to use their equipment (AFM). The authors thank Edi Kranjc from the National Institute of Chemistry Slovenia for the XRD measurements.

The work presented in this paper has been carried out within the 7th Framework Programme of the Commission of the European Communities, Project “ORAMA”, Grant Agreement NMP3-LA-2010-246334. Financial support of the European Commission is gratefully acknowledged.

References:

- [1] S.W. Park, Y.K. Baek, J.Y. Lee, C.O. Park, H.B. Im. *Effects of annealing conditions on the properties of tantalum oxide films on silicon substrates*, Journal of Electronic Materials, 21(6):635-639, 1992
- [2] C. Chaneliere, J.L. Autran, R.A.B. Devine, B. Balland. *Tantalum pentoxide (Ta₂O₅) thin films for advanced dielectric applications*, Materials Science and Engineering, R22:269–322, 1998
- [3] J. Robertson. *High dielectric constant oxides*, European Physical Journal Applied Physics, 28: 265–291, 2004
- [4] E. Atanassova, A. Paskaleva. *Challenges of Ta₂O₅ as high- k dielectric for nanoscale DRAMs*. In *Proceedings of the 25th International Conference on Microelectronics*, 2006
- [5] P. Barquinha, L. Pereira, G. Goncalves, R. Martins, D. Kuscer, M. Kosec, E. Fortunato. *Performance and stability of low temperature transparent thin-film transistors using amorphous multicomponent dielectrics*, Journal of the Electrochemical Society, 156(11):H824–H831, 2009
- [6] J. Robertson. *High dielectric constant gate oxides for metal oxide Si transistors*, Reports on Progress in Physics, 69:327–396, 2006
- [7] G.W. Scherer. *Sintering of Sol-Gel*, Journal of Sol-Gel Science and Technology, 8: 353-363, 1997
- [8] F. Tepehan, F. Ghodsi, N. Ozer, G. Tepehan. *Optical properties of sol-gel dip-coated Ta₂O₅ films for electrochromic applications*, Solar Energy Materials & Solar Cells, 59:265–275, 1999
- [9] E. Atanassova, D. Spassov. *Electrical properties of thin Ta₂O₅ films obtained by thermal oxidation of Ta on Si*, Microelectronics Reliability, 38:827-832, 1998
- [10] C. Chaneliere, J.L. Autran, S. Four, R.A.B. Devine, B. Balland. *Theoretical and experimental study of the conduction mechanism in Al/Ta₂O₅/SiO₂/Si and Al/Ta₂O₅/Si₃N₄/Si structures*, Journal of Non-Crystalline Solids, 245: 73-78, 1999

- [11]F. Jolly, M. Passacantando, V. Salerni, L. Lozzi, P. Picozzi, S. Santucci. *Structural and electrical properties of Ta₂O₅ thin films deposited on Si(100) from Ta(OC₂H₅)₅ precursor*, Journal of Non-Crystalline Solids, 38: 233-239, 2003
- [12]S. Ezhilvalavan, T.Y. Tseng. *Conduction mechanisms in amorphous and crystalline tantalum oxide thin films*, Journal of Applied Physics, 83(9): 4797-4801, 1998
- [13]P.C. Joshi, M.W. Cole. *Influence of postdeposition annealing on the enhanced structural and electrical properties of amorphous and crystalline Ta₂O₅ thin films for dynamic random access memory applications*, Journal of Applied Physics, 86(2):871-880, 1999

For wider interest

The trend in electronics nowadays is to produce transparent and flexible devices which could be used in applications such as flat panel displays, thin-film transistors (TFTs), solar cells, organic light emitting diodes (OLEDs), etc.. Since a lot of them are just concept devices, research is made for the development of industry oriented materials and technologies. Transparent materials, possibly with an amorphous structure, are of interest. Furthermore, one main requirement for transparent electronics is the low cost deposition onto substrates requiring low temperature processing, as glass or even plastic.

Several different high-K ($K =$ permittivity, dielectric constant) metal oxides are researched, and tantalum oxide (Ta_2O_5) is a promising candidate due to its high relative permittivity (about 25 for the amorphous state), good thermal and chemical stability. Still, its high leakage currents tend to limit the advantages of pure Ta_2O_5 as high-K dielectric. To improve its electrical properties, novel amorphous multicomponent dielectrics, resulting from mixing in a single phase Ta_2O_5 and low K oxides may be considered.

From the technological point of view, these materials can be fabricated using several methods, including atomic layer deposition, sputtering, chemical solution deposition, and various processes based on chemical vapour deposition. Physically deposited layers of pure or mixtures of Ta_2O_5 were processed at low temperatures to be used in transparent TFTs. However, little work has been done on the sol-gel preparation of such materials.

This study aims at the investigation of structural, optical and electrical properties of low temperature processed high-K thin films from solution. Samples of both the ternary composition $Ta_2O_5 - Al_2O_3 - SiO_2$ with the Ta:Al:Si = 8:1:1 atomic ratio and pure Ta_2O_5 were processed at 300 °C and 400 °C.

Co-sintering of magnetoelectric composites of Co-ferrite and selected ferroelectrics

Petra Jenuš^{1,2}, Darja Lisjak¹, Danjela Kuščer^{3,4}, Darko Makovec^{1,2,5}, Miha Drofenik^{1,6}

¹ Department for Materials Synthesis, Jožef Stefan Institute, Ljubljana, Slovenia

² Jožef Stefan International Postgraduate School, Ljubljana, Slovenia

³ Electronic Ceramics Department, Jožef Stefan Institute, Ljubljana, Slovenia

⁴ Centre of Excellence NAMASTE, Ljubljana, Slovenia

⁵ CENN Nanocenter, Ljubljana, Slovenia

⁶ Faculty of Chemistry and Chemical Engineering, Maribor, Slovenia

petra.jenus@ijs.si

Abstract. Magneto-electric (ME) ceramic composites of cobalt ferrite (CoF) and lead zirconate titanate (PZT) or barium titanate (BT) were prepared by mechanical mixing of the constituent powders followed by co-sintering at low temperatures (900-1000°C). It was found that the CoF powder needs to be pre-sintered at 700°C for 2h in order to minimize the differences in the sintering kinetics of the constituent powders. The optimization of the co-sintering conditions in order to prepare dense ceramic ME composites, which can display ME effect, was under investigation.

Keywords: cobalt ferrite, PZT, barium titanate, magneto-electric composites.

1 Introduction

Magneto-electric (ME) materials, combining piezoelectricity and ferro-(i)magnetism, are the subject of intense research due to their attractive physical properties and potential applications in novel multifunctional devices. There are two kinds of ME materials: single-phase and composite. Single-phase ME materials are rare, and their ME responses are relatively weak or occur at temperatures that are too low for technological applications [1]. On the other hand, the coupling interaction between piezoelectric and magnetostrictive phases in ME composites could produce a giant ME effect at room temperature [1, 2]. The ME response in the composite is the result of the piezoelectric effect in the piezoelectric phase and the magnetostrictive

effect in the magnetic phase [1, 2]. Therefore, the magnetic and electrical phenomena are coupled through an elastic interaction, so the ME response in composites is an extrinsic property of the composite material. This ME response enables the control of the magnetic properties using the electric field and, inversely, the control of the electric properties using a magnetic field [3]. This makes ME composites a promising material in the fields of spintronics, multiple-state memory elements and novel memory devices. Following the theoretical studies of Boomgard *et al.*[4], numerous ME composites have been prepared [1, 2, 5]. The most widely studied materials for the preparation of ME composites are piezoelectric lead zirconate titanate (PZT) or barium titanate (BT), and Ni or Co ferrites (CoF) as the magnetostrictive phase [6-13]. The aim of our work was to investigate how the CoF-PZT and CoF-BT composite's microstructure and properties are influenced by the processing parameters (i.e. starting materials morphology and co-sintering conditions).

2 Experimental work

Cobalt ferrite (CoF) nanopowder with a composition of CoFe_2O_4 was synthesized by a hydrothermal method at 200°C [14]. Aqueous solutions of metal ions (0.1 mol/L Co^{2+} , 0.2 mol/L Fe^{3+}) were prepared from cobalt (II) sulphate heptahydrate ($\text{CoSO}_4 \cdot 7\text{H}_2\text{O}$, Alfa Aesar, 98%) and iron (III) sulphate hydrate ($\text{Fe}_2(\text{SO}_4)_3 \cdot x\text{H}_2\text{O}$, Alfa Aesar, 99+%) salts. The reagents were used as received, without further purification. To the aqueous solution of Co^{2+} and Fe^{3+} , in a stoichiometric ratio, the sodium hydroxide (NaOH, Alfa Aesar, 98%) aqueous solution ($c = 5\text{ mol/L}$) was added at room temperature so that the mixture's pH was 13. The mixture was then put into a Teflon-lined, stainless-steel autoclave and kept at 200°C for 2h. The as-synthesized CoF nanoparticles were washed several times with water and dried during the night at 60°C . $\text{Pb}(\text{Zr}_{0.53}\text{Ti}_{0.47})\text{O}_3$ (PZT) powder was synthesized from a stoichiometric mixture of PbO (99.9 %, Aldrich, Germany), ZrO_2 (99.1 %, Tosoh, Japan) and TiO_2 (99.8 %, Alfa Aesar, Germany) and homogenized in a planetary mill for 2 hours. After drying, the mixture was calcined at 950°C for 2 hours, re-milled and re-calcined. After a second calcination the powder was milled for 8 hours in an attritor mill and dried. BaTiO_3 (BT) nanopowder with an average particle size of 50 nm was obtained from Inframat Advanced Materials (Product No: 5622ON-N2, 99,95% purity).

The powders were mixed in equal proportions and uniaxially pressed into disc-shaped samples with a 6-mm diameter and sintered at 900-1000°C for 4h with heating and cooling rates of 5°/min. The crystallinity and composition of the as-synthesized CoF nanopowders were characterized with a transmission electron microscope (TEM; Jeol 2100) combined with energy-dispersive X-ray spectroscopy (EDXS), while the particles' equivalent diameters were determined with the software Gatan (Digital Micrograph (TM) 1.70.16). The crystal structure of the composites as well as their constituent phases was confirmed by x-ray powder diffraction (XRD). The shrinkage of the constituent materials was studied with a Bähr dilatometer up to 1300°C, with a heating rate of 5°/min. The morphology of the ME composites was investigated with scanning electron microscope (SEM, Jeol 7600F), chemical phase composition was determined with electron diffraction analysis (EDXS). The room-temperature magnetic properties were measured with a vibrating-sample magnetometer (VSM, LakeShore, 7307). In order to measure ME properties, the sample was electroded with InGa paint and connected to the voltage power supply (Power Station 200, Labnet International, Inc.). The ME effect was measured in terms of the magnetization variation as a function of DC electric field (E_{dc}) using the VSM at room temperature.

3 Results and Discussion

The TEM examination of the as-synthesized CoF powders (Fig. 1a) revealed CoF particles with typical octahedral shapes, which suggests a high degree of crystallinity. The average particle size was 20 ± 5 nm. The EDXS analyses confirmed the atomic ratio of Co:Fe \cong 1:2 as in CoFe_2O_4 . The PZT and BT powders were examined with the SEM (Figs. 1c and d). PZT powder was composed from submicron-sized particles with a broad particle-size distribution and an irregular shape, while the BT powder consisted from nanoparticles with a uniform size distribution.

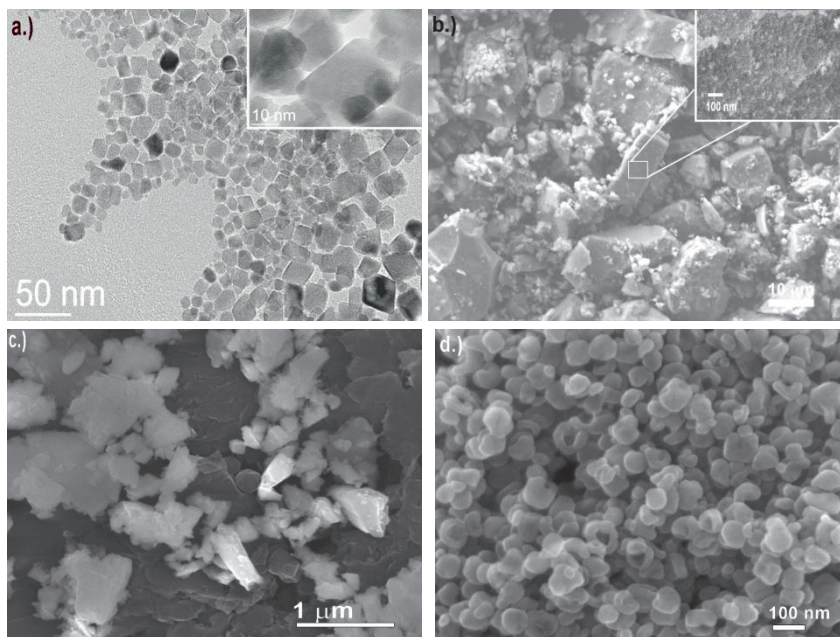


Figure 1: Starting powders for the co-sintering studies: (a) TEM image of the as-synthesized CoF; SEM images of: (b) CoF pre-fired at 700°C for 2h (c) as-synthesized and milled PZT; (d) Inframat BT.

The crystal structures of the constituent materials were confirmed with the XRD analysis (Fig. 2a). The diffraction peaks of the composites co-sintered at 950°C for 4h can be indexed either with perovskite PZT or BT and the spinel CoF structures. The same was true for all samples co-sintered at temperatures between 900 and 1000°C. This suggests that no secondary phases, within the detection limit of the XRD, were formed. Fig. 2b shows the shrinkage *versus* temperature for the starting powders. The shrinkage curve of the as-synthesized CoF powder differs significantly from that of the PZT and BT powder. While the latter two start to sinter above 900°C, the as-synthesized CoF starts to sinter below 800°C, with the highest shrinkage rate being at around 900°C (Fig. 2b). To reduce the particle-size differences we pre-fired the as-synthesized CoF powder to coarsen the particles and to reduce their surface energy and thus their sintering rate. Pre-firing of the as-synthesized CoF powder at 460°C resulted only in a minor difference in the shrinkage curves, that was more significant for the CoF powder pre-fired at 700°C

(Fig. 2b). In the latter case the sintering began above 800°C and the shrinkage rate was lower than for the as-synthesized powder due to the coarser CoF particles (Fig. 1b). All these reduced the dissimilarities between the shrinkage behavior of the constituent powders (CoF and PZT or BT). No significant difference in the shrinkage curves of the CoF was observed for the powders pre-fired at higher temperatures. Therefore, the CoF pre-fired at 700°C was used in further studies.

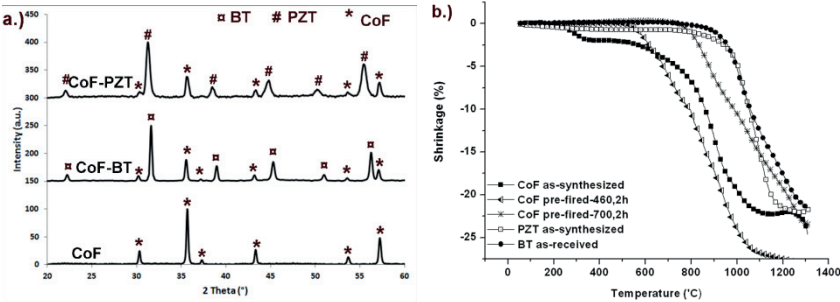


Figure 2: a.) X-ray diffraction patterns of CoF powder, and of the composite ceramics CoF-PZT and CoF-BT sintered at 950°C for 4h; b.) shrinkages of the constituent powders.

The backscattered electron (BEI) images of the polished surfaces of the CoF-PZT and CoF-BT sintered composites at different sintering temperatures are presented in Figure 3. According to the dilatometric analysis (see Fig. 2b) the sintering rate of the CoF is fast at these temperatures; however, the sintering rate of PZT and BT increases above 900°C. This explains the relatively porous PZT and BT matrix when sintered at 900°C (Figs. 3a and b) and denser samples at higher sintering temperatures (Figs. 3c–f). The CoF-BT microstructures show a large number of cracks at the interfaces (Figs. 3b, d and f), while significant cracking in the CoF-PZT composites was observed only when the co-sintering temperature was 1000°C (Fig. 3e). The cracks can reduce the ME coupling between the phases, due to the limited mechanical contact [1,5]. Therefore, the CoF-PZT composites were chosen for further investigations, and the optimum co-sintering temperature was determined to be 950°C, the temperature at which both powders densified efficiently and no cracks were observed at the CoF/PZT interfaces (Fig. 3c).

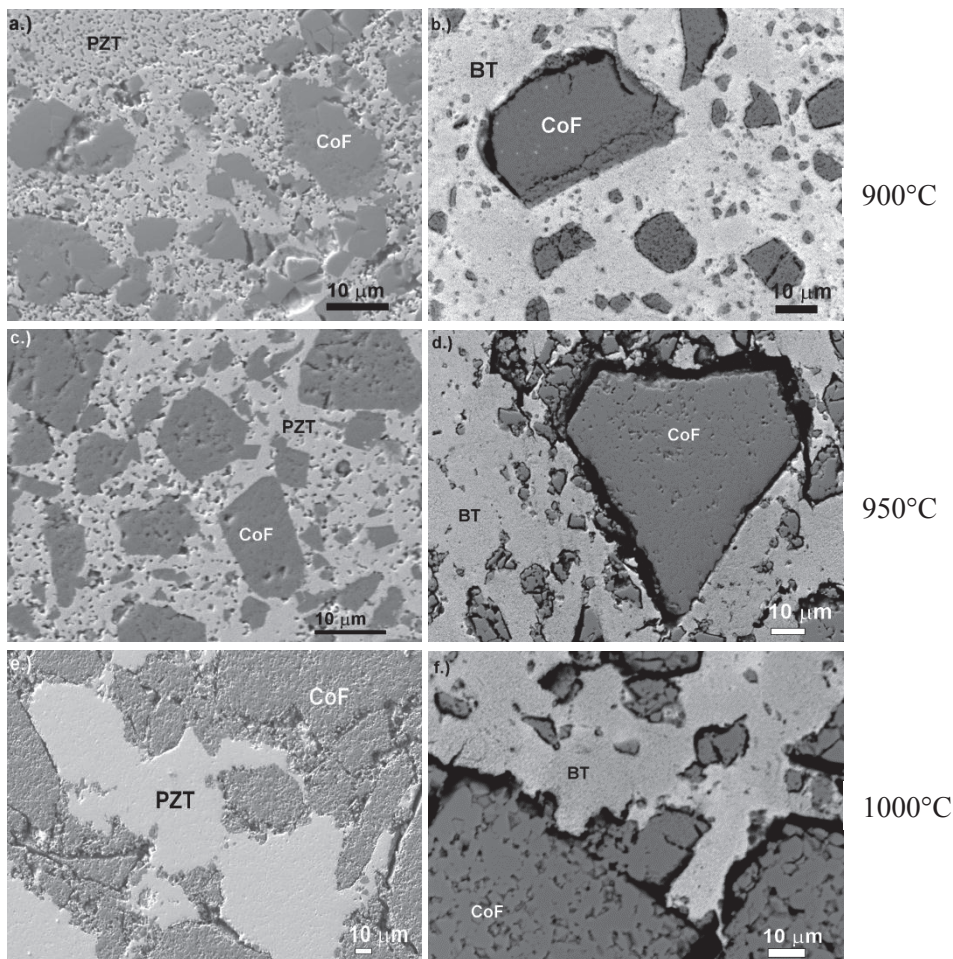


Figure 3: BEI images of CoF-PZT and CoF-BT composites sintered for 4h at a.) and b.) 900°C; c.) and d.) 950°C; e.) and f.) 1000°C.

Figure 4a shows the magnetic properties of CoF powders fired at 950°C for 4h, and ceramic composites co-sintered using the same conditions. The obtained hysteresis loop for the pure CoF displayed characteristics typical for bulk CoF with a saturation magnetization (M_s) of 76 Am²kg⁻¹ and a coercivity (H_c) of 32 kAm⁻¹. As expected, regardless of the composition of a ferroelectric phase, the composites displayed

almost the same M_s and H_c , because latter depend only on the magnetic phase in the composite. As mentioned above, the CoF-PZT was used for further measurements of the magneto-electric (ME) properties. They are presented in Figs. 4b and c, where the room-temperature hysteresis loops' dependence on the applied electric field is shown. The expanded view of the hysteresis loops (Fig. 4c) shows a clear effect of the applied electric field on the M_s . The decrease in the M_s after applying the electric field suggests the converse ME effect and the possibility to tune the magnetic properties of the studied CoF-PZT composites with an electric field. The drop of the M_s was 1.5% and this was confirmed in several parallel samples, while the experimental error was significantly lower, i.e., $\pm 0.1\%$.

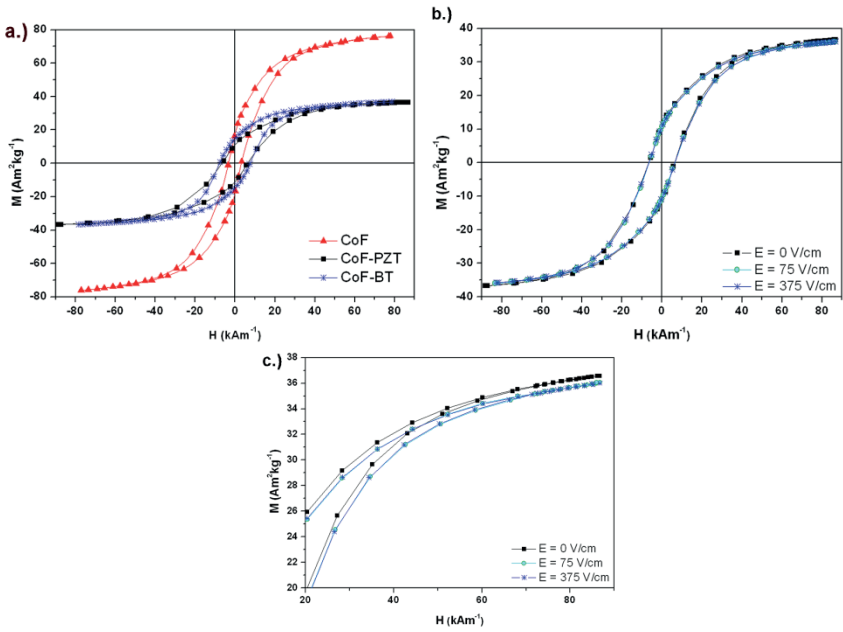


Figure 4: Room-temperature hysteresis loops of the: (a) CoF powder , CoF–PZT and CoF-BT composites co-sintered at 950°C for 4h; (b) CoF–PZT co-sintered composite measured under an applied electric field; (c) expanded view of (b).

4 Conclusions

The co-sintering of CoFe_2O_4 - $\text{PbZr}_{0.53}\text{Ti}_{0.47}\text{O}_3$ and CoFe_2O_4 - BaTiO_3 ceramic composites was investigated. To minimize the chemical interaction between the phases, we studied the co-sintering at relatively low temperatures, between 900 and 1000°C. The properties of the starting powders and the co-sintering conditions had a great impact on the composites' microstructures. The differences in sintering rates of constituent powders were reduced by pre-firing the as-synthesized CoF nanopowder at 700°C for 2h. The optimum co-sintering conditions were determined to be 950°C for 4h and the CoF-PZT composites were chosen for further measurements due to the insignificant number of cracks at the interfaces at selected sintering conditions. The converse magneto-electric effect was measured in terms of the influence of an applied electric field on the magnetization. The saturation magnetization of the CoFe_2O_4 - $\text{PbZr}_{0.53}\text{Ti}_{0.47}\text{O}_3$ co-sintered composite was $36 \text{ Am}^2\text{kg}^{-1}$ and this dropped by 1.5% after an electric field of only 75 V/cm was applied. This suggests that magneto-electric composites with useful properties can be prepared by the optimized co-sintering of suitable CoFe_2O_4 and $\text{PbZr}_{0.53}\text{Ti}_{0.47}\text{O}_3$ powders.

References

- [1] C.-W. Nan, M. I. Bichurin, S. Dong, D. Viehland, and G. Srinivasan, "Multiferroic magnetoelectric composites: Historical perspective, status and future directions," *J. Appl. Phys.*, **103** [3] 031101 35pp. (2008).
- [2] C- W. Nan, "Magnetoelectric effect in composites of piezoelectric and piezomagnetic phases," *Phys. Rev. B*, **50** [9] 6082-88 (1994).
- [3] J. Van Suchetelene, "Product properties: A new application of composite materials," *Philips Res. Rep.*, **27** 28-37 (1972).
- [4] J. Van den Boomgaard, and R. A. J Born, "A Sintered Magnetolectric Composite Material BaTiO_3 - $\text{Ni}(\text{Co},\text{Mn})\text{Fe}_3\text{O}_4$," *J. Mater. Sci.*, **13** 1538-48 (1978).
- [5] J. Ma, J. Hu, Z. Li, and C.-W. Nan, "Recent Progress in Multiferroic Magnetolectric Composites: from Bulk to Thin Films," *Adv. Mater.*, **23** [9] 1062-87 (2011).
- [6] J. de Frutos, J. A. Matutes-Aquino, F. Cebollada, M. E. Botello-Zubiarte, E. Menendez, V. Corral-Flores, F. J. Jimenez, and A. M. Gonzales, "Synthesis and characterization of electroceramics with magnetolectric properties" *J. Eur. Ceram. Soc.*, **27** [13-15] 3663-66 (2007).
- [7] S. Basu, K. Ramesh Babu, and R. N. P. Choudhary, "Studies on the piezoelectric and magnetostrictive phase distribution in lead zirconate titanate – cobalt iron oxide composites," *Mater. Chem. Phys.*, **132** [2-3] 570-80 (2012).
- [8] W. Chen, W. Zhu, and X. Chen, "Enhanced Ferroelectric and Dielectric Properties of CoFe_2O_4 - $\text{Pb}(\text{Zr}_{0.53}\text{Ti}_{0.47})\text{O}_3$ Multiferroic Composite Thick Films," *J. Am. Ceram. Soc.*, **93** [3] 796-99 (2010).
- [9] A. R. Iordan, M. Airimioaiei, M. N. Palamaru, C. Galassi, A. V. Sandu, C. E. Ciomaga, F. Prihor, L. Mitoseriu, and A. Ianculescu, "In situ preparation of CoFe_2O_4 - $\text{Pb}(\text{ZrTi})\text{O}_3$ multiferroic composites by gel-combustion technique," *J. Eur. Ceram. Soc.*, **29** [13] 2808-13 (2009).
- [10] Q. H. Jiang, Z. J. Shen, J. P. Zhou, Z. Shi, and C.-W. Nan, "Magnetolectric composites of nickel ferrite and lead zirconate titanate prepared by spark plasma sintering," *J. Eur. Ceram. Soc.*, **27** [1] 279-84 (2007).
- [11] M. Venkata Ramana, N. Ramamanohar Reddy, B. S. Murty, V. R. K. Murthy, and K. V. Siva Kumar, "Ferromagnetic-Dielectric $\text{Ni}_{0.5}\text{Zn}_{0.5}\text{Fe}_{1.9}\text{O}_4$ -□/ $\text{PbZr}_{0.52}\text{Ti}_{0.48}\text{O}_3$ Particulate Composites:

- Electric, Magnetic, Mechanical, and Electromagnetic Properties,” *Adv. Condens. Matter Phys.*, **2010** 763406 14pp. (2010).
- [12] S. G. Lu, Z. K. Xu, Y. P. Wang, S. S. Guo, H. Chen, T. L. Li, and S. W. Or, “Effect of CoFe_2O_4 content on the dielectric and magnetoelectric properties in $\text{Pb}(\text{ZrTi})\text{O}_3/\text{CoFe}_2\text{O}_4$ composite,” *J Electroceram.*, **21** [1-4] 398-400 (2008).
- [13] A. Testino, L. Mitoseriu, V. Buscaglia, M. T. Buscaglia, I. Pallecchi, A. S. Albuquerque, V. Calzona, D. Marre, A. S. Siri, and P. Nanni, “Preparation of multiferroic composites of $\text{BaTiO}_3\text{-Ni}_{0.5}\text{Zn}_{0.5}\text{Fe}_2\text{O}_4$ ceramics,” *J. Eur. Ceram. Soc.*, **26** [14] 3031-36 (2006).
- [14] S. Gyergyek, M. Drofenik, and D. Makovec, “Oleic-acid-coated CoFe_2O_4 nanoparticles synthesized by co-precipitation and hydrothermal synthesis,” *Mater. Chem. and Phys.*, **133** [1] 515-22 (2012).

For wider interest

Materials synthesis – K8

Head of department: prof. dr. Darko Makovec

Magnetic nanoparticles (magnetic fluids, nanocomposites)

New methods for the controlled synthesis of iron oxide based nanoparticles are being developed. Additionally, we are focused on the functionalization of magnetic nanoparticles, primarily for biomedical applications. The surface properties of nanopowders, which determine their applicability, are tuned with inorganic coatings (i.e., a thin film of amorphous silica), with polymer coatings or with single-molecule layers. The coating prevents the agglomeration of nanoparticles, which further enables their dispersion in various liquids, i.e., magnetic fluids or the homogeneous incorporation of nanoparticles in various matrices.

Multifunctional materials

Nanocomposites combining the various properties of the constituent materials can be prepared by mastering the surface properties of nanoparticles. Examples of our studies include combinations of ferrimagnetics and dielectrics (magnetodielectrics) and ferrimagnetic and ferroelectric (composite multiferroics) materials. Current studies are also related to the development of new, magneto-optic materials for sensors and magneto-catalytic materials for environmental applications.

Magnetic materials for micro- and mm-waves

Magnetic materials suitable for the absorbers of electromagnetic waves and for the non-reciprocal ferrite devices are being developed. Ceramics and composites based on ferrites are studied for the microwave applications, and a new method for the preparation of magnetically oriented thick hexaferrite films for self-biased mm-wave applications has been developed.

The influence of oleic acid on the morphology and magnetic properties of CoFe_2O_4 nanoparticles

Sonja Jovanović^{1,2}, Matjaž Spreitzer¹, Mojca Otoničar^{1,2}, Danilo Suvorov^{1,2}

¹ Advanced Materials Department, Jožef Stefan Institute, Ljubljana, Slovenia

² Jožef Stefan International Postgraduate School, Ljubljana, Slovenia

sonja.jovanovic@ijs.si

Abstract. In this work we examine the influence of oleic acid on the morphology and magnetic properties of cobalt ferrite (CoFe_2O_4) nanoparticles obtained by the solvothermal method. X-ray diffraction (XRD) and transmission electron microscopy (TEM) were used to determine the crystal structure and the particle size of the prepared powders, while a vibrating-sample magnetometer (VSM) was used to measure the magnetic properties. The results show that the sample prepared in the absence of oleic acid consists of agglomerated nanoparticles, while the sample prepared with oleic acid consists of well-dispersed, sphere-like nanoparticles. Furthermore, the magnetic hysteresis loops measured at room temperature indicate that the magnetic properties of the products are closely related to the size of the CoFe_2O_4 nanoparticles. The samples obtained without oleic acid are ferrimagnetic, while the samples obtained with oleic acid exhibit superparamagnetic behaviour.

Keywords: Cobalt ferrite; Nanoparticles; Magnetic properties

1 Introduction

In the past couple of decades spinel ferrites have attracted attention because of their potential for applications in magnetic recording, data storage, solar cells, sensors, biomedicine, etc [1-5]. Among the spinel ferrites, cobalt ferrite has been widely studied as a result of its properties, for example, its large magnetic anisotropy, high coercivity, moderate saturation magnetization, remarkable chemical stability and mechanical hardness [6].

The size of the nanoparticles, which is closely related to the method of preparation, has a major influence on the magnetic properties of the CoFe_2O_4 [7]. For example,

compared to the bulk (~ 80 emu/g [8]) the M_S values of CoFe_2O_4 nanoparticles are smaller due to the spin-canting effect on the surfaces. At the same time, the H_C reaches a maximum value as the crystallite size is close to the single-domain size, which is about 30–40 nm. If the crystallite size is smaller than 10 nm, the CoFe_2O_4 nanoparticles are single-domain and superparamagnetism occurs even at room temperature [9].

Various synthesis methods have been reported for CoFe_2O_4 nanoparticles, such as co-precipitation, sol-gel, solvothermal synthesis, thermal decomposition, etc [10-13]. Of these methods, solvothermal synthesis offers many advantages over other methods, such as the high crystallinity of the products at relatively low temperature, and the ability to control the size of the nanoparticles and their agglomeration.

In our previous work, the hydrothermal synthesis of CoFe_2O_4 was investigated [14]. However, the size of the obtained CoFe_2O_4 particles largely varied, which is disadvantage for the intended application of cobalt ferrite. Therefore, the solvothermal synthesis was applied with cobalt and iron nitrates as reagents and oleic acid as a capping agent. The aim of the present work is to examine the influence of oleic acid on the structural and magnetic properties of cobalt ferrite nanoparticles.

2 Experimental

Cobalt (II) nitrate hexahydrate ($\text{Co}(\text{NO}_3)_2 \cdot 6\text{H}_2\text{O}$, Alfa Aesar, 98-102%), iron (III) nitrate nonahydrate ($\text{Fe}(\text{NO}_3)_3 \cdot 9\text{H}_2\text{O}$, Alfa Aesar, 98-101%), oleic acid ($\text{C}_{18}\text{H}_{34}\text{O}_2$, Alfa Aesar, tech. 90%) and sodium hydroxide (NaOH , ApplChem) were used as purchased, without further purification.

CoFe_2O_4 nanoparticles were prepared by the solvothermal method. In a typical synthesis, 10 mmol of NaOH was dissolved in 2 mL of water and 10 mL of 1-pentanol. Then 12 mmol of oleic acid was added with interspersed energetic stirring. Finally, 2 mmol of iron nitrate nonahydrate and 1 mmol of cobalt nitrate hexahydrate were dissolved in 18 mL of water and added to the above-prepared solution. The resulting mixture was stirred vigorously for 2 h at room temperature

and then transferred into a Teflon-lined, stainless-steel, autoclave that was closed and kept at 180°C for 16 h. After cooling, the final mixture was composed of a liquid organic phase and sediment of particles. The liquid phases were discarded and the remaining particles were washed three times by re-dispersion in n-hexane and precipitation by ethanol. Finally, the particles were separated using a permanent magnet. After washing, they were re-dispersed into n-hexane, transferred to a watch glass and dried in a digester overnight.

The crystal structure of the obtained powders was analyzed by X-ray diffraction (XRD, Bruker AXS D4 Endeavor) with Cu K α ($\lambda=1.5406$ Å) radiation at room temperature in the 2θ range from 20° to 80° (2θ step=0.02° with a counting time of 3s per step). The morphology of the samples was examined using a transmission electron microscope (TEM, JEM-2100, JEOL Ltd.) operated at 200 kV. The magnetic properties were studied using a vibrating-sample magnetometer (VSM, 7307 Lake Shore) at room temperature by varying the magnetic field from – 15 kOe to 15 kOe.

3 Results and Discussion

Figure 1 shows the XRD patterns of the CoFe $_2$ O $_4$ samples obtained without (Fig. 1a) and with (Fig. 1b) oleic acid. The highly crystalline peaks match to the (220), (311), (400), (422), (511), (440), and (533) Bragg-diffraction planes of cobalt ferrite with a face-centred-cubic structure and correspond to the standard pattern of JCPDS card no. 22-1086.

In the case of the sample obtained in the absence of oleic acid the diffraction lines are narrower and more intense compared to the sample obtained with oleic acid. This indicates that the crystallinity and the average crystallite size depend on the presence of oleic acid. The average crystallite size was determined from the full width at the half maximum of the strongest diffraction maximum (311) using the Scherrer formula [15]. The results are listed in Table 1.

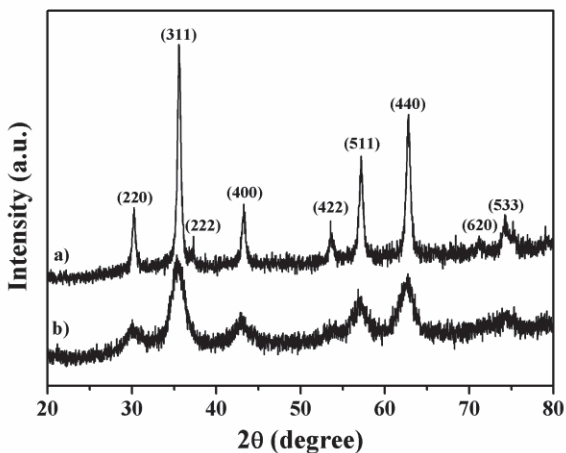


Figure 1: XRD patterns of samples prepared a) without oleic acid and b) with 1 M oleic acid.

Figure 2 shows TEM images of the as-prepared CoFe_2O_4 nanoparticles. It is clear that the morphology and the particle size depend on the presence of oleic acid. The sample obtained without oleic acid (Fig. 2a) consists of the agglomerated nanoparticles of different size and shape. In respect to their size, it can be observed that two groups of particles are formed: one with the size of $\sim 8\text{nm}$ and the other in the range of 10-35 nm. On the other hand, the particles obtained with 1 M oleic acid (Fig 2c) have a uniform morphology and size distribution. The sample consists of sphere-like nanoparticles with an average size of 6 nm.

The selected-area electron diffraction (SAED) patterns of the samples prepared without (Fig 2b) and with (Fig 2d) oleic acid confirm the presence of CoFe_2O_4 . The TEM results support the XRD findings and clearly show an increase in the crystallinity and particle size for the sample prepared without oleic acid. These results confirm that oleic acid acts as a barrier to the mass transfer and thus limits the growth of the already formed particles. At the same time, it is a steric stabilizer that prevents the agglomeration of nanoparticles [16].

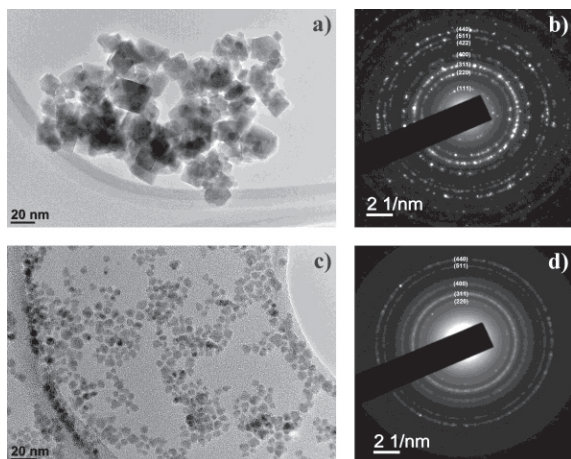


Figure 2: The TEM images and the selected-area electron diffraction (SAED) patterns of the CoFe_2O_4 nanoparticles prepared without (a,b) and with (c,d) oleic acid.

Figure 3 shows the hysteresis loops obtained at room temperature in a magnetic field of ± 15 kOe. The values for the saturation magnetization (M_s), remanent magnetization (M_r) and coercivity (H_c) are presented in Table 1. It is clear that the agglomeration of nanoparticles and their size has a large effect on the magnetic properties of the cobalt ferrite. The sample prepared without oleic acid exhibits ferrimagnetic behaviour, while the sample obtained with oleic acid exhibits superparamagnetic behaviour.

Table 1: Particle size and magnetic properties of the CoFe_2O_4 samples

c[O.A.]* (M)	d (nm) XRD	d (nm) TEM	M_s (emu/g)	M_r (emu/g)	H_c (Oe)
		particles: d = 8			
0	19	platelets: w = 10-25 l = 10-35	55.45	25.09	1399.60
1	5	particles: d = 6	41.66	0.47	21.37

*O.A. = oleic acid, d – size of nanoparticles, w – platelets width, l – platelets length

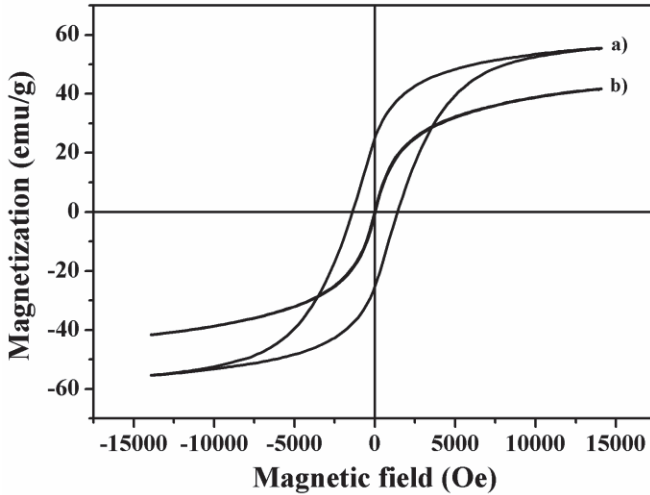


Figure 3: The hysteresis loops of the samples prepared a) without oleic acid and b) with 1 M oleic acid

4 Conclusion

The effect of oleic acid on the structural and magnetic properties of CoFe_2O_4 nanoparticles was investigated. We confirmed that the oleic acid plays an important role in the synthesis of the CoFe_2O_4 nanoparticles. Compared to the synthesis route in which the capping agent was absent, the size distribution of the CoFe_2O_4 nanoparticles, prepared with oleic acid, appeared narrower and the shape uniformity was significantly improved. The layer of oleic acid, which forms on the surface of the nanoparticles, is essential because it prevents the agglomeration and growth of the nanoparticles. As a result, the CoFe_2O_4 nanoparticles prepared with 1M oleic acid are superparamagnetic, in contrast to the ferrimagnetic nanoparticles that are prepared without oleic acid.

References:

- [1] C. A. Ross. Patterned magnetic recording media. *Annual Reviews Materials Research*, 31: 203-235, 2001.
- [2] R. L. Comstock. Modern magnetic materials in data storage. *Journal of Materials Science: Materials in Electronics*, 13 (9): 509-523, 2002.
- [3] R. S. Gaikwad, S.-Y. Chae, R. M. Mane, S.-H. Han, O.-S. Joo. Cobalt Ferrite Nanocrystallites for Sustainable Hydrogen Production Application. *International Journal of Electrochemistry*, 2011: 729141, 2011.
- [4] O. F. Caltun, G. S. N. Rao, K. H. Rao, B. P. Rao, C.-G. Kim, C.-O. Kim, I. Dumitru, N. Lupu, H. Chiriac. High Magnetostrictive Cobalt Ferrite for Sensor Application. *Sensor Letters*, 5 (1): 45-47, 2007.
- [5] A. Akbarzadeh, M. Samiei, S. Davaran. Magnetic nanoparticles: preparation, physical properties, and applications in biomedicine. *Nanoscale Research Letters*, 7: 144, 2012.
- [6] G. B. Ji, S. L. Tang, S. K. Ren, F. M. Zhang, B. X. Gu, Y. W. Du. Simplified synthesis of single-crystalline magnetic CoFe_2O_4 nanorods by a surfactant-assisted hydrothermal process. *Journal of Crystal Growth*, 270 (1-2): 156-161, 2004.
- [7] M. Rajendran, R. C. Pullar, A. K. Bhattacharya, D. Das, S. N. Chintalapudi, C. K. Majumdar. Magnetic properties of nanocrystalline CoFe_2O_4 powders prepared at room temperature: variation with crystallite size. *Journal of Magnetism and Magnetic materials*, 232 (1-2): 71-83, 2001.
- [8] M. P. Gonzalez-Sandoval, A. M. Beesley, M. Miki-Yoshida, L. Fuentes-Cobas, J. A. Matutes-Aquino. Comparative study of the microstructural and magnetic properties of spinel ferrites obtained by co-precipitation. *Journal of Alloys and Compounds*, 369 (1-2): 190-194, 2004.
- [9] Y. Zhang, Y. Liu, C. Fei, Z. Yang, Z. Lu, R. Xiong, D. Yin, J. Shi. The temperature dependence of magnetic properties for cobalt ferrite nanoparticles by the hydrothermal method. *Journal of Applied Physics*, 108 (8): 084312-1-084312-6, 2010.
- [10] M. M. El-Okri, M. A. Salem, M. S. Salim, R. M. El-Okri, M. Ashoush, H. M. Talaat. Synthesis of cobalt ferrite nano-particles and their magnetic characterization. *Journal of Magnetism and Magnetic Materials*, 323 (7): 920-926, 2011.
- [11] J. Sun, Z. Wang, Y. Waang, Y. Zhu, T. Shen, L. Pang, K. Wei, F. Li. Synthesis of the nanocrystalline CoFe_2O_4 ferrite thin films by a novel sol-gel method using glucose as an additional agent. *Materials Science and Engineering B*, 177 (2): 269-273, 2012.
- [12] S. Yáñez-Vilar, M. Sánchez-Andújar, C. Gómez-Aguirre, J. Mira, M. A. Señaris-Rodríguez, S. Castro-García. A simple solvothermal synthesis of MFe_2O_4 ($\text{M} = \text{Mn}, \text{Co}$ and Ni) nanoparticles. *Journal of Solid State Chemistry*, 182 (10): 2685-2690, 2009.
- [13] A. P. Herrera, L. Polo-Corrales, E. Chavez, J. Cabarcas-Bolivar, O. N. C. Uwakweh, C. Rinaldi. Influence of aging time of oleate precursor on the magnetic relaxation of cobalt ferrite nanoparticles synthesized by the thermal decomposition method. *Journal of Magnetism and Magnetic Materials*, 328: 41-52, 2013.
- [14] S. Jovanović, M. Spreitzer, M. Otoničar, D. Suvorov. Synthesis of cobalt ferrite nanoparticles using a combination of the co-precipitation and hydrothermal methods. In *Proceedings of the IPSSC, 5th Jožef Stefan International Postgraduate School Student's Conference 2012*, Ljubljana, Slovenia, 2012.
- [15] Z. Zi, Y. Sun, X. Zhu, Z. Yang, J. Dai, W. Song. Synthesis and magnetic properties of CoFe_2O_4 ferrite nanoparticles. *Journal of Magnetism and Magnetic Materials*, 321 (9): 1251-1255, 2009.
- [16] S. Gyergyek, M. Huskić, D. Makovec, M. Drogenik. Superparamagnetic nanocomposites of iron oxide in a polymethyl methacrylate matrix synthesized by in situ polymerization. *Colloids and Surfaces A: Physicochemical and Engineering Aspects*, 317 (1-3): 49-55, 2008.

For wider interest

In the last couple of decades cobalt ferrite has become an interesting magnetic material as a result of its properties, such as a large magneto-crystalline anisotropy, moderate saturation magnetization, good chemical stability and mechanical hardness. On the basis of these properties it can be used in high-density information storage devices, spintronic devices, drug-delivery systems, sensors, etc. The presented results are obtained within a project that aims to enhance the applicability of cobalt ferrite nanoparticles by improving their size and shape uniformity as well as their dispersibility and magnetic properties.

Microstructure, Yield Stress and Hardness in Weld Heat-Affected Zone of 9-12% Cr Steels

Fevzi Kafexhiu^{1,2}, Franc Vodopivec¹, Jelena V. Tuma²

¹ Department of Surface Engineering and Applied Surface Science, Institute of Metals and Technology, Ljubljana, Slovenia

² Jožef Stefan International Postgraduate School, Ljubljana, Slovenia

fevzi.kafexhiu@imt.si

Abstract. The effect of welding and tempering on microstructure and room-temperature mechanical properties of two types of creep-resistant steels, X20CrMoV121 and P91, was investigated. Samples were welded and then tempered for 17 520 h at 650°C and 8 760 h at 750°C. After tempering, the room-temperature yield stress and hardness of two regions of weld heat-affected zone (HAZ) were determined. In addition, the scanning electron microscopy (SEM) imaging was carried out. It was found that the effect of tempering at 750°C on the microstructure, room-temperature yield stress and hardness was greater than the effect of tempering at 650°C. It was also found that the weakest part of the HAZ for both tempering temperatures, with regard to the yield stress and hardness, was the coarse-grained (γ) microstructure.

Keywords: welding, HAZ, tempering, microstructure, yield stress, hardness.

1 Introduction

Issues arising in fossil-fired power plants that operate at ultra-supercritical (USC) steam parameters (300 bar, 720°C) are largely material related. Materials mainly used for vital parts of such power plants are the 9-12% Cr steels, where the key parameter is their resistance to creep, i.e., resistance to permanent deformation due to constant load at elevated temperature.

Studies on creep resistance of modified 9-12% Cr steels have been largely focused on the rupture strength of the parent steel and much less attention has been given to welded joints. However, long-term experience of creep-exposed welded structures

has shown that the heat affected zone (HAZ), a narrow zone of base material adjacent to the weld fusion line, altered by the weld thermal cycle, in respect to the creep strength, is often regarded as the weakest link in welded constructions [1, 2].

A routine checking of materials properties in terms of the residual lifetime after certain periods of operation in power plants is always necessary. Accelerated creep test, as one of these routine methods, is expensive and time consuming, so it does not represent the most suitable method for the lifetime prediction. Room-temperature mechanical tests and microstructure examinations after certain tempering time, simulating changes of microstructure and properties in power plant conditions, could offer faster and less expensive means for this purpose [3 - 5].

2 Experimental

Two steel grades, X20CrMoV121 and P91, samples of which were extracted from steam pipelines with $\varnothing 38.5 \times 7.1$ mm and $\varnothing 177 \times 23.5$ mm, respectively, were chosen for the present study. Their chemical composition is given in Table 1.

Table 1: Chemical composition of the X20 and P91 steels

Chemical composition, wt %													
Elements	C	Si	Mn	P	S	Cr	Ni	Mo	V	Cu	Nb	Al	N
X20CrMoV121	0.2	0.29	0.52	0.019	0.011	11	0.64	0.94	0.31	0.059	0.024	0.032	0.017
P91	0.1	0.38	0.48	0.012	0.002	7.9	0.26	0.98	0.23	0.14	0.11	0.016	0.064

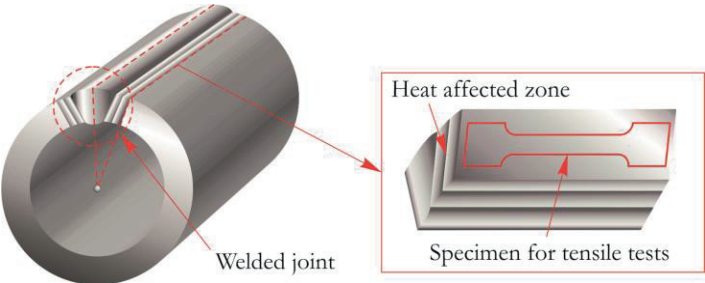


Figure 1: Extraction of specimens for tensile tests

A multilayer tungsten inert gas (TIG) welding was performed, inducing the creation of HAZ, from which the inter-critical ($\alpha+\gamma$) and coarse-grained (γ) microstructures were taken into account only. After welding, samples were tempered up to 17 520 h (2 years) at 650°C and up to 8 760 h (one year) at 750°C. Afterwards, static tensile tests and hardness measurements were performed at room temperature. The microstructure changes as a function of tempering were evaluated using the JEOL JSM-6500F Field Emission SEM.

3 Results and Discussions

Tempering at 650°C for 2 years has an almost negligible effect on the yield stress (σ_y) and hardness of the inter-critical ($\alpha+\gamma$) microstructure of both steels. On the other hand, the coarse-grained (γ) microstructure shows a different behaviour; after 1 year of tempering at 650°C, there is an almost linear decrease of the σ_y from 741 to 538 N/mm² for the X20CrMoV121 and from 847 to 626 N/mm² for the P91. After an additional year of tempering at 650°C, there is virtually no change in σ_y for the X20CrMoV121, while for the P91, σ_y drops for 13% of the total reduction (Fig. 2).

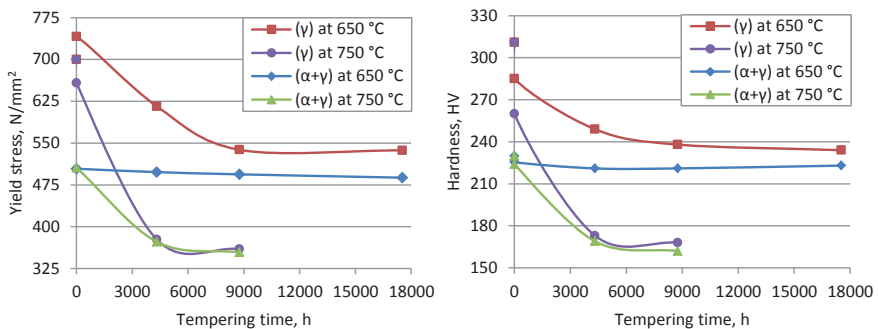


Figure 2: Changes of yield stress and hardness of the steel X20 due to the tempering

In the first year of tempering at 650°C, the hardness of γ microstructure of the X20CrMoV121 reduces from 285 to 238 HV, while an additional year of tempering caused less than 8% of the total reduction. For the P91, the total hardness reduction goes from 311 to 246 HV, 80% of which appears in the first year of tempering.

The σ_y of $(\alpha+\gamma)$ microstructure of the X20CrMoV121 and P91 after half year of tempering at 750°C, decreased from 517 to 366 N/mm² and from 506 to 373 N/mm², respectively. In the second half year of tempering, the σ_y decreased only 12% for the X20CrMoV121 and 20% for the P91, relative to the total reduction.

Quite a similar fashion was observed for the hardness of $(\alpha+\gamma)$ microstructure. During the first half year of tempering, hardness of the X20CrMoV121 reduced from 224 to 169 HV, while during the second half only for 11%. In the case of the P91, this difference is smaller, so the hardness reduction was from 215 to 170 HV and from 170 to 156 HV, for the first and the second halves, respectively (Fig. 3).

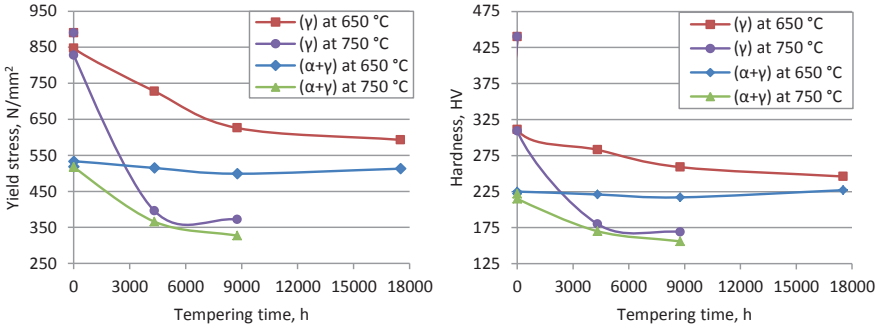


Figure 3: Changes of yield stress and hardness of the steel P91 due to the tempering

The effect of 1 year tempering at 750°C on the properties of coarse-grained (γ) microstructure for both steels was greater than that of the inter-critical $(\alpha+\gamma)$. During the first half year of tempering, the σ_y of the X20CrMoV121 decreased from 658 to 377 N/mm², while that of the P91 from 828 to 396 N/mm². The second half-year of tempering had the least effect on both steels, where the decrease of σ_y for the X20CrMoV121 was 5.7% and for the P91 5.3%.

Similarly, the hardness showed the highest reduction during the first half year of tempering, i.e., from 260 to 173 HV and from 309 to 180 HV, for the X20CrMoV121 and P91, respectively. The second half year of tempering caused the hardness reduction of only 5.4% for the X20CrMoV121 and 8% for the P91.

It is worth mentioning that after half year of tempering at 750°C, the σ_y and hardness of the γ and $(\alpha+\gamma)$ microstructures of both steels almost equalize even though the initial σ_y and hardness of γ are approximately twice as big as those of the $(\alpha+\gamma)$. From this point on, their changes are very small and follow a mutually similar fashion. This phenomenon could be explained having in mind that precipitates initially found along the grain and sub-grain boundaries dissolve, by making sub-boundaries disappear, so the initially important role of grain size is vanished.

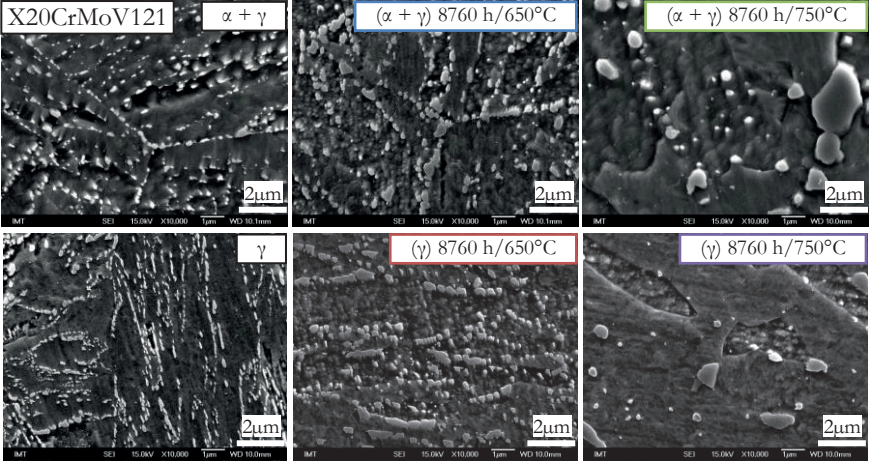


Figure 4: Microstructure evolution in the steel X20 due to the tempering

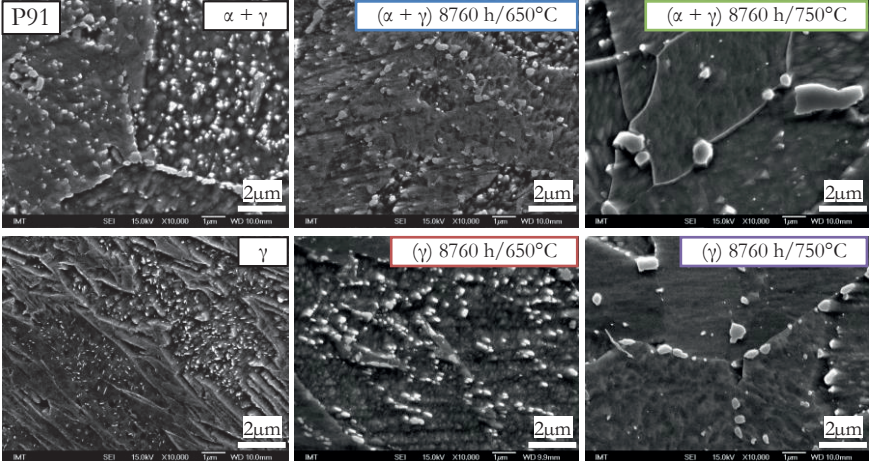


Figure 5: Microstructure evolution in the steel P91 due to the tempering

From Figs. 4 and 5, it is obvious that the tempering causes the carbide precipitates to coarsen, their mutual spacing to increase and their distribution to change. These processes are much faster at 750°C compared to 650°C, because of the exponential temperature effect on the diffusivity of carbide-forming elements (Cr, Mo, Fe, V and Nb) found in solid solution of ferrite. The initial microstructure contains a large number of precipitates, the majority of which are cementite Fe_3C also containing Cr, and some of them are carbides Cr_{23}C_6 also containing Fe and Mo [6]. Carbides lie along the boundaries and sub-boundaries of the initial martensitic microstructure.

After 8760 h of tempering at 650°C, precipitates haven't change much in size and there is virtually no size difference between Fe, Cr and V precipitates either, but their distribution changes to even, so the martensitic sub-boundaries disappear. After 8760 h of tempering at 750°C, the number of precipitates is much smaller, whereas their mutual spacing much bigger, which is an important factor causing the properties to deteriorate. From Figs. 4 and 5, there is an obvious difference between fine, white and thermally more stable V precipitates, and bigger greyish Cr carbides.

4 Conclusions

The difference between two regions of the heat affected zone (HAZ), namely coarse-grained γ and inter-critical ($\alpha+\gamma$), with regard to microstructure and properties is noticeable. This difference is also evident after tempering at two different temperatures and durations. Two years of tempering the ($\alpha+\gamma$) microstructure of both steels at 650°C, caused virtually no change in yield stress (σ_y) and hardness. However, the γ microstructure of both steels, having coarse grains, showed the greatest changes of σ_y and hardness in the first year of tempering. Tempering at 750°C causes greater changes in microstructure, with regard to the precipitate size, mutual spacing and distribution. These changes were also reflected on more pronounced property deterioration. The equalisation of the properties of initially quite different γ and ($\alpha+\gamma$) microstructures, after half year of tempering at 750°C, leads us to a conclusion of a greater role of stable precipitates in the microstructure of creep-resistant steels, compared to the role of the grain size.

References:

- [1] F. Abe, T. U. Kern, R. Viswanathan. *Creep-resistant steels*. Woodhead Publishing, CRC Press, Cambridge, England, 2008.
- [2] P. Mayr, T. A. Palmer, J. W. Elmer, H. Cerjak. In situ Observation of Phase Transformations and their Effects in 9-12% Cr Steels during Welding. *Advanced Materials Research*, 15-17, 1014-1019, 2007
- [3] F. Vodopivec, J. Vojvodič – Tuma, M. Jenko, R. Celin, B. Šuštaršič. Dependence of accelerated creep rate at 580°C and room temperature yield stress for two creep resistant steels. *Steel research*, 81(7), 576-580, 2010
- [4] D. J. Allen. A hardness normalized model of creep rupture for P91 steel. In *Creep & Fracture in High Temperature Components*. Ed. I. A. Shibli, S. R. Holdsworth, DEStech Publ. Inc, 659-688, 2009.
- [5] F. Kafexhiu, F. Vodopivec, J. V. Tuma. Effect of tempering on the room-temperature mechanical properties of X20CrMoV121 and P91 steels. *Materiali in tehnologije*, 46(5):459-464, 2012
- [6] D. A. Skobir, F. Vodopivec, M. Jenko, S. Spajčić, B. Markoli. *Zeitschrift für Metallkunde*, 95: 1020-1024, 2004

For wider interest

The efficiency (electricity produced per unit of heat input) of power plants that use coal as an energy source, is obtained through higher temperatures and pressures of the steam that enters the turbine. Such conditions require materials with high creep resistance, i.e., the ability to withstand a long-term loading at high temperatures. This requires a careful material selection and a periodical checking of its properties and remaining lifetime after the certain period of operation in power plants. The checking of the creep strength is expensive and time-consuming. For this reason, simpler methods are being developed. Such methods use less expensive and faster tests and enable a quite reliable establishment of materials condition. One among these methods is to check the room-temperature mechanical properties and microstructure after a certain heat treatment, simulating changes of microstructure and properties that occur after a longer operation in a power plant (real conditions). The measured properties are then correlated with the creep rate, which is either measured using the standard creep test, or obtained through calculations using the most reliable models known up to date.

Welding, as the fundamental joining technique of vital parts of power plants, mainly made of steels with 9-12% Cr content, causes the creation of so-called heat affected zone (HAZ) consisting of few regions with different microstructures. This is because the welding process itself causes temperatures that are near the melting point of these steels. Two of these regions, namely coarse-grained (γ) and inter-critical ($\alpha+\gamma$) have been chosen for the present study, because the majority of failures in welded constructions made of 9-12% Cr steels occurred within these two regions.

Single-step decoration of MoSI based nanowires with platinum nanoparticles

Andrej Kovič^{1,2}, Sumeet Kumar^{3,4}, Aleš Mrzel¹, Mojca Vilfan¹

¹ Jožef Stefan Institute, Jamova 39, Ljubljana, Slovenia

² Jožef Stefan International Postgraduate School, Ljubljana, Slovenia

³ Atoms Italia, Rossano Veneto, Italy

⁴ Innovation Factory, AREA Science Park, Trieste, Italy.

andrej.kovic@ijs.si

Abstract. Solution based *in situ*, single step coatings with platinum nanoparticles of MoSI-based nanowires is presented in this communication. An average particle diameter of 2.25 nm (± 0.66 nm) was obtained for Pt-coated MoSI nanowires, showing a narrow size distribution. Single-step *in situ* reduction method could be applied for large-scale applications, given the economic and environment viability of such synthesis process.

Keywords: Nanowires, platinum, nanoparticles, decoration, coating, molybdenum

1. Introduction

Nanotechnology and its potential application a field of interest ranging in different sectors, bio-medical, industrial to recently electronic industry. There exists an interesting subclass of nanowires (NWs), which offers a very high degree of freedom in modifying its surface and thus rendering it capable for various applications. It is quite noteworthy that the nanowires have already been employed as templates for coatings. In the same line the carbon nanotubes (CNTs) have been recently used as templates for the deposition of metal particles via supercritical fluid [1,2,3], adsorption[4], electrochemical deposition[5], physical vapor deposition (PVD)[6], and electroless plating[7].

Furthermore inorganic nanotubes were decorated to improve their properties. TiO₂ nanotubes were uniformly decorated with Pt nanoparticles (diameter ~ 5 nm) by a two-step photo irradiation method. The resulting hybrid nanotube arrays show an

excellent catalytic activity for methanol electrooxidation [8]. SnO₂ nanowires were investigated after their surface functionalization by the atomic layer deposition (ALD) of Pt nanoparticles. The morphology, size, and concentration of Pt particles on SnO₂ nanowires can be controlled by varying the number of ALD reaction cycles, and therefore, the gas-sensing properties of the nanowires can be altered *via* the Pt catalyst effect and the modification of Schottky barrier junctions on the nanowire surface in the vicinity of Pt nanoparticles [9]. Au porous nanotubes (PNTs) were synthesized by a templating technique that involves the chemical synthesis of Ag nanowire precursors, electroless surface modification with Au, and selective etching. A subsequent galvanic replacement reaction between [PtCl₆]²⁻ and residual Ag generates Pt-decorated Au porous nanotubes (Pt/Au-PNTs), which represents a new type of self-sustained high surface area electrocatalysts with ultra-low Pt loading [10]. Also Platinum nanoparticles were uniformly deposited on ZnO nanowires for photon-sensing applications. The morphology, size, and concentration of Pt particles on the ZnO nanowires can be controlled by varying the number of atomic layer deposition reaction cycles. The Pt-decorated ZnO nanowires exhibit much faster photon response and recovery speeds than the pristine ZnO nanowires [11]. Recently, high-density aligned n-type silicon nanowire (SiNW) arrays were decorated with 5-10 nm platinum nanoparticles (PtNPs), which have been fabricated by aqueous electroless Si etching followed by an electroless platinum deposition process. Coating of PtNPs on SiNW sidewalls yielded a substantial enhancement in photoconversion efficiency and in energy conversion efficiency. The results demonstrate PtNP-decorated SiNWs to be a promising hybrid system for solar energy conversion [12]. Although numerous methods have produced metal-coated nanostructures, only a few techniques have produced coatings with enhanced density, uniformity, and short production.

Here we report Pt decorations formed on MoSI nanowires (NWs) [Mo₆S_yI_z (8.2 ≤ y+z ≤ 10)] using single step *in situ* reduction method in aqueous medium. Particle geometries produced by the described method are similar to those previously mentioned; however particle densities are substantially greater and can be varied as a function of the concentration of nanoparticles' precursor salts.

Our method of coating is relatively simple to produce and requires a short processing time (typically < 15 min). This method may be a new way to produce superior coatings of metals on various categories of MoSI NWs and may be applicable also to other nanotubes and nanowires. The NWs used for this study were produced as described elsewhere [13].

2. Experimental

Here we report on a novel and very efficient way of decoration of bundles of $\text{Mo}_6\text{S}_y\text{I}_z$ ($8.2 \leq y+z \leq 10$) nanowires with Pt nanoparticles. The decoration is carried out in a single step, at room temperature, and without reducing agents, which results in decoration of both side walls and ends of NW bundles.

Bundles of $\text{Mo}_6\text{S}_y\text{I}_z$ ($8.2 \leq y+z \leq 10$) nanowires were synthesized directly from the elements in a one-step procedure. The ampoule was left for 60 hours in a temperature gradient with lower temperature being 750 °C and higher temperature 850 °C. At the higher-temperature end, the remaining material was a dark-brown powder. We have shown previously that the obtained powder consists of bundles of nanowires, molybdenum grains and MoS_2 crystals [14]. After sonication, the supernatant was extracted and separated by centrifugation (1250g for one hour) to remove heavier MoS_2 crystals, molybdenum grains and bundles with larger diameters. The supernatant was micro-filtrated and dried at 50 °C, with resulting yield around 10 wt% and the average diameter of the bundles was around 20-80 nm.

By using a 2.5 mM water solution of $\text{Na}_2[\text{PtCl}_4]$ as a source of Pt, the bundles were self-decorated in 20 mg/L MoSI water dispersion. The density of Pt nanoparticles on NWs was controlled simply by changing the amount of the added $\text{Na}_2[\text{PtCl}_4]$ solution.

The end materials were observed and analyzed high-resolution transmission electron microscope (HR-TEM, Jeol JEM-2100F, 200 keV) equipped with energy dispersive spectrometer (EDS). The diameters of nanowires and platinum nanoparticles were determined using Image Pro Analyzer. Distributions in particle size were obtained by evaluating at least 100 nanoparticles per sample.

3. Results and Discussions

We find that platinum nanoparticles appear on nanowires already after a short-time deposition. A proof that the observed material are indeed $\text{Mo}_6\text{S}_y\text{I}_z$ ($8.2 \leq y+z \leq 10$) nanowires covered with platinum (Fig. 1) is given by the energy-dispersive X-ray spectrum (EDS), shown in Fig. 2.

The TEM images of Pt coated $\text{Mo}_6\text{S}_y\text{I}_z$ ($8.2 < y+z < 10$) NWs are shown in Fig. 1 and Fig. 3. The NW in Fig. 1 has an approximate diameter of 50 nm, while the NW in Fig. 3 has a diameter of nearly 25 nm. In both images a thorough decoration of NWs is observed.

Particle analysis was performed on Pt-decorated NWs with initial NW diameters of approximately 20-80 nm. Particle size distributions are shown in Fig. 4 and Fig. 5. In the case of Fig. 4 an average overall particle size was determined to be 2.25 nm with a standard deviation of 0.66 nm and 2.82 nm with a standard deviation of 0.83 nm as shown in Fig. 5.

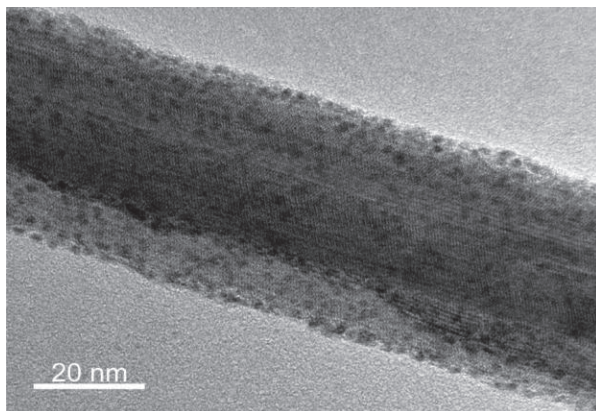


Figure 1: TEM image of MoSI nanowire decorated with platinum nanoparticles

For determination of the average particle sizes and the histograms (Fig. 4, Fig. 5) showing the particle size distribution, several wires were analyzed for each coating

condition: 5 nanowires with varying diameters were analyzed; approximately 100 particle diameters per wire were measured to determine the average particle size. The measurement also shows that the particle diameter is independent of the nanowire diameters.

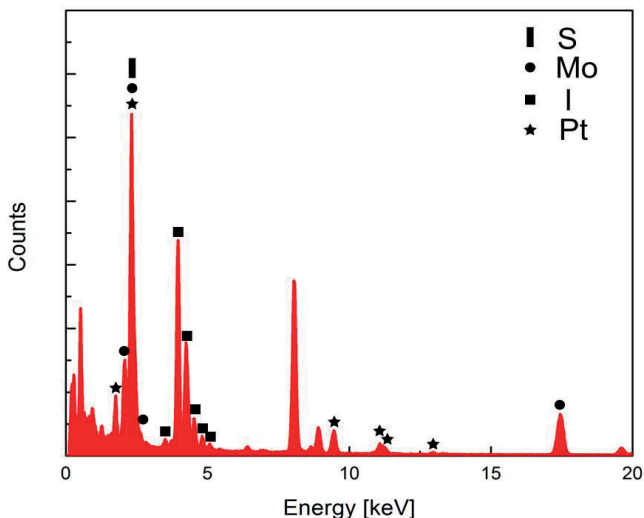


Figure 2: EDS spectrum confirming the composition of the obtained material. The marked peaks are belonging to molybdenum, sulfur, iodine and platinum. The unmarked peaks are belonging to copper, carbon and oxygen, which are present on a holy carbon coated copper mesh.

Higher magnification images of the coated NWs shown in Fig. 6. The high-resolution image shows that the coatings are very dense, however, some areas remain uncoated. This is not uncommon, as several previous studies of coatings on CNTs [1,2,3].

It can be seen clearly in Figs. 4 and 5 that the particle size distribution for Pt is small, with all the particles appearing very similar in shape and size and the decoration appears to be homogeneous. The coatings reported in this study offer the possibility for these nano-coated materials to act as an excellent catalyst thanks to the immense surface area observed due to large particle densities and small particle size.

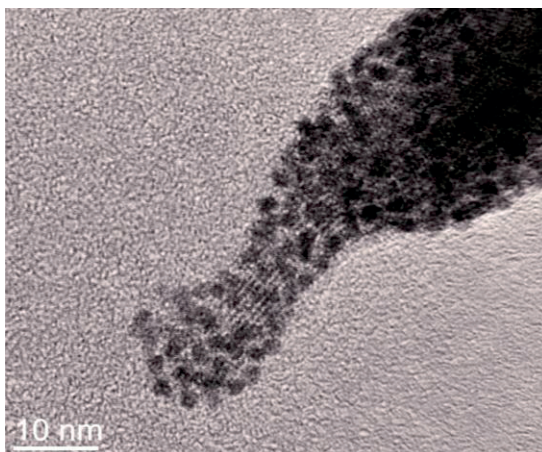


Figure 3: TEM image of MoSI nanowire decorated with a high amount of platinum nanoparticles

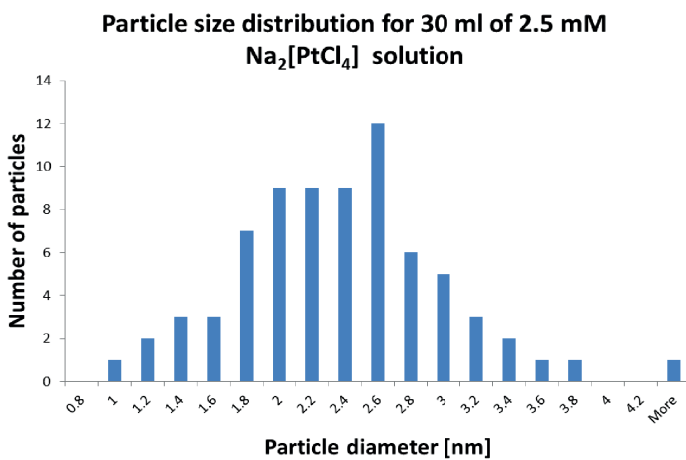


Figure 4: Particle size distribution for 30 ml of 2.5 mM $\text{Na}_2[\text{PtCl}_4]$ solution

Particle size distribution for 50 ml of 2.5 mM $\text{Na}_2[\text{PtCl}_4]$ solution

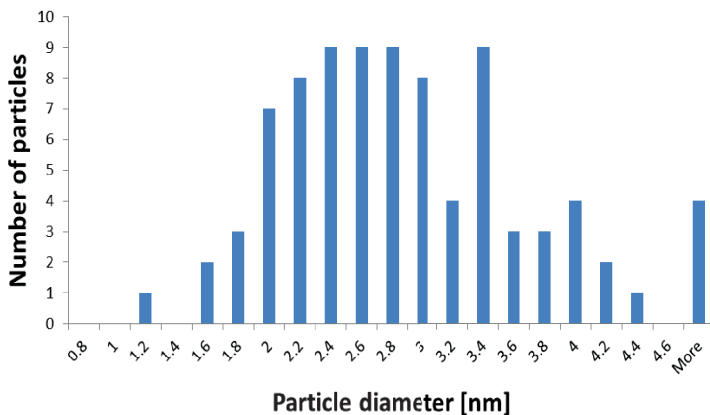


Figure 5: Particle size distribution for 50 ml of 2.5 mM $\text{Na}_2[\text{PtCl}_4]$ solution

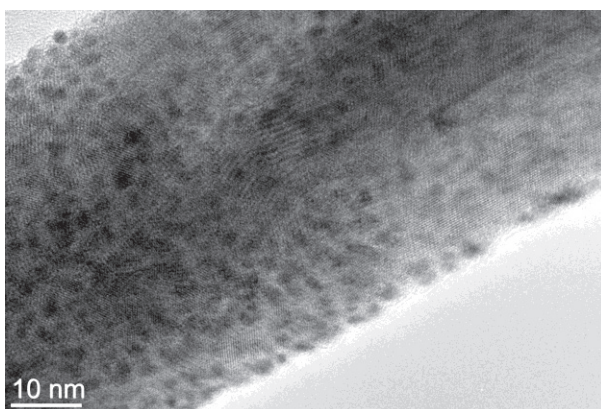


Figure 6: HRTEM image of a MoSI nanowire densely covered with platinum nanoparticles

Clubbed with this, the use of highly stable support materials (MoSI NWs), taking advantage of their excellent mechanical and thermal properties, is also a motivation for using molybdenum (Mo) based templates for metal nanoparticles coated nanostructures [13].

4. Conclusions

We presented a simple step efficient self-decoration of $\text{Mo}_6\text{S}_y\text{I}_z$ ($8.2 \leq y+z \leq 10$) nanowires with platinum nanoparticles at room temperature without any additional reducing reagents. We were able to successfully decorate nanowires with platinum in the solution. The described procedure is one of the few examples of redox templating at room temperature without use of reducing agent to produce noble metal-decorated nanowires, which enables large scale production for different applications including sensors and platinum catalyzed reactions.

Acknowledgments

The authors acknowledge the support of COINAPO COST Action plan MP0902 and the Slovenian research Agency (P1-0192, P1-0040).

References:

- [1] X-R. Ye, Y. Lin, C. Wang, and C.M. Wai: Supercritical fluid fabrication of metal nanowires and nanorods templated by multiwalled carbon nanotubes. *Adv. Mater.* 15, 316 (2003).
- [2] X-R. Ye, Y. Lin, and C.M. Wai: Decorating catalytic palladium nanoparticles on carbon nanotubes in supercritical carbon dioxide. *Chem. Commun.* 5, 642 (2003).
- [3] X-R. Ye, Y. Lin, C. Wang, M.H. Engelhard, Y. Wang, and C.M. Wai: Supercritical fluid synthesis and characterization of catalytic metal nanoparticles on carbon nanotubes. *J. Mater. Chem.* 14, 908 (2004).
- [4] J.M. Planeix, N. Coustel, B. Coq, V. Bretons, P.S. Kumbhar, R. Dutartre, P. Geneste, P. Bernier, and P.M. Ajayan: Application of carbon nanotubes as supports in heterogeneous catalysis. *J. Am. Chem. Soc.* 116, 7935 (1994).
- [5] Q. Xu, L. Zhang, and J. Zhu: Controlled growth of composite nanowires based on coating Ni on carbon nanotubes by electrochemical deposition method. *J. Phys. Chem. B* 107, 8294 (2003).
- [6] Y. Zhang, Q. Zhang, Y. Li, N. Wang, and J. Zhu: Coating of carbon nanotubes with tungsten by physical vapor deposition. *Solid State Commun.* 115, 51 (2000).
- [7] Q. Li, S. Fan, W. Han, C. Sun, and W. Liang: Coating of carbon nanotube with nickel by electroless plating method. *Jpn. J. Appl. Phys.* 36, L501 (1997).
- [8] Yan-Yan Song, Zhi-Da Gao, Patrik Schmuki: Highly uniform Pt nanoparticle decoration on TiO_2 nanotube arrays: A refreshable platform for methanol electrooxidation, *Electrochemistry Communications*, vol. 13 (1), 290-293.
- [9] Yu-Hung Lin, Yang-Chih Hsueh, Po-Sheng Lee, Chih-Chieh Wang, Jyh Ming Wu, Tsong-Pyng Perng and Han C. Shih: Fabrication of tin dioxide nanowires with ultrahigh gas sensitivity by atomic layer deposition of platinum, *J. Mater. Chem.*, 2011, 21, 10552-1055.

- [10] Xiaohu Gu, Xiao Cong, and Yi Ding: Platinum-Decorated Au Porous Nanotubes as Highly Efficient Catalysts for Formic Acid Electro-Oxidation, *Chem. Phys. Chem*, 2010, 11, 841–846
- [11] Yu-Hung Lin, Yang-Chih Hsueh, Chih-Chieh Wang, Jyh-Ming Wu, Tsong-Pyng Perng, Han C. Shih: Enhancing the Photon-Sensing Properties of ZnO Nanowires by Atomic Layer Deposition of Platinum, *Electrochem. Solid-State Lett.*, 2010, volume 13, issue 12, K93-K95.
- [12] Kui-Qing Peng, Xin Wang, Xiao-Ling Wu, Shuit-Tong Lee: Platinum Nanoparticle Decorated Silicon Nanowires for Efficient Solar Energy Conversion, *Nano Lett.*, Vol. 9, No. 11, 2009, 3704–3709.
- [13] KOVIČ A., Žnidaršič A., Jesih A., Mrzel A., Gaberšček M., Hassanien A.: A novel facile synthesis and characterization of molybdenum nanowires. *Nanoscale research letters*, 2012, vol. 7, str. 567-1-567-7.
- [14] Rangus M, Remškar M, Mrzel A: (2008) Preparation of vertically aligned bundles of $\text{Mo}_6\text{S}_9\text{I}_x$, ($4.5 < x < 6$) nanowires. *Microelectron J.* 39, 2008, 475–477.

Photocatalytic water treatment with TiO₂: slurry reactor vs. microreactor

Matic Krivec^{1,2}, Luka Suhadolnik¹, Kristina Žagar¹, Miran Čeh^{1,2}, Goran Dražić^{1,2}

¹ Department for Nanostructured Materials, Jožef Stefan Institute, Ljubljana, Slovenia

² Jožef Stefan International Postgraduate School, Ljubljana, Slovenia

matic.krivec@ijs.si

Abstract. Microreactor was constructed from a titanium sheet with CNC machining and a TiO₂ film was immobilized on the microchannel inner walls. As prepared microreactor possesses high surface-to-volume ratio (6780 m²/m³) and high illumination homogeneity (1.2 mW/cm²) through the entire reactor. Its photocatalytic activity was evaluated with the degradation of caffeine and compared to a conventional slurry reactor with suspended Degussa P25 particles. Microreactor exhibits approximately one order of magnitude higher initial reaction rates in a continuous flow regime than reactions in a slurry reactor.

Keywords: TiO₂, photocatalysis, microreactor

1 Introduction

Nowadays, remediation of different hazardous wastes, contaminated grounds and air has attracted attention all over the world. In order to overcome this problem, extensive research is being conducted to develop new analytical, biochemical and physicochemical methods for the characterization and elimination of hazardous chemicals from air, soil and water. One among several solutions of this problem is the usage of photocatalytic reaction with the presence of TiO₂, which can oxidize various contaminations such as alkanes, aliphatic carboxylic acids, dyes, simple aromatics, halogenated alkanes, pesticides, etc. [1]

Most research in photocatalysis for water treatment is done using TiO₂ catalyst in the form of dispersed powders. Slurry reactors with suspended TiO₂ particles have a

uniform catalyst distribution and a high photocatalytic surface-to-volume ratio.^[2] For any practical use, this is not the preferred configuration; TiO₂ particles have to be additionally separated from the products and recycled, which is an expensive and time-consuming process. Furthermore, the penetration depth of UV light is rapidly decreasing due to the strong absorbing properties of suspended TiO₂ particles and other organic molecules. Immobilized photocatalysts are therefore the desirable option for photocatalytic reactions. The only drawback of the photocatalysis in the presence of immobilized TiO₂ is the insufficient amount of exposed TiO₂ surface area which in most cases leads to the mass-transfer limitations. [2]

During recent years, microreactors have become an important tool for conducting different catalytic reactions. Inorganic catalysts (TiO₂) and organic ones (enzymes, cells) can be either immobilized on the inner surface of the microchannel or they can be suspended in a suspension [3]. In both ways, this technique has many advantages over the conventional reactors; laminar flow, short molecular diffusion distances, large surface-to-volume ratios, high spatial illumination homogeneity and good light penetration through the entire reactor depth are some of many characteristics that give processes inside microreactors the advantage in comparison to the conventional reactors. [4,5] Moreover, photocatalytic microreactors can be optimized to their applicable version in the research laboratories while they do not have to undergo the scale-up: the ‘numbering up’ process enables a potential continuous reaction inside a microreactor system on an industrial scale.

Herein, we report a construction of a photo-microreactor with immobilized TiO₂ from a titanium substrate with integrated UV-LED light source. Microreactor (MR) was compared to a slurry quartz reactor (SR) with identical light source and with a suspended Degussa P25 powder. The kinetic parameters, initial reaction rates and photonic efficiencies of the two experimental set-ups were evaluated with the degradation of caffeine molecules.

2 Experimental

2.1 Microreactor design

Figure 1 shows the image of the serpentine shaped microreactor. The microreactor device was fabricated from a titanium sheet in which serpentine microchannel with cross dimension of approximately 500 μm x 500 μm and length of 390 mm was engraved using a high-precision CNC milling machine. The substrate was then

rinsed with absolute ethanol in an ultrasonic bath for several minutes and then inner walls of the microchannel as well as the rest of the titanium surface were coated with a layer of TiO₂-nanotubes and TiO₂-nanoparticles in a two-step synthesis which included anodic oxidation and hydrothermal treatment. After the synthesis, TiO₂ coating inside the microchannel was protected with high-purity wax and the upper surface of microreactor was grinded and polished in order to prepare a smooth titanium surface for the next step of the microreactor fabrication: sealing. UV-transparent plexi glass with the the same dimensions as titanium sheet and with two holes of 2 mm in diameter (inlet and outlet) was put on the top of the microchannel and sealed with epoxy glue. Plastic inert tubings were used for connecting the inlet of the reactor with a high-precision syringe pump (Aladdin, World Precision Instruments, Sarasota, USA) and the outlet with the tubes for sample collection. The whole device was afterwards mounted in stainless steel housing. 4 UV-LED lights (Roithner Lasertechnik GmbH, Vienna, Austria) with emission maximum at 365 nm were mounted in a carefully designed circuit board. The UV source was integrated on the top of the microreactor housing and the incident light intensity of 1.2 mW cm⁻² was measured.

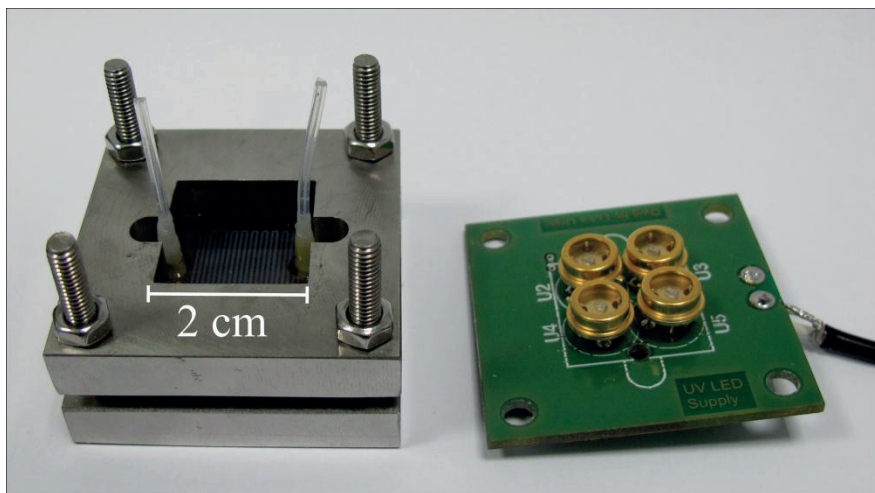


Figure 1: TiO₂-based microreactor with housing and UV-LED supply.

2.2 Photocatalytic experiments

2.2.1 Slurry reactor

10 mg of a Degussa P25 TiO₂ was mixed with 10 mL of the caffeine aqueous solution (25, 10, 5, 2.5 mg/L) inside a 10-mL quartz reactor. The suspension was firstly stirred for 30 min in the dark to achieve the absorption-desorption equilibrium of caffeine on the surface of the particles. Afterwards, the reactor was exposed to the illumination source (UV-LED, I = 1.2 mW cm⁻²) and samples were taken from it during different periods of the reaction. The concentration of caffeine was monitored by a high-precision UV-Vis-IR spectrometer (PerkinElmer Lambda 950).

2.2.2 Microreactor

Four different initial concentrations of caffeine (25, 10, 5, 2.5 mg/L) were continuously pumped through illuminated microreactor (UV-LED, I = 1.2 mW cm⁻²) and a high-precision UV-Vis-IR spectrometer was used for characterization of caffeine concentration for 6 different volumetric flow rates (100, 80, 60, 40, 30, 20 μL/min). 200 μL of caffeine solution was pumped through the microreactor before each sample being collected in order to avoid the errors. A dark sample (without illumination) was collected at each flow rate to get an insight of the caffeine adsorption on TiO₂ film. The degradation of each initial caffeine concentration was repeated two times and an average is presented in the results.

3 Results and discussion

3.1 Dimensions and characteristics: SR vs. MR

Table 1 shows the dimensions and characteristics of SR and MR. The volume of SR is more than 100 times larger than the volume of MR. Surface-to-volume ratios are similar in both experimental set-ups. While a rather high surface-to-volume ratio of SR was expected (2000-7000 m²/m³), the actual illuminated surface area per volume is much lower due to the smaller penetration depth of UV light through the TiO₂ suspension. High surface-to-volume ratio (6780 m²/m³) of immobilized microreactor is one of essential advantages of this technology. Moreover, the illuminated surface area per volume is similar to surface-to-volume ratio while the reactor design provides a homogeneous distribution and penetration of UV light through the entire reactor depth. The UV intensity was the same in both experiments.

Table 1

Dimensions and characteristics of slurry reactor and microreactor.

Characteristic	SR	MR
State of TiO ₂	Suspended (Degussa P25)	Immobilized (nanotubes + particles)
TiO ₂ phase	Anatase:rutile (80:20)	Anatase
Reactor volume [mL]	10	0.07
Surface-to-volume ratio [m ² /m ³]	2000-7000 ^{[1], [2]}	6780 ^[3]
UV-LED intensity [mW/cm ²]	1.2	1.2

^[1] The illuminated surface area per volume is much lower than this value due to the smaller penetration depth of UV light through the suspension.

^[2] Calculated from the dispersive particle sizes, adopted from Nguyen et. al. (2005) and Cabrera et. al. (1996).

^[3] The value was calculated without taking into account the specific surface area of TiO₂ film.

3.2 Photocatalytic activity

The results of photocatalytic degradation of caffeine in two different reactors are presented in Figure 2. The residence times of both reactors are not comparable due to the different types of reactor processing; therefore, the direct comparison has to be done with the calculated initial reaction rates (R_i). The initial degradation rates in the slurry reactor are approximately one order of magnitude smaller than those in the microreactor. This indicates that the reaction on micro-level possesses many advantages in comparison to the conventional reactor. In both cases, the initial degradation rates increase with the increasing initial caffeine concentration and come to the plateau at a certain concentration. This suggests that the rate of the degradation is limited by the adsorption of the caffeine molecules on the photocatalyst which follows the Langmuir-Hinshelwood (L-H) equation [6]:

$$R_i = - \frac{d[\text{caffeine}]}{dt} = \frac{k_a K c_i}{1 + K c_i} \quad (1)$$

where k_a is the apparent reaction rate constant, K is the adsorption coefficient and c_i is the initial concentration of caffeine. The linearization of Langmuir-Hinshelwood

equation (Eq. 1) results in a linear relationship with an intercept of k_a^{-1} and a slope of $(k_a K)^{-1}$:

$$\frac{1}{R_i} = \frac{1}{k_a} + \frac{1}{k_a K} \frac{1}{c_i} \quad (2)$$

The reaction rate constants and adsorption coefficients (Table 2) were derived from intercepts and slopes of the linear lines shown in the insets of Figure 3. While the k_a values strongly vary with the experimental conditions, the K value determined with the slurry reactor (15 L mmol^{-1}) agrees with the value determined with the microreactor (17 L mmol^{-1}). This proves that the adsorption of caffeine on TiO_2 is independent of the type of the reactor or the state of the photocatalyst.

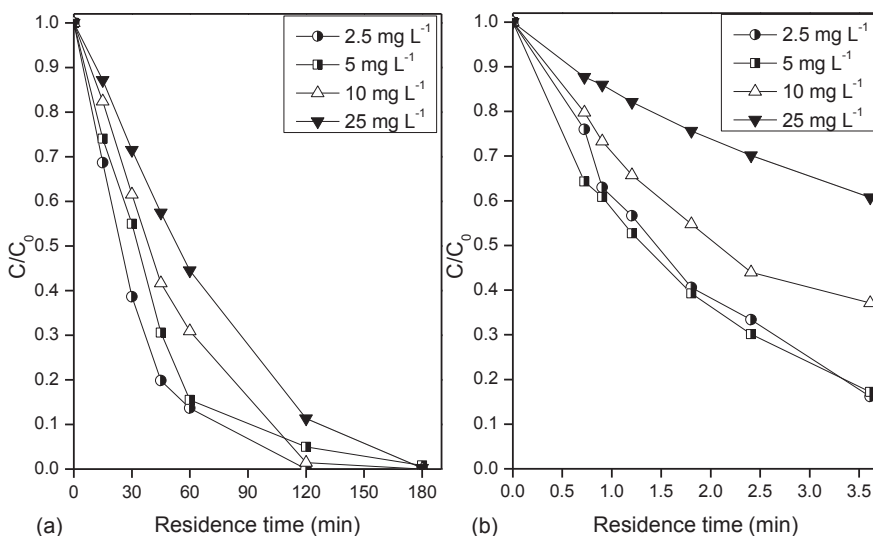


Figure 2: Photocatalytic degradation of caffeine at different residence times for different initial concentrations inside (a) a slurry reactor with suspended Degussa P25 particles (1 g L^{-1}) and (b) microreactor with immobilized TiO_2 nanotube/nanoparticle film.

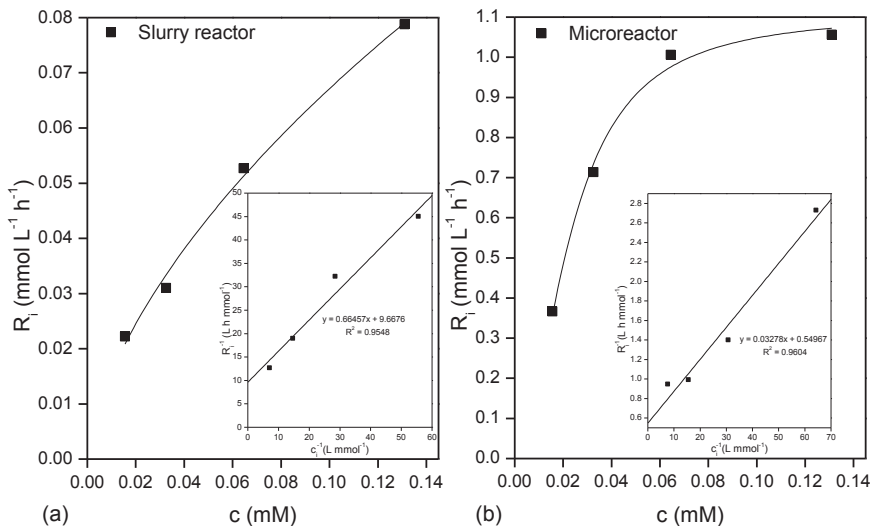


Figure 3: Initial oxidation rates (R_i) at different initial concentrations (c_i) inside (a) a slurry reactor with suspended Degussa P25 particles (1 g L⁻¹) and (b) microreactor with immobilized TiO₂ nanotube/nanoparticle film. The inset diagrams show the linearization of the data.

Table 2

Reaction rate constants and adsorption coefficients of slurry reactor and microreactor.

Reactor type	k_a [mmol L ⁻¹ h ⁻¹]	K [L mmol ⁻¹]
Slurry reactor	0.10	15
Microreactor	1.82	17

Photonic efficiency (ξ) is a well-recognized parameter in photochemistry. It is defined as the number of transformed reactant molecules divided by the number of incident photons of monochromatic light on the catalytic surface. Photonic efficiencies in slurry reactor (0.42 – 1.49%) are a lot higher than efficiencies in microreactor (0.1 – 0.3%). Direct comparison of the photonic efficiencies in the two set-ups is not possible due to different amount of TiO₂ particles during the photocatalysis; therefore, a standardized photonic efficiency per catalytic surface area inside the reactor gives more comparable results. In this case, the standardized

efficiencies values of the reaction in the microreactor are a lot higher than in a slurry reactor set-up.

Table 3

Photonic efficiencies and standardized photonic efficiencies for slurry reactor and microreactor at different initial concentrations of caffeine.

Reactor type	C_i [mg L ⁻¹]	ξ [%]	ξ_{stand} [cm ⁻²]*10 ⁻³
Slurry reactor	25	1.49	0.006
	10	0.10	0.008
	5	0.59	0.014
	2.5	0.42	0.021
Microreactor	25	0.30	0.62
	10	0.29	0.61
	5	0.20	0.42
	2.5	0.10	0.22

4 Conclusion

A photocatalytic microreactor with immobilized TiO₂ film with high surface-to-volume ratio (6780 m²/m³) was constructed and compared with a conventional slurry reactor. The initial reaction rates inside a microreactor (0.36 – 1.38 mmol L⁻¹ h⁻¹) are one order of magnitude higher than those in a slurry reactor (0.02 – 0.08 mmol L⁻¹ h⁻¹). The reaction rates are in both cases limited by the adsorption of caffeine molecules on the photocatalyst; the adsorption coefficients (K) are similar in both reaction set-ups, therefore, the differences in the efficiencies are exclusively the result of the individual reaction design. Lower standardized photonic efficiencies inside the slurry reactor confirm the advantages of the photocatalytic reaction in a microreactor design.

References:

- [1] M.R. Hoffmann, S.T. Martin, W. Choi, D.W. Bahnemann. Environmental Application of Semiconductor Photocatalysis. *Chemical Reviews*, 95: 69-96, 1995.
- [2] A.K. Ray, A.A.C.M. Beenackers. Novel photocatalytic reactor for water purification. *AIChE Journal*. 44: 477-483, 1998.
- [3] P. L. Urban, D.M. Goodall, N.C. Bruce. Enzymatic microreactors in chemical analysis and kinetic studies. *Biotechnology Advances* , 24: 42-57, 2006.
- [4] K. Jänisch, V. Hessel, H. Löwe, M. Baerns. Chemistry in microreactors. *Angewandte Chemie International*, 43: 406-446, 2004.
- [5] R. Gorges, S. Meyer, G. Kreisel. Photocatalysis in microreactors. *Journal of Photochemistry and Photobiology A: Chemistry*, 167: 95-99, 2004.
- [6] J. Theurich, M. Lindner, D.W. Bahnemann. Photocatalytic degradation of 4-chlorophenol in areated aqueous titanium dioxide suspensions: a kinetic and mechanistic study. *Langmuir*, 12: 6368-6376, 1996.
- [7] V. Nu Hoai Nguyen, R. Amal, D. Beydoun. Photocatalytic reduction of selenium ions using different TiO₂ photocatalysts. *Chemical Engineering Science*. 60: 5759-5769, 2005.
- [8] M.I. Cabrera, O.M. Alfano, A.E. Cassano. Absorption and scattering coefficients of titanium dioxide particulate suspensions in water. *Journal of Physical Chemistry*. 100: 20043-20050, 1996.

For wider interest

Remediation and elimination of hazardous chemicals and wastes from contaminated waters is a growing concern of societies all over the world. Photocatalytic degradation with TiO_2 is a prospective solution to overcome this problem, although the procedure contains several engineering limitations which prevent the scale-up of the process. Photocatalytic degradation inside a microreactor with immobilized TiO_2 has several advantages in comparison to the conventional TiO_2 -type reactors: the system works in the continuous operation mode, there is no need for an additional catalyst separation operation and the provided light is homogeneously distributed in the whole reactor depth. Moreover, the reactor can be optimized to its final version in a laboratory as the numbering-up process replaces the standard scale-up process in the industry. The parallel binding of these reactors results in higher flows and consequently higher efficiencies of this system without changing (reducing) the activity of the reactor during scale-up.

Raziskave tekočkristalnih elastomerov z jedrsko magnetno resonanco

Jerneja Milavec^{1,2}

¹ Odsek F5, Inštitut Jožef Stefan, Ljubljana, Slovenija

² Mednarodna podiplomska šola Jožefa Stefana, Ljubljana, Slovenija

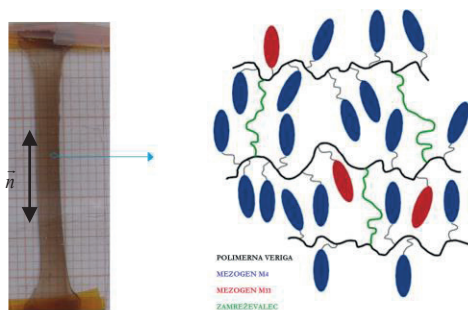
jerneja.milavec@ijs.si

Povzetek. Tekočkristalni elastomeri (TKE) so v zadnjih nekaj letih zbudili veliko zanimanja med raziskovalci, najverjetneje zaradi njihove potencialne uporabe v različnih tehnoloških napravah, kot so umetne mišice, pametne površine, mikrovalovi in drugo. Njihove makroskopske in fizikalne lastnosti so zelo povezane z elastičnostjo polimerne mreže in orientacijskimi lastnostmi mezogenov. Elastične lastnosti stransko-verižnih monodomenskih tekočkristalnih elastomerov smo določili s termo-mehanskimi meritvami, z devterijevo jedrsko magnetno resonančno (²H JMR) spektroskopijo pa smo raziskali domensko urejanje selektivno devteriranih monodomenskih tekočkristalnih elastomerov.

Gljučne besede: Stransko-verižni tekočkristalni elastomer, ureditveni parameter, ²H JMR, termo-mehanske lastnosti.

1 Uvod

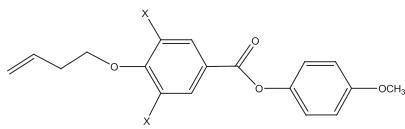
Tekočkristalni elastomeri kombinirajo orientacijsko urejenost tekočih kristalov in elastičnost polimerne mreže. Sestavljeni so iz polimerne verige na katero so pripete molekule mezogena (slika 1). Polimerne verige so nato zamrežene, da dobijo elastične lastnosti. Orientacijsko urejenost molekul mezogena lahko dosežemo z mehanskim raztezanjem elastomera med pripravo. Tekočkristalni elastomeri spadajo v skupino pametnih materialov, saj imajo sposobnost zapomniti si makroskopsko obliko pod posebnimi pogoji [1,2,3].



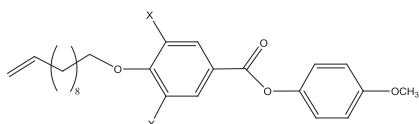
Slika 1: Fotografija in skica strankoverižnega monodomeskega TKE z ureditvenim vektorjem \vec{n} v vertikalni smeri. Z modro barvo so označene molekule mezogena M4, z rdečo molekule mezogena M11, z zeleno zamreževalec in s črno polimerna veriga.

2 Priprava tekočerkristalnih elastomerov

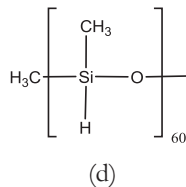
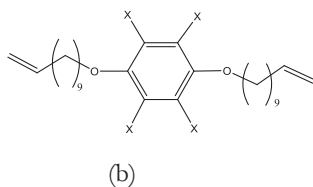
Kemijsko strukturo devteriranih molekul za pripravo TKE vidimo na sliki 2. Selektivno devterirani TKE so narejeni iz devteriranega mezogena M4, mezogena M11, zamreževalca in polimera. Za pripravo elastomerov smo uporabili dobro znano metodo (zamreževanje v dveh korakih), ki sta jo prva iznašla Kupfer in Finkelman [4]. Pripravili smo tri monodomske stransko-verižne TKE s 33,6 % mezogena M4, 51,4 % mezogena M11 in 15 % zamreževalca (tabela). V enem vzorcu je bila samo ena od sestavin devterirana, da smo lahko s pomočjo ^2H JMR spektroskopije ugotovili povprečno urejenost lokalnih domen znotraj vzorca. Prosojnost vzorca v nematski fazi nam pove, da so domene dobro poravnane v vertikalni smeri (slika 1).



(a)



(b)



Slika 2: Kemijska struktura molekule mezogena M4 (a), mezogena M11 (b), zamerževalca (c) in polisiloksanske verige. (d). Z x so označena devterijeva mesta v molekuli.

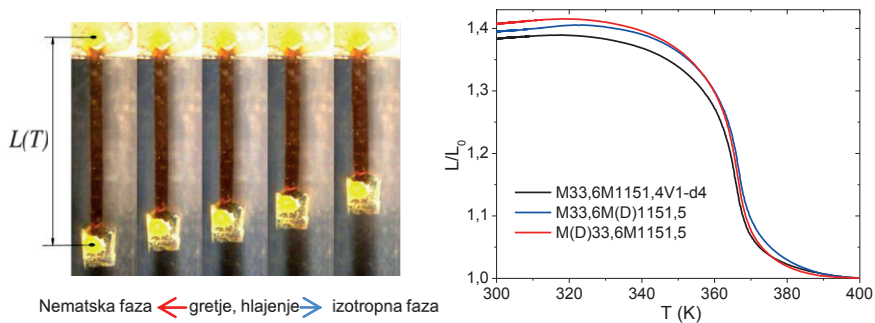
Tabela 1: V tabeli so zbrani podatki o količini sestavin za pripravo selektivno devteriranih stransko-verižnih monodomenskih tekočerkristalnih elastomerih.

Name of LCE samples	M(mmol)	dM(mmol)	CL(mmol)	dCL(mmol)	M11(mmol)	dM11(mmol)
M(d)33.6M(11)(d)51.4	-	0.336	0.150	-	0.514	-
M33.6M(11)(d)51.4	0.336	-	0.150	-	-	0.514
M33.6M(11)51.4 (CL-d)	0.336	-	-	0.150	0.514	-

3 Lastnosti tekočerkristalnih elastomerov

3.1 Termo-mehanske lastnosti

Fizikalne lastnosti TKE smo določili s termo-mehanskimi meritvami v odvisnosti od temperature. Ponovljivost rezultata po nekajkratnih spremembah temperature nam poda podatek o kvaliteti vzorca. Kot je razvidno iz grafa (slika 3), se vsi trije vzorci podobno odzivajo. To potrjuje, da so bili vzorci dobro izdelani. Pri 362 K je viden prehod iz nematske v paranematsko fazo, raztezek L/L_0 pri minimalni masi 100g pa je 1,4 oz. 40%.



Slika 3 : Fotografija elastomera pri različnih temperaturah [1]. (b) Termo-mehanske meritve stransko-verižnih monodomenskih TKE pri minimalni masi 100g pri gretju in hlajenju vzorca.

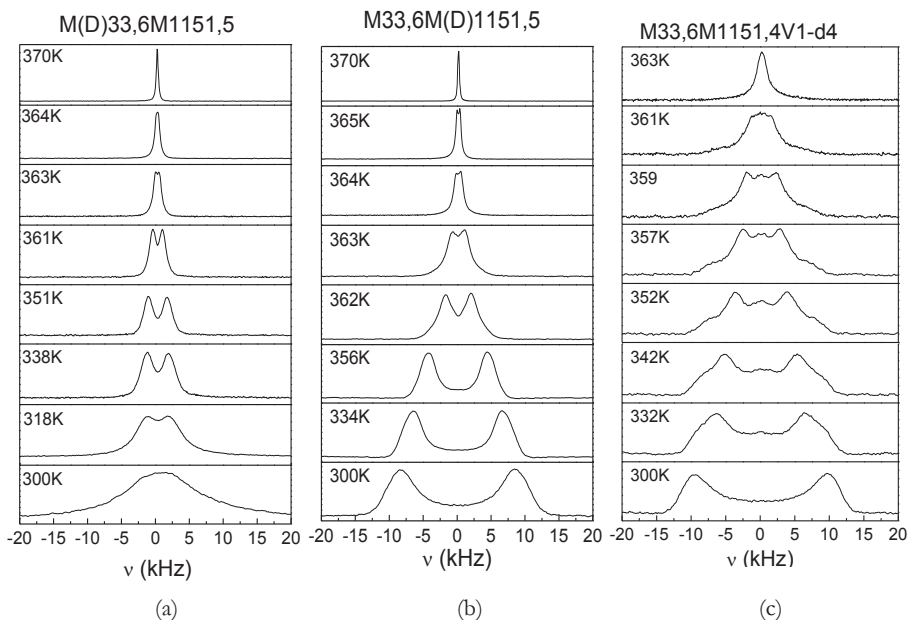
3.2 Ureditveni parameter

S pomočjo ^2H JMR spektroskopije smo določili orientacijsko urejenost TKE v bližini nematsko-paranematskega prehoda. Za te meritve smo uporabljali Ultrashield Advance III Bruker spektrometer s 500MHz superprevodnim magnetom, ki ima Larmorjevo frekvenco za devterij pri 76,7 MHz.



Slika 4: Fotografija Ultrashield Advance III Bruker spektrometra s 500 MHz superprevodnim magnetom.

Iz oblike spektrov smo nato določili povprečno orientacijsko urejenost devteriranih molekul.

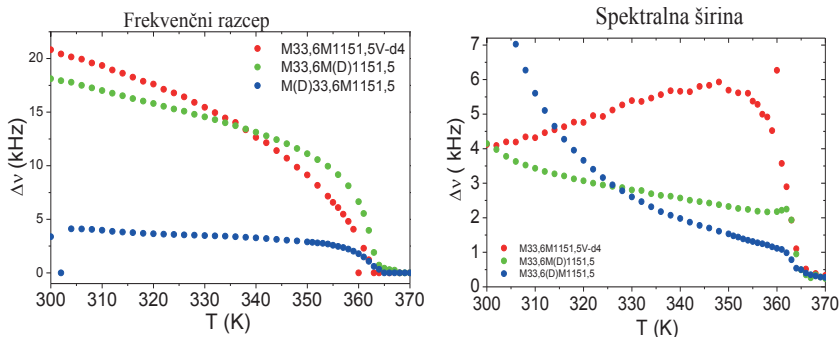


Slika 5: ^2H JMR spektri stransko-verižnih monodomenskih TKE z devteriranim mezogenom M4 (a), mezogenom M11 (b) in zamreževalcem. Direktor \vec{n} , ki meri povprečno smer ureditve mezogena je bil vedno vzporeden s smerjo magnetnega polja.

Iz ^2H JMR spektrov je razviden standardni prehod iz paranematske v nematsko fazo, ki je pri 362 K. Pri visoki temperaturi je vzorec v izotropni fazi, zato opazimo v spektru le en vrh. Z nižanjem temperature pa molekule preidejo v nematsko fazo (bolj urejeno), zato se v spektru pojavita dva vrhova, ki z nižanjem temperature postajata vse bolj široka, to je zaradi delne urejenosti in povprečne orientacije molekul.

Z opisom spektra z enojno ali dvojno Lorentzovo funkcijo smo določili urejenost devteriranih molekul v TKE-ju. Frekvenčni razcep, ki ga opazimo, ko hladimo

vzorec iz paranematske v nematsko fazo, je v idealno orientiranem vzorcu sorazmeren z ureditvenim parametrom.



Slika 6: (a) Frekvenčni razcep treh stransko-verižnih vzorcev, dobljenih s pomočjo opisa spektrov z enojno ali dvojno Lorentzovo funkcijo v odvisnosti od temperature. (b) Spektralna širina spektrov v odvisnosti od temperature.

Iz grafa in spektrov (slika 5, 6) je razvidno, da so molekule z devteriranim zamreževalcem in mezogenom M11 bolj urejene, kot molekule elastomera z devteriranim mezogenom M4. Slabša urejenost molekul mezogena je najverjetneje posledica krajše dolžine molekule. Krajše molekule so bolj občutljive na temperaturne spremembe, in je zato povprečna orientacijska urejenost slabša. Iz grafa (6(a)), ki prikazuje spektralno širino v odvisnosti od temperature, je lepo viden prehod iz nematske v paranematsko fazo.

4 Zaključek

S pomočjo ^2H JMR spektroskopije smo lahko izmerili orientacijsko urejenost selektivno devteriranih molekul v tekočokristalnem elastomeru. Dokazali smo, da je povprečna orientacijska urejenost krajših molekul mezogena M4 slabša, kot urejenost daljših molekul mezogena M11 in zamreževalca, ki je vpet na obeh koncih na polimerno verigo. S termo-mehanskimi meritvami smo dokazali, da so bili vsi trije vzorci enako dobro pripravljene, da imajo okoli 40% raztezka in so zaradi teh lastnosti dobri kandidati za različne aplikacije [5].

Literatura:

- [1] V. Domenici, G. Ambrožič, M. Čopič, A. Lebar, I. Drevenšek-Olenik, P. Umek, B. Župančič, M. Žigon. Interplay between nematic ordering and thermomechanical response in a side-chain liquid single crystal elastomer containing pendant azomesogen units. *Polymer*, 50: 4837–4844, 2009
- [2] V. Domenici, B. Zalar. Paranematic–nematic phase transition in liquid crystalline elastomers: a ^2H -NMR study. *Phase Transitions: A Multinational Journal*, 83:10–11, 1014–1025, 2010
- [3] V. Domenici, M. Conradi, M. Remškar, M. Viršek, B. Župančič, A. Mrzel, M. Chambers, B. Zalar. New composite films based on MoO_{3-x} nanowires aligned in a liquid single crystal elastomer matrix. *J. Mater. Sci.*, 46: 3639–3645, 2011
- [4] Kupfer J, Finkelmann H. *Macromol Chem Rapid Commun*, 12:717–26, 1991
- [5] B. Župančič, B. Zalar, M. Remškar, V. Domenici. Actuation of Gold-Coated Liquid Crystals Elastomes. *Appl. Phys. Express*, 6 : 021701-0217015, 2013

Za širši interes

Tekočekristalni elastomeri (TKE) so v zadnjih nekaj letih zbudili veliko zanimanja med raziskovalci, najverjetneje zaradi njihove potencialne uporabe v različnih tehnoloških napravah, kot so umetne mišice, pametne površine, mikrovalovi in drugo. Njihove makroskopske in fizikalne lastnosti so zelo povezane z elastičnostjo polimerne mreže in orientacijskimi lastnostmi mezogenov. Elastične lastnosti stransko-verižnih monodomenskih tekočekristalnih elastomerov smo določili s termo-mehanskimi meritvami, z devterijevo jedrsko magnetno resonančno (^2H JMR) spektroskopijo pa smo raziskali domensko urejanje selektivno devteriranih monodomenskih tekočekristalnih elastomerov. Dokazali smo, da je povprečna orientacijska urejenost krajših molekul mezogena M4 slabša, kot urejenost daljših molekul mezogena M11 in zamreževalca, ki je vpet na obeh koncih na polimerno verigo. S termo-mehanskimi meritvami pa smo dokazali, da so bili vsi trije vzorci enako dobro pripravljene, da imajo okoli 40% raztezka in so zaradi teh lastnosti dobri kandidati za različne aplikacije.

Synthesis of LaF₃ nanoparticles

Olivija Plohl^{1,2}, Darja Lisjak^{1,2}, Darko Makovec^{1,2,4}, Miha Drofenik^{1,3}

¹ Department of K8, Jožef Stefan Institute, Ljubljana, Slovenia

² Jožef Stefan International Postgraduate School, Ljubljana, Slovenia ³ Faculty of chemistry and chemical engineering, Maribor, Slovenia ⁴ CENN Nanocenter, Ljubljana, Slovenia

olivija.plohl@ijs.si

Abstract. In this paper the syntheses of LaF₃ nanoparticles with solvothermal method using different solvents (i.e., water, ethylene glycol) is described. LaF₃ nanoparticles were previously synthesized with different syntheses and superior properties were obtained by high-temperature organic-precursors decomposition method. Since this method uses toxic reagents (e.g., oleylamine, octadecene) our aim was to study more in details the synthesis of LaF₃ nanoparticles with an ecologically more acceptable solvothermal synthesis. Morphology and chemical composition of synthesized nanoparticles was characterized with transmission and scanning electron microscopies combined with energy-dispersive X-ray spectroscopy while their crystal structure was analysed with X-ray powder diffraction.

Keywords: fluorescence, lanthanides, nanoparticles, solvothermal synthesis

1. Introduction

There is a growing interest for the development of fast, inexpensive and sensitive techniques that enable analysis of biocomponents in one step. Bioimaging provides most of these options using biolabels. Recently, lanthanide-doped nanoparticles, which show upconversion (i.e., process, where wavelength of emission is smaller than wavelength of excitation), were proposed as alternative biolabels for fluorescence bioimaging. In lanthanide-doped upconverting nanoparticles the crystalline host matrix is doped with sensitizer ion (e.g., Yb³⁺), which absorbs the excitation radiation with specific wavelength and with active ions (e.g., Er³⁺, Tm³⁺, Ho³⁺), which emit at shorter wavelength after a nonradiative energy transfer from

the sensitizer (Figure 1). The most extensively studied host matrices are fluorides, because they can incorporate lanthanide ions, exhibit low phonon energies and high chemical stability. Therefore, they are often used as host materials for upconversion process [1,2]. One of suitable upconversion fluorescent host matrix is lanthanum fluoride (LaF_3). In this report we describe solvothermal syntheses of LaF_3 nanoparticles using two different solvents, water and ethylene glycol.

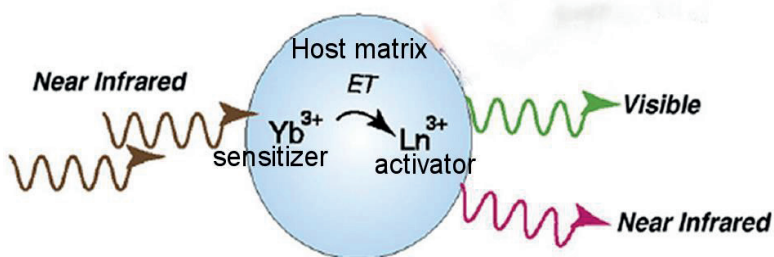


Figure 1: Schematic presentation of upconversion mechanism in lanthanide-doped nanoparticles [3].

2. Experimental work

LaF_3 nanoparticles were synthesized with solvothermal synthesis at 160 °C or 180 °C for 6-24 h using water or ethylene glycol (EG) as a solvent.

In the case of using water as a solvent, $\text{La}(\text{NO}_3)_3 \cdot 6\text{H}_2\text{O}$ was used as a source of La^{3+} and NaBF_4 as a F^- source. For the preparation of LaF_3 nanoparticles 5 mL of $\text{La}(\text{NO}_3)_3$ was added to 10 mL of aqueous solution containing 2 mmol of trisodium citrate (Na_3Cit) to form La-Cit complex. Cit^{3-} plays an important role in the morphology and size of the final products. After stirring, 15 mL of aqueous solution containing 25 mmol of NaBF_4 was introduced into first solution. The pH of the mixture was adjusted to 1 with diluted HNO_3 (1 M). Strong acidic environment is advantageous to form LaF_3 products instead of NaLaF_4 . After additional agitation for 15 min, the mixture was transferred into a Teflon vessel tightly sealed in a stainless steel autoclave and maintained at 180 °C or 160 °C for 6 or 24 h. Under solvothermal conditions, the La^{3+} released from the complexes, reacts with F^- produced during slow hydrolysis of NaBF_4 , to form LaF_3 [4].

For the preparation of LaF_3 nanoparticles with solvothermal synthesis in EG, NaBF_4 (8 mmol) was dissolved in 20 mL of EG. Afterward, a solution of 2 mmol

$\text{La}(\text{NO}_3)_3 \cdot 6\text{H}_2\text{O}$ in 20 mL of EG was added into the above solution under vigorous stirring. After 20 min, the mixed solution was transferred into a 70 mL Teflon vessel as described above and maintained at 160 °C or 180 °C for 6-12 h.

The crystal structure of synthesized LaF_3 nanoparticles was verified by X-ray powder diffraction (XRD). The crystallite size was determined from the X-ray diffractograms with the Pawley method [5] using the crystallographic program Topas2R 2000 (Bruker AXS). Morphology and chemical compositions of synthesized LaF_3 nanoparticles was analysed with transmission electron microscopy (TEM) and scanning electron microscopies (SEM) combined with energy dispersive X-ray spectroscopy (EDXS).

3 Results and discussion

XRD patterns of LaF_3 nanocrystals synthesized with solvothermal synthesis using water or EG as a solvent at different temperatures and reaction times are showing pure hexagonal structure of LaF_3 (JCPDS 32-0483). Well defined XRD peaks suggest on the high crystallinity of nanoparticles synthesized in water or in EG. The broader diffraction peaks in the case of EG indicate that the size of LaF_3 nanocrystallites, synthesized in EG is smaller in comparison to those synthesized in water. This was confirmed with XRD analysis (Table 1), which also revealed that the particles size increases with the increasing temperature and time of solvothermal synthesis for both solvents. These results are in good agreement with SEM and TEM analyses.

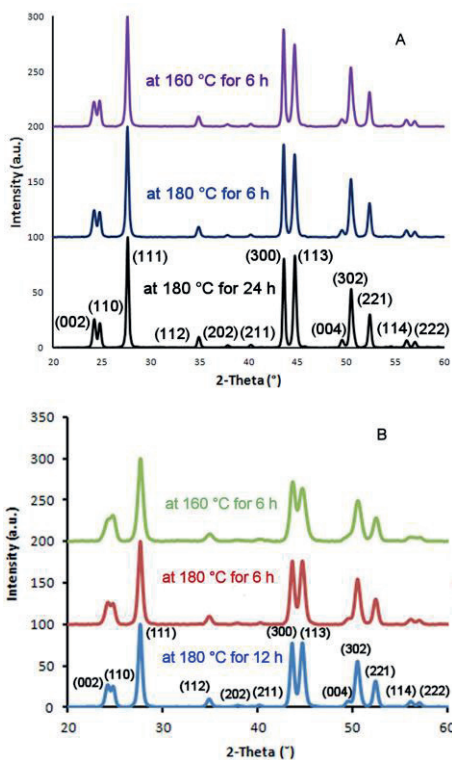


Figure 2: XRD patterns of as-synthesized LaF_3 nanoparticles obtained at different solvothermal temperatures and reaction times (A in water, B in EG).

The SEM image shows LaF_3 nanoparticles synthesized at 160 °C for 6 h in water and clearly indicates that the products consist of aggregated hexagonal nanoplates (Figure 3 - left-hand side). Meanwhile, the as-prepared LaF_3 sample at 160 °C for 6 h in EG reveals irregular shape of particles, which are in some way connected to each other (Figure 3 – right-hand side).

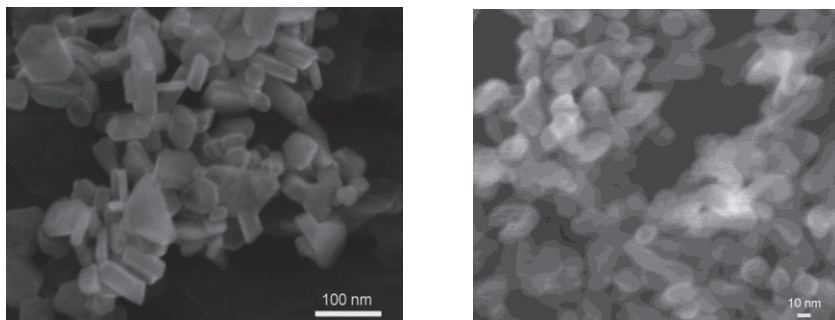


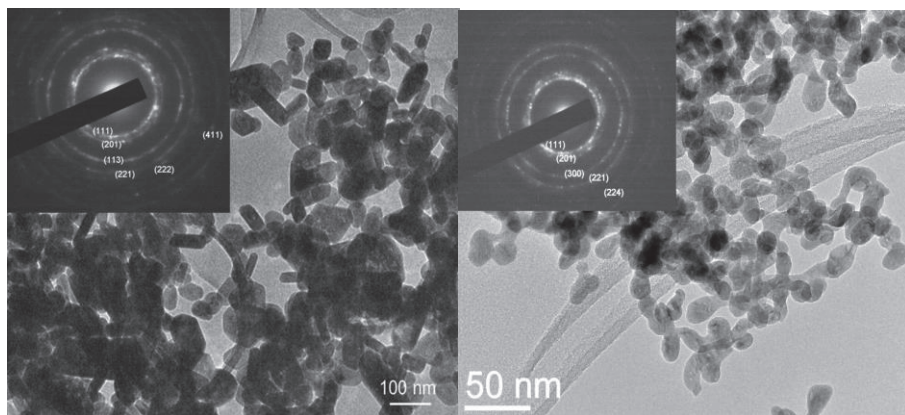
Figure 3 :SEM images of LaF_3 nanoparticles synthesized in water at 160 °C for 6 h (left) and in EG at 160 °C for 6 h (right).

TEM studies show that the size of nanoparticles synthesized in water varies between 60 and 80 nm, depending of reaction temperature and time. The particles are aggregated and in form of hexagonal nanoplates (Figure 4 – left-hand side). Some of them appear like rods since they are oriented perpendicular to the supporting grid. As suggested from selected area electron diffraction (SAED) particles are well crystalline with the hexagonal structure of LaF_3 (see inset in Figure 4 – left-hand side).

In the case, where EG was used as a solvent, synthesized nanoparticles were of irregular shape and particles were connected to each other. The particle size varies between 20 and 30 nm (Figure 4 – right-hand side). The crystallinity of the particles was confirmed with SAED (see inset in Figure 4 – right-hand side), similar to the above.

Table 1: Crystalline size of as-prepared LaF₃.

water		EG	
Temperature and reaction time	Crystal size (nm)	Temperature and reaction time	Crystal size (nm)
180 °C for 24 h	80 ± 1	180 °C for 12 h	30 ± 1
180 °C for 6 h	60 ± 2	180 °C for 6 h	25 ± 2
160 °C for 6 h	60 ± 3	160 °C for 6 h	20 ± 1

**Figure 4:** TEM images of LaF₃ nanoparticles synthesized at 180 °C for 24 h in water (left) and in EG at 180 °C for 6 h (right).

EDXS analysis confirmed that in the case of LaF₃ nanoparticles synthesized in water the atomic ratio of the La:F ~ 1:3. However, a minor fraction of oxygen was also detected. Although XRD results confirm hexagonal LaF₃ crystal structure, the oxygen can be incorporated into fluoride crystal lattice forming LaOF as confirmed with SAED on some of the particles. Possible source of O₂ can be O₂ dissolved in water, from citric acid or reagent La(NO₃)₃x6H₂O.

EDXS analysis of LaF₃ nanoparticles, synthesized in EG revealed, that the atomic ratio of the La:F was not stoichiometric as in LaF₃ and oxygen was also detected. Similar as above, SAED of some of the particles was attributed to LaOF. As oppose to the synthesis in water the only source of O₂ can be the reagent La(NO₃)₃x6H₂O. Therefore, it was assumed that the main source of unwanted oxygen was the reagent. The incorporation of O²⁻ into fluoride lattice was not reported previously. One of

the reasons may be that previous studies were limited to the characterization with XRD and simple TEM or SEM observation without detailed SAED and/or EDXS analyses. It is possible that the incorporation of O^{2-} reduces the fluorescence emission intensity of fluorides. Namely, oxides possess larger phonon energy than the fluorides. This may also explain why fluorescent fluoride nanoparticles with better optical properties have been obtained by high-temperature organic-precursors decomposition method [6]. In this later case, the purity of products may be higher.

4 Conclusion

In this work different solvents for solvothermal synthesis of LaF_3 nanoparticles are tested. When water was used as solvent, synthesized particles were composed of aggregated hexagonal nanoplates. Morphology of nanoparticles, synthesized in EG differs from those synthesized in water. Those particles were of irregular shape and were connected between each other. In both cases XRD results confirmed hexagonal LaF_3 crystal structure but on the other hand EDXS and SAED analysis revealed the presence of oxygen in some of the particles, which can be incorporated into fluoride crystal lattice forming $LaOF$. One of possible solution to synthesize oxygen-free LaF_3 is to replace reagent $La(NO_3)_3$ with $LaCl_3$ and will be tested in future.

References

- [1] F. Wang, X. Liu Recent advances in the chemistry of lanthanide-doped upconversion nanocrystals. *Chemical Society Reviews*, 38: 976-989, 2009.
- [2] A. Gnach, A. Bednarkiewicz Lanthanide-doped up-converting nanoparticles: Merits and challenges. *Nano today*, 7: 532-563, 2012.
- [3] J. Shen, L. Zhao, G. Han Lanthanide-doped upconverting luminescent nanoparticle platforms for optical imaging-guided drug delivery and therapy. *Advanced Drug Delivery*, 2012.
- [4] C. Li, J. Yang, P. Yang, H. Lian, J. Lin Hydrothermal synthesis of lanthanide fluorides LnF_3 ($Ln = La$ to Lu) nano-/microcrystals with multiform structures and morphologies. *Chemistry of materials*, 20: 4317-4326, 2008.
- [5] G.S. Pawley Unit-cell refinement from powder diffraction scans. *Journal of Applied Crystallography*, 14: 357-361, 1981.
- [6] Y.W. Zhang, X. Sun, R. Si, L.P. You, C.H. Yan Single-crystalline and monodisperse LaF_3 triangular nanoplates from a single-source precursor. *Journal of the American Chemical Society*, 127: 3260-3261, 2005.

For wider interest

Materials synthesis – K8

Head of department: prof. dr. Darko Makovec

Magnetic nanoparticles (ferrofluids, nanocomposites)

New methods for the controlled synthesis of iron oxide nanoparticles are developing. Therefore, our department is focused on the functionalization of magnetic nanoparticles for biomedical applications. The surface properties of nanoparticles are tuned with organic/inorganic coatings (e.g., thin layer of amorphous silica). The coating prevents the agglomeration of nanoparticles and further enables easier preparation of their dispersion in various liquids. *Multifunctional materials*

By mastering the surface properties of nanoparticles nanocomposites combining the various properties of the constituent materials can be prepared. For example, our studies include combinations of ferrimagnetics and dielectrics materials. Current studies are also related to the development of new magneto-optic materials for sensors and magneto-catalytic materials for environmental applications.

Magnetic materials for micro- and mm-waves

Magnetic materials suitable for the absorbers of electromagnetic waves and for the non-reciprocal ferrite devices are being developed. Ceramics and composites based on ferrites are studied for the microwave applications and a new method for the preparation of magnetically oriented thick hexaferrites films for self-biased mm-wave applications has been developed.

Inorganic fluorescent nanoparticles

Inorganic fluorescent nanoparticles are considered as a promising alternative for biomedical applications. Lanthanide-doped nanoparticles with appropriate surface modification can be used in bioapplications such as bioimaging.

Analysis of the background under the e-beam and x-ray induced Auger peaks

Besnik Poniku^{1,2}, Igor Belič¹, Monika Jenko¹

¹ Institute of Metals and Technology, Ljubljana, Slovenia

² Jožef Stefan International Postgraduate School, Ljubljana, Slovenia

besnik.poniku@imt.si

Abstract. The main goal in our research work is achieving the complete automation of the Auger electron spectra processing and interpretation. To achieve this goal removal of the background and reduction of the noise are unavoidable preconditions. The spectra in both electron spectroscopies, namely Auger electron spectroscopy and X-ray photoelectron spectroscopy, consist of the characteristic peaks, the background¹, and noise. Due to different modes of excitation in Auger electron spectroscopy and in X-ray photoelectron spectroscopy, the level of background is different. In this work we analyzed a number of samples using both techniques and investigated the differences in background in both cases in order to come to some conclusion about the contribution of the backscattered electrons to the background.

Keywords: Auger electron spectroscopy, X-ray photoelectron spectroscopy, automation, background removal, noise reduction.

1 Introduction

As nanotechnology is already at the forefront of modern technological development in the World, the need to better understand the structures at that level through different techniques of characterization, including surface analysis such as Auger Electrons Spectroscopy (AES) and X-ray Photoelectron Spectroscopy (XPS), is becoming ever more evident. When performing measurements in AES, the background and noise are inseparable parts of the Auger electron (AE) spectra [1]. In our attempt to better understand the different contributors to the background in

¹ Considering here the peak base as part of the background.

order to better define it for its successful removal, we have performed a number of AES measurements and XPS measurements on a number of samples of different materials. If we have in mind the excitation-relaxation mechanism in electron spectroscopies shown in fig. 1 [2],

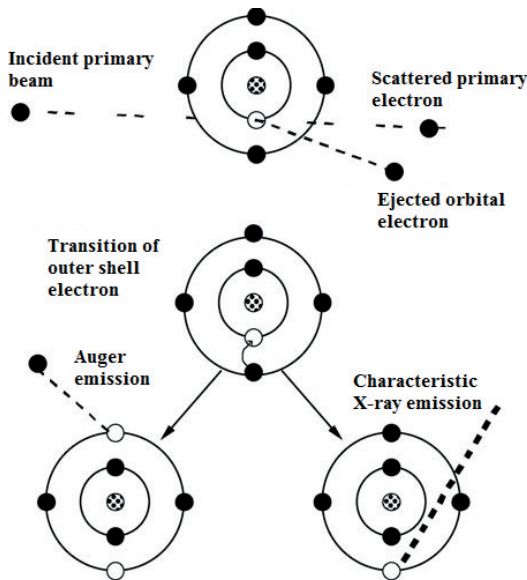


Figure 1: Inner shell ionization and de-excitation tree for carbon.

the sample is excited through an electron beam in AES as shown in Step 1, whereas in XPS the X-ray beam typically generated from a Mg or Al cathode is used for exciting the sample. The signal in AES comes from measuring the energy of the emitted Auger electrons (Step 3), whereas in XPS the energy of the ejected orbital electrons (Step 1) is measured. As it may be evident from observing fig. 1, although the XPS peaks emerge from measuring the energy of the ejected orbital electrons, the atoms undergo the relaxation processes shown there and there is Auger emission as well, meaning that we will find characteristic Auger peaks of the elements in the sample whose XPS spectrum using X-rays is being measured [6]. This is evident in fig. 2 where an Auger spectrum (a) and an XPS spectrum (b) measured on the same sample of Copper are presented.

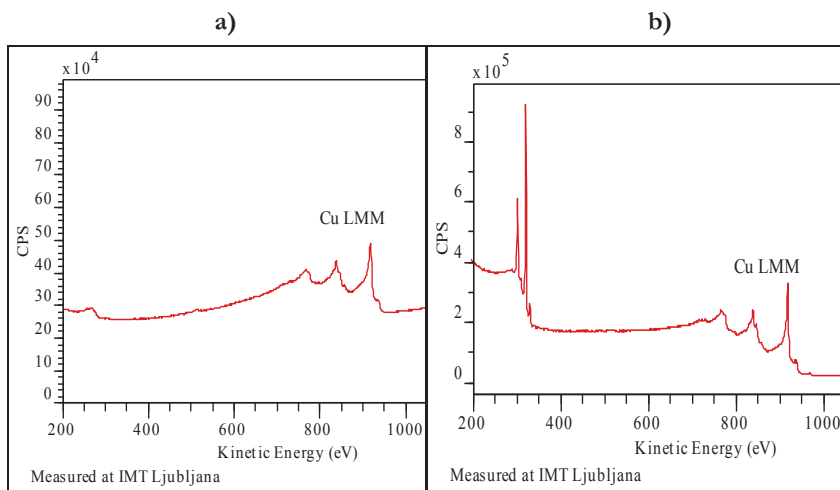


Figure 2: Cu LMM Auger peaks as they appear in a Cu AES spectrum (a) and in a Cu XPS spectrum (b).

While the main contributors to the background in the AES are the backscattered electrons, the secondary electrons, and the attenuated Auger electrons [3], in XPS the contribution of the backscattered electrons to the background is missing. And understandably so, because the backscattered electrons are the electrons of the primary electron beam that penetrate the surface of the sample, get deflected and come back out of the sample surface, whereas in XPS there is no electron beam, but the excitation of the atoms in the sample is achieved using X-rays.

2 Experimental part

All of the measurements for collecting the spectra that were used in our investigation were carried out using MicroLab 310-F, an instrument that integrates both AES and XPS, enabling us to take spectra in both modes without having to exchange samples too often. Only by recalling that Ultra High Vacuum (UHV) conditions have to be reached in the sample chamber in order to carry out the measurements one may see the practicability of this option of carrying out both AES and XPS in the same chamber with minor alterations.

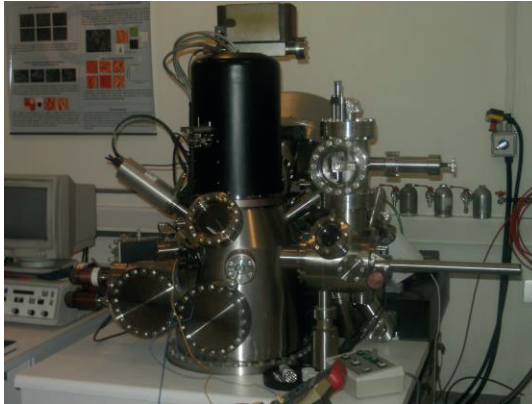


Figure 3: Microlab 310-F situated at IMT laboratory for surface analysis.

We used 11 samples in total: Al(100), Al(110), Al(111), Cu, Fe(100), Fe(110), Fe(111), Fe₂%Si (100), Ni, Ti, and W(110). The energy of the primary electron beam for all the AES measurements was 10 000 eV. We must recall that once the energy of the primary beam surpasses the threshold energy for inducing a transition, the energy of the Auger electrons is independent of the energy of the primary beam, since the energy of the Auger electrons depends on the electronic structure of the atoms [4]. Most of the XPS measurements on the other hand were carried on using an Mg source with 1253.6 eV, while some measurements were also carried out using an Al source with energy of 1486.6 eV.



Figure 4: Samples used to measure the AES and XPS spectra.

3 Discussion

The Auger transition will occur once the threshold energy has been reached and a core hole has been created in the atom by the primary beam [5], be it electron beam, X-ray beam, or any other mode of excitation. Thus in both AES and XPS spectra we will find the characteristic Auger peaks. The only thing that will differ in these cases in regard to the Auger peaks is the background underneath the peaks.

In the literature various authors have described the contribution of the backscattered electrons and the secondary electrons to the spectrum. Among others, Jousset and Langeron [7] worked on defining the spectrum resulting from the contribution of the backscattered electrons, where they proposed a model which predicts in a wide energy range, from about 0.2 to 0.75 E_p (energy of the primary beam), an exponential law for this contribution to the spectrum in the integral form [the $N(E)$ spectrum]. Eq. (1) gives the relationship, in a simplified form:

$$n_B(E) \sim \exp(E/E_1) \quad (1)$$

where n_B represents the number of backscattered primary electrons leaving the surface at energies E , whereas E_1 corresponds to a minimum loss which is a fixed value for a certain energy of the primary beam. Fig. 5 [7] shows the spectra obtained by the mathematical model for copper at an energy $E = 2$ keV of the primary beam.

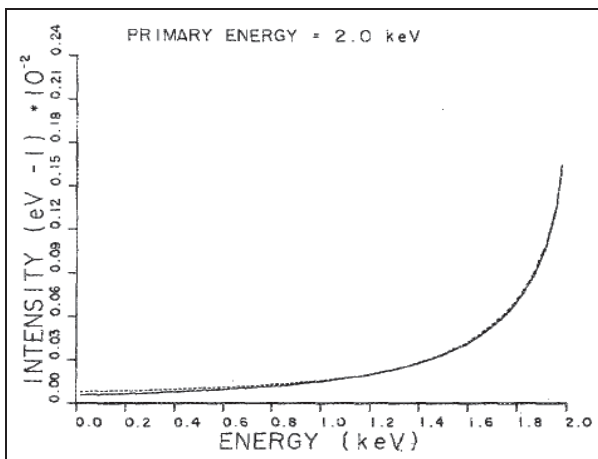


Figure 5: Spectra of copper for $E_p = 2$ keV calculated from the mathematical model.

Sickafus [8, 9] on the other hand, worked on describing the contribution of the secondary electrons to the spectrum. A schematic representation of an idealized secondary electron emission spectrum in the $\log j(E)/\log (E)$ display mode as proposed by Sickafus is shown on Fig. 6 [8].

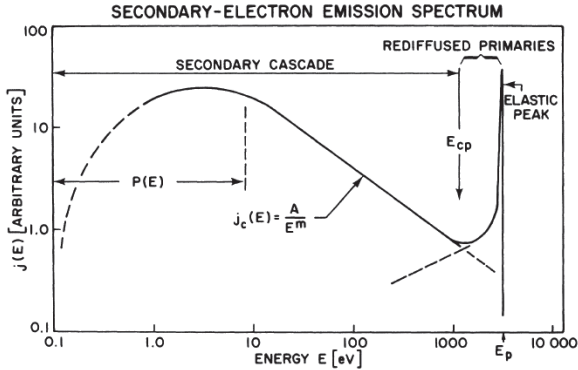


Figure 6: Schematic representation of the secondary electron spectrum.

According to Sickafus, this is the characteristic spectrum to be associated with a monoenergetic external primary beam in the absence of other types of emission. The spectrum is divided into three sections, the secondary electron cascade, the rediffused primaries, and the elastic peak. The boundary, E_{cp} , can be thought of as the region where one distribution begins to exceed the other. A simplified background function describing the energy dependence of the secondary electron cascade from elements is given by

$$B(E) = AE^{-m} \quad (2)$$

where $B(E)$ is the number distribution of secondary electrons emitted with kinetic energy E from a solid sample, A and m are constants characteristic of the material, but A also depends upon the energy of the primary beam [10].

Since the backscattering contribution originates from the primary beam, based on the examples shown above in fig. 5 and fig. 6, and taking into consideration that the intensity and energy of the primary beam should stay fairly stable during the measurement, I expected to see a fairly smooth line, either a straight one, or a steadily increasing one as the backscattering contribution increases while moving to higher energies in the spectrum. But the results obtained showed a rather different

shape of that backscattering contribution represented as the difference between the intensity (represented as Counts Per Second – CPS of electrons reaching the detector) of the Auger peaks in the AES spectrum and the Auger peaks in the XPS spectrum:

$$B_{e-} = CPS_{AES} - CPS_{XPS} \tag{3}$$

I should note here that in my opinion no normalization is required to correlate the signals, since both the experiments are being measured in the same equipment and we are looking directly at the number of electrons that are reaching at the detector per second from the sample, be it e-beam excited or x-ray excited. This means that subtracting the signals directly is completely meaningful.

In the case of Iron, Fe (100), if the difference spectrum (the last one in fig. 7) is closely inspected, one can notice that the AES – XPS difference continues to rise until the threshold energy of the peak is reached.

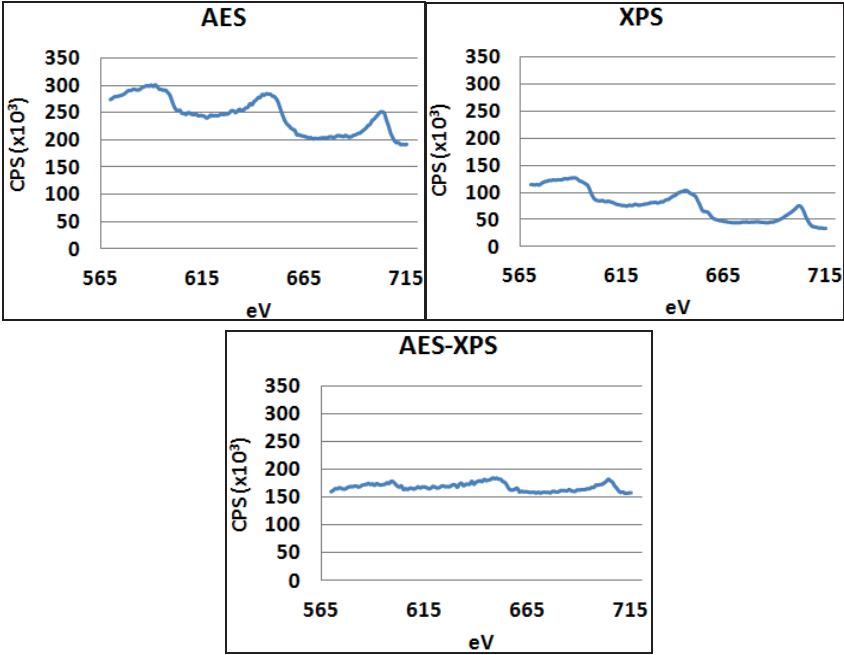


Figure 7: Intensity values (CPS) for the energy region of the Fe peaks for AES spectrum, XPS spectrum, and their difference.

Then immediately after the threshold energy we notice a drop in the AES – XPS difference, followed again by a steady rise until the threshold energy of the next peak and the followed drop. This means that the intensities do not change with the same rhythm, because that way we would have straight lines with positive, negative, or zero slope, but when we start approaching the peak from the left the AES intensity increases quicker than that measured in XPS for the same energy region, and when the intensity after the threshold energy starts to fall, the AES intensity falls quicker than that measured in XPS, for this reason we observe the decline in the difference spectrum after the threshold energy. In my opinion this cannot be attributed to backscattered electrons per se, but they still are the cause of these observed “hills” in the difference spectrum which resembles the peaks. This can be explained as the extra Auger electrons that are being excited due to the traveling of the backscattered electrons on their way out of the sample, which Auger electrons are absent then when we move away from the threshold energy characteristic of the transition.

Something similar is observed also for the rest of the samples which were used for the investigation. Fig. 8 shows the difference spectrum (AES – XPS) for all 11 samples, and there one can see that even though the shape may differ slightly from sample to sample, it is still far from the smooth line predicted by equations 1 and 2.

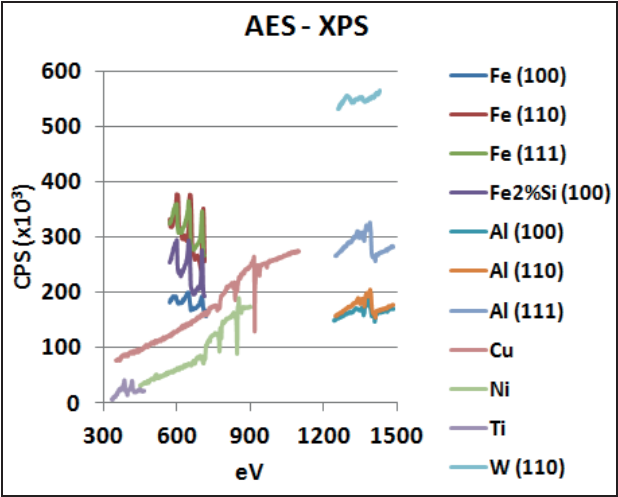


Figure 8: Difference spectrum (AES -XPS) for 11 samples.

References:

- [1] B. Poniku, I. Belič, M. Jenko. The Modeling of Auger Spectra. *Materials and Technology*, 45(1):39-46, 2011.
- [2] F. A. Settle. *Handbook of Instrumental Techniques for Analytical Chemistry*. New Jersey: Prentice Hall, 1997.
- [3] B. Poniku, I. Belic, M. Jenko. The peak base as a characteristic feature of the Auger electron spectra. *4th Jožef Stefan International Postgraduate School Students Conference*, Ljubljana, 2012.
- [4] J. T. Grant. AES: Basic Principles, Spectral Features and Qualitative Analysis. *Surface Analysis by Auger and X-ray Photoelectron Spectroscopy*. IM Publishing, 2003
- [5] Y. Strausser. Auger Electron Spectroscopy. *Encyclopedia of Materials Characterization*. Reed Publishing, 1992.
- [6] D. Briggs. XPS: Basic Principles, Spectral Features and Qualitative Analysis. *Surface Analysis by Auger and X-ray Photoelectron Spectroscopy*. IM Publishing, 2003.
- [7] D. Jousset and J. P. Langeron. Energy distribution of primary backscattered electrons in Auger electron spectroscopy. *J. Vac. Sci. Technol. A*, 5(4): 989-995, 1987.
- [8] E. N. Sickafus. Linearized secondary – electron cascades from the surfaces of metals. I. Clean surfaces of homogeneous specimens. *Physical Review B*, 16(4): 1436-1447, 1977.
- [9] E. N. Sickafus. Linearized secondary – electron cascades from the surfaces of metals. II. Surface and subsurface sources. *Physical Review B*, 16(4), 1448-1458, 1977.
- [10] J. C. Greenwood, M. Prutton, and R. H. Roberts. Atomic – number dependence of the secondary – electron cascade from solids. *Physical Review B*, 49(18): 12485-12495, 1994.
- [11] C. R. Brundle. XPS - X-ray Photoelectron Spectroscopy. *Encyclopedia of Materials Characterization*. Reed Publishing, 1992.
- [11] D. Briggs, J. T. Grant, Perspectives on XPS and AES. *Surface Analysis by Auger and X-ray Photoelectron Spectroscopy*. IM Publishing, 2003.

For wider interest

Our research work aims to find suitable ways to achieve full automation of the Auger spectra processing. Apart from simplifying greatly the manipulation of data after the measurement, we believe this will also improve greatly the reliability of the results obtained.

In order to make this automation possible, a precondition is the removal of background and noise from the Auger spectra, in order to “feed” the program with the data which represent only the characteristic peaks of elements. For a successful removal, a better understanding of the background and noise, and the factors that contribute to them is needed. This work was done in order to understand better the contribution of the backscattered electrons to the background.

To complete this work the spectra of 11 samples in total were measured using Auger Electron Spectroscopy (AES) and X-ray Photoelectron Spectroscopy (XPS). Samples such as Al(100), Al(110), Al(111), Cu, Fe(100), Fe(110), Fe(111), Fe₂%Si(100), Ni, Ti, and W(110) were used. The idea here was to use two different modes of excitation and observe the intensity under the Auger peaks of the same element. Since in AES an electron beam is involved and as a result backscattered electrons which constitute the background are also part of the signal measured, and on the other hand in XPS an X-ray beam is involved and therefore no backscattered electrons are involved, this made it possible to investigate the contribution of backscattered electrons to the background by taking the difference between the spectra measured in AES and those measured in XPS.

Since in the literature a power law is given to describe the contribution of backscattered electrons to the spectrum, having used a 10 keV beam the difference between the two spectra was expected to yield a smooth, steadily increasing line with increasing energy. But instead as a result was obtained something that resembled the peaks. This could be explained only by taking into consideration that the contribution of the backscattered electrons is not only a simple, smooth power law as it would be if they entered the sample and got back elastically, but due to inelastic collisions some of them which have enough energy excite additional Auger electrons on their way back as well.

Preparation of stable colloidal aqueous suspensions of magnetic iron-oxide nanoparticles using aspartic acid as surfactant

Klementina Pušnik^{1,2}, Mihael Drogenik^{1,3}, Darko Makovec^{1,2,4}

¹ Department for Materials Synthesis, Jožef Stefan Institute, Ljubljana, Slovenia

² Jožef Stefan International Postgraduate School, Ljubljana, Slovenia

³ Faculty of Chemistry and Chemical Engineering, Maribor, Slovenia

⁴ CENN Nanocenter, Slovenia

klementina.pusnik@ijs.si

Abstract.

Magnetic nanoparticles are a major class of nanoscale materials, with the potential to revolutionize current biological and technological applications. For most of these applications, stable aqueous suspensions of iron-oxide nanoparticles are required. To ensure stability of the aqueous suspensions, different surfactants can be used. One possible type of surfactant used in the stabilization of aqueous nanoparticles suspensions are amino acids, which play an important role in the body, in the cell growth in tissue repair. In our study, the adsorption of aspartic acid was studied with two different approaches. In both approaches, nanoparticles dispersions have narrow hydrodynamic size distribution, suggesting a good colloidal stability. The adsorption of aspartic acid onto the maghemite nanoparticles resulted only in minor changes of the suspension's zeta potential. The nanoparticles size measured with TEM changed with the type of synthesis, from $8\pm$ nm for one-step to $10\pm$ nm for two-step synthesis.

Keywords: magnetic nanoparticles, stable aqueous suspension of iron-oxide nanoparticles, surfactants, amino acids.

1 Introduction

Magnetic iron-oxide nanoparticles are used for biomedical applications as drug delivery systems, for cell separation, as mediators in magnetic hyperthermia, as MRI contrast agents, etc. Most of these applications require stable, well-dispersed aqueous suspensions of the nanoparticles, which could be stabilized in a carrier liquid using different surfactants. The adsorption of the surfactants usually increases the surface

charge and thus provides electrostatic repulsive forces acting between the nanoparticles in the aqueous suspension. For in vivo applications, the organic shell of the surfactants should be nontoxic and biocompatible. One possible type of surfactant used for the stabilization of the aqueous nanoparticles' suspensions is amino acids [1, 2]. The amino acids also play an important role in the body.

In our study, aspartic acid was used as surfactant for preparation of stable aqueous suspensions of magnetic iron-oxide nanoparticles. Two different approaches of suspension preparation were applied: In the two-step approach, the aspartic acid was adsorbed onto the as-synthesized nanoparticles, whereas in the so the one-step approaches, the nanoparticles were synthesized using coprecipitation in the presence of the amino acid.

Maghemite iron-oxide ($\gamma\text{-Fe}_2\text{O}_3$) nanoparticles were synthesized using precipitation of Fe^{3+} and Fe^{2+} ions from their aqueous solutions with aqueous ammonia as precipitating agent. In the latter case, the amino acid influences the formation mechanism of the nanoparticles. Characterization using transmission electron microscopy (TEM) detected difference between the size of iron-oxide nanoparticle stabilized with aspartic acids and iron-oxide nanoparticle without the surfactant. Therefore, we propose that in one-step approach, amino acids effect on the crystals growth of maghemite. The stability of the suspensions of aspartic-acid-coated iron-oxide nanoparticles was investigated by measuring the zeta potentials and the hydrodynamic-size distribution using the dynamic light-scattering method (DLS).

2 Experimental Section

Stable aqueous suspensions of maghemite nanoparticles using aspartic acids as a surfactant were prepared with two approaches: a two-step and a one-step approach. In two-step approach aspartic acid was adsorbed onto the pre-synthesis maghemite nanoparticles. The maghemite iron-oxide ($\gamma\text{-Fe}_2\text{O}_3$) nanoparticles were synthesized using co-precipitation of Fe^{3+} and Fe^{2+} ions from their aqueous solutions with aqueous ammonia as precipitating agent, as described in literature [3]. In brief, pH of an aqueous solution (500 mL) containing sulphates of Fe^{3+} (0.027 mol L^{-1}) and Fe^{2+} (0.023 mol L^{-1}) ions was increased to 3 with addition of concentrated aqueous ammonia (25%). After 0.5 hours, the pH was further increased to 10.5 with further addition of aqueous ammonia (250 mL, 25%) under vigorous stirring. After edging

time of 0.5 hours the suspension of precipitated magnetic nanoparticles is separated on a permanent magnet, washed four times with diluted aqueous ammonia at pH 10.5 and suspended in distilled water. To prepare stable aqueous suspension, the aspartic acid was adsorbed onto the as-synthesized nanoparticles. 200 mL of aqueous solution of aspartic acid (0.05 mol L^{-1}) was added to 25 mL of suspension containing 500mg of the nanoparticles at pH=4.0, sonicated for 10 minutes and vigorously stirred for 5h at room temperature. After adsorption, the nanoparticles were washed with distilled water using centrifugation and finally dispersed. The aspartic-acid-adsorbed maghemite nanoparticles were dispersed in water at pH=11. In one-step approach, the nanoparticles were synthesized in the presence of aspartic acid. The procedure used for the nanoparticles synthesis was equal to that used in the two-step procedure, except that the aspartic acid (0.01mol) was added to the $\text{Fe}^{3+}/\text{Fe}^{2+}$ solution before addition of the aqueous ammonia.

The synthesized nanoparticles were characterized and transmission electron microscopy (TEM) (Jeol 2100). For the TEM investigations the nanoparticles were deposited on a copper-grid-supported perforated transparent carbon foil. The room temperature magnetic properties of the nanoparticles were measured with a vibrating-sample magnetometer (VSM) (Lake Shore 7307 VSM).

The adsorbed aspartic acid on the dried nanoparticles from the suspension and acid, which was dissolved in the suspension (un-adsorbed) were gravimetrically determined. The stability of the suspensions of aspartic-acid-adsorbed iron-oxide nanoparticles was followed by measuring the zeta-potentials (Brookhaven, Instruments Corporation, Zeta PALS) and the hydrodynamic-size distribution using the dynamic light-scattering method (DLS) (Fritsch, ANALYSETTE 12 Dynasizer).

3 Results and Discussion

TEM images of aspartic-acid-coated maghemite nanoparticles, prepared by one-step and two-step synthesis are shown in Figure 1. The nanoparticles exhibited a globular shape. The size distribution was obtained by measuring at least 150 nanoparticles and fitted by using a log-normal distribution. The size of aspartic-acid-adsorbed maghemite nanoparticles by one-step synthesis is $8 \pm \text{ nm}$, whereas the nanoparticles prepared by the two-step approach were considerably larger, showing the average particles size of $10 \pm \text{ nm}$. The result indicates that the aspartic acid during the one-

step synthesis limits the particles growth, most probably by adsorption onto the growing nanoparticles thus impeding the mass transport.

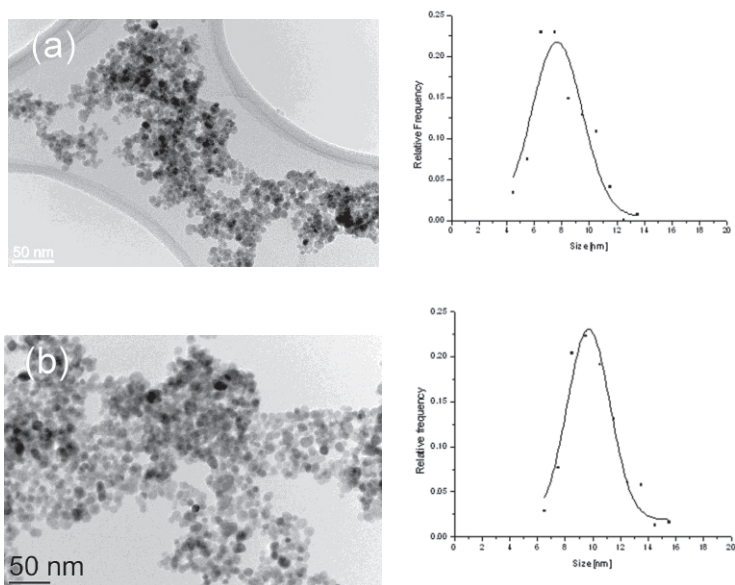


Figure 1. TEM images and the corresponding size distribution of aspartic-acid-adsorbed maghemite nanoparticles, prepared by the one-step approach (a), and the two-step approach (b).

A stable suspension of aspartic-acid-adsorbed maghemite nanoparticles was prepared using two approaches, two-step and one-step. We assume that the aspartic acid adsorb onto the as-synthesized nanoparticles in the aqueous suspension at pH 4 due to the electrostatic attraction between the negatively charged carboxyl groups and the positively charged surface. As-synthesized maghemite nanoparticles exhibited an isoelectric point (IOP) around pH 6 and were positively charged at pH 4 (Fig. 2).

The adsorption of aspartic acid onto the maghemite nanoparticles resulted only in minor changes of the suspension's zeta potential (Fig. 2). The nanoparticles with adsorbed aspartic acid display a positive zeta potential under acidic conditions, which can be described to positive charge origination from protonated amino

groups in aqueous conditions. But under basic condition, nanoparticles showed negative zeta potential. As the pH increases carboxyl groups lose the hydrogen and get negatively charged [4]. The IOP for the aspartic-acid adsorbed nanoparticles was around 5.5. (Fig. 2). Zeta-potential measurements showed no significant differences between the two adsorption approaches.

However, whereas the suspension of the as-synthesized nanoparticles rapidly sedimented, the aspartic-acid-adsorbed nanoparticles formed a stable aqueous suspensions (ferrofluids).

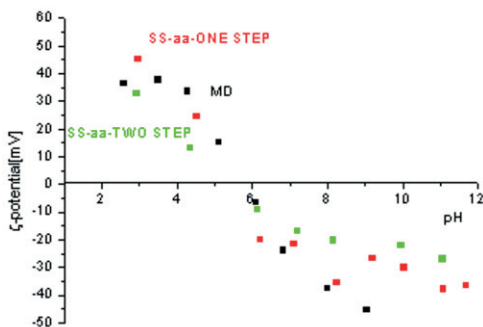


Figure 1. ζ -potential of: uncoated maghemite nanoparticles (MD), aspartic-acid adsorbed nanoparticles prepared by one-step procedure (SS-aa-ONE STEP), and aspartic-acid adsorbed nanoparticles prepared by two-step procedure (SS-aa-TWO STEP).

The content of the aspartic acid on the tried nanoparticles from the suspension was gravimetrically determined. Both the adsorbed acid and acid, which was dissolved in the suspension (un-adsorbed) were determined in this way. The content aspartic acid of was determined to be 12 wt.% for the sample prepared in two-steps and 10 wt.% for the sample prepared in one-step.

The stability of the suspensions of aspartic-acid-coated iron-oxide nanoparticles synthesized by one-step and two-step approaches was followed with the hydrodynamic-size distribution using DLS. In both cases, nanoparticles dispersions had narrow hydrodynamic-size distribution, which did not change with time significantly, suggesting a good colloidal stability (Fig. 3). In this case, the

hydrodynamic size of the nanoparticles in the suspension corresponds well to the size measured from TEM images.

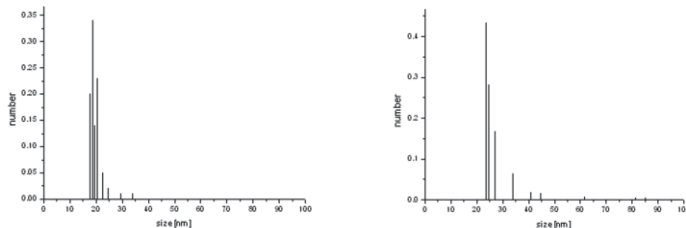


Figure 3. Particles size distribution of aspartic-acid- adsorbed maghemite nanoparticles in aqueous suspension (5 mg/mL): left prepared by two-step approach and right prepared by one-step approach.

4 Conclusions

Two different approaches for obtaining stable aqueous suspension of superparamagnetic maghemite nanoparticles in the presence of aspartic acid as surfactant were systematically studied.

The nanoparticles exhibited a globular shape. The size of aspartic-acid-adsorbed maghemite nanoparticles by one-step synthesis is $8 \pm$ nm, whereas the nanoparticles prepared by the two-step approach were considerably larger, showing the average particles size of $10 \pm$ nm. The result indicates that the aspartic acid during the one-step synthesis limits the particles growth, most probably by adsorption onto the growing nanoparticles thus impeding the mass transport.

The narrow hydrodynamic-size distribution of the nanoparticles in the suspension, which did not change with time significantly, suggesting a good colloidal stability, corresponds well to the size measured from TEM images.

The zeta measurements showed that the adsorption of aspartic acid onto the maghemite nanoparticles resulted only in minor changes of the suspension's zeta potential.

The content of aspartic acid was determined to be 12 wt.% for the sample prepared in two-steps and 10 wt.% for the sample prepared in one-step approach. So, the

gravimetrically determined results indicated on adsorption process of aspartic acid onto the surface of maghemite nanoparticles.

References:

- [1] Qu, H.; Ma, H.; Zhou, W.; O'Connor, C. J. In situ surface functionalization of magnetic nanoparticles with hydrophilic natural amino acids. *Inorganica Chimica Acta*, **389**: 60-65 (2012).
- [2] Theerdhala, S.; Bahadur, D.; Vitta, S.; Perkas, N.; Zhong, Z.; Gedanken, A. Sonochemical stabilization of ultrafine colloidal biocompatible magnetite nanoparticles using amino acid, L-arginine, for possible bio applications. *Ultrasonics Sonochemistry*, **17**: 730-737 (2010).
- [3] Kralj, S.; Drogenik, M.; Makovec, D. Controlled surface functionalization of silica-coated magnetic nanoparticles with terminal amino and carboxyl groups. *J Nanopart Res*, **13**: 2829-2841 (2010).
- [4] Durmus, Z.; Kavas, H.; Toprak, M.S.; Bayakal, A.; Altinçekiç T.G.; Aslan.A.; Bozkurt, A.; Coçgun,S. L-lysine coated iron oxide nanoparticles: Synthesis, structural and conductivity characterization. *Journal of Alloys and Compounds*, **484**: 371-376 (2009).

For wider interest

Nano-sized materials such as magnetic nanoparticles, which are a major class of nanoscale materials (ferro/ferrimagnetic materials, such as iron, nickel, cobalt, and magnetic oxides like iron oxides, including magnetite and maghemite), have fascinating physical-chemical properties that if tuned properly, can design new bio-diagnostics and therapeutic strategies, as well as, innovative biotechnology methodologies. The most common synthesis methods of iron-oxides nanoparticles are: co-precipitation, thermal decomposition, hydrothermal synthesis, microemulsion, sonochemical synthesis.

For biological applications, the magnetic nanoparticles are coated with biocompatible coating of organic molecules. Thus, the magnetic nanoparticles have usually core-shell structure. The organic shell prevents agglomeration of the iron-oxide nanoparticles in the aqueous suspensions and enables bonding of different molecules needed in application to their surfaces.

For in vivo applications, the organic shell of the surfactants should be nontoxic and biocompatible. One possible type of surfactant used in the stabilization of aqueous nanoparticles suspensions is amino acids. The amino acids also play an important role in the body. In our study, aspartic acids were successfully used as surfactant for preparation of stable aqueous suspensions of magnetic iron-oxide nanoparticles.

Obdelava polimernih podlag z nizekotlačno kisikovo plazmo za boljše vezavo malignih človeških kostnih celic

Nina Recek^{1,2}, Alenka Vesel¹, Miran Mozetič¹

¹ Odsek F4, Inštitut Jožef Stefan, Ljubljana, Slovenija

² Mednarodna podiplomska šola Jožefa Stefana, Ljubljana, Slovenija

nina.recek@ijs.si

Povzetek. Vakuumske tehnologije si postopoma utirajo pot v biologiji in medicini. Sodobni tehnološki postopek za obdelavo podlag, na katerih se razraščajo biološke celice, je obdelava z nizekotlačno plinsko plazmo. V prispevku opisujemo vpliv plazemske obdelave polimera PS (Polistiren), ki ga uporabljamo kot podlago za razraščanje malignih človeških kostnih celic. Že kratkotrajna obdelava povzroči spremembo površinskih lastnosti polimera, kar vodi k bistvenemu izboljšanju vitalnosti tovrstnih celic. Začetno fazo razraščanja smo opazovali z elektronsko mikroskopijo. Ugotovili smo, da maligne kostne celice že v kratkem času tvorijo nitaste (fibrilarne) strukture na podlagah, obdelanih z kisikovo plazmo, medtem, ko tega pojava nismo opazili na neobdelanih podlagah. Tovrstni eksperimenti predstavljajo prvi korak k selektivni vezavi rakastih celic na plazemsko obdelanih materialih.

Gljučne besede: biološke celice, nizekotlačna plinska plazma, PS polimer

1 Uvod

Termodinamsko neravnovesna stanja plinov so se dodobra uveljavila kot medij za površinsko modifikacijo različnih vrst trdnih materialov [1-5]. Bistvena prednost tovrstnega stanja plinov pred ravnovesnim je v izredno visoki kemijski reaktivnosti plina že pri sobni temperaturi. To dejstvo lahko izkoristimo predvsem za modifikacijo površinskih lastnosti materialov [16], ki ne prenesejo segrevanja do visokih temperatur [6-13]. Neravnovesno stanje plina je mogoče doseči z različnimi tehnikami, najpomembnejša pa je prehod plina skozi nizekotlačno razelektritev. V plinski razelektritvi so prisotni prosti elektroni, ki se v električnem polju pospešujejo do kinetične energije, ki ustreza temperaturi več 10.000 K. Elektroni s tako visoko

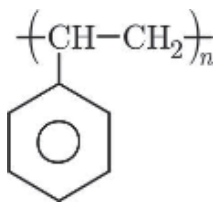
temperaturo lahko predajo del svoje kinetične energije molekulam plina in jih s tem vzbujajo, disociirajo ali ionizirajo. Zaradi izredno majhnega razmerja med maso elektronov in maso plinskih molekul, elektroni ne morejo predajati znatnega dela svoje kinetične energije kinetični energiji molekul, zato ostane plin hladen. V nizkotlačni plazmi imamo tako sočasno prisotne vroče elektrone in hladne molekule, ki se običajno nahajajo v vzbujenih stanjih. Ob dotiku plazme s površino trdnih snovi molekule v vzbujenih stanjih kemijsko reagirajo z atomi na površini trdne snovi, ne da bi jo segrevali. Vroči elektroni prav tako zanemarljivo segrevajo trdno snov zaradi njihove majhne mase in s tem zanemarljive toplotne kapacitete. Tovrstno stanje plina običajno imenujemo neravnovesna plinska plazma.

Plazmo lahko vzbujamo v katerikoli plinih ali plinskih mešanica. Za obdelavo površine polimernih materialov je še posebej zanimiva kisikova plazma [14,15]. Notranje molekule kisika se ob neprožnih trkih z elektroni vzbujajo v stanja, ki so metastabilna. Zaradi izredno velike življenjske dobe obeh metastabilnih stanj nevtralne molekule kisika, se lahko le te disociirajo ob naslednjem trku s prostimi elektroni. Posledica navedene stopenjske disociacije je izredno velika stopnja disociiranosti kisikovih molekul že pri razmeroma nizki temperaturi in gostoti elektronov. Že pri majhnih močeh plinske razelektritve zaradi tega zlahka dosežemo stopnjo disociiranosti reda velikosti 10%. Tako visoko disociiranost bi v ravnovesnem stanju plina dosegli šele pri temperaturi okoli 100.000 K.

Kisikovi atomi so kemijsko izredno reaktivni, tako da reagirajo s polimernimi materiali že pri sobni temperaturi. Na površini polimera tako nastane izredno tanka plast, ki je bogata s kisikovimi funkcionalnimi skupinami, kar se odraža v izredno veliki hidrofilnosti prvotno hidrofobnega materiala [7].

2 Eksperimentalne metode

Kot podlago za razraščanje celic smo izbrali polistiren (PS). Gre za zmerno hidrofoben material, na katerem je kontaktni kot vodne kapljice okoli 85°. Strukturna formula tega polimera je prikazana na sliki 1.



Slika 1: Strukturna formula polistirena (PS)

Polimerne folije smo obdelali s kisikovo plazmo v ustreznem plazemskem reaktorju [17,18]. Osrednji del reaktorja je steklena cev premera 4 cm in dolžine 60 cm. Okoli cevi je ovita bakrena tuljava, ki je priključena na visokofrekvenčni generator. Generator deluje pri industrijski frekvenci 27,12 MHz in ima nazivno moč 400 W. Zaradi slabe usklajenosti med primarnim resonančnih krogom generatorja in sekundarnim krogom, ki ga predstavlja bakrena tuljava, je koristna moč skoraj 10-krat manjša od nazivne moči generatorja.

Stekleno cev na eni strani črpamo z dvostopenjsko rotacijsko črpalko nazivne črpalne hitrosti 16 m³/h, na drugi pa neprestano vpihujemo kisik iz jeklenke. Tlak merimo s kalibriranim Piranijevim merilnikom. Za vzbujanje plazme smo izbrali takšne razmere, pri katerih je tlak plina med črpanjem 75 Pa. Pri tem tlaku namreč dosežemo največjo stopnjo disociiranosti kisikovih molekul, ki je okoli 20%. Čas obdelave vzorcev v kisikovi plazmi je 30 s.

Funkcionalne skupine na površini obdelovancev pred in po plazemski obdelavi smo določili z rentgensko fotoelektronsko spektroskopijo (XPS). Vzorce smo vzbujali z monokromatizirano rentgensko svetlobo AlK_α s kinetično energijo fotonov 1486,6 eV in merili energijo izsevanih fotoelektronov. V spektru fotoelektronov, ki predstavlja porazdelitev fotoelektronov po njihovi vezavni energiji, so prisotni vrhovi, značilni za elemente, ki so na površini vzorca. Iz takšnega preglednega spektra fotoelektronov je mogoče oceniti sestavo površinske plasti debeline reda nekaj nanometrov, visokoločljivostni spekter ogljika pa omogoča prepoznavanje specifičnih funkcionalnih skupin, ki nastajajo na površini polimera med plazemsko obdelavo.

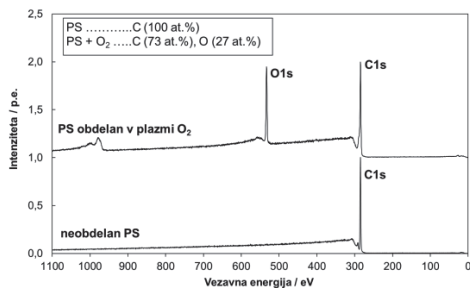
2.1 Priprava HOS celic

Človeške maligne kostne celice (HOS) so bile dobavljene iz American Type Culture Collection (ATCC). Vzorce smo po plazemski obdelavi inkubirali v hranilnem mediju za rast celic (DMEM), kateremu smo dodali 10% telečji serum (FCS), 2mM L-glutamina in penicilin/streptomycin (1000 U/mL in 1000 µg/L) [19]. Celice smo postavili v inkubator na temperaturo 37 °C pri konstantni vlažnosti s 5% CO₂. Nato smo semikonfluentni kulturi za 5 min dodali 0.25% (w/v) raztopino tripsina, kar je povzročilo, da so se celice odlepile od podlage. Dodali smo jim tripanko modrilo, pri čemer so se žive celice obarvale modro, mrtve pa so ostale ne obarvane [20]. Žive celice smo nato prešteli s Bürker-Turk hemocitometrom in jih nato dalje uporabili za poskus.

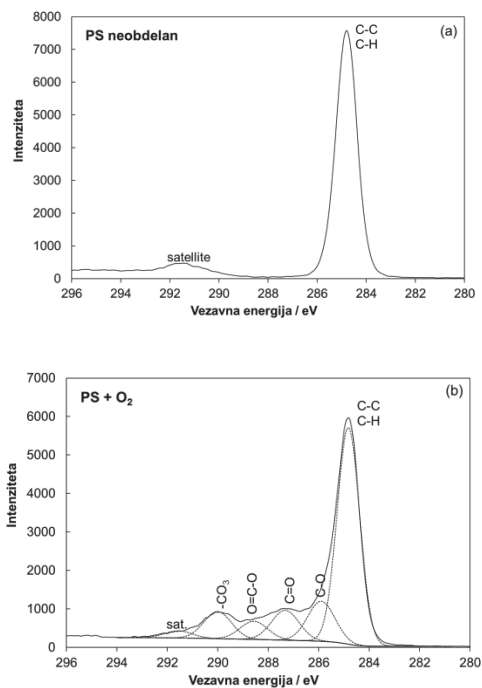
3 Rezultati in diskusija

Na sliki 2 prikazujemo pregledni spekter fotoelektronov za neobdelan in plazemsko obdelan polistiren. Na neobdelanem vzorcu prevladuje vrh ogljika, kar je posledica sestave tega polimera (slika 1). Po plazemski obdelavi lahko opazimo tudi izrazit vrh kisika, ki ga pripišemo kemijski vezavi atomarnega kisika iz plazme. Podrobnejša analiza funkcionalnih skupin [14] je razvidna iz visoko resolucijskega spektra, ki je prikazan na sliki 3a. Za neobdelan vzorec opazimo enovit ogljikov vrh, ki pripada vezavi ogljikovih atomov na sosednje ogljikove in vodikove atome. Levo od glavnega vrha lahko opazimo tudi nižji, vendar lepo opazen vrh, ki je značilen za aromatske polimere.

Na sliki 3b je prikazan tudi visokoločljivostni vrh ogljika po obdelavi s kisikovo plazmo. Odsotnost vrha, ki je značilen za aromatske polimere, pripišemo cepljenju benzenovih obročev na površini polimera zaradi oksidacije materiala. Ogljikov vrh sedaj ni enovit, ampak opazimo več podvrhov, ki ustrezajo različnim s kisikom bogatim funkcionalnim skupinam. Kisikova plazma je torej povzročila nastanek polarnih funkcionalnih skupin, kar se na makroskopskem nivoju odraža z velikim povečanjem površinske energije materiala.



Slika 2: Pregledni XPS spekter za neobdelan PS in PS, obdelan v kisikovi plazmi



Slika 3: Visokoločljivostni ogljikov vrh C1s za (a) neobdelan PS in (b) PS po obdelavi s kisikovo plazmo (označeni so podvrhovi, ki prikazujejo različne funkcionalne skupine, nastale na površini PS po obdelavi s kisikovo plazmo)

Tako obdelane vzorce smo inkubirali z malignimi kostnimi celicami. Na sliki 4 prikazujemo značilno sliko celice na površini neobdelanega materiala, na sliki 5 pa na

površini materiala, ki je bil predhodno obdelan s kisikovo plazmo. Bistvena razlika med obema slikama je v pojavu nitastih (fibrilarnih) struktur, ki jih opazimo na sliki 5 in se odraža v obliki drobnih izrastkov, ki se širijo v okolico celice.

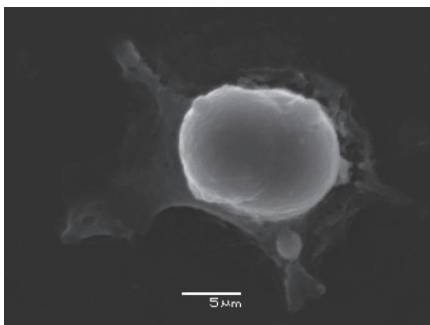


Figure 4: SEM-slika maligne kostne celice (HOS-celice) na površini neobdelanega PS

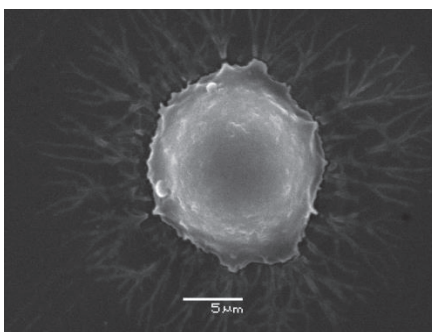


Figure 5: SEM-slika maligne kostne celice (HOS-celice) na površini PS, obdelanega s kisikovo plazmo

Tovrstne strukture omogočajo odličen oprijem celice na podlago in s tem zagotavljajo pogoje za celično rast in razmnoževanje. Tovrstnih struktur ni opaziti v okolici celic, ki smo jih nanесли na neobdelane polistirenske podlage.

Razliko v oprijemu celic pripišemo funkcionalnih skupinam, ki so prisotne na površini polimernih podlag. Dokler imamo na površini zgolj nepolarne funkcionalne skupine, celica ne prepozna polistirena kot optimalne podlage za rast in

razmnoževanje. Po daljšem času bi se celice sicer prilagodile tudi na to podlago, saj je znano, da je prav polistiren zelo pogost material, ki se uporablja za tovrstne raziskave. Z znanstvenega vidika je zelo pomembno dejstvo, da se celice zelo hitro čvrsto vežejo na plazemsko obdelane podlage. Tako čvrsta vezava lahko omogoča zajemanje malignih celic že v krvnem obtoku, s čimer je mogoče zaustaviti prenos metastaz od žarišča v odročne dele telesa in s tem upočasniti metastaziranje. Za praktično uporabo je izredno pomembno dejstvo, da je mogoče z neravnovesno kisikovo plazmo enakomerno funkcionalizirati polimerne materiale kompleksnih oblik.

Kot smo že omenili je temperatura plinskih molekul enaka sobni. Pri teh razmerah se molekule in atomi kaotično gibljejo v plazemskem reaktorju. Gostota toka atomov in molekul je zaradi tega izotropna, kar v praksi pomeni, da lahko reaktivni kisikovi atomi dosežejo površino polimera tudi v vdolbinah in režah. Pri tlaku 75 Pa je povprečna prosta pot kisikovih atomov in molekul reda velikosti 0.1 mm, tako da zlahka dosežejo površine v notranjosti por tovrstnih dimenzij. V notranjost manjših in globljih por kisikovi atomi sicer lahko prodirajo, vendar pa njihova gostota z globino postopno pada. Razlog za to je izguba atomov zaradi kemijskih reakcij na površini obdelovanca, kakor tudi postopne rekombinacije atomov v molekule. K sreči sta oba procesa razmeroma malo verjetna, zaradi česar je omogočena tudi funkcionalizacija obdelovancev s precej kompleksno obliko. Oba procesa sta sicer eksotermna, zaradi česar se material med plazemsko obdelavo segreva, ker pa sta malo verjetna, lahko vseeno dosežemo primerno stopnjo funkcionaliziranosti pri dovolj nizki temperaturi, s čimer se izognemo morebitnim spremembam ostalih funkcionalnih lastnosti polimernih materialov.

4 Sklep

V prispevku smo opisali odziv malignih kostnih celic na funkcionalne skupine na površini polistirena. Ugotovili smo, da že kratkotrajna obdelava s kisikovo plazmo omogoči bistveno boljši oprijem celic na podlago. Izboljšanje vezave je posledica visoke omočljivosti plazemsko obdelanih površin, ki jo dosežemo z nasičenostjo s kisikovimi funkcionalnimi skupinami. Maligne kostne celice na tako obdelanih površinah že po kratkotrajni inkubaciji razvijejo nitaste strukture, kar omogoča odličen oprijem, ki je nujen za rast in razmnoževanje celic. Opisane raziskave

predstavljajo prvi korak k razvoju materialov za selektivno adsorpcijo rakastih celic, kar lahko v končni fazi privede k zmanjšanju razvoja metastaz pri rakastih obolenjih.

5 LITERATURA

- [1] Asadinezhad A, Novak I, Lehocky M, Sedlarik V, Vesel A, Junkar I, Saha P, Chodak I. *Plasma Processes Polym* 2010;7:504-514.
- [2] Lehocky M, Lapcik L, Neves MC, Trindade T, Szyk-Warszynska L, Warszynski P, Hui D. *Mat Sci Forum* 2003;426:2533-2538.
- [3] Asadinezhad A, Novak I, Lehocky M, Sedlarik V, Vesel A, Saha P, Chodak I. *Colloids Surf B Biointerfaces* 2010;77:246-256.
- [4] Velzenberger E, Pezron I, Legeay G, Nagel MD, El Kirat K. *Langmuir* 2008;24:11734-11742.
- [5] Legeay G, Poncin-Epaillard F, Arciola CR. *Int J Artif Organs* 2006;29:453-461.
- [6] Kasemo B. *Surf Sci* 2002;500:656-677.
- [7] D. Klee, H. Höcker, *Adv. Polym. Sci.* 149 (2000) 1-57.
- [8] Ramires PA, Mirengi L, Romano AR, Palumbo F, Nicolardi G. *J Biomed Mater Res* 2000;51:535-539.
- [9] Pu FR, Williams RL, Markkula TK, Hunt JA. *Biomaterials* 2002;23:4705-4718.
- [10] Alves CM, Yang Y, Carnes DL, Ong JL, Sylvia VL, Dean DD, Agrawal CM, Reis RL. *Biomaterials* 2007;28:307-315.
- [11] Dowling DP, Miller IS, Ardhaoui M, Gallagher WM. *J Biomater Appl* 2010;21:1-21.
- [12] Desmet T, Morent R, De Geyter N, Leys C, Schacht E, Dubruel P. *Biomacromolecules* 2009;10:2351-2378.
- [13] Geckeler KE, Wacker R, Martini F, Hack A, Aicher WK. *Cell Physiol Biochem* 2003;13:155-164.
- [14] Vesel A. *Surf Coat Technol* 2010;205:490-497.
- [15] Vesel A, Junkar I, Cvelbar U, Kovac J, Mozetic M. *Surf Interface Anal* 2008;40: 1444-1453.
- [16] Vesel A. *Inf Midem* 2009;38:257-265.
- [17] Vujosevic D, Vranica Z, Vesel A, Cvelbar U, Mozetic M, Drenik A, Mozetic T, Klanjsek Gunde M, Hauptman N. *Mater Tehnol* 2006;40:227-232.
- [18] Cvelbar U, Mozetic M, Hauptman N, Klanjsek-Gunde M. *J Appl Phys* 2009;106:103303-1-103303-5.
- [19] Mrakovcic L, Wildburger R, Jaganjac M, Cindric M, Cipak A, Borovic-Sunjic S, Waeg G, Milankovic AM, Zarkovic N. *Acta Biochim Pol* 2010;57:73-178.
- [20] Jaganjac M, Matijevic T, Cindric M, Cipak A, Mrakovcic L, Gubisch W, Zarkovic N. *Acta Biochim Pol* 2010;57:179-183.

Za širšo javnost

Vakuumske tehnologije si postopoma utirajo pot v biologiji in medicini. Sodobni tehnološki postopek za obdelavo podlag, na katerih se razraščajo biološke celice, je obdelava z nizekpotlačno plinsko plazmo. Polimeri imajo nizko površinsko energijo in zato tudi slabe adhezijske lastnosti in biokompatibilnost. Plazemske tehnologije so obetavna tehnika za spremembo površinskih lastnosti polimerov. Z plazemsko obdelavo polimerov ustvarimo na površini polimera nove funkcionalne skupine in s tem spremenimo kemijsko sestavo površine. Že kratkotrajna obdelava povzroči spremembo morfoloških lastnosti površine polimera, spremembo hrapavosti in omočljivosti površine, kar vodi k bistvenemu izboljšanju adhezije in proliferacije celic na plazemsko obdelanih podlagah. V prispevku opisujemo vpliv plazemske obdelave na morfološke in kemijske lastnosti polimera PS (Polistiren), ki ga uporabljamo kot podlago za razraščanje malignih človeških kostnih celic. Polimer PS je bil obdelan s kisikovo plazmo v ustreznem plazemskem reaktorju. Spremembo morfologije površine polimera smo spremljali s pomočjo mikroskopa na atomsko silo (AFM), spremembo kemijske sestave z rentgenskim fotoelektronskim spektrometrom (XPS), omočljivost polimerne površine pa smo določili z merjenjem kontaktnega kota vodne kapljice. Začetno fazo razraščanja celic smo opazovali z elektronsko mikroskopijo. Ugotovili smo, da maligne kostne celice že v kratkem času tvorijo nitaste (fibrilarne) strukture na podlagah, obdelanih z kisikovo plazmo, medtem, ko tega pojava nismo opazili na neobdelanih podlagah. Tovrstni eksperimenti predstavljajo prvi korak k selektivni vezavi rakastih celic na plazemsko obdelanih materialih.

The effect of silica sol infiltration on the properties of dental 3Y-TZP ceramics

Anastasia Samodurova^{1,2}, Andraž Kocjan, Irena Pribošič, Tomaž Kosmač

¹ Department of Engineering Ceramics, Jožef Stefan Institute, Ljubljana, Slovenia

² Jožef Stefan International Postgraduate School, Ljubljana, Slovenia

anastasia.samodurova@ijs.si

Abstract. The effect of adding silica on the phase composition, microstructure, mechanical properties and low temperature degradation (LTD) of 3 mol% yttria-stabilised zirconia (3Y-TZP) ceramics, produced from two ready-to-press granulated powders of the same nominal chemical composition, but differing in content of alumina, is presented. Silica doped 3Y-TZP materials were prepared by the infiltration of silica sol *in situ* synthesized by the sol-gel method using dynasylan as a precursor into the biscuit-sintered porous zirconia discs followed by sintering at 1450 °C. The results of transmission electron microscopy (TEM) and energy dispersive X-ray spectroscopy (EDS) analyses revealed that silica was mainly present as an amorphous phase concentrated at triple grain junctions. The presence of silica substantially decreases the amount of transformed monoclinic fraction in sintered 3Y-TZP after accelerated ageing, compared to the monolithic 3Y-TZP sintered at the same temperature and does not show any significant effect on flexural strength, Vickers hardness and indentation toughness.

Keywords: zirconia, infiltration, X-ray diffraction (XRD), microstructure, LTD.

1 Introduction

Yttria partially stabilized tetragonal zirconia (Y-TZP) is becoming increasingly popular as an alternative material in restorative dentistry. Nowadays dental zirconia frameworks are produced by computer-assisted design and manufacturing (CAD/CAM) technology followed by pressure-less sintering to nearly-theoretical density [1].

One of the issues concerning tetragonal Y-TZP ceramics, not only in dentistry, is their sensitivity to low temperature degradation in aggressive environments, i.e. ageing [2]. Such degradation occurs by a slow surface transformation from metastable tetragonal phase to a more stable monoclinic phase in the presence of water or water vapor. Being subject to a volume increase, tetragonal to monoclinic (t-m) transformation induces the formation of microcracks at the surface. This offers a path for the water to penetrate and exacerbate the process of surface degradation and the transformation process. The growth of the transformation zone results in severe microcracking and grain pull out, and finally surface roughening which leads to strength degradation.

LTD resistance of dental zirconia can be improved by decreasing grain size or increasing the yttria content in the starting powder. However, both of these approaches lead to the reduction of the mechanical properties of zirconia, thus making it unattractive. Another way to tackle the problem is by adding of dopants. It was also reported that the addition of silica to Y-TZP ceramic improves the LTD resistance [3-5]. All studies were carried out by introducing appropriate levels of SiO₂ as dopants to a commercial Y-TZP powder. Another way of introducing silica into the Y-TZP ceramic could be the pressureless infiltration of pre-sintered specimens with silica precursors or with silica sol synthesized *in situ* by the sol-gel method. In this way, silica can be easily included into the already soft milled zirconia frameworks.

In the present work, silica was added through the infiltration with silica sol into the pre-sintered porous ceramic specimens. After final sintering ceramic specimens were verified for fractional density, mean grain size, mechanical properties and subjected to accelerated ageing. The final aim was to improve LTD resistance without affecting mechanical properties.

2 Experimental

Two commercially available, ready-to-press, granulated, biomedical-grade Y-TZP powders (Tosoh, Japan) with different amount of alumina were used for the preparation of specimens: TZ-PX-242A contains 0.05% alumina and the TZ-3YB

grade is essentially alumina-free. Both powders contain 3 mol% yttria in the solid solution to stabilize the tetragonal structure and 3 wt% of an acrylic binder.

Uni-axial dry pressing at 150 MPa in a floating die was used to shape green disks of 20 mm in diameter and 2 mm in thickness. Afterwards they were pre-sintered in air for 2 h at 900 °C. After pre-sintering specimens of each material were randomly divided into two groups. One group was left untreated and served as a control group. Other group of specimens was infiltrated with silica sol, synthesized in situ by the sol-gel method through hydrolysis of dynasylan (Dynasylan® 6490, Evonik, Germany): specimens were immersed in a mixture of absolute ethanol and dynasylan; the hydrolysis was carried out by dropwise addition of an aqueous ammonia (25%) at room temperature. The concentration of SiO₂ in final solution was 0.24 mol/l. Specimens were infiltrated for 1 cycle, soaking for 30 min. Thereafter they were dried and finally sintered at 1450 °C for 4 h together with the controls. After sintering ceramic specimens were verified for fractional density, mean grain size, mechanical properties and subjected to accelerated ageing.

The fractional density of sintered disks was determined with Archimedes method using distilled water as the immersion liquid. The relative densities were calculated by adopting a theoretical density of $\rho_T = 6.08 \text{ g/cm}^3$. The grain size evaluations were made on FE-SEM (Jeol JSM-7600F, Japan) micrographs of polished (3 μm diamond paste) and thermally etched (1350 °C, 1 h) specimens, using the linear interception method, based on the ASTM E112-96(2004)e2 standard. The specimens for the TEM were prepared by cutting 3-mm diameter discs from the ceramic bodies. These discs were reduced to $\sim 120 \mu\text{m}$ by grinding. A region about 20- μm thick at the centre of the disc was produced using a dimple grinder. Finally, the specimens were thinned by argon-ion erosion at 4 kV with an incident angle of about 10°.

The biaxial flexural strength of the pellets was measured using a piston-on-three-balls test, at a loading rate of 1 mm/min (Galdabini Quasar 50, Italy). The indentation technique was used to determine fracture toughness of SiO₂-doped and undoped Y-TZP. A load of 30 N was applied to the specimens with a Vickers hardness indenter. Fracture toughness was calculated using the length of the cracks emanating from the Vickers impression.

No surface treatment, such as grinding and/or polishing was applied to specimens' surface before *in vitro* ageing experiments. These were conducted in distilled water under isothermal conditions at 134 °C for 6–48 h.

X-ray diffraction patterns in the 25–40° 2 θ range were collected from the specimen's surfaces before and after accelerated ageing experiments using Cu K α radiation (Endeavor D4, Bruker AXS). The relative amount of the transformed monoclinic zirconia (m-ZrO₂) on all the surfaces was determined from the integral intensities of the monoclinic ($\bar{1}$ 1 1)_m and (1 1 1)_m, and the tetragonal (1 0 1)_t peaks according to the method of Garvie and Nicholson [6], which is the most commonly applied to determine the phase composition of zirconia powders and compacts with randomly distributed m-ZrO₂ and t-ZrO₂ phases at any distance from the surface exposed to the XRD analysis.

3 Results and discussion

The relative densities of pre-sintered TZ-PX-242A and TZ-3YB bodies were 58.8% and 56.3% respectively. The relative densities of sintered at 1450 °C silica doped and undoped TZ-PX-242A and TZ-3YB disks are listed in Table 1.

Table 1: Relative density of sintered at 1450 °C monolithic and SiO₂-doped sintered TZ-PX-242A and TZ-3YB disks.

	TZ-PX-242A	TZ-3YB
As sintered	98.6±0.3	96.0 ± 0.7
SiO ₂ -doped	99.2±0.5	96.5±0.4

The mean of grain size for monolithic TZ-PX-242A and TZ-3YB materials sintered at 1450 °C were 0.29±0.03 and 0.31±0.04 μm respectively. SiO₂-doped TZ-PX-242A and TZ-3YB materials sintered at the same temperature exhibit average grain sizes 0.28±0.02 and 0.32±0.04 μm. This result revealed, that the addition of silica into the Y-TZP ceramic by the infiltration of pre-sintered specimens with silica sol for 30 min practically does not change the grain size of material.

TEM and EDS analyses of sintered SiO₂-doped TZ-PX-242A material revealed the presence of amorphous silica phase, which is mainly located in triple grain junctions rather than grain-boundaries (Fig. 1).

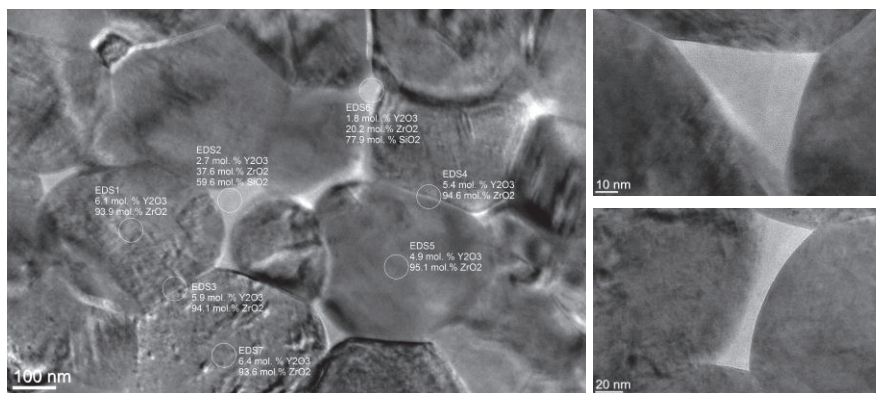


Figure 1: TEM micrographs and results of EDS analysis of TZ-PX-242A/SiO₂ specimen sintered at 1450 °C for 4 h, showing that amorphous silica is mainly present in the grain junctions.

The flexural strength, hardness and fracture toughness of monolithic and SiO₂-doped TZ-PX-242A and TZ-3YB materials are listed in Table 2. No significant differences in Vickers hardness and indentation toughness was observed between SiO₂-doped and monolithic specimens for all materials.

Table 2: Flexural strength, Vickers hardness and indentation toughness of monolithic and SiO₂-doped TZ-PX-242A and TZ-3YB materials.

Sample	Flexural strength, MPa	Hardness, H _v (GPa)	Indentation toughness, K _{IC} (MPa·m ^{1/2})
TZ-PX-242A	1072 ± 48	15.2 ± 0.5	4.5 ± 0.7
TZ-PX-242A/SiO ₂	1150 ± 150	14.1 ± 0.4	4.2 ± 0.3
TZ-3YB	1051 ± 136	14.5 ± 0.5	4.4 ± 0.3
TZ-3YB/SiO ₂	1076 ± 114	13.9 ± 0.3	4.3 ± 0.1

Characteristic XRD patterns obtained in the 21–36 2θ range from SiO₂-doped TZ-PX-242A and TZ-3YB ceramic surfaces sintered for 4 h at 1450 °C, before and after

accelerated ageing at 134 °C in water for different periods of time (6, 12, 24 and 48 h), are represented in Fig. 2a and 2b, respectively. The pattern for as sintered surfaces displays three characteristic peaks positioned at 2θ of 30.2°, 34.7° and 35.2° corresponding to the $(1\ 0\ 1)_t$, $(0\ 0\ 2)_t$ and $(1\ 1\ 0)_t$ planes of the t-ZrO₂ phase, respectively. The amount of silica in SiO₂-doped sintered specimens was below the detection limit.

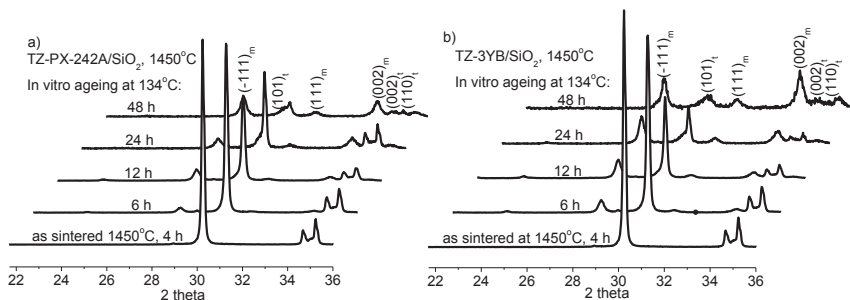


Figure 2: XRD patterns obtained from a) SiO₂-TZ-PX-242A and b) SiO₂-TZ-3YB ceramic surfaces, sintered for 4 h at 1450 °C and aged in water at 134 °C for 6, 12, 24 and 48 h.

After 6 h of ageing, monoclinic $(\bar{1}\ 1\ 1)_m$, $(1\ 1\ 1)_m$, and $(0\ 0\ 2)_m$ peaks (positioned at 2θ of 28.15°, 31.3°, and 34°, respectively) start emerging with a tendency for their intensity to increase with still longer ageing times at the expense of reduced intensity of the tetragonal $(1\ 0\ 1)_t$, $(0\ 0\ 2)_t$ and $(1\ 1\ 0)_t$ peaks. Notice that the intensity of the monoclinic peaks of the aged SiO₂-doped TZ-PX-242A material considerably lower, compared to the aged for the same time SiO₂-doped TZ-3YB material. This result can be explained by the presence of 0.05% alumina in TZ-PX-242A powder. It is well-documented, that addition of small amounts of alumina to 3Y-TZP helps to reduce the tetragonal-to-monoclinic phase transformation upon ageing in water [7,8], but it is not clear why.

The variation of the calculated fraction of the monoclinic zirconia for SiO₂-doped and pure TZ-PX-242A and TZ-3YB materials sintered at 1450 °C with *in vitro* ageing time is represented in Fig. 3. For both materials the presence of silica substantially decreases the monoclinic fraction after ageing, as compared to the monolithic Y-TZP sintered at the same temperature. It seems, that small additions of oxides with

limited solubility in zirconia hinders the nucleation of LTD, but the mechanism is not known.

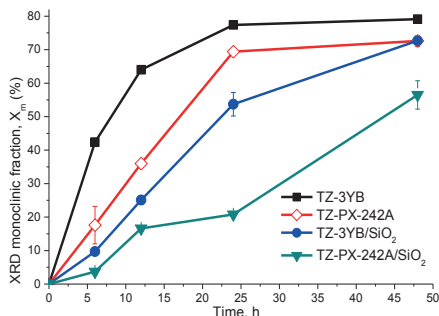


Figure 3: Calculated monoclinic fraction versus *in-vitro* ageing time for monolithic and silica doped TZ-PX-242A and TZ-3YB materials.

4 Conclusions

Silica doped 3Y-TZP ceramics with the same grain size were prepared by the pressureless infiltration of pre-sintered specimens with silica sol synthesized *in situ* by the sol-gel method. The results of XRD, TEM and EDS analysis revealed that silica was mainly present as an amorphous phase concentrated at triple grain junctions. No glassy phase was detected in zirconia grain boundaries. The presence of silica substantially improves the LTD resistance and does not show any significant effect on flexural strength, hardness and fracture toughness of Y-TZP ceramics.

References:

- [1] I. Denry, J. Kelly. State of the art of zirconia for dental applications. *Dental materials*, 24:299-307, 2008.
- [2] J. Chevalier, L. Gremillard. The tetragonal-monoclinic transformation in zirconia: lessons learned and future trends. *Journal of the American Ceramic Society*, 92:1901-1920, 2009.
- [3] L. Gremillard, T. Epicier, J. Chevalier, G. Fantozzi. Microstructural study of silica-doped zirconia ceramics. *Acta mater*, 48:4647-4652, 2000.
- [4] A. Adamski, P. Jakubus, Z. Sojka. Metastabilization of tetragonal zirconia by doping low amounts of silica. *Solid state phenomena*, 128:89-96, 2007.
- [5] T. Nakamura, H. Usami, H. Ohnishio, M. Takeuchit, H. Nishida, T. Sekino and H. Yatani. The effect of adding silica to zirconia to counteract zirconia's tendency to degrade at low temperatures. *Dental Materials Journal*, 30(3):330-335, 2011.
- [6] R. C. Garvie, P.S. Nicholson. Phase analysis in zirconia systems. *J Am Ceram Soc*, 55:303-305, 1972.

- [7] E.S. Elshazly, M.El-Sayed Ali and S.M. El-Hout. Alumina Effect on the Phase Transformation of 3Y-TZP Ceramics. *J. Mater. Sci. Technol*, 24(6):873-877, 2008.
- [8] H. Tsubakino, T. Fujiwara, K. Satani, S. Ioku. Composition of grain boundary phase formed in zirconia-3 mol% yttria containing alumina. *Journal of materials science letters*, 16:1472-1475, 1997.

For wider interest

Yttria partially stabilized tetragonal zirconia (Y-TZP) is becoming increasingly popular as an alternative material in restorative dentistry. One of the issues concerning tetragonal Y-TZP ceramics is their sensitivity to low temperature degradation (LTD), i.e. ageing. LTD appears from spontaneous transformation of metastable tetragonal grains to a more stable monoclinic phase in the presence of water or water vapour.

LTD resistance of dental zirconia can be improved by decreasing grain size or increasing the yttria content in the starting powder. Unfortunately, both of these approaches lead to the reduction of the mechanical properties of zirconia, thus making it unattractive for dental applications. Other way to tackle the problem is by adding of dopants.

Our research is focused on the study of the effects of silica on the phase composition, microstructure, mechanical properties and LTD of the Y-TZP ceramics in order to understand, whether ageing resistance can be increased without decreasing mechanical properties. The other goal of work is to understand the mechanism, by which silica gives rise to increasing ageing resistance of Y-TZP. The understanding of this can help to explain the mechanism of LTD. In order to reach the desired final properties of tetragonal zirconia ceramics, the mechanism of LTD must be known.



**MEDNARODNA
PODIPLomsKA ŠOLA
JOŽEFA STEFANA**

Jamova 39, 1000 Ljubljana

Tel: (01) 477 31 00

Faks: (01) 477 31 10

E-pošta: info@mps.si

<http://www.mps.si/>

